CHEMICAL REVIEWS

pubs.acs.org/CR

Review

Transparent Electronics for Wearable Electronics Application

Published as part of the Chemical Reviews virtual special issue "Wearable Devices".

Daeyeon Won,[§] Junhyuk Bang,[§] Seok Hwan Choi,[§] Kyung Rok Pyun, Seongmin Jeong, Youngseok Lee, and Seung Hwan Ko*

Cite This: *Chem. Rev.* 2023, 123, 9982−10078

Read Online

ACCESS | Metrics & More | Article Recommendations

ABSTRACT: Recent advancements in wearable electronics offer seamless integration with the human body for extracting various biophysical and biochemical information for real-time health monitoring, clinical diagnostics, and augmented reality. Enormous efforts have been dedicated to imparting stretchability/flexibility and softness to electronic devices through materials science and structural modifications that enable stable and comfortable integration of these devices with the curvilinear and soft human body. However, the optical properties of these devices are still in the early stages of consideration. By incorporating transparency, visual information from interfacing biological systems can be preserved and utilized for comprehensive clinical diagnosis with image analysis techniques. Additionally, transparency provides optical imperceptibility, alleviating reluctance to wear the device on exposed skin. This review discusses the recent advancement of transparent wearable electronics in a comprehensive way that includes materials, processing, devices, and applications. Materials for transparent wearable electronics are discussed regarding their characteristics, synthesis, and engineering strategies for property enhancements. We also examine bridging techniques for stable integration with the soft human body. Building blocks for wearable electronic systems, including sensors, energy devices, actuators, and displays, are discussed with their mechanisms and performances. Lastly, we summarize the potential applications and conclude with the remaining challenges and prospects.

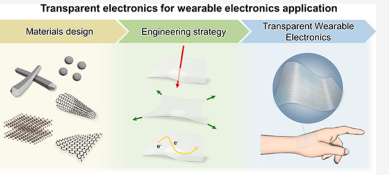

CONTENTS

Received: March 7, 2023
Published: August 5, 2023

https://doi.org/10.1021/acs.chemrev.3c00139
Chem. Rev. 2023, 123, 9982−10078

1. INTRODUCTION

With the remarkable developments of biology, electronics, and artificial intelligence, the interface between the human and machine is blurring and being integrated into a single system.[1] It aims not only to solve problems that have not been conquered so far, such as incurable diseases, but also to augment human abilities. The great attention to human−machine integration led to the intensive development of multidisciplinary technologies to monitor and maintain human health. Now, accurate diagnosis of health status is possible through bulky machines composed of sophisticated electronic devices, but such systems can only be utilized in specialized spaces by skilled people which limits daily life healthcare. Wearable electronics integrated with miniaturized sensors, energy devices, and data processing units enable wireless precise extraction of various biosignals from the human body, making it possible to directly check health status in remote situations (e.g., Apple Watch).[2] Accordingly, the paradigm of the medical system is shifting to real-time monitoring and treatment without being constrained by space. This "free of space constraint" concept using wearable electronics is not just limited to the healthcare industry but has begun to spread to contactless industries such as webinars and virtual shopping and job training (e.g., Metaverse), which opens the prosperity of human−machine integration applications.[3]

However, current commercialized wearable electronics normally in the form of watches, bands, and head-mounted extended reality (XR) devices have limitations in forming intimate contact with the human body due to the large employment of rigid materials such as metals and silicon. Distinct mismatch of mechanical properties with biological tissues hinders precise extraction of biosignals and leads to uncomfortable wearability which potentially results in the reluctance of wearing electronic devices.[4] Therefore, researchers aim to provide "mechanical imperceptibility", which means the paramount convenience to users, so people become oblivious to wearing the devices (Figure 1A). To integrate wearable electronics with the curvilinear and dynamic human body environment, intensive studies have been proposed to achieve skin-like mechanical properties (e.g., high failure strain, low Young's modulus). Conventional rigid materials are structurally designed for stretchability to adapt to the human body,[5−7] and through the advancement of material science and chemistry, intrinsically stretchable and soft electronic materials have emerged.[8−10] Securing these skin-like properties devoted to human−device interfaces by lowering interfacial impedance and mechanical discomfort, thereby enhancing the qualities of biosignals in the long-term period without giving trauma to users.

Despite efforts to form intimate human−device interfaces, the consideration of the optical property is still in its infancy. Current wearable devices heavily rely on biosignal data collected by various sensors without utilizing visual data of the target area in the body. Providing transparency to wearable electronics can preserve visual information on interfacing biological systems. This preserved information can be effectively utilized for image analysis techniques which enable a comprehensive understanding of health conditions by combining with biosignals obtained from sensor systems. For instance, when we are attaching wearable electronics for medical treatments, we lose visual information on the damaged tissue, which is the most intuitive and efficient data for analyzing the healing process. In recent times, more than ever, research in the integration of vision-based sensors and AI has been advancing both in academia and industry, enabling data processing, perception, and predictive capabilities for object movement. In this regard, the fusion of AI-integrated vision data through cameras and analogue data obtained from wearable electronics can offer precise control of industrial robots or the delicate operation of wearable actuators based on human movements (Figure 1B). For XR applications, by allowing high transparency of wearable devices, the consensus of the visual perception of the body wearing the device and the sensory feedback can be minimized which can enhance cognitive abilities in XR environments. For example, users wearing XR devices can experience fully immersive visual representations that seamlessly bridge the gap between virtual reality and the real world. This high transparency enables users to be more immersed in the virtual environment and facilitates natural interaction with the actual surroundings. From the futuristic point of view, the high transparency of electronic devices can give "optical imperceptibility". This optical imperceptibility not only allows wearers to use the device without psychological objection in everyday life but also bridges gaps between the XR environment and the real world, enabling users to be more immersed in the virtual environment. Therefore, "optical imperceptibility" together with "mechanical imperceptibility" is a key feature to overcome the limitations of current wearable electronics (e.g., uncomfortable user experience, asymmetry of optical and mechanical information) and related industries (e.g., gaps between real life and virtual world) (Figure 1C).

In this Review, we comprehensively highlight recent advances in transparent electronics for wearable electronics applications. We first discuss various electronic materials used in transparent and wearable electronics by dividing them into the electrode, active, and packaging materials in terms of their unique properties and synthesis approaches. Then, the engineering strategies to acquire optical imperceptibility with high electrical properties are broadly discussed mainly focusing on electrodes and active materials. We also review developments to bridge electronic devices with biological systems for mechanical imperceptibility. Various techniques to impart stretchability, softness, and long-term stability will be discussed

https://doi.org/10.1021/acs.chemrev.3c00139
Chem. Rev. 2023, 123, 9982−10078

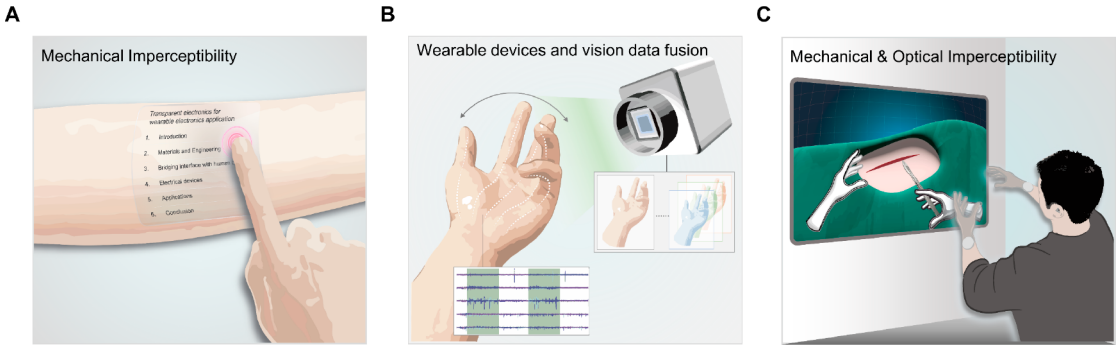

Figure 1. The mechanical and optical imperceptibility of wearable electronics. The mechanical imperceptibility of wearable devices for skin-conformal integration. (B) Optical imperceptibility for the fusion of vision data and wearable electronics. (C) The mechanical and optical imperceptibility of wearable electronics for efficient XR applications.

including conventional rigid materials and intrinsically stretchable materials. Thereafter, individual components in transparent wearable devices such as sensors, energy devices, and actuators are discussed with their operation mechanisms and performances. We then review applications of wearable electronics, in which substantial benefits are achieved by having optical imperceptibility. Finally, we provide perspective views of next-generation transparent electronics for wearable electronics focusing on its great potential applications and remaining challenges.

2. MATERIALS

Along with the recent development of wearable electronics, it is in great demand to develop materials that can conform to human skin while maintaining functionality. Conventionally, the best-developed material for flat-panel electronics is inorganic, but it's high modulus and brittle mechanical qualities render it unsuitable for wearable electronics.[11] Moreover, their opaqueness restricts their use in various wearable applications where transparency is essential. To overcome these limitations, extensive research has been conducted in materials science and related fields to develop alternative materials that offer improved performance without compromising functionality.[12,13]

The materials employed in transparent and wearable electronics can be classified into three primary categories: conducting materials, semiconducting materials, and insulating materials. Conducting materials, which assume a fundamental role as electrical pathways in circuit configurations, should exhibit stability and insensitivity to external stimuli to prevent potential defects, including heat generation and current leakage. These defects pose risks to both the human body and the devices themselves. Additionally, appropriately designed electrodes can serve as sensors that are responsive to mechanical stimuli, such as strain and pressure, making them valuable for healthcare monitoring applications. However, we will primarily focus on delivering a comprehensive overview of recent advancements in conducting materials, specifically concerning their essential function as stable electrical pathways in wearable electronics. For a thorough comprehension of the use of conducting materials as wearable sensors, we recommend consulting other comprehensive review articles. On the other hand, semiconducting materials, predominantly comprised of transistors and sensors, serve a critical purpose as sensing components in wearable devices, with their effectiveness in responding to diverse physiological and physical signals contingent upon the intended application. Lastly, insulating materials act as substrates and/or passivation layers, effectively preventing inadvertent contact between wearable devices and the external environment or human skin.

2.1. Conducting Materials

The development of electrodes with stable characteristics that effectively mitigate current leakage and power loss resulting from defects assumes paramount importance in ensuring both user safety and performance stability in electronic devices. The escalating demand for wearable electronics has significantly amplified the need for the advancement of transparent and flexible electrodes. Transparent conductive oxides, notably indium tin oxide (ITO) and fluorine-doped tin oxide (FTO), have conventionally served as the first choices for transparent electrodes in conventional electronics. However, their intrinsic brittleness and limited fracture strain render them unsuitable for wearable applications. To overcome this limitation, researchers have investigated an array of alternative electrode materials capable of simultaneously offering mechanical compliance (e.g., flexibility and stretchability) along with transparency while sustaining stable conductivity. Within the realm of transparent wearable electronics, a range of candidate conducting materials, including metals, carbons, conducting polymers, and MXenes, have witnessed substantial progress in recent decades and will be comprehensively discussed in this chapter, as summarized in Table 1.

2.1.1. Metals. Owing to its large density of free electrons, metal is one of the most conductive of all conducting materials. However, metal is not intrinsically transparent or flexible when it is in bulk form due to its high reflectivity and high modulus, respectively. In order to utilize metal as an electrode for wearable electronics, a reasonable approach should be employed. Recently, several approaches have been widely studied, including fabricating metals in ultrathin form[50] or constructing conductive networks based on metal nanomaterials,[51] in an effort to achieve desirable optical/mechanical properties.

Ultrathin metal films generally have a thickness of 10 nm or less to ensure appropriate optical transparency. When metal films become sufficiently thin (below 10 nm), the opacity of the metal in the bulk state disappears, and the total transmittance of the visible light and near-infrared (NIR) spectra (400−1000 nm) increases as the film thickness decreases. For example, Çetinkaya et al. conducted an investigation to examine the influence of Ag thickness on the transparency of the MoO_3/Ag/WO_3 system. The results

https://doi.org/10.1021/acs.chemrev.3c00139
Chem. Rev. 2023, 123, 9982−10078

Table 1. Electrical Properties of Representative Electrode Materials

materials	synthesis method	dimension	electrical properties	ref
Ultrathin Film (Wetting Layer)				
ZnO/Ag/ZnO	RF and DC sputtering	thickness: 20/6/20 nm	sheet resistance: 3 Ω sq^{-1}	14
TiO_2/Ag/TiO_2	RF and DC sputtering	thickness: 30/9.5/30 nm	sheet resistance: 5.7 Ω sq^{-1}	15
WO_3/Ag/WO_3	thermal evaporation	thickness: 30/12/30 nm	sheet resistance: 7.22 Ω sq^{-1}	16
ITO/Ag/ITO	RF and DC sputtering	thickness: 55/14/55 nm	sheet resistance: 4 Ω sq^{-1}	17
MoO_3/Ag/MoO_3	RF and DC sputtering	thickness: 20/7.5/20 nm	sheet resistance: 8 Ω sq^{-1}	18
Ultrathin Film (Doping)				
$Mg_{0.28}Zn_{0.72}O$/Ag/$Mg_{0.28}Zn_{0.72}O$	RF sputtering and E-beam Eevaporation	thickness: 50/14/50 nm	sheet resistance: 6.36 Ω sq^{-1}	19
AZO/Ag/AZO	E-beam evaporation	thickness: 25/11/25 nm	sheet resistance: 5.34 Ω sq^{-1}	20
Ultrathin Film (Metal Seed Layer)				
Ag/Ge/SiO_2/Si	E-beam evaporation	thickness: 10/2/100 nm	sheet resistance: 20 Ω sq^{-1}	21
Ag/Ge	E-beam evaporation	thickness: 100/1 nm	resistivity: 2.58 μm cm	22
Ag/Ti	RF sputtering	thickness: 6 μm/5 nm	sheet resistance: 0.023 Ω sq^{-1}	23
Ag/Al	thermal evaporation	thickness: 6/1 nm	sheet resistance: 19.5 Ω sq^{-1}	24
Metal Nanomaterial				
AgNW	chemical reduction	diameter: 100−150 nm length: >500 μm	sheet resistance: ∼9 Ω sq^{-1}	8
AgNW	chemical reduction	diameter: 40−100 nm length: ∼10 μm	sheet resistance: ∼8 Ω sq^{-1}	25
AgNP	chemical reduction	diameter: 14 ± 3 nm	sheet resistance: 9 ± 0.8 Ω sq^{-1}	26
AgNP	chemical reduction	diameter: <10 nm	sheet resistance: 30 Ω sq^{-1}	27
CuNW	chemical reduction	diameter: 80−120 nm length: ∼50 μm	sheet resistance: 37 Ω sq^{-1}	28
CuNW	chemical reduction	diameter: ∼46 nm length: 37.7 μm	sheet resistance: 52.7 Ω sq^{-1}	29
CuNP	chemical reduction	diameter: ∼40 nm	sheet resistance: 16.22 Ω sq^{-1}	30
CuNP	chemical reduction	diameter: ∼40 nm	sheet resistance: 4.7 Ω sq^{-1}	31
AuNW (mesh)	chemical reduction	thickness: 193.7 ± 67.6 nm pore size: 8−52 μm	sheet resistance: 130.1 Ω sq^{-1}	32
AuNP	chemical reduction	diameter: 3.2 nm	sheet resistance: 150 Ω sq^{-1}	33
Carbon-Based Nanomaterial				
single-layer graphene	mechanical exfoliation	lateral size: 10 μm	electron mobility: 10000 cm^2 V^{-1} S^{1-}	34
single-layer graphene/multilayer graphene	LPCVD	0.335 nm for 1 layer	electron mobility: ∼4050 cm^2 V^{-1} S^{-1}	35
single-layer graphene/multilayer graphene	APCVD	0.335 nm for 1 layer	sheet resistance: 1150−220 Ω sq^{-1} electron mobility: 602.4−450.8 cm^2 V^{-1} S^{1-}	36
single-layer graphene/multilayer graphene	PECVD	0.335 nm for 1 layer	sheet resistance: 2661 Ω sq^{-1}	37
SWCNT	blown aerosol CVD	thickness: ∼500 nm	sheet resistance: 40 Ω sq^{-1}	38
SWCNT	aerosol CVD	diameter: 1.3−2.0 nm length: 1−5 μm	sheet resistance: 84 Ω sq^{-1}	39
MWCNT	CVD	diameter: <100 nm film thickness: 6 nm	sheet resistance: 450 Ω sq^{-1}	40
MWCNT	CVD	diameter: ∼15 nm length: 250−350 μm	sheet resistance: ∼699 Ω sq^{-1}	41

https://doi.org/10.1021/acs.chemrev.3c00139
Chem. Rev. 2023, 123, 9982−10078

Table 1. continued

materials	synthesis method	dimension	electrical properties	ref
Carbon-Based Nanomaterial				
rGO	reduction of GO produced by Hummers method	thickness: 10 nm	electrical conductivity: 550 S cm^{-1}	42
rGO	reduction of GO produced by Hummers method	thickness: ∼0.9 nm	sheet resistance: 10^3 Ω sq^{-1}	43
Conducting Polymer				
PANI	electropolymerization	thickness: 5−20 μm	sheet resistance: 1.3 Ω sq^{-1}	44
PANI	chemical oxidative polymerization	thickness: ∼250 nm	sheet resistance: 4.83 Ω sq^{-1}	45
PEDOT	electropolymerization	thickness: ∼1 μm	sheet resistance: 50 Ω sq^{-1} electrical conductivity: 210 S cm^{-1}	46
PEDOT	electropolymerization	thickness: 40−50 nm	electrical conductivity: 10^{-1} S cm^{-1}	47
PEDOT:PSS	chemical oxidative polymerization	thickness: 40−50 nm	electrical conductivity: 10^{-3} S cm^{-1}	
Ppy	electropolymerization	thickness: 6.5 μm	electrical conductivity: 59.53 S cm^{-1}	48
Ppy	chemical oxidative polymerization	particle diameter: ∼40 nm	sheet resistance: 6.5 Ω sq^{-1}	49

indicate that at an Ag thickness of 4 nm, the average visible transmittance (AVT) exceeds 97%. However, as the Ag thickness increases, a decrease in AVT is observed. Notably, when the thickness exceeds 8 nm, the AVT tends to drop below 80%.[52] However, reducing the film thickness results in increased resistivity or even a loss of conductivity due to a nonideal surface with high roughness and defect density. The thickness of a bulk metal is considerably greater than the mean free path (MFP) of the electron. For instance, the calculated MFP of the electron for Ag, Cu, and Au is about 53, 40, and 38 nm, respectively.[53,54] In contrast, the distance between the boundaries of an ultrathin metal sheet is comparable to or smaller than the MFP of an electron; hence, scatterings at the surface and grain boundaries play a considerable role in deciding the resistivity of the film. It was revealed that as the surface roughness of ultrathin metal films increases, it leads to a decrease in the conductivity of the Ag layer and an increase in light scattering.[55] Consequently, these effects contribute to a reduction in transmittance and an increase in resistivity. Hence, surface roughness emerges as a significant factor that cannot be overlooked in evaluating the overall performance of electrode materials during the fabrication of composite electrodes. Therefore, in order to simultaneously optimize electrical conductivity and optical transparency, it is necessary to fabricate metal films that are atomically smooth and continuous.

Ultrathin metal-based transparent electrodes are mostly fabricated by physical vapor deposition (PVD) methods such as thermal evaporation and sputtering, where the solid-phase bulk source is transitioned into the vapor phase, and these vaporized atoms are diffused and condensed to the target substrates to form solid thin films.[56,57] Typically, the growth of a metal film consists of three distinct steps: nucleation, coalescence, and thickness growth.[58] In the early stages of thin film formation, a number of atoms and molecules are condensed and deposited on the substrate. Depending on the interaction between the metal atom, the adjacent metal atom, and the substrate, three nucleation mechanisms occur[59] (Figure 2A). If the interaction between the metal atoms and the substrate is greater than the interaction between the metal atoms themselves, (i) Frank−Van der Merwe mode occurs, which is layer-by-layer growth. Substrate wetting is favorable, hence, the smallest stable nucleus grows mostly in two dimensions as more atoms condense to form a planar sheet. When the interaction of metal atoms is more favorable than the interaction between the atom and the substrate, (ii) Volmer−Weber mode is observed, with the formation of three-dimensional islands rather than a layer. (iii) Stranski−Krastanov mode is characterized by the sequential formation of layers and islands. In this mode, one or two monolayers of material are formed first, thereby affecting the free energy of the films. Consequently, the growth of individual islands occurs at the top of the layer. Metals usually grow following the Volmer−Weber mode due to their high surface energy[60,61] (Figure 2B). Therefore, isolated metal islands are formed at the early nucleation stage. As the deposition proceeds, those islands grow in size and are finally connected, which is known as the coalescence process. The transition from fragmented islands to interconnected conductive networks can be decided by percolation thresholds. When the percolation threshold is exceeded, additional growth promotes an increase in the metal film thickness, resulting in an improvement in electrical conductivity. However, the transmittance is inevitably compromised by the increase of the metal film due to the intrinsic nature of metals, i.e., high reflectance. Therefore, it is paramount to adjust the growth condition of the metal to hamper the Volmer−Weber growth mode, thereby reducing the penetration threshold, to obtain a smooth surface with superior optical properties.

Diverse techniques, including the introduction of wetting layers, doping, and surfactants, have been implemented to inhibit the Volmer−Weber growth mode and decrease the penetration threshold. Metal island growth, which induces poor electrical/optical characteristics, is generally credited to the weak adhesion of the metal atoms to the substrate, such as SiO_2. Prior deposition of a wetting layer, such as dielectric materials or metals with higher adhesion energies, is a reasonable approach that improves the adhesion of metal atoms to the substrate, hence suppressing Volmer−Weber growth. Numerous dielectric films, including ZnO,[63,64] TiO_2,[65,66] WO_3,[16,67] ITO,[68,69] MoO_3,[70,71] ZnS,[72,73] Nb_2O_5,[74] TeO_2,[75] CuO,[76] and AlN,[77] which possess transparency in the visible and NIR ranges, have been investigated to facilitate the formation of ultrathin metal films.

https://doi.org/10.1021/acs.chemrev.3c00139
Chem. Rev. 2023, 123, 9982−10078

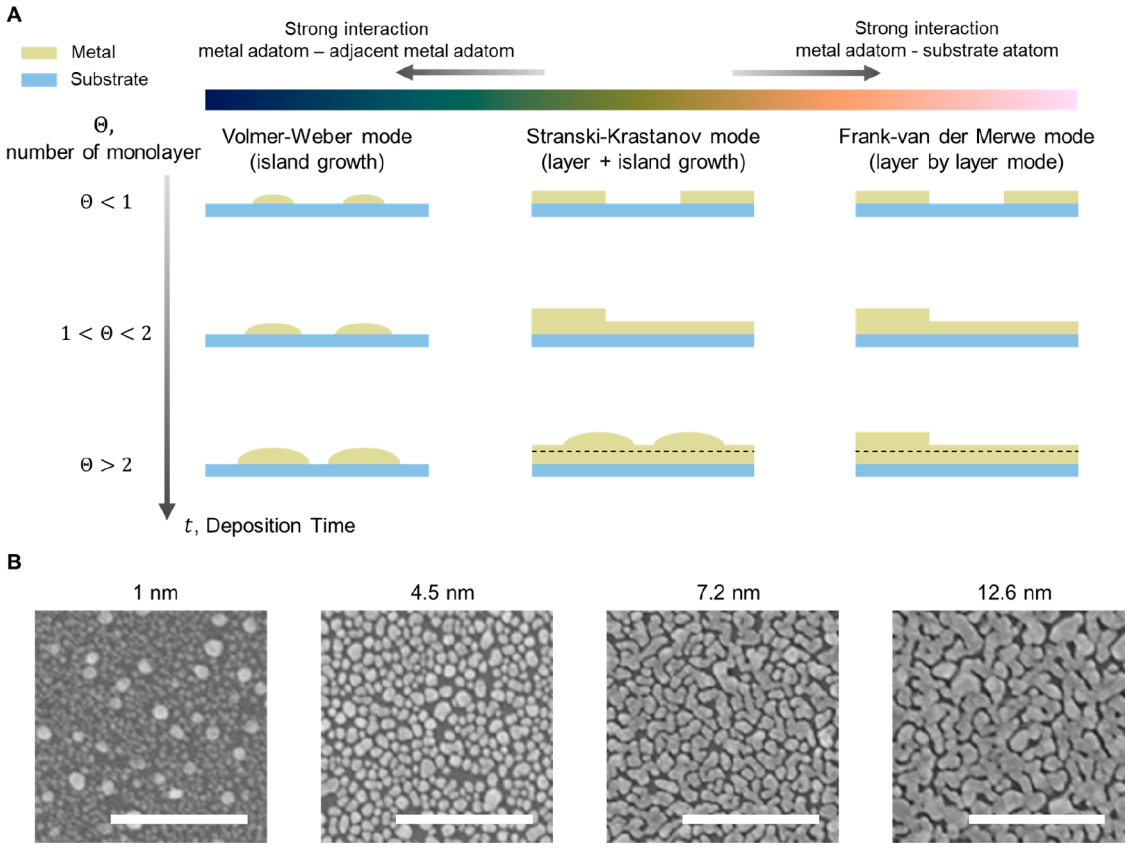

Figure 2. Thin film growth modes. (A) Schematic illustration of thin film growth modes. Depending on the interaction between the metal atom, the adjacent atom, and the substrate, three different mechanisms occur over time: Volmer–Weber mode (island growth), Stranski–Krastanov mode (layer + island growth), and Frank–van der Merwe mode (layer by layer mode). (B) Scanning electron microscopy images representing different morphologies of Ag thin films with thicknesses of 1, 4.5, 7.2, and 12.6 nm. Scale bar, 500 nm. Reproduced with permission from ref 62. Copyright 2017 Springer Nature under the CC BY 4.0 license http://creativecommons.org/licenses/by/4.0/.

ZnO is commonly employed as a wetting layer due to its transparency in the visible and NIR ranges, as well as its favorable electrical properties when doped with metallic elements. For instance, Lee et al. conducted a study to examine the influence of an Mg-doped ZnO layer on the surface morphology of ultrathin Ag layers.[19] The thickness of the Ag layer was systematically increased, resulting in a discernible transition from isolated Ag islands at 4 nm thickness to a continuous and smooth film at 12 nm thickness. The resulting layered structure, consisting of $Mg_{0.28}Zn_{0.72}O$/Ag/$Mg_{0.28}Zn_{0.72}O$, exhibited a sheet resistance of 6.36 Ω sq^{-1} and an average transmittance of 89.2% within the wavelength range of 350–780 nm, with the Ag layer measuring 14 nm in thickness. Moreover, the implementation of this layered structure led to a reduction in root-mean-square (RMS) roughness, with values decreasing from 6.2 nm (ZnO/Ag/ZnO) to 1.1 nm ($Mg_{0.28}Zn_{0.72}O$/Ag/$Mg_{0.28}Zn_{0.72}O$).

Besides operating as a wetting layer to improve the morphology of metal thin films, the dielectric materials can also serve as antireflection layers through structural approaches. In a dielectric–metal–dielectric (DMD) structural configuration, where a metal film is positioned between dielectric materials, the top dielectric layer functions as both an antireflection and protective layer, while the bottom layer serves as a seed layer to ensure the fabrication of high-quality metal thin films. As the transmittance of an ultrathin metal film is limited primarily by its high reflectance rather than its high absorption, the incorporation of antireflection layers at both the top and bottom can promote a substitutional improvement of the transmittance. Formica et al. reported a TiO_2/Ag/Al-doped ZnO transparent electrode with less than 10 Ω sq^{-1} of sheet resistance and 80% of transmittance in the range of 375–700 nm. In the developed electrode, TiO_2 acted as a seed layer, while the Al-doped ZnO layer acted as an antireflection and protective layer for the ultrathin Ag film.[78] Ji et al. devised a quantitative design methodology to optimize the transmittance of transparent conductors based on the DMD structure, yielding relative transmittances exceeding 100%.[79] Employing their design model, the researchers fabricated the DMD structure on a flexible polyethylene terephthalate (PET) substrate using a sputtering deposition technique. The structure comprised successive layers of 24 nm ZnO, 6.5 nm Cu-doped Ag, and 56 nm Al_2O_3. The dielectric layers were deposited through RF sputtering, while the ultrathin layer was deposited via DC sputtering, utilizing Cu and Ag targets with distinct deposition rates. The resulting transparent electrodes displayed exceptional optical properties, characterized by an 88.4% transmittance within the visible spectrum. Concurrently, the sheet resistance of the electrodes measured 18.6 Ω sq^{-1}. Comparatively, the bare substrate exhibited an 88.1% transmittance, highlighting the achievement of more than 100% relative transmittance by the flexible and transparent electrode. Song et al. employed polymer materials with a low refractive index to enhance the optical performance and mechanical stability of the transparent electrode.[80] They successfully fabricated an epoxy-Cu-ITO multilayer system, in which the

https://doi.org/10.1021/acs.chemrev.3c00139
Chem. Rev. 2023, 123, 9982–10078

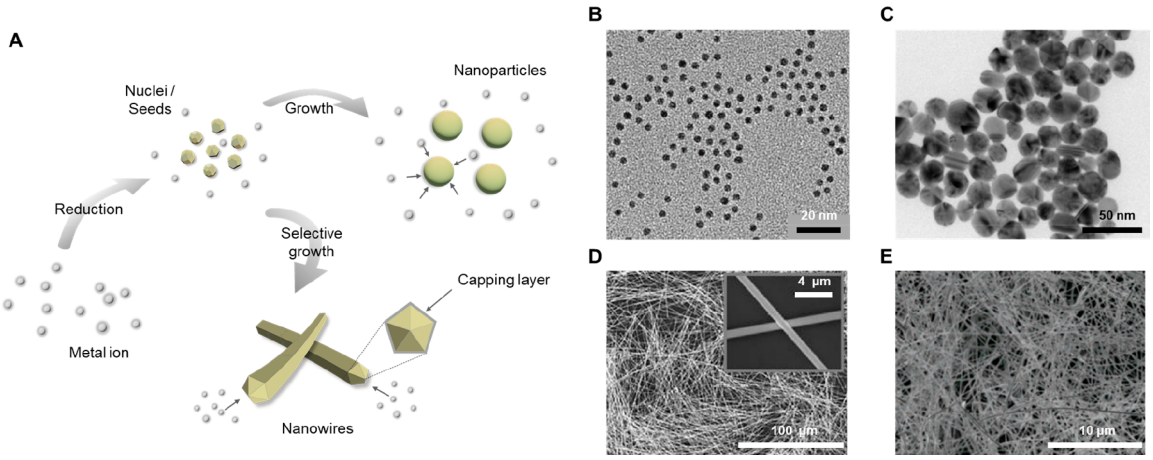

Figure 3. Metal nanomaterials. (A) Graphical illustration of chemical reduction method for synthesizing metal nanomaterials. Representative SEM images of (B) AuNPs. Reproduced from ref 92. Copyright 2016 American Chemical Society. (C) AgNPs. Reproduced with permission from ref 97. Copyright 2009 Elsevier. (D) AgNWs. Reproduced from ref 129. Copyright 2012 American Chemical Society. (E) CuNWs. Reproduced from ref 137. Copyright 2005 American Chemical Society.

inclusion of an epoxy layer reduced the discrepancy with air admittance in the ITO-Cu-ITO system, resulting in increased transparency. The final product exhibited a sheet resistance of 50 Ω sq^{-1} and 90% transparency at 600 nm, utilizing a 7 nm Cu and 50 nm ITO bilayer. Notably, the sheet resistance and transparency varied with the thickness of the Cu layer: a sheet resistance of 78 Ω sq^{-1}, and 92% transparency (at 600 nm) was achieved with a 5 nm Cu thickness, while a 9 nm Cu thickness yielded a sheet resistance and transparency of 17 Ω sq^{-1} and 80%, respectively.

In addition to dielectric materials, it has been demonstrated that additional metal seed layer deposition prior to the desired metal thin film could improve metal adhesion to the substrate, reduce the percolation threshold, and change the morphology of the metal thin film. In order to promote the formation of high-quality ultrathin metal films, diverse metal materials, including Ge,[21,81] Ti,[23,82] Nb,[83] Ni,[83,84] Cr,[85,86] Al,[24] Au,[87] Cu,[88] and Ca,[87] have been extensively explored as candidates for seed layers. Schubert et al. employed 1 nm seed layers of Ca, Al, and Au, which have surface energies (γ) of 0.5, 1.15, and 1.5 J m^{-2}, for reducing the surface energy mismatch of the Ag layer and the MoO_3 substrate.[87] Due to the higher surface energy of gold than Ag, Ag atoms are more energetically advantageous to adhere to the surfaces of gold as opposed to agglomerating, resulting in the transition to a Frank−van der Merwe growth mode. This method enabled the fabrication of high-performance films with 19 Ω sq^{-1} of sheet resistance and 83% transmittance at the visible wavelength. Logeeswaran et al. observed that the deposition of a Ge seed layer with a thickness ranging from 0.5 to 15 nm above SiO_2/Si substrates significantly reduced surface roughness to approximately 0.6 nm (RMS).[21] Although Ge deposited by electron beam evaporation grows following the Volmer−Weber growth mode, Ge islands are significantly smaller in size and denser than Ag deposited directly on the substrate, resulting in smooth, planar Ag layer growth comparable to Frank−Van der Merwe modes.

In the meantime, numerous researchers have focused on developing metal nanomaterial-based conductive networks as a cost-effective and efficient alternative to traditional metals in electronic components. Utilizing metal nanomaterials rather than metals in the form of bulks and foils has a substantial impact on the cost, weight, volume, and physical characteristics of electronic components. In the general manufacturing process of metal nanomaterial-based electrodes, metal nanoparticles or nanowires are synthesized as cornerstones. Then, the synthesized ink containing the cornerstones is printed or coated on the target substrate by numerous solution-based techniques, including spin-coating, spray coating, and inkjet printing, to configure conductive networks. The most widely adopted technique for synthesizing metal nanomaterials is the solution-based chemical reduction method. Figure 3A represents the schematics of solution-based chemical reduction to synthesize metal nanomaterials. Faraday was the first researcher to disclose the successful chemical production of gold nanoparticles.[89] Turkevich et al. established a synthetic approach for fabricating Au nanoparticles (AuNP) using hydrogen tetrachloroaurate ($HAuCl_4$) and sodium citrate.[90] The reaction proceeds at the boiling point of water and citrate functions as a reducing agent and a stabilizer. Frens further specified this method by varying the ratio of citrate, thereby developing it into a method capable of synthesizing AuNPs with different diameters.[91] This method has been widely adopted to obtain solutions of spherical AuNPs with diameters from sub 10 nm up to 100 nm[92] (Figure 3B). However, these AuNPs stabilized with citrate often incur irreversible aggregation during thiolate functionalization, which results in poor quality. Several approaches have been proposed to resolve this issue, including the mixing of a surfactant (e.g., Tween 20) before the ligand modification to prevent aggregation[93] and the use of thioctic acid as an intermediate during a two-step functionalization.[94]

The chemical reduction method for synthesizing Ag nanoparticles (AgNP) involves the reduction of Ag ions by various reducing agents, such as sodium citrate,[95−97] ascorbic acid,[96,98] sodium borohydride,[99] polyol,[100,101] Tollens reagents,[102] and *N*, *N*-dimethylformamide (DMF),[103,104] etc. These reducing agents reduce Ag ions (Ag^+), which results in the formation of metallic Ag atoms (Ag^0) and the subsequent clustering of Ag atoms. As growth continues, these clusters ultimately lead to the production of AgNPs. (Figure 3C). During the synthesis of metal nanoparticles, it is also vital to utilize protective agents to stabilize the dispersion of nanoparticles and shield the surfaces of nanoparticles that can absorb or bind to other nanoparticles, thereby preventing

https://doi.org/10.1021/acs.chemrev.3c00139
Chem. Rev. 2023, 123, 9982−10078

their aggregation. It has been observed that polymeric substances such as poly(vinyl alcohol) (PVA),[105,106] poly(vinylpyrrolidone) (PVP),[101,104,107] and poly(ethylene glycol) (PEG)[108,109] are efficient stabilizing agents for nanoparticles. By manipulating the reaction temperature, the concentration of reactants, and surface stabilizers, the diameter and size distribution of synthesized AgNPs can be adjusted to attain the desired characteristics.

Cu nanoparticles (CuNP) have also gained significant attention as a promising conductive material due to their high electrical conductivity and cost-effectiveness, owing to their mother material, Cu. Similar to AgNPs, chemical reduction is the most common method for producing CuNPs. Various Cu salts, such as $CuSO_4$, Cu(II) acetylacetonate,[110] $CuCl_2$,[111,112] and $Cu(NO_3)_2$,[113] as well as a number of reducing agents, such as sodium borohydride,[111] ascorbic acid,[114,115] hydrazine,[116,117] 1,2-hexadecanediol,[110] and glucose,[118] have been utilized to synthesize high-quality CuNPs. However, unlike AgNPs, CuNPs are highly reactive and readily oxidized by air. To circumvent this problem, various capping agents, such as oleylamine,[110,119] and PVP,[120,121] have been employed to protect the surfaces of CuNPs, thereby preventing their oxidation.

Compared to nanoparticles, nanowires exhibit better mechanical stability and can easily construct conductive networks owing to their high aspect ratio. Various techniques for the synthesis of different shapes of Ag nanowires (AgNW) have been devised, including solvothermal,[122] UV irradiation,[123] photoreduction,[124] and electrochemical deposition.[125] However, the solution-based polyol method, which was first demonstrated by Xia's group in 2002,[126−128] is the most popular due to its processability and efficiency.[129,130] Similar to the synthesis of metal nanoparticles, the production of homogeneous and high-quality nanowires requires the adequate utilization of precursors and capping agents (Figure 3D). Typically, $AgNO_3$, PVP, and ethylene glycol (EG) are used as the precursor, stabilizer, and reducing agent, respectively. PVP capping agents interact more actively with the (100) planes of Ag than with the (111) planes, resulting in one-dimensional growth as PVP leaves the (111) planes exposed and selectively covers the (100) planes.[131] Several researchers have recently attempted to improve the performance and yield of AgNW synthesis by varying the concentration of $AgNO_3$,[132,133] the molecular weight (MW) of PVP,[134] and the use of other surfactants and capping agents, such as clove oil[135] and PVA.[136]

Cu nanowires (CuNW) have also been widely investigated as possible substitutes for Ag NWs in the electrodes of the next generation. Chang et al. established one of the earliest chemical reduction synthesis procedures for CuNWs, utilizing $Cu(NO_3)_2$ as the source of Cu^{2+} ions, hydrazine (N_2H_4) as the reducing agent, and ethylenediamine (EDA, $C_8H_8N_2$) as the capping agent[137] (Figure 3E). Obtained CNWs have diameters between 90 and 120 nm, lengths between 40 and 50 μm, and thus aspect ratios greater than 350. Rathmell et al. modified this method to achieve large-scale synthesis and demonstrated a 200-fold scaled-up synthesis of CuNWs with a 90 ± 10 nm diameter and 10 ± 3 μm length.[138] They also manufactured transparent, and flexible films by printing, which exhibit 65% transmittance and 5−20 Ω sq^{-1} sheet resistance. Besides hydrazine and ethylenediamine, which are typically used for CuNWs synthesis, researchers have utilized other reducing agents, such as glucose,[139] benzoin,[140] and ascorbic acid,[141] and capping agents, such as octadecylamine,[142] hexadecylamine,[139,143] oleylamine,[140] and PVP.[141]

The electrical and optical characteristics of transparent electrodes are influenced by the dimensional configuration of the synthesized nanomaterials, particularly the diameter, shape, and density of the constituent elements. Seo et al. conducted an extensive investigation into the impact of AgNP size and protective agents on the conductivity and morphology of AgNP-based films during the sintering process.[144] Their study revealed that the size of AgNPs and the choice of protective agents played a critical role in the formation of necks during sintering. Specifically, smaller AgNPs (3.4 ± 0.7 nm) initiated the necking process at 100 °C, while larger AgNPs (87.2 ± 13.8 nm) initiated it at 180 °C. The subsequent formation of necks was predominantly influenced by the specific protective agents used. Optimal electrical properties (2.2 $\mu\Omega$ cm) were achieved using 3.4 nm AgNPs with hexyl amine as the protective agent and sintering the film at 220 °C. Ding et al. investigated the impact of AgNP size distribution on the electrical properties of printed conductive patterns.[145] They found that a broad distribution of AgNPs improved electrical properties by filling the void gaps between larger particles, enhancing connectivity, and forming efficient electrical pathways. The optoelectronic performance of metal nanowire networks is affected by various factors, including nanowire properties and network morphology.[146,147] The increase in nanowire diameter directly influences light scattering within the film, resulting in haze formation.[148] Additionally, the aspect ratio of nanowires affects the number of interwire junctions, which directly impacts the conductivity of the transparent electrode. Niu et al. compared the optoelectronic properties of AgNWs with different diameters (13, 16, and 40 nm).[149] Among them, the 13 nm AgNWs (aspect ratio of up to 3000) exhibited superior performance, with a sheet resistance of 28 Ω sq^{-1} at 95% transmittance and a haze factor of ∼1.2%. Moreover, the density of nanowires significantly influences the conductivity of the network. Numerous studies have shown that increasing wire density reduces resistance,[25,150] but it is important to note that this increase in density is accompanied by a decrease in the optical transmission of the network.

As the synthesis method of metal nanomaterials has been established, research on manufacturing transparent electrodes using metal nanomaterials, which can be further utilized in wearable electronics, has also been actively conducted. Matsukawa et al. utilized a citrate-stabilization method to synthesize a monolayer of AuNPs and manufacture flexible, transparent electrodes with visible region transparency of approximately 80% and UV region transparency of approximately 70%.[92] Kister et al. used various ligands to construct submicrometer lines of AuNPs, resulting in a transparent electrode with over 90% transparency and 150 Ω sq^{-1} of sheet resistance.[33] Our group focused on synthesizing metal NWs with high aspect ratios and employing them in transparent electrode fabrication.[151,152] Hong et al. reported a highly stretchable and transparent electrode for wearable electronics using AgNWs fabricated by the modified polyol method.[153] The fabricated electrodes exhibit excellent transparency over 85% and 30 Ω sq^{-1} of sheet resistance. Han et al. developed transparent conductors with CuNWs, which exhibit a sheet resistance as small as 37 Ω sq^{-1} at a high transparency of 80%.[28]

2.1.2. Carbons. Since Novoselov and Geim demonstrated graphene sheets for the first time in 2004,[34] sparking

https://doi.org/10.1021/acs.chemrev.3c00139
Chem. Rev. 2023, 123, 9982−10078

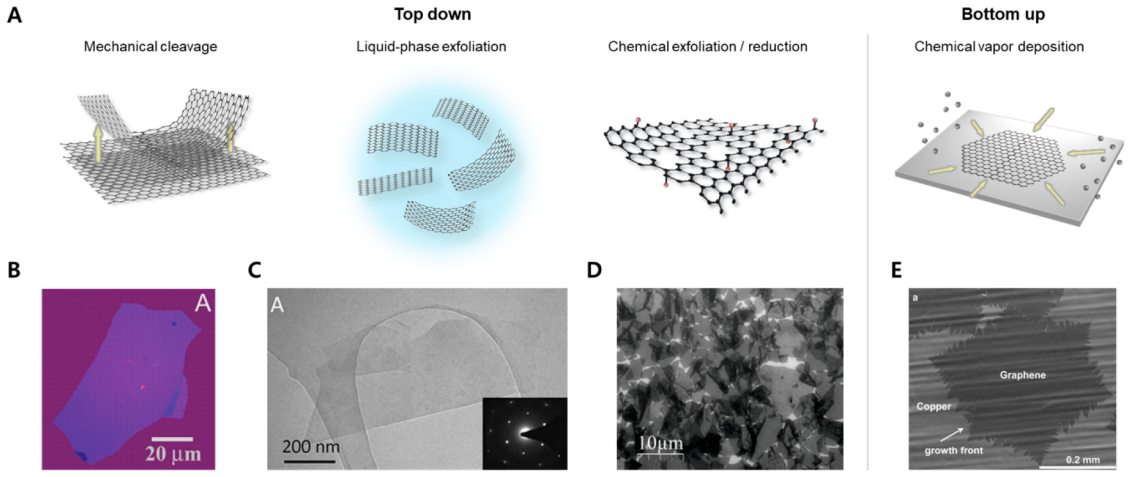

Figure 4. Synthesis of graphene. (A) Major fabrication methods of graphene. Top-down methods include mechanical cleavage and liquid-phase exfoliation of graphite. Additionally, the chemical exfoliation of graphite produces GO, which is then reduced to rGO. CVD is a representative bottom-up method that involves the decomposition of carbon sources and the subsequent deposition of carbon atoms onto substrates. (B) Photograph of a multilayer graphene flake fabricated by micromechanical cleavage. Reproduced with permission from ref 34. Copyright 2004 American Association for the Advancement of Science. (C) TEM images of a typical monolayer graphene flake fabricated by the liquid-phase exfoliation method. Inset: a diffraction pattern taken from a monolayer. Reproduced with permission from ref 165. Copyright 2010 Wiley-VCH. (D) SEM image of rGO flakes on Si/SiO_2 substrate. Reproduced with permission from ref 178. Copyright 2013 Wiley-VCH. (E) SEM images of graphene on Cu grown by CVD. Reproduced from ref 185. Copyright 2011 American Chemical Society.

worldwide interest, carbon-based materials have been intensely researched for decades. Graphene attracted the most attention for transparent conductors owing to its unique physical and chemical characteristics, such as ultrahigh tensile strength (~1 TPa) with zero effective mass, superior chemical stability, high optical transparency (97.7%), and high electron mobility (250 000 cm^2 V^{-1} s^{-1}).[154,155] Numerous researchers have made significant advancements in the development of transparent electrodes using graphene. For instance, Bae et al. successfully produced a graphene-based, transparent, and flexible electrode using roll-to-roll manufacturing techniques.[156] Their electrode exhibited a sheet resistance of approximately 30 Ω sq^{-1} and a transparency of around 90%. This production method allowed for the fabrication of large-area electrodes, even up to a 30 in. scale. Additionally, Zhao et al. synthesized reduced graphene oxide (rGO) through a solution-based process and fabricated a large-area transparent conductive film measuring approximately 7000 μm^2.[157] Their film demonstrated a sheet resistance of 840 Ω sq^{-1} at 78% transmittance.

Generally, graphene fabrication techniques are developed into the following categories: top-down and bottom-up techniques, as shown in Figure 4A. The top-down techniques, including mechanical cleavage and exfoliation, involve dimensional decrement of the precursors, whereas the bottom-up techniques, such as chemical vapor deposition (CVD), involve dimensional increment of the precursors, such as gaseous carbon.

As mentioned above, Geim and Novoselov pioneered the top-down approach to graphene production through mechanical cleavage.[34] This method employs repeated peeling of small mesas of graphite, providing single or multilayer graphene films up to 10 μm in size (Figure 4B). The graphene produced through this method exhibits 10 000 cm^2 V^{-1} s^{-1} of electron mobility, which is compatible with the theoretically predicted values.[158] Blake et al. successfully fabricated graphene through the process of mechanical cleavage and subsequently employed it as a transparent conductor within a liquid crystal device.[159] To effectively reduce the sheet resistance, the researchers introduced PVA, which induced n-type doping and resulted in noteworthy sheet resistance of approximately 400 Ω sq^{-1}. The fabricated graphene conductor exhibited an impressive optical transmission rate of approximately 98%. In their investigation, the authors observed a correlation between the number of graphene layers and both sheet resistance and light absorption. Specifically, they found that an increase in the number of layers led to a reduction in sheet resistance, while concurrently increasing the absorption of light. For each additional layer of graphene, there was an approximate 2% increase in light absorption, and when five layers of graphene were utilized, the absorption reached 10%.

Compared to mechanical cleavage, liquid-phase exfoliation reduces time costs and exhibits higher yields. This method enables large-scale graphene fabrication at sizes ranging from submicrometer to micrometers without compromising its quality. Gee et al. successfully fabricated high-quality graphene through the process of electrochemical exfoliation, resulting in predominantly bilayer thin graphene sheets with lateral sizes ranging from several to 20 μm.[160] Subsequently, they utilized the fabricated graphene to produce transparent electrodes via spray coating. The resulting film exhibited a sheet resistance of 1.35×10^5 Ω sq^{-1}, coupled with a light transmittance of approximately 70%. Various approaches involving external factors such as ultrasonic,[159,161] stabilizer,[162,163] and ionic liquid[164] have been attempted to produce high-quality graphene. Two different groups, Coleman's and Novoselov's, first reported the liquid-phase exfoliation of graphite powders using ultrasonication in *N*-methyl-pyrrolidone and DMF, which are typical organic solvents.[159,161] Coleman's group reported that their method produces unoxidized graphite and graphene flakes of high quality dispersed at a concentration of up to 0.01 mg mL^{-1} with a monolayer yield of ~1 wt %. They found that the proper solvent to produce a large amount of graphene film should have a surface energy matching that of graphene, which is about 70−80 mJ m^{-2}. Other variables, including ultrasonication duration and power, have been

https://doi.org/10.1021/acs.chemrev.3c00139
Chem. Rev. 2023, 123, 9982−10078

studied in an effort to improve yield. Khan et al. achieved higher concentrations of graphene up to 1.2 mg mL^{-1} with 4 wt % monolayers by utilizing ultrasonication with low power for 460 h (Figure 4C).[165] Ball milling process in a wet or dry state and the shear mixing method were also found to be capable of large-scale production of graphene.[166,167] Utilizing stabilizers, such as sodium dodecylbenzenesulfonate,[162] PVP,[168] and pyrene derivatives,[163] the surface tension of the solution can be efficiently modified for exfoliation and improved dispersion stability.

On the other hand, in order to find alternative techniques to employ graphite oxide instead of graphite, chemical exfoliation has been investigated for graphene synthesis. This involves the production of graphene oxides (GO) and typically includes the following steps: (i) oxidation of graphite to graphite oxide, (ii) exfoliation of graphite oxides into GO, and (iii) reduction of GO. The oxidation of graphite and fabrication of GO are primarily conducted via Brodie method,[169] Hummers' method,[170,171] and Staudenmeier method.[171] Among these, the Hummers method, which employs sodium nitrate, sulfuric acid (H_2SO_4), and potassium permanganate, is currently the most commonly used. The resulting GO can be reduced to graphene via several reduction procedures, including chemical reduction,[172,173] thermal reduction,[174,175] photothermal reduction,[176] and microwave reduction.[177] The graphene fabricated via these processes is commonly referred to as rGO. However, rGO typically contains significant structural defects as well as a large amount of residual oxygenated group, which compromises electrical properties. Recently, several methods to significantly enhance the quality of rGO have been published.[178,179] (Figure 4D) For instance, maintaining temperatures below 10 °C during oxidation allows for the minimization of CO_2 formation, resulting in the preservation of the carbon framework of rGO. After reduction, fewer defective rGO sheets exhibiting charge carrier mobilities surpassing 1000 $cm^2\ V^{-1}\ s^{-1}$ are obtained, which is a superior value to conventional rGO.[178]

Transparent conductor films can be synthesized using various deposition methods, including vacuum filtration, spin-coating, the Langmuir−Blodgett technique, and roll-to-roll production, with rGO as a synthesized material. Zheng et al. successfully fabricated a transparent conductive sheet utilizing the Langmuir−Blodgett method, achieving a resistance of 459 Ω sq^{-1} at 90% transparency (at a wavelength of 550 nm).[180] On the other hand, Ning et al. developed a roll-to-roll technique capable of producing a 25 cm wide flexible and transparent conductive film based on rGO.[181] The resulting film exhibited transmittance values ranging from 82.9% to 91.9% and resistance levels of 800−3840 Ω sq^{-1}.

From low-dimensional carbon precursors rather than 3D graphite, graphene of high quality can also be synthesized by bottom-up methods, including epitaxial growth and CVD. CVD, in particular, has attracted the most attention for fabricating large areas of homogeneous graphene. This method typically involves the thermal decomposition of carbon-containing precursors (e.g., CH_4 or solid hydrocarbons), which are then deposited onto a substrate, such as Ni[182] and Cu,[35] to form a honeycomb-like graphene layer. Following the pioneering work of Somani et al. in 2006, who demonstrated the first application of CVD to synthesize multilayer graphene on Ni films,[183] numerous advancements in CVD techniques have emerged (Figure 4E). These include atmospheric-pressure CVD (APCVD),[184] low-pressure CVD (LPCVD),[185] and plasma-enhanced CVD (PECVD).[186] These variations have been developed with the aim of achieving the successful production of high-quality graphene on a large scale, as the quality of graphene directly impacts the performance of transparent electrodes. For instance, Bi et al. utilized APCVD to fabricate high-performance graphene films and integrate them as transparent electrodes in solar cells.[36] By adjusting the H_2 flow rate, they controlled the layer number of graphene. The resulting graphene exhibited transparency ranging from 97% (for 1-layer films) to 84% (for 7-layer films) across the 350−2200 nm range, with corresponding sheet resistances varying from 1150 to 220 Ω sq^{-1}. On the other hand, Cui et al. employed LPCVD with N-type doping agents to fabricate highly conductive graphene on a large scale (5 in. scale).[187] The resultant graphene had dimensions of 6 cm × 10 cm, a transmittance of approximately 93%, and a sheet resistance of approximately 1.1 Ω sq^{-1}. Although the synthesis of large domain sizes exceeding 100 μm via PECVD process has not been reported, it has been found that the growth temperature of graphene can be lowered compared to conventional CVD.[37,188]

Besides graphene and its derivatives, a lot of research has focused on one-dimensional carbon nanotubes (CNTs) in the last few decades. CNTs are usually divided into two types based on the number of carbon layers. Single-walled carbon nanotubes (SWCNTs) consist of a single graphene sheet that is rolled with diameters ranging from 0.4 to 2 nm, whereas multiwalled carbon nanotubes (MWCNTs) are made of two or more layers of rolled graphene with a 0.34 nm interlayer gap.[189] Historically, Iijima first reported a successful synthesis of MWCNTs in 1991 through an arc-discharge evaporation method.[190] Carbon by arc-discharge evaporation was utilized to produce CNTs with 4 and 30 nm diameters and about 1 mm lengths on the negative end cathode of a carbon electrode. Ebbesen et al. modified this arc-discharge evaporation method for the gram-scale of MWCNTs.[191] Two years after the first experimental discovery of MWCNTs, Iijima et al. also showed the first SWCNTs with diameters of about 1 nm.[192] Unlike the MWCNTs, which are formed on the carbon cathode, these SWCNTs are found to be grown in the gas phase. The arc-discharge method offers a viable approach for the fabrication of CNTs, which can be effectively utilized in the production of transparent conductor films. In a study by Zhang et al., the vacuum filtration method was employed to fabricate a transparent film based on SWCNTs.[193] It was observed that as the amount of SWCNTs increased, the thickness of the film also increased, resulting in a monotonic decrease in film transmittance. The optimized film exhibited a sheet resistance of approximately 160 Ω sq^{-1} and a transparency of 87% at a wavelength of 520 nm.

In addition to the arc-discharge evaporation method, numerous technologies such as laser ablation, CVD, and vapor-phase growth have also been utilized for the synthesis of CNTs. In general, these methods employ catalysts such as Ag,[194] Au,[195] Fe,[196] Ni,[197] Co,[198] Pd,[199] and MgO,[200] among others, and the diameter and crystallinity, as well as the growth rate of CNTs, can be controlled by the appropriate catalyst. For instance, Lee et al. showed that the growth rate is most favorable with Ni catalysts, followed by Co and Fe, while the average diameter of CNTs is largest with Fe catalysts, followed by Co and Ni.[198] For the laser ablation, the vaporization of graphite occurred through a high-energy continuous or pulsed laser in a high-temperature chamber filled with an inert gas

https://doi.org/10.1021/acs.chemrev.3c00139
Chem. Rev. 2023, 123, 9982−10078

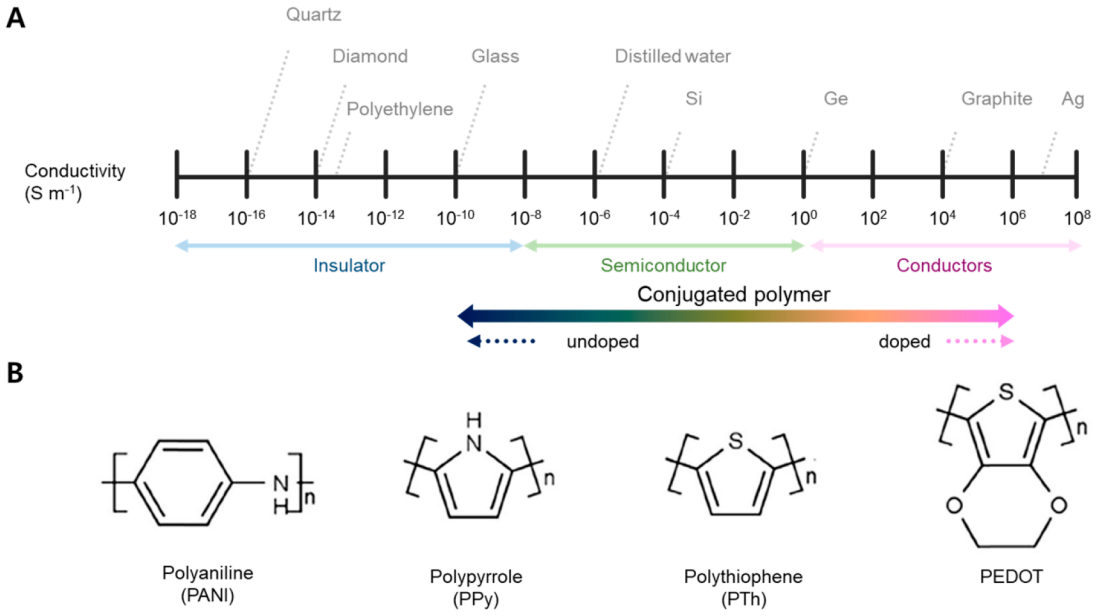

Figure 5. Conducting polymers. (A) Log-scale conductivity charts that compare the conductivity range of conjugated polymers to metallic conductors, semiconductors, and insulators. (B) Chemical structures of representative conducting polymers.

such as N_2, Ar, or He. The synthesis of CNTs using the laser ablation method was first reported by Guo et al. in 1995,[201] which was modified by Thess et al. in 1996, thereby improving the yields of CNTs to over 70%.[202] Several parameters, such as the target,[203,204] power, wavelength of the laser,[205] pressure and temperature of the chamber,[206] and catalytic agents,[201] have been found to affect the synthesis of CNTs. Compared with the arc-discharge evaporation method, the laser ablation method produces higher yields of CNTs, and the synthesized CNTs exhibit a similar narrow diameter distribution.[207]

CVD has evolved into the most popular method for synthesizing CNTs due to its ability to regulate their growth direction and synthesize a large quantity on the substrate. In addition, compared to arc-discharge and laser-ablation techniques, CVD is a straightforward and cost-effective approach for synthesizing CNTs at lower temperatures and atmospheric pressure.[208] In general, a gaseous carbon source is introduced into the reaction chamber, and hydrocarbons are decomposed at a sufficiently high temperature (600−1200 °C), causing atomic carbon to be deposited and forming CNTs. Methane,[209] ethylene,[210] acetylene,[211] benzene,[212] xylenes,[213] and carbon monoxide[214] are the most frequently used precursors for CNTs. Kong et al., for example, utilized methane as a carbon source with the aid of $FeCl_3$ in the CVD process to produce high-quality SWCNTs,[215] whereas Huang et al. synthesized MWCNTs with 10−500 nm of diameters and 0.1 to 50 m of lengths from acetylene.[216] Several variations of the CVD process, including catalytic CVD (CCVD),[217] PECVD,[218] microwave plasma CVD,[219] laser-assisted CVD,[220] and water-assisted CVD,[221] have been devised to improve CNT fabrication performance.

2.1.3. Conducting Polymers. Conducting polymers have gained significant interest in wearable and implantable electronics owing to their unique characteristics of favorable electrical and mechanical properties, reliable electrochemical stability, and solution processability. The vast majority of conducting polymers used in wearable electronics are conjugated polymers, which have a backbone with alternating single and multiple bonds, resulting in π-conjugation by orbital overlap and the establishment of electrical pathways for mobile charge carriers. Nevertheless, in their initial stages of development, conjugated polymers were found to have poor electrical conductivity in their pristine form and operate like insulators or semiconductors. In 1977, Heeger, MacDiarmid, and Shirakawa et al. discovered that doping with suitable materials imparts excellent electrical properties to conjugated polymers and announced the first demonstration of high conductivity in doped polyacetylene,[222,223] for which they were awarded the Nobel Prize in Chemistry in 2000. This accomplishment confirmed that polymers with the appropriate molecular designs and doping are capable of transporting current and can be used as electrical pathways in electronic devices. Since then, numerous scientists and engineers have been absorbed in developing conducting polymers and improving their properties (Figure 5A). Polyaniline (PANI), polypyrrole (Ppy), and poly(3,4-ethylenedioxythiophene) (PEDOT) are among the representative conducting polymers that have demonstrated promise as candidate materials for next-generation wearable devices and are widely adopted (Figure 5B).[224]

PANI is one of the most attractive conducting polymers due to its simplicity of synthesis, low cost, high processability, high stability, and tunability. Depending on the oxidation state, there are three types of basic PANI, including totally reduced leucoemeraldine base (LEB), partly oxidized emeraldine base (EB), and fully oxidized pernigraniline base (PAB).[225] Among them, LEB and PAB are intrinsically insulating, exhibiting poor conductivity even with doping. On the other hand, with suitable doping, EB states can be converted to the conductive emeraldine salt (ES) state. In recent decades, a vast amount of research on the various synthesis methods and processing techniques of PANI has been published, regardless of whether the material is doped or undoped and is in bulk or film forms.[226] Chemical and electrochemical oxidative polymerization are the two most popular techniques of PANI synthesis. For chemical oxidative polymerization, an oxidant and a

https://doi.org/10.1021/acs.chemrev.3c00139
Chem. Rev. 2023, 123, 9982−10078

dopant are employed to produce PANI from an aniline monomer, with the polymerization reaction typically occurring in an acidic aqueous medium.[227] Tai et al. fabricated PANI on FTO glass via chemical polymerization for utilization as a transparent electrode in dye-sensitized solar cells.[45] Ammonium persulfate (APS) was utilized as the oxidant, while hydrochloric acid (HCl) served as a dopant. The resulting PANI electrode on FTO glass exhibited a transmittance of 75% at 510 nm and a sheet resistance of 4.83 Ω sq^{-1}. Diverse chemicals, such as ammonium sulfate ($(NH_4)_2S_2O_8$), cerium sulfate ($Ce(SO_4)_2$), hydrogen peroxide (H_2O_2), sodium vanadate ($NaVO_3$), potassium dichromate ($K_2Cr_2O_7$), potassium free cyanide ($K_3(Fe(CN)_6$), and potassium iodate (KIO_3), have been utilized as oxidants, while phosphoric acid (H_3PO_4) and H_2SO_4 have been used as dopants.[228] During polymerization, the dopant removes a proton from the aniline monomer via a redox reaction, thereby linking an aniline unit to the growing chain. After further processes such as filtering and washing, conductive PANI in ES form is produced. The morphology, crystallinity, and hence conductivity of the produced PANI can be adjusted depending on synthesis parameters such as types and concentrations of the oxidant and dopant and temperature.[229,230]

The electrochemical approach for synthesizing PANI has numerous benefits over the chemical method, including cost-effectiveness, ease of operation, and the deposition of a highly pure and homogeneous polymer on the electrode. In electrochemical oxidative polymerization, electrodes soaked in a solution of solvent, monomer, and doping agent are subjected to an electrical current.[231] The applied current induces monomer deposition followed by oxidation of the working electrode, which results in the coating of a thin layer of PANI on the electrode over time. By simply adjusting synthetic parameters such as types of electrodes, applied voltage, temperature, solvent, and dopant, it can control the thickness, conductivity, and morphology of the thin PANI layer.[226,232]

PPy is also a promising conducting polymer due to its simple synthesis and high stability, attracting the interest of several materials scientists.[233,234] Similar to PANI, chemical[235] and electrochemical[236] oxidative polymerization have been extensively utilized to produce PPy in diverse organic solvents (acetonitrile, propylene carbonate, etc.) and aqueous mediums (water and solutions of acids). For the chemical method, polymerization of Py proceeds via oxidation of Py monomer in aqueous and nonaqueous media, allowing for the facile and economical production of PPy in large quantities. In PPy polymerization, oxidants such as aqueous or anhydrous $FeCl_3$ and APS are commonly utilized.[237,238] Zhao et al. utilized a chemical oxidative polymerization method to synthesize PPy on a flexible PET substrate, aiming to produce a flexible and transparent electrode for large-scale flexible organic transistors.[239] To enhance the electrode's functionality, photolithography techniques were employed to pattern the resulting PPy electrode, resulting in improved transparency and high resolution. The fabricated PPy electrode demonstrated a transparency of approximately 86% in the wavelength range of 330−800 nm, with an area coverage of 41.6%. Moreover, the electrode exhibited a conductivity of approximately 80 S cm^{-1}. In terms of conductivity, the optimal chemical oxidant and solvent for PPy polymerization are considered to be $FeCl_3$ and water.[240,241] Besides the oxidants, various parameters have been reported to influence the performance of the produced PPy, such as temperature, polymerization time,[242] dopant type, and dopant concentration.[243] Electrochemical polymerization offers several benefits over chemical processes. The first is that the resultant products exhibit high conductivity. Second, the yield in terms of charge is near 100%, allowing for mass and thickness control. Lastly, the properties of the PPy can be easily modified during the synthesis procedure. Numerous studies have reported the electrochemical polymerization synthesis of PPy.[244,245] Several variables, such as the types of solvent, the pH of the electrolyte, the purity and concentration of the initial monomer, and the types and concentration of the electrolytic salt, have been discovered to influence the mechanical properties, morphology, and electrical behavior of PPy.[246,247]

Polythiophene and its derivatives have garnered considerable attention due to their high stability and optical properties. Among them, PEDOT is a significant derivative of polythiophene that has been extensively explored for its exceptional optical transparency, as well as its capacity for simple doping and solution processing. PEDOT was initially found to be insoluble in water, exhibiting hydrophobicity.[248] This limitation was successfully overcome by introducing a hydrophilic surfactant additive (i.e., poly(styrenesulfonate) (PSS)) into the PEDOT matrix, therefore enhancing the aqueous processability for thin film fabrication.[249] The water-soluble long chains of PSS are connected with the hydrophobic short molecular chains of PEDOT via ionic bonds to form grains, resulting in good dispersion in water.

There are several methods for synthesizing PEDOT, including chemical oxidation polymerization, electrochemical polymerization, transition metal-mediated coupling polymerization, etc. Chemical polymerization is the most fundamental and extensively developed process for manufacturing PEDOT. Due to its continual development, it has settled in as a general method to prepare PEDOT and its derivatives over time. The oxidative polymerization of PEDOT can be explained in two stages.[250] The first stage is the oxidation of the 3,4-ethylenedioxythiophene (EDOT) monomer to generate cationic radicals, which is followed by the dimerization of the radicals. The resultant dimer undergoes deprotonation to generate an active neutral dimer that enhances chain development in the subsequent oxidation process. The neutral PEDOT is doped with oxidants, whose anions serve as counterions for the stabilization of the charged PEDOT.[251] Various oxidants such as $FeCl_3$,[252,253] APS,[254] cerium(IV) sulfate,[255] and $CuCl_2$[256] have been utilized to synthesize PEDOT.

Electrochemical synthesis of PEDOT involves the oxidation of EDOT in an organic solvent using an electrochemical cell. The general electrochemical synthesis system is comprised of EDOT monomers, supporting electrolytes, and an electrochemical cell with a working electrode, counter electrode, and reference electrode. Instead of using oxidants, the EDOT is oxidized through the transfer of electrons from the monomer to the oxidizing species in the supporting electrolyte, which forms the active species that initiate the polymerization reaction. Lithium perchlorate ($LiClO_4$), 1-butyl-3-methylimidazolium hexauorophosphate ($BMIMPF_6$), and lithium bis-(trifluoromethanesulfonyl)amide (LiTFSI) have been widely adopted as supporting electrolyte.[257,258] The electropolymerization process involves doping the anions of the electrolyte into PEDOT as counterions to maintain charge stability. By altering the electrolyte, different counterions can be intro-

https://doi.org/10.1021/acs.chemrev.3c00139
Chem. Rev. 2023, 123, 9982−10078

duced, allowing for adjustment of the morphological and electrical properties of the PEDOT film.[259]

As previously stated, PSS, a water-soluble polyelectrolyte, was the commonly accepted method for generating soluble/dispersible PEDOT until now. Poly(3,4-ethylenedioxythiophene):polystyrenesulfonate (PEDOT:PSS) possesses exceptional advantages, including the ability to form high-quality films, high transparency in visible wavelengths, and outstanding thermal stability.[260] Additionally, the conductivity of PEDOT:PSS can be tuned and improved through secondary doping. Over the past few decades, numerous efforts have been undertaken to improve the conductivity of PEDOT:PSS, including thermal,[261] light,[262] and chemical treatments.[263] In 2002, Kim et al. discovered that by using different solvents, including dimethyl sulfoxide (DMSO), DMF, and tetrahydrofuran, the conductivity of PEDOT:PSS films could be increased.[264] Since 2008, Xu's group has investigated the influence of DMSO and EG additives on the conductivity of PEDOT:PSS in its various forms.[265] They demonstrated that the PEDOT:PSS nanofilm doped with DMSO can function as an organic electrode for electrochemical polymerization.[266] Furthermore, there have been considerable research efforts focused on the utilization of PEDOT:PSS for the development of semitransparent or transparent electrodes. Zhang et al. successfully fabricated a highly conductive PEDOT:PSS transparent electrode specifically for solar cells.[267] To improve the electrical conductivity, a post-treatment approach was employed, involving the application of a precise quantity of DMSO onto the dried, pristine PEDOT:PSS films, followed by spin-coating. This post-treatment resulted in a notable enhancement, leading to an impressive electrical conductivity of 1335 S cm^{-1}. The optimized film, with a thickness of 80 nm, exhibited a sheet resistance of 100 Ω sq^{-1} and a transmittance of 92.3% at a wavelength of 550 nm.

2.1.4. MXenes. Apart from the exclusive utilization of the materials mentioned earlier, researchers are actively engaged in the exploration and discovery of novel materials for fabricating transparent electrodes with exceptional optoelectric performance. Notably, MXenes, which are a class of two-dimensional inorganic compounds comprising atomically thin layers of transition metal carbides, nitrides, or carbonitrides, have emerged as highly promising materials that have attracted significant attention in diverse fields.[268,269] MXenes can be described by the formula $M_{n+1}X_nT_x$, where M represents a transition metal (e.g., Ti, Mo), *X* denotes carbon or nitrogen, and T_x refers to surface terminal groups (e.g., O, F, OH, Cl). Typically, MXenes are synthesized via an etching process from precursor materials known as MAX phases.[270] This involves the removal of the "A" layer, which consists of an A-group element (primarily IIIA and IVA, or groups 13 and 14). Hydrofluoric acid (HF)[271] or a mixture of fluoride salts (e.g., lithium fluoride (LiF)) and HCl[272] is commonly employed as the etchant. The etching process causes the intercalation of water molecules into the MAX phase, resulting in layer expansion and the delamination of the "A" layer. The etched MAX phase is thoroughly washed to eliminate residual etchant and byproducts. Delamination is typically achieved through sonication or mechanical shearing, resulting in the exfoliation of the MAX phase into few-layer or single-layer MXene sheets. Surface terminations (represented as "T" in the MXene formula) of MXene sheets typically comprise hydroxyl (OH) or oxygen (O) groups.[273] Surface functionalization involves replacing these terminations with other elements or molecules to modify the properties of MXene.[274] Common techniques include treatment with various acids or reactive agents. The synthesized MXene is typically dried under vacuum or low-temperature conditions to eliminate residual water or solvents. Subsequently, it can be redispersed in desired solvents to form an ink for subsequent applications. Furthermore, additional post-treatment steps, such as thermal annealing[275] or surface modification,[276] may be applied to further enhance the properties of MXene.

More than 70% of MXene research has focused on $Ti_3C_2T_x$, which is the first discovered MXene. Dillon et al. produced nanometer-scale $Ti_3C_2T_x$ films from aqueous solutions, exhibiting a remarkable conductivity of 6500 S cm^{-1} along with a high transmittance exceeding 97%.[277] To achieve this, they employed a combination of LiF and HCl to generate HF, which served as the etchant. The fabricated $Ti_3C_2T_x$ films possessed single- or few-layer structures with lateral dimensions in the hundreds of nanometers range. The films were fabricated using spin-coating, allowing for control of thickness. Interestingly, a linear correlation between film thickness and transmittance was observed, with each additional layer resulting in a reduction of approximately 3% in transmittance at 550 nm. To achieve enhanced electrical conductivity in $Ti_3C_2T_x$ films, it is crucial to ensure a compact and highly organized morphology, as well as the utilization of high-quality large-sized flakes to reduce interflake resistance. Guo et al. fabricated $Ti_3C_2T_x$ films with a conductivity of 19325 S cm^{-1}, while maintaining transmittances of 83.4% with a thickness of approximately 6.7 nm.[278] This was achieved by employing large-size $Ti_3C_2T_x$ flakes (~12.2 μm) and adopting a blade coating technique to construct a compact film morphology. The researchers observed that blade coating improved flake orientation, leading to improved film morphology. This improvement was validated through the analysis of the Lorentzian curve and the Hermann orientation factor (*f*). Specifically, the blade-coated film exhibited an orientation factor of 0.77, while spin-coated films exhibited a lower value of 0.63.

2.1.5. Hybrids. In addition to the pursuit of novel materials, the academic and industrial research communities widely adopt a hybridization approach to achieve improved performance in the field of transparent and wearable electronics. This approach involves the combination of metal-based, carbon-based, conducting polymer-based materials, and MXenes both within the same category but with different dimensional configurations, as well as the incorporation of materials from distinct categories. The resulting hybrid structures exhibit a synergistic combination of properties and characteristics that surpass those of individual materials, enabling enhanced performance and multifunctionality. By leveraging the unique properties of each constituent material, researchers strive to optimize and tailor the desired optoelectronic properties required for transparent and wearable electronics applications. The combination of conducting and insulating materials is also a compelling strategy for fabricating transparent electrodes and improving their performance for wearable electronics. A detailed exploration of this strategy, along with its implications and outcomes, will be presented in Section 4. In this section, we will briefly review the notable prior research studies that employed hybridization approaches within conducting materials to improve the optoelectric performance of transparent electrodes.

https://doi.org/10.1021/acs.chemrev.3c00139
Chem. Rev. 2023, 123, 9982−10078

The utilization of distinct metal nanomaterials in various dimensional configurations offers several advantages, as the void spaces in one species can be effectively filled with smaller nanomaterials.[279] This filling process transforms the voids into localized electrical paths, resulting in enhanced electrical properties without compromising the optical properties of the composite material. Suh et al. combined AgNWs and AgNPs to create a nanocomposite material with enhanced mechanical and electrical properties.[280] The researchers conducted a detailed characterization of the nanocomposite's morphology and a comprehensive analysis of its optoelectric properties. It was determined that the AgNWs acted as the reinforcement, imparting strength and flexibility to the material, while the AgNPs primarily served as the matrix, facilitating electron transport. The nanocomposite exhibited improved mechanical properties while maintaining excellent electrical conductivity and transparency. The fabricated transparent electrode shows a sheet resistance of 5 Ω sq^{-1} at a relative transmittance of about 90% in the visible range. Even when subjected to bending with a radius less than 1 mm, the electrode showed a small relative resistance change.

CNT and AgNWs possess similar one-dimensional configurations but exhibit distinct dimensional scales. The combination of these materials gives rise to the formation of multiscale and hierarchical structures within the percolation networks, leading to a remarkable enhancement of the optoelectric properties demonstrated by transparent electrodes. In a study by Lee et al., they demonstrated the synergistic improvement effect by integrating AgNWs with larger dimensions ($d \sim 150$ nm, $L \sim 50-100$ μm) and CNTs with smaller dimensions ($d \sim 1.2$ nm, $L \sim 2-10$ μm), generating a hierarchical multiscale AgNW/CNT composite.[281] The researchers observed that the AgNW/CNT electrode effectively establishes percolation networks as the smaller CNTs fill the voids within the AgNW network, creating local paths for electrons. These electrons are then efficiently collected by the larger-diameter AgNW backbone mesh, maintaining the transparency of the electrode. Additionally, the hierarchical multiscale AgNW/CNT hybrid nanocomposite electrode exhibited superior mechanical compliance, demonstrating a stretchability of over 460%, a large twisting angle of over 540%, and a folding angle close to 0°.

Hybrid structures incorporating two-dimensional materials such as graphene, rGO, and MXenes with metal nanowires have emerged as promising candidates for transparent electronics. Lee et al. demonstrated that the integration of graphene and AgNWs could achieve significant improvements in electrical properties, including low sheet resistance and robust mechanical/electrical stability while maintaining a high level of optical transmittance.[282] The researchers fabricated the hybrid structure by spin-coating an AgNW solution onto a graphene layer synthesized via CVD and transferred onto a PET substrate. The resulting film exhibited a sheet resistance of 33 Ω sq^{-1} with a transmittance of 94% at 550 nm. Furthermore, when the hybrid structure was fabricated with the graphene layer positioned on the AgNWs, the graphene layer effectively protected the AgNWs from thermal oxidation, resulting in negligible changes in resistance even after exposure to hot (85 °C) and humid (85%) condition for 240 h. Li et al. presented a notable study highlighting the exceptional performance of transparent conductive films (TCFs) comprising composites of reduced rGO and AgNWs, fabricated through photoinduced reduction of GO.[283] The introduction of rGO resulted in a significant reduction in resistance, with values decreasing from 20 Ω sq^{-1} for AgNW TCFs and 11.6 Ω sq^{-1} for GO/AgNW TCFs to below 8 Ω sq^{-1} for rGO/AgNW TCFs, while maintaining respectable transmittance levels of 89.7%, 86.8%, and 86.2% at 550 nm, respectively. Remarkably, the incorporation of the rGO layer further enhanced the electrical and mechanical stability of the TCFs, especially when subjected to harsh conditions of high temperature and humidity (85 °C/85%). Meanwhile, Chen et al. conducted a study where they synergistically combined $Ti_3C_2T_x$ MXene with AgNWs to fabricate a transparent electrode, resulting in a low sheet resistance of 10.91 Ω sq^{-1} and a high transmittance of 82.84%. Additionally, the AgNW:MXene composites demonstrated remarkable mechanical robustness and long-term stability under ambient conditions with 60% relative humidity and exposure to 120 °C for 240 h.

Conducting polymers are actively employed in hybridization strategies with metal nanomaterials, graphene, and CNT due to their unique combination of conductivity and mechanical compliance, offering enhanced softness and stretchability compared to other conducting materials. For instance, Kim et al. demonstrated a multilayered AgNW/PEDOT:PSS structure with a sheet resistance of 22 Ω sq^{-1} and a transmittance of 90.8% at 550 nm, while a single-layered AgNW/PEDOT:PSS structure exhibited a sheet resistance of 23 Ω sq^{-1} and a transmittance of 88.6% at the same wavelength.[284] Saeed et al. utilized composites of PEDOT:PSS and Ag-coated CuNWs to fabricate transparent electrodes for organic photovoltaic applications, resulting in optimized electrodes with a sheet resistance of approximately 135 Ω sq^{-1} and a high transmittance of around 90% at a wavelength of 460 nm.[285] Furthermore, Liu et al. developed a novel hybrid ink comprising exfoliated graphene and PEDOT:PSS, which was subsequently used for spray-coating transparent electrodes.[286] The resulting films exhibited transmittance values of 90% and 80% at 550 nm, depending on the number of spray-coating cycles, with corresponding sheet resistances of 500 and 1200 Ω sq^{-1}.

2.2. Semiconducting Materials

As the demand for wearable technology continues to grow, a comprehensive understanding of materials capable of actively responding to various stimuli is crucial to the development of these devices. Such materials play a pivotal role in determining the functionality, performance, and durability of wearable electronics. As previously mentioned, well-designed conducting materials can detect basic physical signals like strain and pressure. However, semiconducting materials play a critical and irreplaceable role in wearable electronics. They enable the detection of changes in human conditions and environmental parameters, including temperature, light, and chemicals, as well as pressure and motion, and facilitate the conversion of these changes into electrical signals for processing and analysis by the device. Furthermore, they can be utilized in the fabrication of transistors, which constitute paramount components in electronic systems. Transistors offer the capability to amplify weak electrical signals. By incorporating transistors within sensors, their sensitivity can be enhanced, enabling the detection and amplification of minute changes in the input signal. This amplification improves the accuracy and reliability of the sensor's measurements. Specific transistor configurations, such as field-effect transistors (FETs), allow semiconducting materials to detect changes in temperature,

https://doi.org/10.1021/acs.chemrev.3c00139
Chem. Rev. 2023, 123, 9982−10078

Table 2. Distinctive Properties of Representative Semiconducting Materials

materials	device	semiconducting properties	ref
Metal Oxides			
ZnO (thin film)	thin film transistor (dielectric, SiO_2/substrate, PI)	mobility: 0.35 $cm^2 V^{-1} S^{-1}$ on/off ratio: ~10^6	287
ZnO (thin film)	thin film transistor (dielectric, Al_2O_3/substrate, PET)	mobility: 37.1 $cm^2 V^{-1} S^{-1}$ on/off ratio: ~10^7	288
ZnO (thin film)	thin film transistor (dielectric, Al_2O_3/substrate, PEN)	mobility: 11.56 $cm^2 V^{-1} S^{-1}$ on/off ratio: ~10^8	289
ZnO (thin film)	thin film transistor (dielectric, SiO_2/substrate, PDMS)	mobility: 1.3 $cm^2 V^{-1} S^{-1}$ on/off ratio: ~10^6	290
ZnO (thin film)	thin film transistor (dielectric, PMMA/substrate:, PET)	mobility: 7.53 $cm^2 V^{-1} S^{-1}$ on/off ratio: ~10^4	291
ZnO NPs	gas sensor (target gas: NO_2)	sensing range: 0.5−5 ppm response/recovery times = 5/2.5 min (at 1 ppm) $\Delta R/R$ = 208.5 (at 1 ppm) working temperature: 150 °C	292
ZnO NPs	gas sensor (target gas: CO)	sensing range: 5−25 ppm $\Delta I/I$ = 0.06 (at 25 ppm) working temperature: room T	293
ZnO NWs	gas sensor (target gas: NH_3)	sensing range: 1−1000 ppm response/recovery times = 88/65 s (at 50 ppm) $\Delta R/R$ = 20 (at 50 ppm) working temperature: room T	294
IGZO	thin film transistor (dielectric, SiO_2/substrate, PI)	mobility: 19.6 $cm^2 V^{-1} S^{-1}$ on/off ratio: ~10^9	295
IGZO	thin film transistor (dielectric, Al_2O_3/ substrate, PES)	mobility: 71.8 $cm^2 V^{-1} S^{-1}$ on/off ratio: ~10^8	296
IGZO	thin film transistor (dielectric, Al_2O_3/ substrate, PI)	mobility: 5.41 $cm^2 V^{-1} S^{-1}$ on/off ratio: ~10^8	297

https://doi.org/10.1021/acs.chemrev.3c00139
Chem. Rev. 2023, 123, 9982−10078

Table 2. continued

materials	device	semiconducting properties	ref
Metal Oxides			
In_2O_3 (thin film)	thin film transistor (dielectric, Al_2O_3/substrate, PI)	mobility: 2.83 $cm^2\ V^{-1}\ S^{-1}$ on/off ratio: $\sim 10^6$	298
In_2O_3 NWs	gas sensor (target gas: NO_2)	sensing range: 0.01−10 ppm response/recovery times = 200/20 s (at 5 ppm) $\Delta R/R$ = 740 (at 5 ppm) working temperature: room T	299
In_2O_3 NWs	gas sensor (target gas: NO_2)	sensing range: 0.01−0.5 ppm $\Delta R/R$ = 5.52 (at 0.5 ppm) working temperature: room T	300
In_2O_3 nanosheets	gas sensor (target gas: NO_2)	sensing range: 1−50 ppm response/recovery times = 5/14 s (at 50 ppm) $\Delta R/R$ = 164 (at 50 ppm) working temperature: 250 °C	301
NiO_x (doped with 5% Li)	thin film transistor (dielectric, ZrO_2/substrate, PET)	mobility: 1.41 $cm^2\ V^{-1}\ S^{-1}$ on/off ratio: $\sim 10^5$	302
NiO_x (doped with 5% Cu)	thin film transistor (dielectric, ZrO_2/substrate, ITO)	mobility: 1.5 $cm^2\ V^{-1}\ S^{-1}$ on/off ratio: $\sim 10^4$	303
NiO NPs	temperature sensor	sensing range: 25−70 °C temperature coefficient of resistance: −9.2% $°C^{-1}$ (at RT)	304
TMDCs			
MoS_2	thin film transistor (dielectric, -/substrate: SiO_2/Si)	mobility: 1.2 $cm^2\ V^{-1}\ S^{-1}$ on/off ratio: $\sim 10^6$	305
MoS_2	thin film transistor (dielectric, HfO_2/substrate, PET)	mobility: 13.9 ± 2 $cm^2\ V^{-1}\ S^{-1}$ on/off ratio: $\sim 10^5$	306
MoS_2	thin film transistor (dielectric, SiO_2/substrate, PET)	mobility: 12.24 $cm^2\ V^{-1}\ S^{-1}$ on/off ratio: $\sim 10^6$	307
MoS_2	thin film transistor (dielectric, Al_2O_3/substrate, PET)	mobility: ∼55 $cm^2\ V^{-1}\ S^{-1}$	308

https://doi.org/10.1021/acs.chemrev.3c00139
Chem. Rev. 2023, 123, 9982−10078

Table 2. continued

materials	device	semiconducting properties	ref
TMDCs			
		on/off ratio: $\sim 10^{10}$	
MoS_2	textile sensor	(strain) sensing range: −1.98% to 1.98% GF: −72.5 ± 1.9 (sompressive)/−56.5 ± 4.8 (tensile) (pressure) sensing range: 0−100 kPa sensing limit: ΔP = 1.24 kPa resistance change: 2.03% (ΔP = 1.24kPa)/9.78% (ΔP = 20 kPa) (temperature) sensing range: 30−40 °C temperature coefficient of resistance: 14.2% $°C^{-1}$ (at RT)	309
MoS_2	gas sensor (target gas: NH_3, NO_2)	(NO_2) sensing range: 25−500 ppm $\Delta I/I$ = 97% (at 25 ppm) working temperature: room T (NH_3) sensing range: 25−500 ppm $\Delta I/I$ = ∼−5% (at 25 ppm)	310
$MoSe_2$	thin film transistor (dielectric, SU-8/substrate, PI)	mobility: ∼121 cm^2 V^{-1} S^{-1} on/off ratio: $\sim 10^4$	311
$MoSe_2$	pressure sensor	sensing range: 0.001−100 kPa sensitivity ($\Delta I/I$ kPa^{-1}): 18.42 (0.001−0.5 kPa)/7.28 (1−35 kPa)/2.63 (40−100 kPa)	312
$MoSe_2$	gas sensor (target gas: NH_3, NO_2)	(NO_2) sensing range: 2−10 ppm response/recovery times = 250/150 s $\Delta I/I$ = ∼100% (at 10 ppm) working temperature: room T (NH_3) sensing range: 5−25 ppm $\Delta I/I$ = ∼100% (at 25 ppm)	313
WSe_2	gas sensor (target gas: NH_3, NO_2)	(NO_2) sensing range: 0.12−5 ppm $\Delta R/R$ = ∼−25% (at 1 ppm) (NH_3) sensing range: 0.12−5 ppm $\Delta R/R$ = ∼2% (at 1 ppm)	314
WSe_2	gas sensor (target gas: NO_2)	sensing range: 0.05−10 ppm limit of detection: 0.05 ppm $\Delta R/R$ = 11.01 (at 10 ppm) working temperature: room T	315
WSe_2	gas sensor (target gas: NO_2)	sensing range: 0.05−10 ppm limit of detection: 0.008 ppm	316

https://doi.org/10.1021/acs.chemrev.3c00139
Chem. Rev. 2023, 123, 9982−10078

Table 2. continued

materials	device	semiconducting properties	ref
TMDCs			
		$\Delta R/R$ = 5.36 (at 10 ppm) working temperature: room T	
Organic Semiconductors			
pentacene	OFET	mobility: 2.5 $cm^2 V^{-1} S^{-1}$ on/off ratio: $\sim 10^7$	317
TIPS-pentacene	OFET	mobility: 4.59 $cm^2 V^{-1} S^{-1}$ on/off ratio: $\sim 10^7$	318
diF-TES-ADT	OFET	mobility: 6.7 $cm^2 V^{-1} S^{-1}$ on/off ratio: $\sim 10^6$	319
DNTT C_{10}-DNTT DPh-DNTT	OFET	mobility: 1.38 $cm^2 V^{-1} S^{-1}$ mobility: 1.08 $cm^2 V^{-1} S^{-1}$ mobility: 0.36 $cm^2 V^{-1} S^{1-}$	320
C_8−BTBT DPh-BTBT	OFET	mobility: 2.21 $cm^2 V^{-1} S^{-1}$ mobility: 1.19 $cm^2 V^{-1} S^{-1}$	320
DNTT	OFET	mobility: 9.9 $cm^2 V^{-1} S^{-1}$	321
p3HT	OFET	mobility: 8.0 $cm^2 V^{-1} S^{-1}$ on/off ratio: $\sim 10^3$	322
(DPP based) PDBPyBT	OFET	mobility (electron): 6.30 $cm^2 V^{-1} S^{-1}$ mobility (hole): 2.78 $cm^2 V^{-1} S^{-1}$ on/off ratio: $\sim 10^3$	323
(DPP based) P-29-DPPDBTE (dielectric: octadecyltri-chlorosilane (OTS)-modified SiO_2)	OFET	mobility (hole): 10.54 $cm^2 V^{-1} S^{-1}$ on/off ratio: $\sim 10^6$	324

https://doi.org/10.1021/acs.chemrev.3c00139
Chem. Rev. 2023, 123, 9982−10078

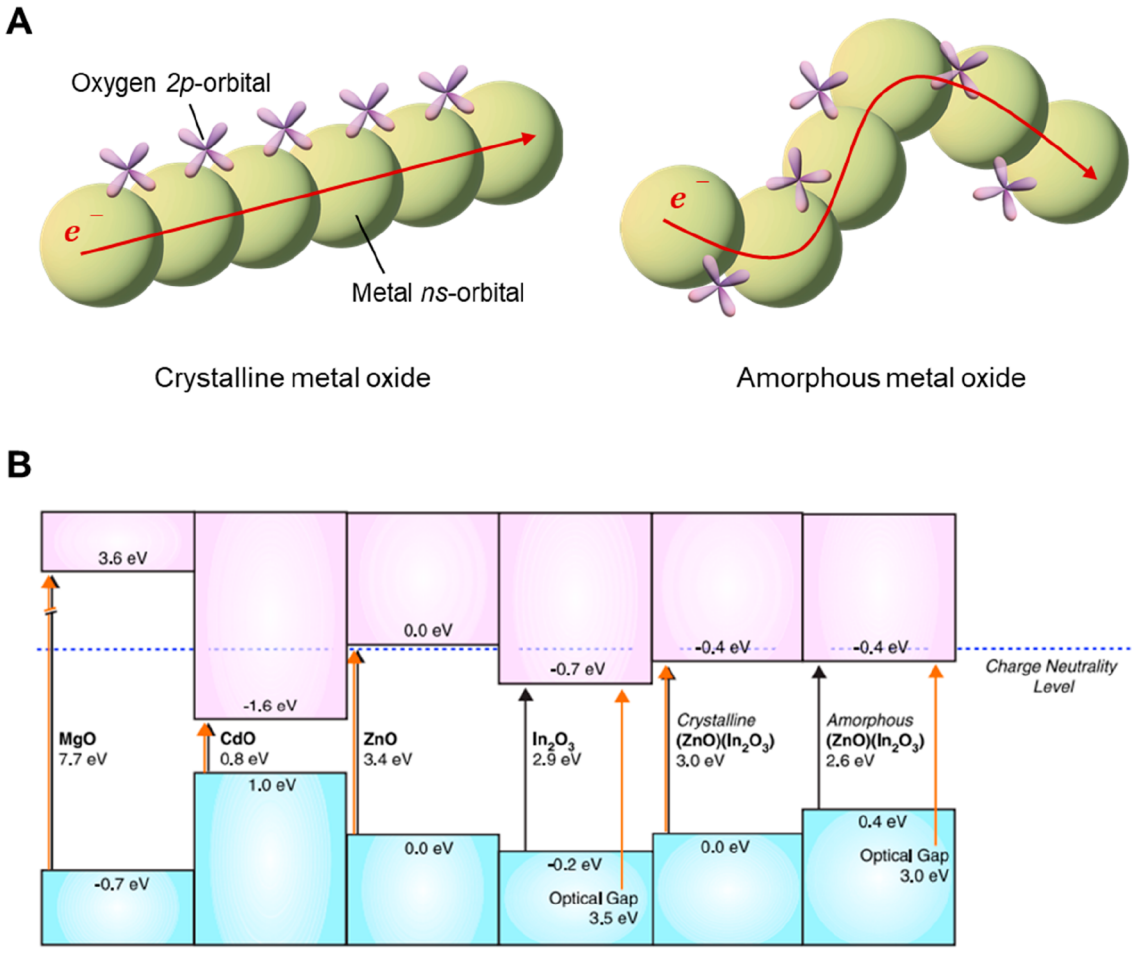

Figure 6. Metal oxides. (A) Schematic orbital diagrams representing the carrier transport pathways in crystalline and amorphous metal oxides. (B) Band alignment of the representative metal oxides. Reproduced with permission from ref 328. Copyright 2011 IOP Publishing Ltd.

pressure, strain, and even biological signals with higher sensitivity compared to sensors made solely from the materials themselves. This flexibility enables the development of versatile sensors that cater to a wide range of applications. By measuring these physical quantities, semiconducting materials enable wearable devices to interact with the environment, gather wearer information, and facilitate monitoring, control, and feedback. Consequently, the user experience is significantly enhanced, and wearable technology can be applied in innovative ways.

In addition to their roles as sensors and transistors, semiconducting materials offer various other functions, including displays and energy harvesting. For instance, organic light-emitting diode displays (OLED) employ organic semiconductors that emit light when an electric current passes through them, resulting in vibrant and energy-efficient displays. Moreover, semiconducting materials form the basis of solar cells, which absorb photons and generate electric current through the photovoltaic effect. Detailed explanations of these functions will be discussed in Section 6.

This chapter focuses on various semiconducting materials with distinctive properties that are frequently employed in transparent and wearable electronics. Examples include metal oxides, transition metal dichalcogenides (TMDCs), and semiconducting polymers, as summarized in Table 2.

2.2.1. Metal Oxides. Metal oxides have been the focus of intense research as a promising semiconducting material for next-generation electronic devices due to their numerous benefits. These benefits include high electron mobility, low preparation costs, good optical transparency, and the ability to achieve uniformity over a large area of fabrication. In metal oxide structures, the conduction band minimum and valence band maximum consist primarily of unoccupied ns metal bonding states and occupied 2p antibonding states, respectively. The interaction between the metal and oxide orbitals results in significant disparities in charge carrier transport. The s-orbitals of the metal possess a spherical geometry, resulting in their flexibility. This flexibility leads to charge transfer through these orbitals being insensitive to long-range ordering and exhibiting comparable behavior in both crystalline and amorphous states (Figure 6A).[325] In general, the metal ns orbitals have a highly dispersive character, while the oxygen 2p orbitals are localized. This results in a smaller effective mass for electrons in comparison to holes, contributing to the unique properties of metal oxides.[326,327] In many cases, metal oxides have energy gaps greater than 3 eV, making them transparent in the visible spectrum (Figure 6B).[328] This is in contrast to traditional semiconductors with lower energy gaps, which are often opaque in the visible spectrum. As such, metal oxides provide a superior option for fabricating transparent electronics, with great potential for applications in fields such as transparent thin film transistors (TFT),[325,326] sensors,[329,330] light emitting diode (LED),[331] and solar cells.[332]

https://doi.org/10.1021/acs.chemrev.3c00139
Chem. Rev. 2023, 123, 9982−10078

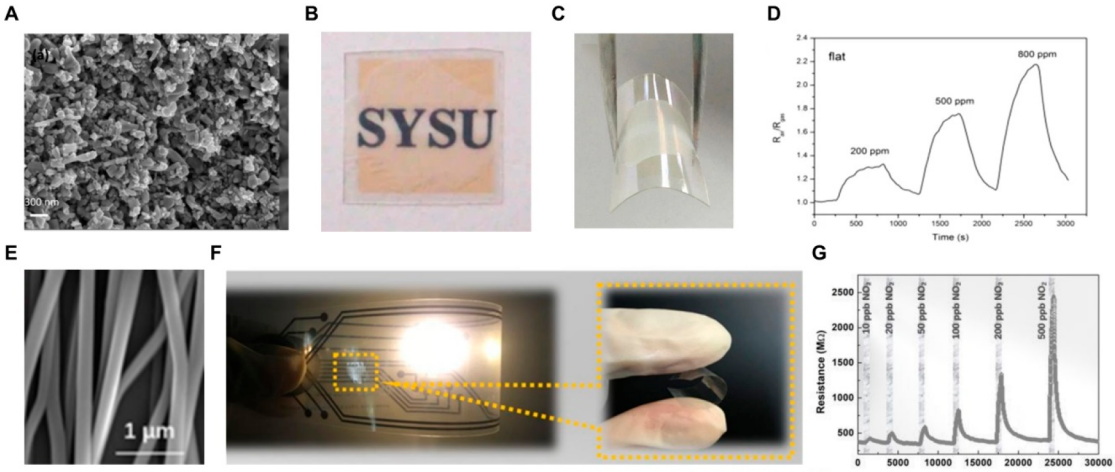

Figure 7. Metal oxide-based transparent and flexible sensors. (A) SEM image of ZnO nanoparticle. (B,C) Optical images showing transparency and flexibility of PET-ITO-ZnO device. (D) The gas sensing performance of the device under 370 nm light illuminations (5 mW) at room temperature. Reproduced with permission from ref 350. Copyright 2015 Springer Nature under the CC BY 4.0 license http://creativecommons.org/licenses/by/4.0/. (E) SEM image of In_2O_3 nanowires. (F) Transparent and flexible gas sensor based on In_2O_3 nanowires. (G) Sensor response depending on NO_2 concentrations under blue LED illumination. Reproduced with permission from ref 300. Copyright 2012 Royal Society of Chemistry.

However, bulk crystalline/polycrystalline metal oxides, which manifest an intrinsically brittle nature, can sustain maximum fracture levels of ∼1%, hindering the complete utilization of metal oxides in wearable electronics. To address this issue, structural approaches, such as the design and fabrication of wavy and nanomesh structures, have been conducted to achieve a certain degree of stretchability for wearable electronics, which is further discussed later. In the meantime, the utilization of metal oxides in the form of thin films or nanostructures is attracting a substantial amount of attention due to the assurance of mechanical stability while retaining sensitivity. Due to their high sensitivity, excellent reproducibility, stability, and cost-effective fabrication processes, various metal oxides, such as ZnO, In_2O_3, and NiO, have been widely adopted as sensor materials for wearable electronics.

ZnO is a typical example of an n-type metal oxide, which is widely employed in electronic applications as an functional material due to its biocompatibility, low processing temperatures, wide band gap (3.37 eV), and good optical transparencies.[333] In 2003, Hoffman et al. fabricated a transparent ZnO thin-film transistor for the first time, which triggered worldwide attention to the development of transparent and flexible displays.[334] The fabricated devices possess optical transmission of ∼75% in the visible spectrum with threshold voltages and channel mobilities of ∼10−20 V and ∼0.3−2.5 $cm^2\ V^{-1}\ s^{-1}$, respectively. In a study by Elvira et al., fully transparent ZnO TFTs were developed using a room temperature process and exhibited high mobility of 20 $cm^2\ V^{-1}\ s^{-1}$.[335] However, these devices required relatively high gate voltages to turn on as they operated in enhancement mode. In enhancement mode, however, these transistors required relatively large gate voltages to switch on. Lim et al. overcame this problem by doping ZnO with nitrogen during deposition.[336,337] Nitrogen doping was accomplished by injecting NH_4OH during atomic layer deposition, which not only improved device mobility but also its stability.

In addition to the numerous benefits of ZnO, the ability to modulate its electrical properties by doping or alloying with other elements allows for the adjustment of device performance and, consequently, their multiple capabilities. For example, Nomura et al. reported the successful fabrication of transparent TFTs on flexible substrates in 2004.[325] The TFTs were fabricated using amorphous In−Ga−Zn oxide (a-IGZO) films deposited onto the plastic substrates through a pulsed laser deposition process with a polycrystalline $InGaZnO_4$ target. The elemental composition of the resultant films was In:Ga:Zn = 1.11:1.1:0.9. These films exhibited stability up to 500 °C in air and had an optical bandgap of 3.0 eV, similar to the crystalline IGZO (3.4 eV). By adjusting the oxygen partial pressure from 7 to 0.1 Pa, the carrier concentration of a-IGZO films could be adjusted between 10^{14} and 10^{20} cm^{-3}. At high carrier densities, the Hall mobility of both amorphous and crystalline IGZO films converged to around 10 $cm^2\ V^{-1}\ s^{-1}$. Furthermore, the TFTs fabricated on PET were mechanically flexible, with electron mobilities ranging from 6 to 9 $cm^2\ V^{-1}\ s^{-1}$. Iwasaki et al. achieved optimal performance of IGZO TFTs through the use of combinatorial studies involving varying levels of In, Ga, and Zn compositions.[338] The resulting devices showed high mobility and low I_{on}/I_{off} ratios when In concentrations were high. Also, it was discovered that sputtering power has an impact on TFT composition, which affects its characteristics.[339]

Meanwhile, several reports have focused on the sensing and energy conversion capabilities of ZnO.[340,341] Researchers have demonstrated that ZnO has the ability to detect various gases, such as NO_2,[292] CO,[293,342] NH_3,[294] H_2S,[343] and EtOH,[344] and can therefore be utilized for monitoring air quality and controlling pollution. Various synthesis methods for developing electronic devices from ZnO nanostructures have been attempted, including thermal oxidation,[345,346] wet-chemical,[347] hydrothermal,[348] and sol−gel methods.[349] Zheng et al. fabricated a transparent and flexible gas sensor based on ZnO nanoparticles for ethanol detection that is suitable for integration into wearable devices (Figure 7A−D).[350] The sensitivity can be modified by controlling the irradiation intensity of the UV light source, providing an added level of control and versatility. He et al. utilized the piezoelectric properties of ZnO to convert mechanical energy generated by body movement into electrical energy. They developed a

https://doi.org/10.1021/acs.chemrev.3c00139
Chem. Rev. 2023, 123, 9982−10078

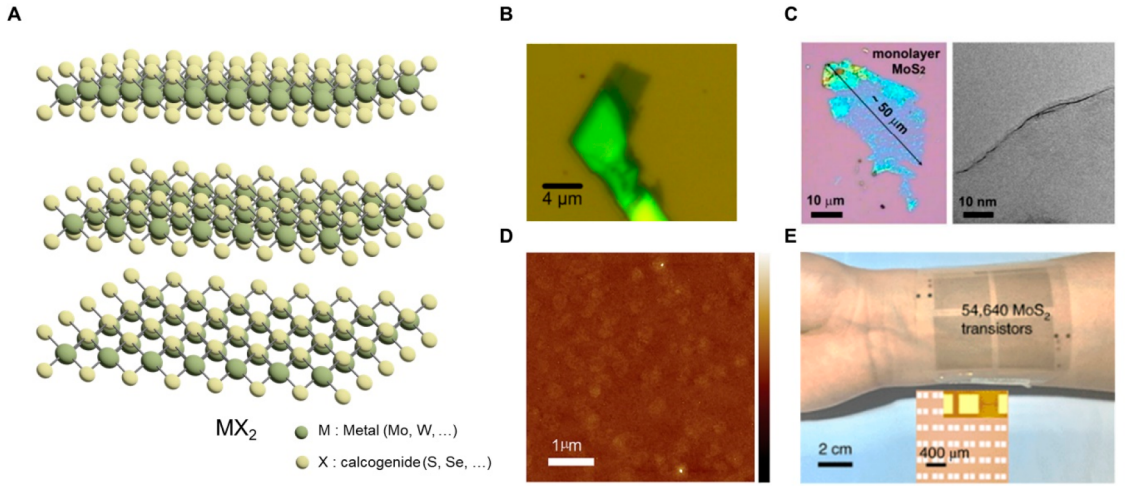

Figure 8. TMDCs. (A) Schematics of the 3D structure of TMDCs with the common formula MX_2. (B) Optical micrographs of MoS_2 ultrathin crystals fabricated by modified micromechanical cleavage. Reproduced with permission from ref 397, Copyright 2010 AIP Publishing. (C) Optical microscope (left) and SEM (right) images of an electrochemically exfoliated monolayer MoS_2 nanosheet deposited on SiO_2 substrate. Reproduced from ref 305. Copyright 2014 American Chemical Society. (D) AFM image of the MoS_2 grown by CVD. The height scale bar is 20 nm. Reproduced with permission from ref 306. Copyright 2016 Wiley-VCH. (E) Photograph of transparent and flexible MoS_2 transistor arrays on the human wrist. Inset: the magnified image of FET arrays. Reproduced with permission from ref 308. Copyright 2020 Springer Nature.

wearable textile nanogenerator with P−N junction-based ZnO.[351] By increasing the frequency of shaking from 19 to 26 Hz, 0.2−1.81 V of output voltage was obtained by the device with ZnO nanorods.

In_2O_3 is another preferred N-type semiconductor for its wide band gap (3.6 eV) and optical transparency.[352,353] After the early study was conducted on the semiconducting properties of In_2O_3,[354] the majority of research has focused on the doping process to fabricate ITO and its applications as a transparent conductor due to its superior optical and electrical properties.[355,356] Only within the last decades has the utility of In_2O_3 and related metal oxides as wide-bandgap semiconductors been re-established, leading to a comprehensive investigation of their properties from a semiconductor physics perspective. Recent research has indicated that In_2O_3 displays remarkable potential in multiple areas, including TFT,[357,358] optoelectronics,[358] supercapacitors,[359] field emissions,[360] solar cells,[361] and sensors.[362] Several synthesis methods, including electrospinning,[363] sputtering,[364,365] sol−gel,[366] and thermal annealing,[367] have been employed to fabricate In_2O_3 with diverse morphologies, such as nanorods,[366] nanowires,[367] nanotubes,[368] and thin film.[365] Wang et al. manufactured a flexible and transparent NO_2 sensor based on In_2O_3 nanowires capable of operating at room temperature (Figure 7E−G).[300] The authors used ITO electrodes and In_2O_3 nanowires to achieve sensor transparency. To reduce the operating temperature of the sensor, visible light was illuminated, thus decreasing the activation energy required for detection. Under illumination from both monochromatic (blue) and polychromatic (white) light, the limit of detection for NO_2 was as low as 10 ppb, and the sensor displayed a recoverable response to 500 ppb NO_2 in low irradiance conditions of 0.56 W m^{-2}. Also, the sensor exhibits highly selective responses to NO_2 compared to other gases, including H_2S, NH_3, trimethylamine, CH_3COCH_3, benzene, EtOH, toluene, and xylene.

NiO is a P-type semiconductor with a bandgap energy range of 3.6−4.0 eV.[369] Due to its unusual features, including transparency to visible light and excellent thermal and chemical stability, it has been the subject of extensive research. Additionally, NiO has exceptional electrical, electrocatalytic, and superconducting characteristics, contributing to its widespread utilization in various fields, including sensor technology,[370,371] solar cells,[372] energy storage systems,[373] and memristors.[374] Over the years, the deposition of NiO thin films has been accomplished using a variety of synthesis techniques including spin-coating,[375] spray pyrolysis,[376] thermal evaporation,[377] RF sputtering,[378] and DC reactive magnetron sputtering.[379] By controlling parameters including oxygen flow rates and film thickness, the physical properties of NiO can be tailored. For example, Sharma et al. investigated the effect of deposition time and annealing time on the structural, morphological, and optical properties of transparent NiO thin films fabricated by the spray pyrolysis technique.[376] The results showed that a 5 min deposition resulted in an amorphous film structure, while an increased deposition time resulted in partial crystallization with a preferred orientation along the (111) direction.

To improve the applicability of NiO as building blocks in some electronic devices, new strategies have been sought to produce low-dimensional nanostructures,[380] such as nanoparticle,[381] nanorods,[382] and nanowires.[383] The most commonly utilized method to fabricate NiO nanostructures is chemical synthesis routes, such as hydrothermal methods,[384] sol−gel,[381] and thermal decomposition.[385] Huang et al. utilized well-dispersed NiO nanoparticle ink to fabricate flexible thermistors via inkjet printing.[386] The printed thermistor can function over a wide temperature range from room temperature to 200 °C with high sensitivity (B values of 4300 K) and without hysteresis.

2.2.2. Transition Metal Dichalcogenides. Several 2D materials, including graphene, carbides, nitrides, chalcogenides, and halides, have shown great potential in a number of fields, such as transistors, solar cells, batteries, sensors, drug delivery, and cancer therapy. TMDCs, in particular, have gained significant interest in the field of wearable electronics due to their cost-effectiveness, eco-friendliness, semitransparency, and exceptional thermal and chemical stability.[387,388] Additionally, they have moderate bandgaps ranging from 1 to 2 eV,[389,390]

https://doi.org/10.1021/acs.chemrev.3c00139
Chem. Rev. 2023, 123, 9982−10078

which distinguishes them from gapless graphene. As the thickness of TMDCs decreases, the bandgap increases, offering a distinct approach to tailoring the energy band structure to specific requirements.[388]

In general, TMDCs are represented by the chemical formula MX_2, where M represents transition metals (groups 4−10) such as Mo and W, and X stands for chalcogens like S, Se, and Te (Figure 8A). The monolayer TMDCs are constructed by alternating weak van der Waals (vdW) force-bonded layers of metal and chalcogen atoms, resulting in different structural phases such as trigonal prismatic (hexagonal, H), octahedral (tetragonal, T), and their distorted phase (T′), depending on the arrangement of the atoms.[390,391] Various crystal phases result in unique electronic structures, which are principally attributable to the electron-filling state of the transition metal's valence d orbitals. For example, the 1T MoS_2 phase is known to be metallic and conductive 10^7 times more than the 2H phase.[392] Owing to their multitude of electronic structures, TMDCs show a range of electrical properties, including semiconducting, metallic, insulating, and superconducting characteristics. These unique features make the materials suitable to be utilized in electronic wearables.[393,394]

Similar to the preparation of graphene, the production of TMDCs can be achieved through mechanical[395] and chemical[396] exfoliation methods. Since the discovery that the mechanical cleavage method can produce single-layer graphene,[34] it has been widely utilized to generate nanosheets of various lamellar crystals, including numerous TMDCs where the parent crystal is available. Castellanos-Gomez et al. have demonstrated that viscoelastic stamps can be used to achieve the same effect in exfoliating lamellar crystals. By repeatedly peeling TMDC crystals using a poly(dimethylsiloxane) stamp, nanosheets of $NbSe_2$,[397] $TaSe_2$,[398] and MoS_2[397] have been obtained (Figure 8B). Geim and Novoselov showed that shear force applied by the simple rubbing of a lamellar crystal (e.g., $NbSe_2$ and MoS_2) delaminated nanosheets from their parent crystal.[399] Mechanical cleavage can produce immaculate, large-sized, single-layer TMDC nanosheets; nevertheless, its low productivity has limited its practical applications. Instead, chemical and electrochemical exfoliation technologies have been developed to produce TMDC nanosheets at a high yield and on a wide scale. The high quality of the produced TMDC nanosheets is evident from their superior values of μ_e and I_{on}/I_{off} in fabricated devices. Liu et al. utilized electrochemical exfoliation of bulk MoS_2 crystals to produce atomically thin-layered MoS_2 nanosheets with lateral sizes in the range of 5−50 μm (Figure 8C).[305] These nanosheets were considerably larger than those produced by liquid-phase, mechanical, and chemical exfoliation techniques. Monolayer MoS_2 nanosheets prepared by electrochemical exfoliation demonstrated a field-effect mobility (μFE) of 1.2 $cm^2\ V^{-1}\ s^{-1}$ and an I_{on}/I_{off} current ratio of 10^6, which are comparable to those obtained using mechanical exfoliation techniques.

The bottom-up growth approach has been shown to be superior in the synthesis of TMDCs, especially for large-scale films intended for practical applications. The bottom-up growth method encompasses various techniques such as CVD,[400] metal−organic chemical vapor deposition (MOCVD),[401] atomic layer deposition (ALD),[402] physical vapor transport,[403] and magnetron sputtering.[404] Moreover, molecular beam epitaxy was employed for the scalable deposition of atomically thin TMDCs; however, this technique necessitated the utilization of costly ultrahigh vacuum chambers and exhibited suboptimal electrical characteristics.[390] On the other hand, CVD is considered one of the most effective methods for producing large areas of atomically thin, two-dimensional TMDs for device applications. The growth and quality of the TMDCs are dependent on the substrate, temperature, and gas flux used in the process. The typical process of using CVD to grow TMDCs involves the simultaneous evaporation of metal oxide and chalcogen precursors, resulting in a vapor phase reaction that forms a stable 2D TMDCs on an appropriate substrate. In a study by Zhao et al., high-quality monolayer MoS_2 was successfully fabricated on a centimeter scale using the CVD process (Figure 8D).[306] This material was then utilized to produce flexible TFTs with remarkable characteristics, including mobilities of approximately 14 $cm^2\ v^{-1}\ s^{-1}$ and an I_{on}/I_{off} ratio higher than 10^5. The stability of the device's performance under a uniaxial strain of approximately 1% was attributed to the uniformity of the continuous MoS_2 film. Notably, metal−organic MOCVD, which elaborately controls the flow rate of gas phase metal−organic precursors, enabled wafer-scale deposition of high-quality TMDCs in facile manners and with low fabrication costs.[405,406] A three-atom-thick ultrathin MoS_2 film was fabricated by MOCVD with a high electron mobility of 30 $cm^2\ V^{-1}\ s^{-1}$ at room temperature.[405] CVD-grown scalable transparent MoS_2 showed high transmittance in the visible spectrum with controllable transmittance in the visible range (96.7% at 550 nm for 2 layers of MoS_2, and 69.4% for 8 layers).[407]

Owing to their broad compatibility with different substrates, and excellent mechanical properties, TMDCs have been intensively studied for flexible electronic devices such as FETs,[308] memories,[408] OLED,[409] and sensors.[410] It is noteworthy that the use of TMDCs in the fabrication of flexible and deformable FETs provides simple, efficient, and cost-effective options for modern wearable electronics, as FETs have been extensively used in the manufacture of wearable devices. To date, the utilization of 2D TMDCs, including MoS_2,[411] WS_2,[412] $MoSe_2$,[413] and WSe_2,[414] in FETs has been widely adopted. These materials have demonstrated exceptional performance, with I_{on}/I_{off} ratios exceeding 10^6, which represents a four-orders-of-magnitude improvement over silicon FETs with comparable channel thickness. Yoon et al. developed a highly flexible and transparent FET using MoS_2 as a channel, even with a bending radius as low as 2.2 mm.[415] After 10 000 cycles of bending, the device experienced only a 20−30% decrease in mobility, which was easily restored following low-temperature annealing treatment. Li et al. reported the successful integration of transparent transistors and logic circuits onto a flexible substrate utilizing large-area MoS_2 monolayers (4 in. wafer-scale) (Figure 8E).[308] The resulting device had a high density of 1,518 transistors per cm^2. The fabricated FET showed excellent performance, including high I_{on}/I_{off} ratios of 10^{10}, mobilities of ∼55 $cm^2\ V^{-1}\ s^{-1}$, current densities of ∼35 $\mu A\ \mu m^{-1}$, and flexibility.

Due to their 2D structure, TMDCs possess a large surface area. As a result, even small alterations in the surface environment can cause significant variations in their electrical transport properties. This attribute makes TMDCs a highly desirable material for the development of sensitive wearable sensors capable of detecting and transmitting gaseous, biological, and mechanical information. Cho et al. reported the successful fabrication of a WSe_2-based flexible, wearable, and launderable gas sensor that is sensitive to both NO_2 and

https://doi.org/10.1021/acs.chemrev.3c00139
Chem. Rev. 2023, 123, 9982−10078

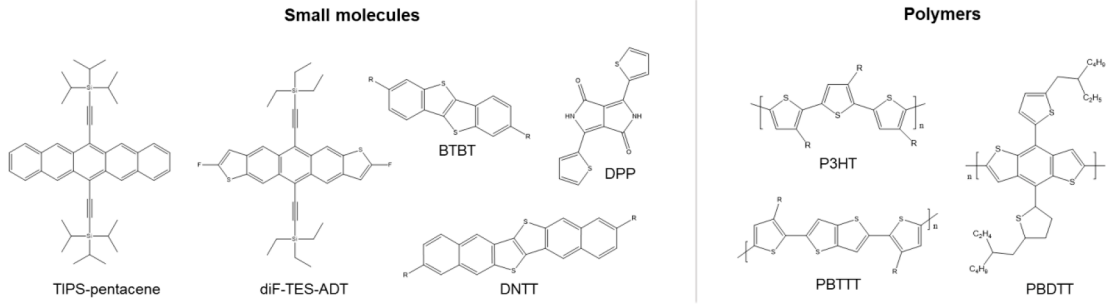

Figure 9. Chemical structures for a range of commonly used small-molecule and semiconducting polymers.

NH_3.[314] Even after 10 000 bending cycles and a 2 mm bending radius, the performance of the devices remains stable. Surprisingly, even after laundering and dry cleaning, the devices stitched onto a T-shirt continued to function normally. Guo et al. presented a method for producing epidermal gas sensors based on large-area $MoSe_2$.[313] The sensors demonstrated a high sensitivity to low concentrations of NO_2 and NH_3 (2 ppm) and fast response (250 s) and recovery (150 s) times. The devices maintained their performance with up to 30% tensile strain, allowing for integration onto human skin. Moreover, by connecting the sensors wirelessly to a cloud database, accurate remote diagnosis and timely warning were achieved. Park et al. introduced a large-area tactile sensor array based on MoS_2, covering 2.2 cm × 2.2 cm.[309] The sensor demonstrated high sensitivity, good uniformity, and linearity over 10 000 loading cycles. The compressive and tensile strain gauge factors (GF) were found to be -72.5 ± 1.9 and -56.5 ± 4.8, respectively. It also exhibited exceptional mechanical flexibility up to 1.98% strain and a high optical transparency of 80%.

2.2.3. Organic Semiconductors. Organic semiconductors refer to a group of materials consisting of π-conjugated organic (carbon-based) compounds, such as small molecules and polymers, that exhibit semiconducting properties (Figure 9).[416] Small molecules are composed of a limited number of conjugated monomer units and typically form oligomers, whereas polymers are composed of multiple conjugated monomer units that arrange into long chains and, in some cases, more complicated structures.[417] Unlike conventional inorganic semiconductors, such as silicon, organic semiconductors offer the advantages of being lightweight, flexible, low-cost, and readily available. Their unique electrical, optical, and mechanical characteristics make them suitable materials for wearable electronics, including sensors,[418,419] organic field-effect transistors (OFETs),[420] organic photovoltaics,[421] and OLEDs.[422] Furthermore, organic semiconductors can be processed from solutions, making it possible to create large-area devices, such as OLED displays, with high uniformity and low defects.

Organic semiconductors can be further subdivided into categories that include P-type, N-type, and ambipolar transport channels in OFETs according to the primary type of charge carriers they transport in devices. As the injection of metals with low work functions (2−3 eV) into the semiconductor's lowest unoccupied molecular orbital is challenging, the majority of organic semiconductor materials favor P-type charge transport. Moreover, electron mobility is hindered relative to hole mobility due to the more easily trapped nature of electrons within the semiconductor−dielectric interface or within charge trapping centers, including impurities or grain boundaries, owing to their smaller effective mass.[423] In contrast to unipolar semiconductors, ambipolar semiconductors have the ability to conduct both types of charge carriers, either electrons or holes, depending on the conditions under which they are utilized.[424,425] To be ambipolar, a material must have energy levels that allow both electrons and holes to be injected into the material and transported through the material with similar efficiency.[426] One challenge in developing ambipolar organic semiconductors is achieving balanced electron and hole transport properties, which requires careful optimization of the molecular structure and processing conditions. However, recent advances in material design and processing techniques have led to the development of many new ambipolar organic semiconductors with improved performance and stability.

Small-molecule organic semiconductors usually exhibit a higher degree of crystallinity compared to those polymer semiconductors, which results in improved performance in organic thin-film transistors.[416] The most frequently used small organic molecule semiconductors in OFETs are derived from polyacenes and heteroacenes.[427,428] Due to their simple molecular structure, which consisted just of carbon and hydrogen, pentacene and rubrene garnered considerable attention in the early 2000s.[429,430] As a result of the pursuit of solution-processable small molecules, various other classes of materials have been discovered. To enhance the solubility of pentacene, different pentacene derivatives have been produced through functionalization with side groups. These include 6,13-bis(triisopropylsilylethynyl)pentacene (TIPS-pentacene),[431,432] and heteroacene derivatives such as 5,11-bis(triethylsilylethynyl)anthradithiophene (TES-ADT) and 2,8-difluoro-5,11-bis(triethylsilylethynyl)anthradithiophene (diF-TES-ADT).[433,434] In addition, these functionalized materials also display improved π-stacking, resulting in hole mobilities above 4 $cm^2\ V^{-1}\ s^{-1}$.[318] Heteroacenes, such as [1]benzothieno[3,2-*b*][1]benzothiophene (BTBT) and dinaphtho[2,3-*b*:2′,3′-*f*]thieno[3,2-*b*]thiophene (DNTT), have a ladder-shaped molecular structure composed of fused thiophene rings. The P-type transport mobilities of their derivatives are as high as 16.4 $cm^2\ V^{-1}\ s^{-1}$ and 11 $cm^2\ V^{-1}\ s^{-1}$, respectively.[435−438] Furthermore, due to their improved stability, OFETs produced from BTBT, DNTT, and their derivatives can operate without deterioration in ambient conditions.[439,440]

Compared to small-molecule organic semiconductors, polymer semiconductors exhibit higher MW and reduced crystallinity, which generally leads to inferior electrical performance.[416] However, the advantageous mechanical flexibility and film-assembling capability of polymer semiconductors make them well-suited as functional materials in wearable electronics. Furthermore, their controllable molecular structure is beneficial for increasing carrier mobility. In recent

https://doi.org/10.1021/acs.chemrev.3c00139
Chem. Rev. 2023, 123, 9982−10078

studies, polymer semiconductor-based organic transistors have exhibited charge carrier mobilities comparable to those of the highest-performing small molecules, demonstrating the potential of these materials for electronic applications.[324,441−443] Poly(3-hexylthiophene) (P3HT) and its derivatives are widely known as solution-processable organic semiconductor materials that possess flexible, long alkyl chains in their thiophene rings. Various protocols, such as electropolymerization,[444] oxidative method (mainly by FeCl3),[445] Ni-catalyzed methods (McCullough, Rieke, GRIM),[446,447] Pd- catalyzed methods[448] and, more recently, direct arylation polymerization (DArP) have been utilized to synthesize these materials depending on the desired regioregularity and MW, which significantly affect their performance.

The effect of MW on charge carrier mobility and thin film morphology has been extensively investigated in transistors based on P3HT.[449,450] Low Mn P3HT, which has an MW of less than 10 kDa, forms highly crystalline nanorods, whereas high Mn P3HT, which has an MW greater than 30 kDa, has smaller crystalline domains with greater connections between crystalline regions. Due to the absence of connections between domains and the presence of grain boundaries, low Mn P3HT exhibits low charge carrier mobility. In addition, P3HT MW affects its mechanical properties, such as Young's modulus, tensile strength, and toughness.[451] Longer and more entangled polymer chains resulting from higher MWs lead to improved mechanical strength and stiffness. This increased chain entanglement also reduces the amorphous region of the polymer and increases its crystallinity, further enhancing its mechanical properties. However, the higher MW of P3HT may negatively affect its processability and film-forming abilities, which can limit its use in some applications. Therefore, achieving a balance between the desired mechanical properties and adequate processability and film-forming properties of P3HT is crucial.

Meanwhile, it has been extensively established within the literature that the regioregularity of polymer semiconductors exerts a profound influence on the physical properties, structural characteristics, and ultimately, the performance of resultant devices. The incorporation of an asymmetrical monomer presents an intriguing prospect, as it introduces the possibility of three distinctive configurations in which a singular monomeric unit can form bonds with another monomer: head-to-tail (H−T), head-to-head (H−H), and tail-to-tail (T−T). Within the specific context of P3HT, the term "head-to-tail" (H−T) denotes the ordered arrangement of the hexyl side chains on the thiophene rings of the monomeric units. In a comprehensive study conducted by Kim et al., an investigation was conducted to explore the impact of regioregularity on both the mechanical and electrical properties of P3HTs.[452] The research findings revealed a discernible correlation between the concentration of regio-defects (specifically, H−H defects) and the crystallinity of the polymer in a systematic manner. Although P3HT samples with a regioregularity as high as 98% demonstrated a notably elevated charge carrier mobility of 1.81×10^{-1} cm^2 V^{-1} s^{-1}, their inherent brittleness and stiffness rendered them susceptible to failure during tensile and bending tests, even under relatively modest strains. Additionally, a significant reduction in the tensile modulus was observed, with values declining from 287 MPa for samples possessing a regioregularity of 98% to a mere 13 MPa for those with a regioregularity of 64%.

At scales beyond those of individual monomers, the mechanical and electrical properties of polymers at the macroscopic level are influenced by the sequence of monomers and the overall design of the polymer structure. Various methods, including backbone engineering,[453] functionalization (side chain engineering),[454] and blending,[455] have been employed to improve the mechanical and electrical properties of organic semiconductors. For example, O'Connor and colleagues demonstrated that incorporating a thieno[2,3,*b*]-thiophene (TT) unit into P3HT to create PBDTT improved long-range order packing and resulted in enhanced charge mobility from 0.06 to 0.34 cm^2 V^{-1} s^{-1}.[456] However, the enhanced long-range order packing also led to reduced ductility and crack onset strain in the PBDTT film. More recently, new paradigms for polymeric semiconductors have emerged with the use of donor−acceptor copolymers, which involve the polymerization of two or more different oligomers. Diketopyrrolopyrrole (DPP) is one of the most extensively researched building blocks in this field.[457,458] D−A polymers based on DPP have been found to exhibit high hole mobilities exceeding 10 cm^2 V^{-1} s^{-1}[324] and high electron mobilities of over 5 cm^2 V^{-1} s^{-1}.[323] Notwithstanding the absence of long-range order, these polymers exhibit superior performance compared to certain highly ordered semiconducting polymers that have been produced to date.

2.3. Insulating Materials

Insulating materials play a critical role in wearable electronics, serving as substrates or passivation layers. As passivation layers, these materials perform multiple essential functions in the device, including the prevention of short circuits, mitigation of electrical noise, and isolation of individual components or circuit elements. They effectively preserve the integrity of electrical signals, preventing unintended interactions or interference between adjacent conductive traces, electrodes, or circuits. Moreover, insulating materials act as robust barriers, safeguarding the underlying electronic components from environmental factors such as moisture, oxygen, corrosive agents, and mechanical damage. The presence of moisture and contaminants can lead to the deterioration of electrical connections and the occurrence of short circuits, resulting in device malfunction or failure. Similarly, physical damage caused by bending, stretching, or external impacts can have detrimental effects on wearable devices. Given the frequent exposure of wearable devices to outdoor conditions and the constant movement and mechanical stresses they experience, the implementation of a resilient passivation layer is of utmost importance to ensure the maintenance of structural integrity and prevent malfunctions resulting from unintended damage. In addition to its role as a passivation layer, the insulating material serves as a substrate for wearable electronics, preventing potential harm to the users' skin caused by electrical leakage or thermal dissipation. The substrate layer should exhibit mechanical compliance, including flexibility and stretchability, to accommodate the bending, twisting, and stretching movements that wearable devices undergo without compromising the integrity of the electronic components. Conformal attachment to human skin while maintaining functionality is critical to reducing noise and accurately transmitting signals, as wearable sensors heavily rely on the physical, chemical, and biological information obtained from or transmitted through the skin. Therefore, insulating materials with superior mechanical properties, such as high failure strain

https://doi.org/10.1021/acs.chemrev.3c00139
Chem. Rev. 2023, 123, 9982−10078

and low Young's modulus, are highly required for effective adhesion to human skin. Furthermore, optical transparency is highly required in various applications in wearable electronics, such as displays, contact lenses, and augmented/virtual reality, where visual information is highly desirable. For example, biosensors on contact lenses for diagnostic purposes must be stretchable and transparent to achieve intimate contact and imperceptibility.[459,460] In optogenetics, the substrate as well as the device must be transparent to ensure that light is not blocked as it controls the activity of neurons or other cell types.[461,462]

In the subsequent sections, we aim to provide an in-depth exploration of prevalent insulating materials and their distinctive properties within the field of transparent and wearable electronics. Specifically, we have classified these materials into three categories: polymers, hydrogels, and cellulose. While it is acknowledged that hydrogels and cellulose fall within the polymer classification, we have opted for this categorization to facilitate a more comprehensive examination of their individual characteristics.

2.3.1. Polymers. Insulating polymeric materials, including PET, polyimide (PI), parylene, polyurethane (PU), and various commercial elastomers, have gained significant traction as highly suitable substrates and passivation layers for wearable electronic devices.[463,464] The several properties of these materials are presented in Table 3.

Each material possesses distinctive characteristics that render it advantageous for specific applications. Notably, PET, a thermoplastic polyester polymer, offers exceptional attributes such as exceptional flexibility, transparency, and dimensional stability. Furthermore, it exhibits excellent resistance to moisture, chemicals, and thermal stresses. An exemplary study by Wang et al. demonstrated the utilization of PET as a substrate for a transparent and flexible chemical sensor, where the substrate was spin-coated with polydopamine/MoS_2.[465] The inherent flexibility of PET played a pivotal role in the realization of a wearable wrist strap sensor. PI stands out for its exceptional thermal stability, mechanical strength, and flexibility. PI finds extensive utilization as passivation layers and substrates in wearable electronics, particularly in applications necessitating high-temperature resistance and mechanical durability, such as flexible printed circuit boards and medical devices. Although conventional PI films exhibit a slight yellow hue, recent advancements in polymer technology have enabled the development of colorless polyimides (cPI), enabling the realization of transparent electronic devices. An instance of this is demonstrated by Choi et al., who employed colorless PI to fabricate a flexible and transparent heater for a wearable chemical sensor.[466] This involved the imidization of polyamic acid via solution coating onto an AgNWs percolation network. The resulting embedded structure of AgNWs within the cPI film ensured stable performance even under dynamic bending conditions. Parylene, known as poly(*p*-xylylenes), is commonly employed as a coating through CVD under vacuum conditions. These coatings offer excellent electrical insulation properties and effectively protect against moisture and chemicals. Moreover, parylene exhibits uniform deposition capabilities on complex and irregular-shaped surfaces, guaranteeing comprehensive coverage without gaps or voids. This remarkable conformal coating capability positions parylene as an outstanding substrate[460,467] for achieving conformal contact with human skin and as a protective layer[468] to mitigate

Table 3. Representative Physical Properties of Various Insulating Polymeric Materials for Transparent Wearable Electronics

	PET	PI	PEN	PC	PU	parylene	PDMS	ecoflex
Young's modulus	1.57−5.20 GPa	0.107−46.9 GPa	5.00−5.50 GPa	1.79−3.24 GPa	0.00114−3.54 GPa	2.8−3.0 GPa	1.32−2.97 MPa	0.05−0.1 MPa
tensile strength (ultimate)	22.0−95.0 MPa	0.0480−345 MPa	200 MPa	28.0−75.0 MPa	0.138−65.0 MPa	48.3−68.9 GPa	6.7 MPa	0.37−1.7 MPa
elongation (yield) (%)	4.00−6.00	2.00−90.0		3.00−60.0		2.4−2.9		
elongation (break) (%)	40.0−600	0.350−200	60	10.0−138	0.400−1300	10−250	135	800−900
refractive Index	1.575	1.68−1.78	1.7	1.58	1.5−1.7	1.59−1.66	1.4	1.4
transmittance	good	poor	good	good	good	good	good	poor
glass transition temperature (°C)	70.0−78.0	−20.0−385	120	141−150	−46.0−40.0	13−66	−120	−33
melting temperature (°C)	200−260	247−388	270	288−316	80.0	290−435	−40	
specific heat capacity (J/g K)	1.00−1.50	0.920−1.13	2.59	1.17−1.70		0.711−0.837	1.38	
thermal conductivity (W/m K)	0.190−0.290	0.0330−1.73	0.18	0.173−0.210	0.140−0.390	0.081−1.000	0.27	

https://doi.org/10.1021/acs.chemrev.3c00139
Chem. Rev. 2023, 123, 9982−10078

interference and safeguard delicate components within wearable devices.

However, it should be noted that the aforementioned polymers may not possess the desired level of stretchability required for wearable applications. On the other hand, elastomers possess a distinct characteristic within the polymer category, namely their exceptional elasticity. Unlike other types of polymers that may exhibit rigidity or limited flexibility, elastomers are distinguished by their ability to stretch under applied stress and then return to their original shape once the stress is removed. This unique behavior is attributed to the presence of long polymer chains that are loosely cross-linked, allowing them to undergo significant deformations without undergoing permanent changes in shape or structure. The inherent elasticity of elastomers endows them with high suitability for applications demanding flexibility, resilience, and the capacity to withstand repetitive mechanical stress, as these properties permit accommodating movements, conforming to diverse shapes, and providing wearer comfort. Consequently, a range of elastomers, including PU, thermoplastic PU (TPU), and silicone-based elastomers, have been utilized for transparent and wearable electronics.[469,470]

PU is synthesized through the reaction of diisocyanates with polyols, resulting in the formation of a three-dimensional network structure. The cross-linking of polymer chains establishes physical or chemical bonds and imparts PU with its distinctive elastic properties, making it a suitable material for stretchable substrates in wearable electronics. Moreover, PU serves a crucial role as a passivation layer, enhancing the performance and longevity of wearable devices. By acting as a protective coating, it effectively safeguards against moisture infiltration, the accumulation of dust particles, and mechanical damage. The application of PU coatings significantly enhances the durability and reliability of wearable devices, particularly in challenging environmental conditions or scenarios involving physical contact. To harness this characteristic, Lee et al. employed PU in the form of nanomesh, fabricated via the electrospinning technique, as a passivation layer.[471] The resulting passivation layer exhibited an impressively thin thickness of only 2.5 μm. Notably, the fabricated passivation layer demonstrated outstanding durability, enduring 300 cycles of rubbing with a weight of 50 g while maintaining the pressure sensor signals at a remarkable level of 95.4%.

Commercial silicone-based elastomers, such as Sylgard 184 (Dow Chemical), Dragon Skin, and Ecoflex (Smooth-on), typically belong to the category of addition-curing elastomers incorporating platinum-based catalysts. They find extensive utilization in electronic applications due to their desirable properties, including insulating characteristics, optical transparency, biocompatibility, flexibility, low moduli, high failure strains, thermal stability, and chemical resistance.[470] These properties enable them to undergo substantial deformation without failure and adhere to various surfaces of the human body, including the arms, knees, and finger joints. Moreover, several technologies and methods have been developed to impart desired characteristics to elastomers, thereby enhancing their applicability and making them ideal materials for packaging. The surface of polydimethylsiloxane (PDMS) can be modified to create adhesive and nonadhesive regions for selective bonding of sensing materials. Altering the composition of prepolymers prior to polymerization can modify their elasticity, self-healing capacity, modulus, and transparency characteristics.[472,473]

2.3.2. Hydrogels. Hydrogels, characterized by their hydrophilic polymer networks and substantial water content, typically possess inherent electrical insulating properties. However, it is pertinent to acknowledge the potential for modifying the electrical conductivity of hydrogels through the integration of conductive additives or the introduction of ionically conductive elements. Notably, certain engineering approaches enable the attainment of electrical conductivity in hydrogels by incorporating conductive polymers, nanoparticles, or ions that facilitate the conduction of electrical charges. Extensive investigations have been undertaken to advance the fabrication of conductive hydrogels, and a comprehensive exploration of these endeavors will be expounded upon in Section 4.

From the perspective of insulating materials, hydrogels have garnered significant attention as a promising candidate for seamless integration between humans and electronic devices. This interest stems from their remarkable similarity to biological tissues and epidermis, as well as their biocompatibility. Furthermore, hydrogels offer the ability to engineer their mechanical and biofunctional characteristics, making them versatile for various applications. In the realm of wearable electronics, a major hurdle lies in the mechanical disparity between the supple human skin and rigid electronic systems. While human skin exhibits substantial stretchability (30−70%) and encompasses a wide spectrum of Young's modulus (5−140 MPa),[474] conventional electronic devices typically manifest a limited stretchability of less than 5% and boast a significantly higher Young's modulus, generally measured in the GPa scale.[475,476] Such incongruity can elicit discomfort and compromise device functionality, necessitating effective resolutions for wearable electronics and, subsequently, implantable electronics. In this regard, hydrogel coatings emerge as a viable solution. Hydrogels possess a compliant, adhesive, and aqueous nature, rendering them amenable to conforming to diverse cellular structures, tissues, and even dynamically deforming skin.[477] Spencer et al. undertook a study wherein they applied a polyethylene glycol dimethacrylate (PEGDMA) hydrogel coating onto rigid borosilicate implants.[478] This approach effectively reduced the interface's elastic modulus in close proximity to brain tissue. The reduction in elastic modulus proved instrumental in mitigating strain at the interface, thereby making it less damaged even at chronic time scales (>4 weeks). In addition to the hydrogel coating method, several techniques have been explored to fabricate electronics encapsulated with hydrogels, thereby expanding the potential applications of the hydrogel as a protective layer and capitalizing on its inherent biocompatibility. These techniques encompass the entrapment of liquid metals within preformed channels[479] and the direct encapsulation of titanium wires,[480] enabling the creation of stretchable electronics enveloped by hydrogels. Liu et al. successfully developed ultrastretchable bioelectronics composed entirely of hydrogels through the implementation of a novel fabrication approach.[479] The method involved the utilization of prefabricated microfluidic channels, created via laser engraving for the encapsulation of liquid metals. The liquid metal served as the resistive strain sensor, while the hydrogel employed was a double network hydrogel consisting of polyacrylamide (PAAm) and alginate. This hydrogel not only functioned as the substrate but also served as a protective passivation layer. The inherent biocompatibility of the hydrogel facilitated the seamless

https://doi.org/10.1021/acs.chemrev.3c00139
Chem. Rev. 2023, 123, 9982−10078

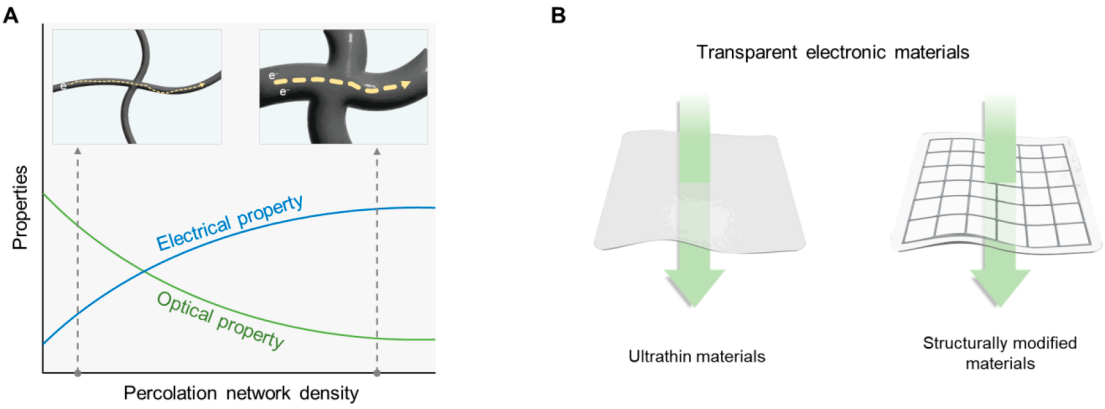

Figure 10. The optical and electrical properties of transparent electronics. (A) Trade-off relationship of optical and electrical properties. (B) Concepts to secure transparency of electronic devices.

Table 4. Engineering Strategies for Enhancing Transparency and Their Corresponding Optical and Electrical Characteristics

engineering strategy	materials	transparency (visible range)	electrical properties	FoM	ref
Ultrathin Film Deposition					
PVD	ultrathin metal	88.40%	sheet resistance: 18.6 Ω sq^{-1}		79
PVD	rGO	97%	resistivity: 30.3 mΩ cm		490
CVD	graphene	84%	sheet resistance: 600 Ω sq^{-1}		182
CVD	MoS_2	89.2%	mobility: 0.07 cm^2 $V^{-1}s^{-1}$ @ RT		407
ALD	Pt doping on graphene	93.40%	sheet resistance: 86.8 Ω sq^{-1}		491
transfer	ultrathin film transfer	85%	mobility: 0.1 cm^2 V^{-1} s^{-1} sheet resistance: 100 Ω sq^{-1}		492
Random Percolation Networks					
spin-coating	AgNW	90.70%	sheet resistance: 8.6 Ω sq^{-1}	σ_{dc}/σ_{op}: 600	493
spin-coating	CNT	71%	sheet resistance: 59 Ω sq^{-1}	σ_{dc}/σ_{op}: 17	494
spin-coating	PEDOT:PSS	96.10%	conductivity: 2084 S cm^{-1}	σ_{dc}/σ_{op}: 185.2	495
spray coating	PEDOT:PSS	90%	conductivity: 936 S cm^{-1}	σ_{dc}/σ_{op}: 39	496
spray coating	AgNW	90%	sheet resistance: 47 Ω sq^{-1}	σ_{dc}/σ_{op}: 415	497
spray coating	graphene, PEDOT:PSS	90%	sheet resistance: 1200 Ω sq^{-1}		286
vacuum filtration transfer	AuNW	83%	sheet resistance: 49 Ω sq^{-1}	σ_{dc}/σ_{op}: 54	498
electrospinning	metal nanotrough	90%	sheet resistance: 2 Ω sq^{-1}		499
electrospinning	Cu	90%	sheet resistance: 50 Ω sq^{-1}	T^{10}/R_s: 11 × 10^{-3} Ω^{-1}	500
Grid Patterning					
nanoimprinting	AuNW	92%, pattern resolution: 250 nm	sheet resistance: 227 Ω sq^{-1}		501
nanoimprinting	Ni	75%, pattern resolution: 4 μm	sheet resistance: 0.036 Ω sq^{-1}	σ_{dc}/σ_{op}: 3.4 × 10^4	502
nanoimprinting	Metal	83.1%, pattern resolution: 210 nm	sheet resistance: 9.8 Ω sq^{-1}	σ_{dc}/σ_{op}: 198.3	503
nanoimprinting	Ag	91.10%	sheet resistance: 8.2 Ω sq^{-1}	σ_{dc}/σ_{op}: 350−1000	504
laser ablation	Cu	83%	sheet resistance: 17.48 Ω sq^{-1}	σ_{dc}/σ_{op}: 109.74	505
laser sintering	AgNP	91%, pattern resolution: 12 μm	sheet resistance: 22 Ω sq^{-1}		27
laser sintering	AgNP	85%, pattern resolution: 20 μm			506
inkjet	AgNP	78.2%, pattern resolution: 10 μm	sheet resistance ∼3.8 Ω sq^{-1}		507
inkjet	AgNP	85%, pattern resolution: 1.6 μm	resistivity: 1.67 × 10^{-6} Ω m		508

integration of the sensor with various biological tissues, including rabbit hearts, as well as human and pig skin.

2.3.3. Cellulose. Cellulose, as a highly abundant material in the natural world, is a naturally occurring polymer that can be derived from wood fibers, cotton, bamboo, etc. It consists of repeating units of glucose, making it a structurally fascinating compound.[481] Within the context of wearable electronics, cellulose emerges as an appealing option for insulating materials due to its remarkable combination of desirable attributes such as flexibility and biocompatibility.[482] Moreover, Zhao et al. demonstrated the exceptional biodegradability of commercial cellulose films, with complete degradation observed after a four-week period in soil, underscoring their eco-friendly and sustainable nature.[483]

Cellulose possesses the ability to be fragmented into nanoscale dimensions through various methods such as mechanical blending[484] and 2,2,6,6-tetramethylpiperidine-1-oxyl (TEMPO) oxidation.[485] When harnessed in the form of nanoscale fibers at appropriate concentrations, cellulose exhibits transparency, further augmenting its potential for transparent electronic applications.[486] Leveraging the unique properties of cellulose nanofibers, various researchers fabricated electronic devices with mechanical robustness. Kang et al. fabricated transparent and foldable electrodes with AgNW percolation on cellulose film, which they named nanopaper.[487]

https://doi.org/10.1021/acs.chemrev.3c00139
Chem. Rev. 2023, 123, 9982−10078

Table 5. Engineering Strategies for Improving Electrical Conductivity and Their Corresponding Optical and Electrical Characteristics

engineering strategy	materials	improved electrical properties	transparency	ref
Directional Alignment				
mechanical stretching	CNT	conductivity increased from 1000 S cm^{-1} to 2500 S cm^{-1} (70% stretching)		509
mechanical stretching	PEDOT:PSS	resistivity decreased by 90% at 60% strain		510
mechanical stretching	PVDF	spontaneous polarization increased from 67 mC m^{-2} to 140 mC m^{-2}		511
solution shearing	AgNW	sheet resistance, aligned AgNW neworks lower by factors of 1.7−3.4 than random AgNW networks	96.7% (aligned networks), 92.9% (random networks)	512
solution shearing	semiconducting polymer (P2TDC17FT4 and PBTTT-C16)	mobility of P2TDC17FT4, from 3.4 × 10^{-3} to 9.6 × 10^{-2} (maximum, shearing speed 3.5 mm s^{-1})		513
solution shearing	PEDOT:PSS	conductivity: 4600 ± 100 S cm^{-1}	97.20%	514
assembly	AgNW nanomembrane	conductivity: 103100 S cm^{-1} parallel direction), 32900 S cm^{-1} (vertical direction)		515
Post-Treatments				
laser welding	CuNW	sheet resistance decreased from 10^7−10^8 to 20 Ω sq^{-1}	84.40%	28
flash welding	CuNW	sheet resistance decreased from several MΩ sq^{-1} to 17 Ω sq^{-1}	88%	516
cold welding	AgNW	sheet resistance decreased from 2.25 × 10^5 Ω sq^{-1} to ∼179 Ω sq^{-1}	89.40%	517
secondary doping	PEDOT:PSS	electric conductivity increased to 767 S cm^{-1}		518
secondary doping	PEDOT:PSS	decreased sheet resistance to 46 Ω sq^{-1}	90%	519

They utilize a transfer method in which cellulose in nanofiber with a diameter of 22 nm and a length of 1 μm solution is poured onto the prefabricated AgNW percolation networks. The thickness of the nanopaper is around 15 μm, and the nanopaper electrode endures the 200 cycles of folding completely back and forth. Remarkably, even after undergoing 200 folding cycles, the conductivity of the nanopaper electrode remained consistently high, below 1 Ω sq^{-1}, which initially started at 0.68 Ω sq^{-1}. These findings highlight the robustness and stability of the nanopaper electrode for transparent and foldable electronic applications. In addition to its use as a 2D substrate, cellulose nanofiber has demonstrated remarkable potential as a nanofiber template for the fabrication of conductive nanofibers through the direct coating of conductive materials. Khamwongsa et al. conducted a study wherein they successfully coated PPy onto the surface of cellulose nanofibers. This was achieved by incorporating pyrrole into a cellulose fiber solution, followed by the polymerization of pyrrole using $FeCl_3$ as an oxidant. The resulting cellulose coated with 20 wt % of PPy exhibited a conductivity of 3.33 × 10^{-5} S cm^{-1}.

Cellulose can also be utilized as a protective layer for mitigating electronic device malfunctions induced by water. Kasuga et al. demonstrated the effectiveness of coating Cu electrodes with cellulose nanofibers, leading to enhanced electrode stability even under conditions of immersion.[488] Notably, a Cu electrode, subjected to a voltage of 3 V and coated with a 5 μm layer of cellulose nanofibers, exhibited uninterrupted functionality for over 24 h, while the uncoated Cu electrode experienced a short circuit within approximately 5 min of immersion. Despite partial coverage due to scratches, the cellulose nanofiber coating maintained its protective performance thanks to the gradual repair of a gelatinous layer composed of cohesive cellulose nanofibers, which eventually enveloped the entire electrode surface.

3. ENGINEERING STRATEGIES FOR THE PROPERTY IMPROVEMENTS

The development of electronic materials has revolutionized the field of engineering, enabling significant improvements in their properties. However, the optical and electrical properties of electronic materials, especially electrode and active materials we mentioned in the previous section, necessitate further enhancement to create and improve transparent and wearable electronics with soft mechanical properties. In this section, we particularly focus on the optical and electrical properties of transparent conductors and active layers and present a broad overview of methods for improving their properties. It is challenging to achieve a linear relationship between optical and electrical properties, as they often trade off against each other (Figure 10A). Despite this challenge, numerous efforts have been made to improve both properties for high-performance transparent electronics. The figure of merit (FoM) is a performance metric for transparent conductors that combines optical and electrical properties, with higher values indicating higher transmittance and lower resistance in transparent electronics (eq 1).[489] The optical and electrical properties of transparent electronics for each engineering strategy are compared and listed in Tables 4 and 5, along with FoM values for transparent conductors if available. It is hoped that this section will provide valuable insights for researchers in the field of transparent electronics.

$$\mathrm{FoM} = \frac{\sigma_{DC}}{\sigma_{OP}} \quad (1)$$

σ_{DC} = direct conductivity, σ_{OP} = optical conductivity

3.1. Optical Properties

Wearable electronics that are optically imperceptible have several advantages, such as preserving visual information for the user and facilitating integration with vision sensor-based

https://doi.org/10.1021/acs.chemrev.3c00139
Chem. Rev. 2023, 123, 9982−10078

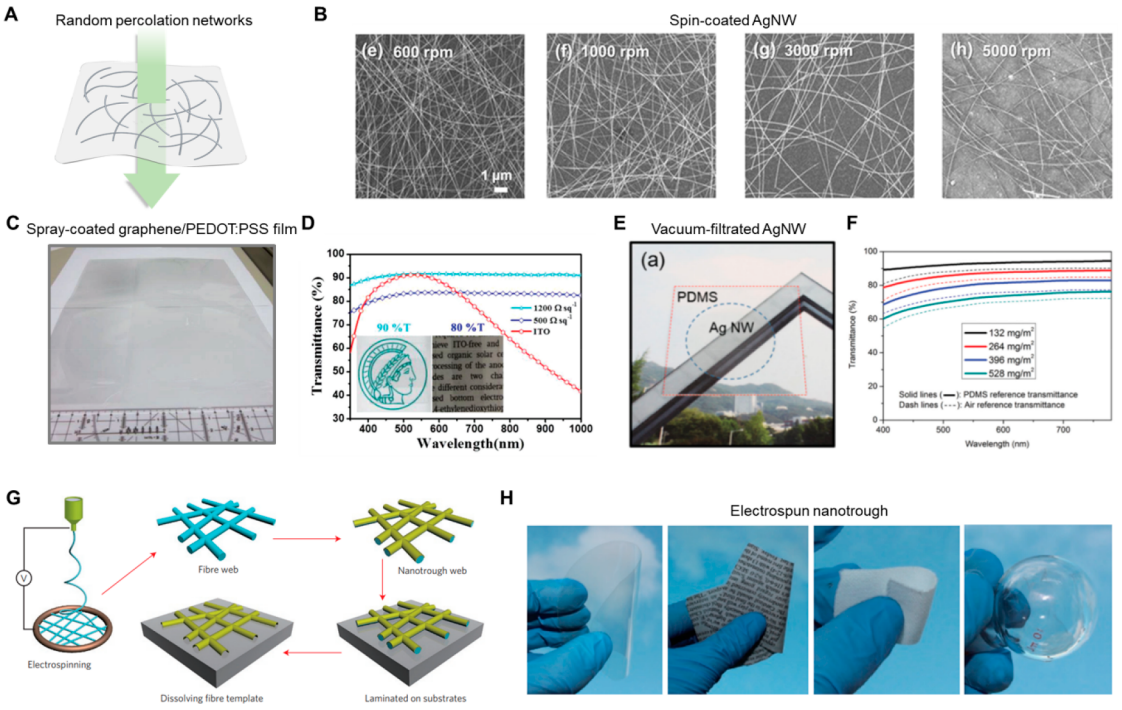

Figure 11. Random percolation networks. (A) Schematic illustration of transparent electronics enabled by random percolation networks of electronic materials. (B) SEM image of spin-coated AgNW random percolation networks depending on spin rates. Reproduced with permission from ref 493. Copyright 2013 Wiley-VCH. (C) Optical image of a spray-coated large area of rGO sheet. (D) The transmittance of a large area of rGO with over 80% in the visible range. Reproduced with permission from ref 286. Copyright 2014 Wiley-VCH. (E) Optical image of vacuum filtration transferred transparent AgNW conductor on PDMS substrate. (F) The transmittance of AgNW transparent conductor by varying the density of random percolation networks. Reproduced with permission from ref 153. Copyright 2015 Wiley-VCH. (G) Schematic illustration of electrospinning-based random percolation networks transparent conductor. (H) Optical images of electro-spun transparent conductors on various substrates. Reproduced with permission from ref 499. Copyright 2013 Springer Nature.

machine learning. It also reduces the psychological discomfort associated with wearing electronic devices. Strategies for achieving transparency in wearable electronics can be divided into depositing ultrathin electronic materials and designing the material's structures (Figure 10B). We already discussed the deposition of ultrathin materials in the previous section. In this section, we focus on the material's structure which can be further divided into creating a network of nanostructured materials and designing light-passing grids using various patterning techniques. We first discuss the strategies to enhance the optical properties of materials that are electrically conducting or semiconducting. Then, we conclude with research on improving the optical properties of packaging materials that comprise the largest area of transparent and wearable electronic devices.

3.1.1. Random Percolation Network. Various solution-based techniques have been developed to fabricate transparent conductors and semiconductors with materials such as metal nanowires, carbon-based materials, and conjugated polymers to create conductive percolation networks. These networks have a mesh-like structure that permits light transmission while also serving as conductive pathways for charge carriers. A significant advantage of solution processes is their ability to deposit materials directly onto soft substrates at low temperatures without damaging them, thereby enabling the production of large-area transparent and soft electronics using low-cost facilities.[520] By forming conductive networks above a percolation threshold, these techniques can achieve both electrical and optical properties, as light can pass through the electrically conductive mesh-like structures (Figure 11A). We highlight several solution processes to form random conductive or semiconducting percolation networks in this subsection.

Among the various solution-based techniques, spin-coating is the most simple, fast, and straightforward method. It involves depositing a solution or liquid state of synthesized materials onto a flat substrate, which is then rotated to spread the solution using centrifugal force. After the solvents evaporate, uniform thin films of percolation networks can be obtained through post-thermal annealing processes. The quality of networks is determined by the hydrophilicity of the material solution and substrate. Therefore, surface treatment of substrate through oxygen plasma or corona gun is performed for better wettability with aqueous solutions. The resulting thin films of networks show promoted adhesion and spreading over the substrate. The optical properties of spin-coated materials are determined by the concentration and viscosity of the material solutions and spin speed. For the low viscous solution and high spin speed, better transparency can be achieved through the thin thickness of the resultant film.[521] Because spin-coating can be used universally for various electronic materials synthesized in a solution or liquid state, various types of random percolation networks have been reported by using metal nanowires,[493,522] carbon materials,[494,523] conducting polymers,[495,524] and their composites.[282,525] As an example, facile control of optical and electrical properties of spin-coated AgNW was possible by modification of spin speed (Figure 11B). High diffusive transmittance of 97.5% at 550 nm of wavelength with 27.6 Ω sq^{-1} of sheet resistance was acquired

https://doi.org/10.1021/acs.chemrev.3c00139
Chem. Rev. 2023, 123, 9982−10078

on a flexible PET substrate.[493] However, it has the limitation of scalability in laboratory-scale fabrication.

Spray coating is a promising strategy to scale up the random percolation networks in a facile and cost-effective manner. In the spray coating system, synthesized materials are carried along with aerosol or carrier gas through the nozzle to the target surface while regulating temperature for solvent evaporation. Because the formation of the percolation network varies depending on the wettability of the solution on the substrates, and the spraying speed, it is necessary to design a suitable process condition for the corresponding material and substrate. Similar to spin-coating, it also can be applied to various materials such as conducting/semiconducting polymer,[496,526] carbon materials,[527−529] and metal nanomaterials[29,497,530] and their composites[286,531] for large areas of transparent electronics fabrication, and it is recommended to use or mix solvents with low boiling points, such as methanol, for rapid solvent evaporation.[530] A large area (21 cm × 30 cm) of the transparent electrode was fabricated using graphene and PEDOT:PSS composite solutions with controllable optical and electrical properties by spraying parameters (Figure 11C).[286] Depending on spraying cycles, the thickness of transparent electrodes varied from 11 to 20 nm with 90% to 80% of transparency at the visible range. The corresponding sheet resistance was from 1.2 to 0.5 kΩ sq^{-1} (Figure 11D). Despite its potential as a large-scale fabrication of transparent electronics, it has disadvantages of uniform quality of electronics.

The vacuum filtration method is an attractive way to prevent material waste. While spin or spray coating wastes large amounts of expensive materials, vacuum filtration can secure high amounts of involved materials to form percolation networks. When the synthesized material solutions are vacuumed by the pump through the filtration membrane, only solvents pass through the filter, and materials remain on it. Then, the materials are transferred to the target substrate by forming percolation networks with little material loss. The thickness of transparent films can be controlled by the amounts of solution to be filtrated for modification of optical and electrical properties. In the case of expensive electronic materials which require high costs of precursors such as AgNW and AuNWs, vacuum filtration is the most effective method for film formation with the minimized waste of materials.[151,153,281,498,532] Highly transparent and stretchable AgNW percolation networks were reported by vacuum filtration of AgNW solutions and transfer to PDMS substrate (Figure 11E). By simply controlling the amount of AgNW solutions, the areal density of AgNW could be controlled from 132 to 528 mg m^{-2} and 132 mg m^{-2} reached 93% of transparency at 550 nm (Figure 11F).[153] Various carbon-based solutions can also be vacuum filtrated and transferred to soft substrates.[533−535] Large areas of ultrathin transparent rGO films were also fabricated by vacuum filtration transfer.[533] The transmittance of ultrathin films was controlled by filtration volume from 95% to 60% at 550 nm and the lowest resistance of 43 kΩ sq^{-1}. While it can fabricate transparent electrodes on various substrates, it is confined to the size of a vacuum filter, limiting its scalability.

Electrospinning is a facile and cost-effective method to form percolation networks of materials with enhanced scale. When a varnish-type polymer solution is ejected to charged collector board with aid of a high electric field, random polymer networks are formed after evaporating the solvent. PU, polyvinylidene fluoride (PVDF), and PVA are typically used.[536] Then, thin metals or conducting polymers are deposited on them to form conductive percolation networks.[537] Electrospinning does not require complicated material synthesis recipes, so the yield of producing percolation networks is quite high[538] and the density of percolation can also be freely controlled depending on the spinning parameters such as rotating speed, and viscosity of polymer varnishes. In the case of etching the polymer backbone after conductive material deposition, free-standing conductive percolation with better conformability on skins can be obtained (Figure 11G).[499,539] Outstanding optoelectric properties with 90% of transmittance at 550 nm and 2 Ω sq^{-1} of sheet resistance were obtained for Cu nanonetworks and could be applied to various surfaces including curved flasks and textiles (Figure 11H).[499] For mechanical robustness and easy handling property, it is preferable to preserve polymer backbones.[500,540] Fabricated percolation networks are not only transparent and conductive but also allow the exchange of mass and air between the living body and the external environment through controlled pores, which is very advantageous for long-term transparent and wearable applications.

3.1.2. Conductive Grid Patterning. Patterning conventional opaque materials into periodic grids is an effective way to create transparent and electrically conductive materials. By forming grid patterns, light can pass through the spaces in the grid and the material retains its electrical conductivity. This method is cost-effective and avoids the time and expense associated with synthesizing new materials and offers a way to produce transparent electronics with similar or better performance than newly synthesized material-based electronics. Unlike random percolation networks which face difficulties in precisely controlling their electrical and optical properties, grid-patterned transparent electronics can easily manipulate these properties by adjusting the width and spacing of their patterns, resulting in mass production of electronics with consistent and uniform characteristics.[541] It is typical to create grid patterns of thin metals on polymer substrates, but in the case of transparent materials also such as PEDOT:PSS, CNT, and graphene, if voids are created through grid patterning, the optical properties are further enhanced by sacrificing some degree of electrical properties. Here, we will explain the processes to secure transparency by patterning various electronic materials.

Template-assisted printing techniques are simple solution-based patterning methods that apply solution states of materials on prepatterned templates. Depending on the use of templates, various printing techniques have been reported such as screen printing[542−546] and nanoimprinting.[30,501,502,547,548] For screen printing, templates are used for the masking layer that blocks the applied solutions. Solutions are directly poured on the target substrate where the mask template is covered. After drying the solvents, the template is removed and only areas that are filtrated with materials in templates remain as the pattern. Nanoimprinting also requires a prepatterned imprinting template and solutions are infiltrated in it. A patterned template containing materials is directly imprinted on the target substrate to transfer the pattern. Polymer resins are also poured on them to transfer patterned electronics on stretchable substrates. Various materials can be applied to these methods including metal nanoparticles,[30,542,543,548] nanowires,[501,544,547] and graphene.[545] The precision of these techniques is affected by the viscosity,

https://doi.org/10.1021/acs.chemrev.3c00139
Chem. Rev. 2023, 123, 9982−10078

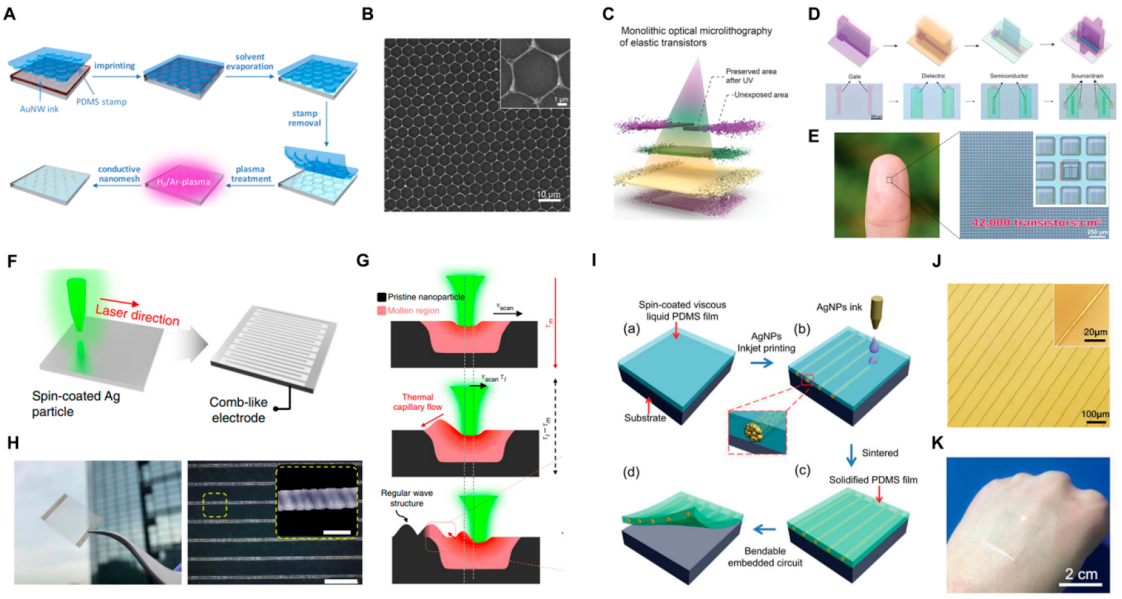

Figure 12. Grid patterning. (A) Schematic illustration of nanoimprinting technique to fabricate AuNW-based transparent conductor. (B) SEM image of grid-patterned AuNW transparent conductor. Reproduced from ref 501. Copyright 2016 American Chemical Society. (C,D) Schematic illustration of optical microlithography for patterning organic semiconductors, conductors, and dielectrics. (E) Optical images of fabricated 42 000 transistors consist of patterned organic materials in a small area. Reproduced with permission from ref 551. Copyright 2021 American Association for the Advancement of Science. (F,G) Schematic illustration of direct laser sintering process to fabricate grid patterned Ag transparent conductor. (H) Optical image and SEM image of grid-patterned transparent Ag conductors. Reproduced with permission from ref 506. Copyright 2019 Springer Nature under the CC BY 4.0 license http://creativecommons.org/licenses/by/4.0/. (I) Schematic illustration of inkjet printing of AgNP inks for grid-patterned transparent conductors. (J,K) Optical images of grid-patterned transparent conductors. Reproduced with permission from ref 508. Copyright 2015 Wiley-VCH.

concentration of the printing solution, and resolution of prepatterned templates. Templates can be fabricated in diverse approaches such as photolithography, nanosphere lithography, and laser machining. Additional thermal annealing could improve the properties of transparent electronics.[30,501,548] For instance, submicrometer resolution of imprinted AuNW grids by direct imprinting methods. The imprinting template was placed onto solutions of AuNW and conformally contacted to the substrate (Figure 12A). After evaporating the solvent, the template was removed for ultrathin grids of the transparent electrode. The fabricated transparent conductor showed honeycomb-shaped nanowire grids with high transparency of 92% at 500 nm and 227 Ω sq^{-1} of sheet resistance (Figure 12B). This process can be assembled with the roll-to-roll process for the mass production of large areas of transparent electronics.[547]

Light-based patterning can fabricate patterns of electronic materials using the photochemical or photothermal reaction induced by the irradiation of light on materials. Photolithography is a conventional method that selectively irradiates light through photomasks on a photoresist (PR). Depending on the type of PR, cross-linking occurs only in the part that receives the light or vice versa. Then, after developing the non-cross-linked part, the pattern is completed by the last etching step. The pattern produced by photolithography is highly precise compared to other processes, and mass production is possible through the matured manufacturing system. However, the temperature or pressure for the process is harsh and toxic chemicals used for etching are not suitable to use directly on the soft polymer substrates. Therefore, metal-based grids were mainly fabricated by photolithography techniques.[503,504,549,550] Nevertheless, direct patternings of soft materials including semiconducting polymers, conducting polymers, and insulating polymers on the soft substrates have recently been reported (Figure 12C). UV-triggerable carbene species were introduced as general cross-linking agents in semiconducting and insulating polymers and PEGDMA for conducting polymers. Direct patterning of soft polymers was possible by serial UV light exposures to polymers with 2 μm for conducting polymer and 4 μm for semiconducting polymer (Figure 12D). It could highly integrate all polymer-based 42 000 transparent transistors in square centimeters, which takes advantage of the mass production of conventional photolithography (Figure 12E).[551]

Compared to the photolithography method, which involves multiple complex steps for pattern generation, laser-based techniques offer a more direct and efficient approach.[552] Laser ablation, for instance, can be used to create precise patterns of materials in a simple and fast way. Selective removal of deposited electronic materials can be achieved by pulsed laser ablation, leaving behind grid patterns. This subtractive laser ablation process offers a wide range of material options, including ultrathin metal films,[505] metal nanowires,[553] and 2D materials,[554] which can further enhance the transparency of the resulting percolation networks. However, for the ablation of materials, relatively high powers of pulse laser are required which results in rough surfaces and irregular pattern resolutions.[555] Additive laser sintering processes can resolve these limitations by using the interaction of electronic materials and the laser.[552] For example, when the metal nanoparticles are synthesized in small sizes, the melting point is drastically decreased compared to the bulk state.[556] These nanomaterials can greatly absorb special wavelengths of the laser by plasmonic effect, so through appropriate selections of nanoparticles and lasers, it is possible to locally melt and transform nanoparticles into thin metal through laser-induced

https://doi.org/10.1021/acs.chemrev.3c00139
Chem. Rev. 2023, 123, 9982−10078

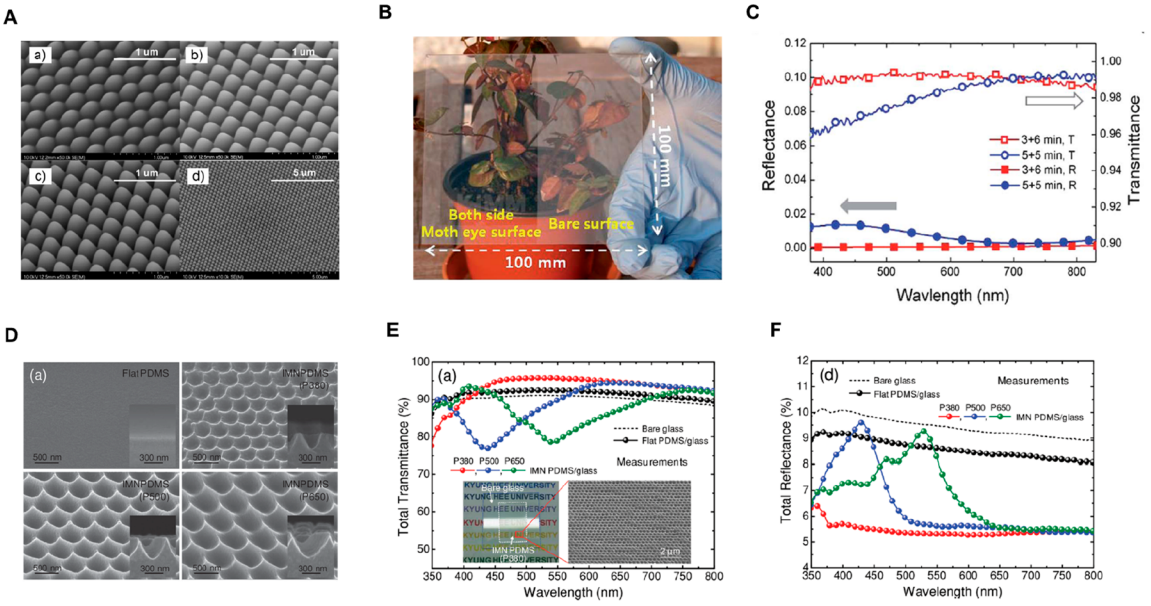

Figure 13. Subwavelength structure. (A) SEM images of the subwavelength structure referred to as the moth-eye structure. Reproduced with permission from ref 564. Copyright 2010 Wiley-VCH. (B) Digital image of bare glass and SWS structured glass showing a clear difference in reflectivity. (C) Reflectance and transmittance of SWS structure depending on process condition. Reproduced with permission from ref 565. Copyright 2009 Royal Society of Chemistry. (D) SEM images of inverted moth-eye structure in PDMS sheet. (E) Total transmittance of bare PDMS and SWS PDMS. (F) Total transmittance of bare PDMS and SWS PDMS. Reproduced with permission from ref 566. Copyright 2014 Wiley-VCH.

photothermal reactions.[27,30,506,557,558] As an example, the AgNP solution was spin-coated on a flexible substrate and a 532 nm laser was scanned for sintering (Figure 12F). When the laser was scanned on a pristine AgNP layer, photothermal energy locally melted the AgNPs and interconnected each other (Figure 12G).[506] Depending on laser parameters, the morphology of sintered Ag lines can be modulated. It showed a 20 μm resolution of line width and 100 μm of intervals (Figure 12H). Because the laser can provide localized heat for the sintering process at ambient conditions, it can minimize thermal damage on soft polymer substrates.

Grid patterns have controllable electrical and optical characteristics according to line width and pitches. Therefore, to secure a database of transparent electronic material properties, it is essential to rapidly prototype each condition of grid patterns. However, in the case of lithography, the fabrication costs greatly increase with photomasks for each pattern condition. Furthermore, while there must be unavoidable wastes of materials in the photolithography or laser processes, inkjet printing can fabricate various prototypes without expensive photomasks and loss of materials.[559] Synthesized solutions states of materials are ejected in the form of droplets through a nozzle (Figure 12I). The size of ejected droplets is determined by the size of the nozzles and the viscosity of the inks. By continuously ejecting these droplets, the programmed patterns are drawn through the compute-aided design program. The quality of grid patterns depends on the discharge conditions (e.g., voltage and waveform) and the characteristics of the inks and substrates. Materials used are usually synthesized metal nanoparticles,[507,508] graphene ink,[560,561] and semiconducting metal oxides.[562] For instance, a stackable transparent integrated circuit is developed by inkjet printing on the PDMS layer. Three layers of 1.6 μm width of conductive Ag gird were stacked by keeping high transparency of 85% at the visible spectrum (Figure 12J, 12K).[508]

3.1.3. Subwavelength Structures. So far, we have discussed various engineering processes aimed at enhancing the optical properties of electrically conducting or semiconducting materials used as functional layers in transparent electronics. However, it is worth noting that packaging materials, such as substrates and encapsulations, occupy a significantly larger area compared to functional layers. Surprisingly, there is a lack of research focused on improving the optical properties of them. For wearable electronics, which often utilize flexible polymers and soft hydrogels as packaging materials, transparency is inherent. However, when these materials are applied to the human skin, they tend to reflect light, creating a noticeable optical contrast with the surrounding unattached areas. As a result, it becomes crucial to develop strategies that reduce light reflection and increase transparency to achieve optical imperceptibility in transparent and wearable electronics.

There have been various studies for antireflective layers for transparent electronics,[563] among them we focus on subwavelength structures (SWS) applied to packaging material that can reduce the Fresnel reflection between the air and the material. Properly designed SWS can greatly reduce reflectivity in the broadband and also increase transparency in the target region in broadband. To minimize the Fresnel reflection between air and materials, the structure needs to be tapered, preferably smaller than the optical wavelength and the height of the tapered structure should exceed the broadband wavelength, which is referred to as the moth-eye structure (Figure 13A).[564] To achieve such an intricate and challenging high aspect ratio of nanostructure array with a high packing density, various processes have been developed such as colloidal lithography,[565] laser interference lithography,[564,566] and photolithography.[567] Colloidal lithography can conven-

https://doi.org/10.1021/acs.chemrev.3c00139
Chem. Rev. 2023, 123, 9982−10078

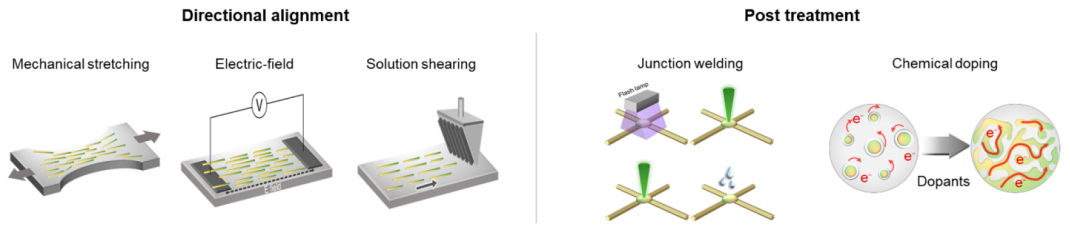

Figure 14. Engineering strategies to enhance electrical properties of transparent electrodes and active materials.

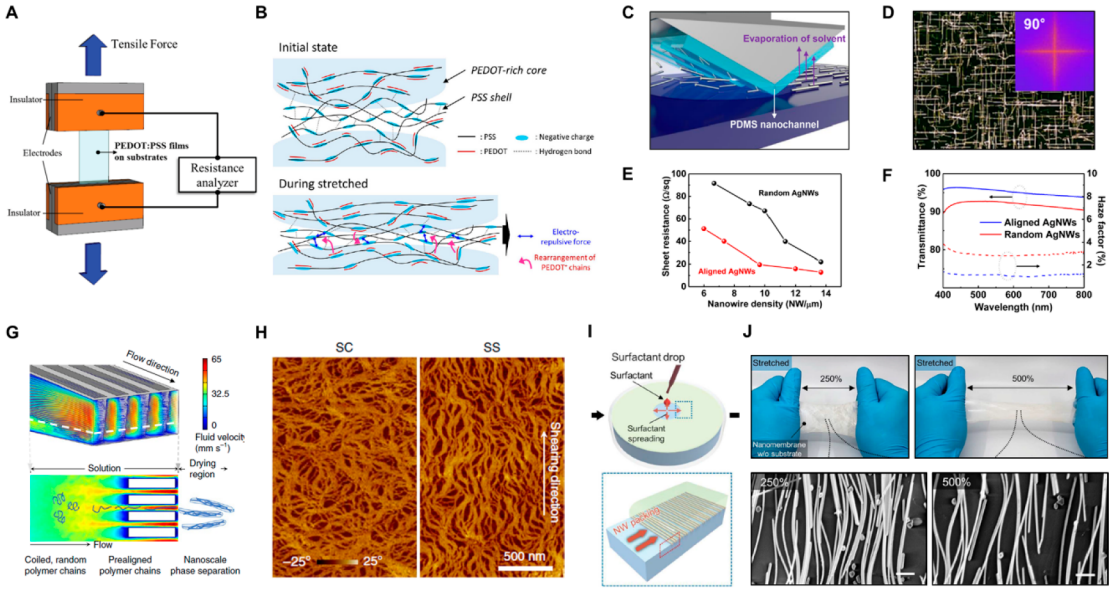

Figure 15. Directional alignment. (A) Schematic illustration of mechanical stretching of PEDOT:PSS for rearrangement of polymer chain structures. Reproduced with permission from ref 510. Copyright 2013 Wiley-VCH. (B) Schematic illustration of polymer chains under mechanical deformation. Reproduced with permission from ref 573. Copyright 2016 Springer Nature under the CC BY 4.0 license http://creativecommons.org/licenses/by/4.0/. (C) Schematic illustration of solution shearing of AgNW solution to directional alignment. (D) SEM image of aligned AgNWs. (E) The sheet resistance of aligned AgNW showing higher conductivity than random percolated AgNW. (F) The transmittance of aligned AgNW-based transparent conductor and random percolated conductor. Reproduced from ref 512. Copyright 2015 American Chemical Society. (G) Schematic illustration of solution shearing of organic semiconductors using the micropatterned channel. (H) AFM images of aligned organic semiconductors and spin-coated counterparts. Reproduced with permission from ref 575. Copyright 2019 Springer Nature. (I) Schematic illustration of floating assembly to align and pack AgNW networks using surfactant dropping. (J) Optical images of aligned AgNW conductors showing high stretchability. Reproduced with permission from ref 515. Copyright 2021 American Association for the Advancement of Science.

iently fabricate SWS by employing a colloidal polystyrene nanoparticle layer as an etching mask.[565] To create a monolayer of nanoparticles, a particle solution with a diameter of several hundred nanometers is coated. The resulting shape of the SWS after etching varies depending on the size of the nanoparticles. Therefore, adjusting the nanoparticle size using O_2 plasma allows for control of the packing density. Plasma etching using a CF_4 and H_2 mixture generates the desired SWS shape, while the remaining polystyrene nanoparticles are subsequently removed. These produced SWS structures exhibit distinct transmittance and reflectance properties based on their shapes. When applied to transparent glass, they achieved higher transmittance and lower reflectance compared to bare glass (Figure 13B), and through controlling etching duration, exceptional transmittance of over 99%, and remarkably low reflectance ranging from 0.7% to 1.2% were achieved (Figure 13C).

Laser interference lithography enables the fabrication of finely controlled SWS without the need for a mask layer. After coating a PR with a thickness of several hundred nanometers on the desired substrate, two laser beams are irradiated to induce an interference pattern in the PR. After developing the pattern, thermal reflow is performed, causing the PR to transform into a lens-like shape. Subsequently, plasma etching is conducted, resulting in the formation of a parabolic SWS structure. The shape of the SWS varies depending on the period of the PR according to the two laser exposures as well as the conditions of thermal reflow and etching. Compared to a flat substrate, the average reflectance of the SWS decreased significantly to 7.8% in the wavelength range of 300−2000 nm, whereas it exceeded 30%.[564]

Despite the above-mentioned studies that enhanced the optical properties of materials, to apply this technology to wearable electronics applications, it is necessary to embed the SWS in soft packaging materials, and several groups have reported highly controlled SWS in flexible substrates or soft elastomers to reduce reflectivity and maximize transparency. By utilizing the above-mentioned processes, a master mold with embedded SWS can be fabricated on rigid materials. Subsequently, soft imprint lithography allows for the imprinting of inverted SWS structures onto soft or flexible packaging materials such as PU[568] and PDMS.[567] In the case of PDMS, a Si master mold was fabricated by laser interference lithography.[566] After dropping and curing PDMS onto the

https://doi.org/10.1021/acs.chemrev.3c00139
Chem. Rev. 2023, 123, 9982−10078

mold, an improved optical characteristic of the PDMS sheet was obtained (Figure 13D). In this process as well, the optical properties varied depending on the period of the SWS, and at the optimal period of 380 nm, it exhibited a total transmittance of 93.8% over a wide wavelength range, whereas flat PDMS showed a transmittance of 91% (Figure 13E). In terms of reflectance, the SWS with a period of 380 nm exhibited 5.5% reflectance, while flat PDMS showed 8.6% reflectance, demonstrating improved optical characteristics (Figure 13F). The proposed structural approach can be applied to various newly developed soft materials to fabricate transparent wearable devices with superior optical properties, which is expected to greatly enhance the optical imperceptibility of transparent wearable devices.

3.2. Electrical Properties

Design parameters of ultrathin materials, random percolation networks, and grid patterns for high optical properties inevitably sacrifice the electrical properties of transparent wearable electronics. This deteriorated electrical property induces severe noise levels to the biosignal when electronic devices are integrated with living bodies. Furthermore, the presence of irregularly high resistance regions can cause uncontrolled heat generation, potentially leading to burns in biological tissues. Therefore, to safely and accurately record the biosignal coming from the living body, sufficient electrical properties have to be ensured. In this section, we broadly review mechanical, electrical, chemical, and thermal strategies that have been developed to improve the electrical properties of transparent electronic materials while maintaining high transparency (Figure 14).

3.2.1. Directional Alignment. Random percolation networks fabricated by nanowires or carbon nanotubes allow charges to flow through the backbones of networks. In the case of semiconducting or conducting polymer, charge flows along the polymer chains. The random distribution of the percolation networks results in random charge flow, leading to increased resistance and delayed electrical signals from living bodies. However, if percolation networks or polymer chains are aligned in a specific direction, the charge prefers to flow in the guided directions by lowering the percolation threshold, which enables signal transmission through fast charge flow. In this section, we will introduce various methods in which polymer chains or percolation networks can impart directionality and discuss the improvement of the electrical properties of applied materials.

Mechanical stretching can induce directional alignment most intuitively. Uniaxial stretching is performed to promote the directional alignment of electronic materials such as CNT,[509,569] graphene,[570,571] metal nanowires,[572] and PEDOT:PSS,[510,573] to modify electrical properties. PEDOT:PSS is known to have a low fracture strain of less than 5%, resulting in a high resistivity increase. It is due to the large difference in mechanical properties from the substrate where PEDOT:PSS is deposited, and the difference in conductivity according to the strain of pristine PEDOT:PSS was reported by matching the mechanical properties with the substrate (Figure 15A).[510] As a result, when tensile strain is applied to PEDOT:PSS, morphological changes occur in which the connection between conductive PEDOT-rich domains is strengthened by the strain, and the resistivity decreases by 90% at 60% tensile strain (Figure 15B).[573] Piezoelectric polymer, PVDF has permanent dipoles inside the molecule structure so that voltage is output according to mechanical strain due to temporal change of the dipole system. It is widely adopted as transparent functional layers for various transparent wearable sensors due to its piezoelectricity. There are three well-established polymorphic phases of α-, β-, and γ-phase coexisting inside PVDF. It is important to produce as much β-phase as possible to get better piezoelectric properties because it has the highest dipole moment among them. Many studies have confirmed that the β-phase is greatly increased through morphological changes inside the polymer chain by mechanically stretching PVDF, and improved piezoelectricity properties have been reported.[511,574] Mechanical stretching, however, can not apply uniform strain across the entire film, resulting in nonuniform electrical properties. In addition, because it is difficult to apply to fragile thin films, it can be seen as suitable for low-quality mass production of electronic materials.

Solution shearing can give local strain to induce morphological change or molecular packing of electronic materials in a facile and precise manner. In solution shearing, shearing plates or nanomicropatterned shearing channels drag the solution or liquid state of synthesized materials on the substrate while the substrate is heated for solvent evaporation (Figure 15C).[512−514,575] When nanowire solutions are dragged through a nanopatterned channel, the charge can flow in programmed pathways, resulting in higher electrical properties with the same density compared to those of random percolation networks of AgNWs fabricated by other solution processes (Figure 15D, 15E).[512] In addition, it is possible to secure high optical transmittance compared to random percolation networks of the same resistance because more light-passing areas can be created through minimal nanowire density (Figure 15F). Semiconducting polymers are also solution-sheared by micropatterned channels to enhance hole mobility by tuning molecular packing in chain structures (Figure 15G).[513,514,575] The molecular packing and crystallinity in the semiconducting film are determined by shearing speed and which showed different lattice spacing. Directional alignment of polymer chain structure showed a high enhancement of electrical mobility by up to 6-fold compared with spin-coated samples and a 3-fold enhancement of mobility under 100% of strain (Figure 15H). Solution shearing methods, which can be applied to various materials described above, are highly effective in that they can easily improve the molecular structures and physical properties of electronic materials without changing sophisticated synthesis recipes.

There exist electric dipole moment systems in certain electronic materials which can react to the external electric field. The external electric field can induce directional alignment or conformational change of such materials with controlled heat treatment. PVDF can react to the external electric field through internal dipole systems. Various studies reported increased ferroelectricity of PVDF through dipole moment alignment by the external electric field (i.e., production of β-phase).[576] PEDOT:PSS also have dipole systems where positively charged PEDOT-rich domains are ionically bonded to negatively charged PSS-rich domains. By applying external electric fields to PEDOT:PSS, electrical conductivity is enhanced by the connection of the conductive PEDOT-rich domain through phase separation.[577] This phenomenon can also be applied to various electronic materials having dipole systems inside their chemical structures.

https://doi.org/10.1021/acs.chemrev.3c00139
Chem. Rev. 2023, 123, 9982−10078

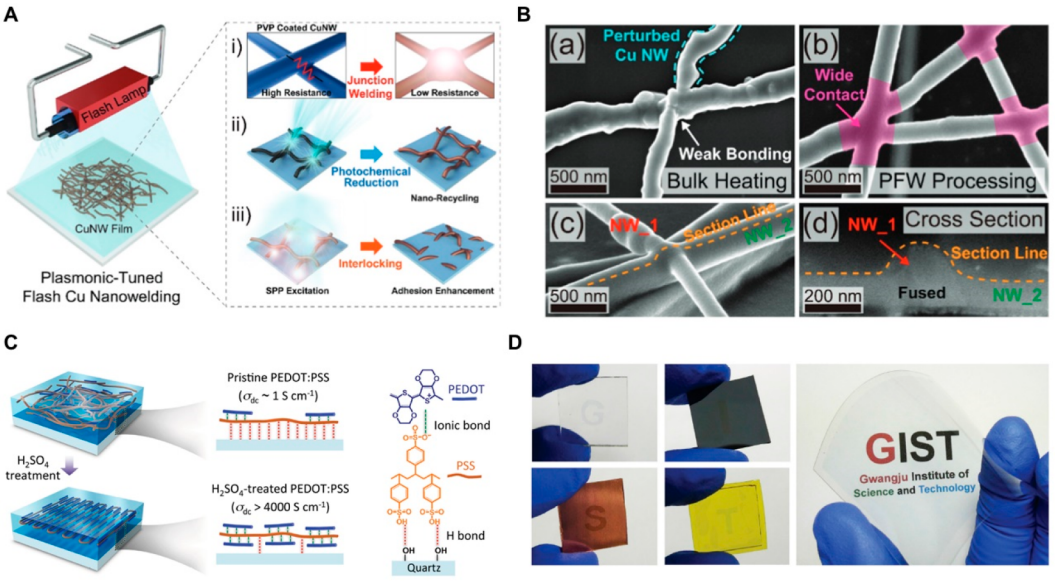

Figure 16. Post-treatments. (A) Schematic illustration of photothermal annealing induced nanowire welding process. (B) SEM images of photothermally welded CuNW percolation networks. Reproduced with permission from ref 516. Copyright 2017 Wiley-VCH. (C) Schematic illustration of post-treatment of PEDOT:PSS in H_2SO_4 for conductivity enhancement. (D) Optical images of PEDOT:PSS after cleaning H_2SO_4 and transferring on the various substrate. Reproduced with permission from ref 519. Copyright 2015 Wiley-VCH.

Interface-based assembly of nanomaterials is also an effective method to fabricate aligned nanomaterials with high scalability. Langmuir−Blodgett assembly is a representative method to coat ultrathin layers of nanomaterials on target surfaces. After dispersing materials on the surface of the water, pressure in a specific direction is applied through the plate to give alignment of materials and transfer them to the substrate. The density of the aligned percolation network can be adjusted according to the number of depositions to control transparency and electrical properties. Various electronic materials synthesized in the solution state such as carbon materials[578,579] and metal nanomaterials[580] can form aligned percolation networks for transparent electronics in large areas through assembly technique. Recently, similar to the Langmuir−Blodgett, a floating assembly is reported to give alignment of various nanomaterials.[515] By dropping surfactant on the surface of dispersed nanomaterials, close packing of materials occurs through Marangoni flow induced by surface tension gradient (Figure 15I). Highly packed and aligned nanowire membranes could be stretched up to 500% of strain which has excellent compliance with the skin (Figure 15J). Although closely packed nanomembranes are not sufficiently transparent in this study, it is expected to be a useful method for transparent electrodes if the packing distance is adjusted or patterned in microgrids with photolithography.

3.2.2. Post-Treatment. Transparent electronic materials fabricated by various processes have unavoidable defects inside. In the case of ultrathin materials deposited by the vacuum processes, there exist too many defects and grain boundaries inside the lattice.[581] Metal nanowire percolations have high resistances at the junctions between nanowires due to the polymer capping layers, which are electrical insulators.[582] For organic semiconductors or conductors, the electrical properties are severely hindered by excessive amounts of insulator components in the polymer chains.[583] To decrease these defects, post-treatments such as high-temperature annealing have been developed. However, to apply for wearable transparent electronics, new types of post-treatment processes that can improve the defects of the material even with heat-sensitive soft materials are required. In this section, we introduce postprocesses that improve the electrical properties of transparent electronics that can be applied on flexible or stretchable soft substrates.

Heat treatment is an important process to control the crystallinity or phases of materials. To induce these changes in materials states, most of the processes require high temperatures over several hundred degrees Celsius or a vacuum environment. However, materials used in wearable electronics are easily burned at high temperatures or mechanically distorted in vacuum environments. Therefore, there is a need for developing methods of increasing electrical properties without damaging soft materials at low temperatures and atmospheric pressure. Light is an energy source that can freely supply thermal energies to materials regardless of surrounding temperature and pressure. Furthermore, in the case of certain nanomaterials, there are characteristics of greatly absorbing light in an instant when exposed to light, which is known as the plasmonic effect. Therefore, various annealing post-treatment based on photon energy termed "photothermal annealing" has been widely developed. A laser can selectively supply a high density of photon energy for recrystallization or phase changes of materials. When the laser is irradiated on metal nanowire percolation networks, light is greatly absorbed by the plasmonic effect at the junctions, heat is generated here, and the junctions are welded together for better charge flows.[28,584,585] Similar phenomena are reported in another light source, the Xenon flash lamp.[516,586] Unlike a laser, the flash lamp has no selectivity, but it has the advantage of scalability to treat a large area of electronic materials with fast processability. When the flash lamp is irradiated on the metal nanowire percolation networks, plasmonic welding occurs in the junctions of nanowires without any oxidation (Figure 16A).[516] These welding spots without insulating PVP shell enabled fast charge transport along the percolation networks that showed significant drops of sheet resistance after the process (Figure 16B). Along with the nanowelding between

https://doi.org/10.1021/acs.chemrev.3c00139
Chem. Rev. 2023, 123, 9982−10078

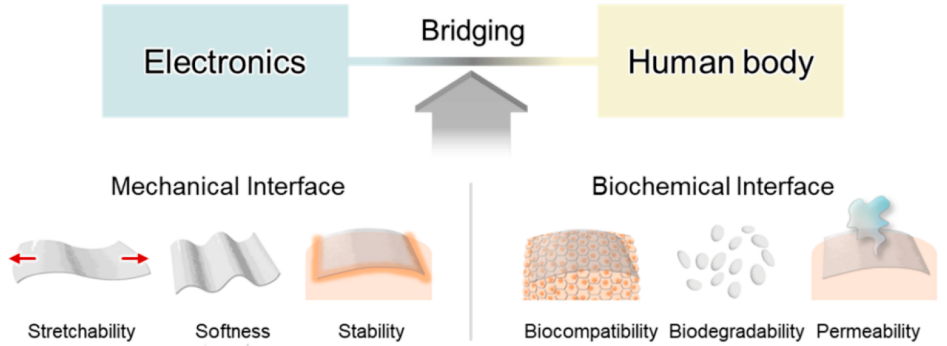

Figure 17. Bridging interface with the human body.

the junctions of nanowires, mechanical interlocking occurred with flexible substrates which enhanced the robust adhesion of percolation networks to substrates. However, its accuracy of property modification is lower than that of a laser, so it would be more desirable to use it for mass production purposes in wearable electronics that do not require high electrical properties.

Cold welding processes without expensive optical equipment are also developed to improve the electrical properties of percolation networks. Even though the processes using photothermal energy apply little thermal stress to the soft substrate, inevitable thermal strain or burning can occur if excessive heat is supplied. Therefore, techniques that induce welding at percolation junctions that do not apply heat at all are being developed at room temperature and pressure with cost-effective equipment. Solvents that can dissolve the capping layers of nanomaterials are also post-treated for percolation networks to improve junction resistance. By applying multiple solvent treatments, exfoliation of the capping layer occurs to decrease the gap of junctions of metal nanowires.[587] Solvents also can induce nanoscale capillary force for cold welding when it is evaporated which can also lower junction resistance. Water is normally used as an evaporation solvent to induce capillary force at staked nanowire percolation networks.[517] Additional mechanical pressing can maximize the welding effect with solvent treatments. By adopting the roll-to-roll system, large areas of transparent electronics with improved electrical properties can be fabricated with enhanced scalability.[522]

Applying solvents or chemical treatment can change the chain structure of organic materials for better electrical properties. For example, PEDOT:PSS has chemical structures composed of the benzoid and quinoid structures where the benzoid structure is disadvantageous for charge transport and the quinoid structure is much more advantageous.[518] When dried pristine PEDOT:PSS film is immersed in H_2SO_4, the benzoid structures are transformed into the quinoid structure with morphological changes from coiled to linear conformations for better charge flow in polymer chains (Figure 16C).[519] The electrical conductivity was enhanced from 1 S cm^{-1} to over 4000 S cm^{-1} by simply dipping in H_2SO_4. It can improve the electrical properties of conducting polymer without composite materials which can affect the optical property because the solvents can be fully removed by evaporation or washing steps. Highly transparent and semimetallic conductive PEDOT:PSS films can be transferred to various substrates for flexible electronics applications (Figure 16D).

4. BRIDGING INTERFACE WITH THE HUMAN BODY

Human body sustains its life through constant mechanical movement and chemical metabolism. Healthy adults take 7000−13 000 steps per day,[588] where joints are folded and flexed continuously and facial muscles are repeatedly stretched and released while talking and eating foods every day. This continuous movement applies continuous stress and strain to wearable electronic devices integrated with bodies.[589] Biofluid such as sweat, secretion, and blood that are continuously generated from the living body easily make the wearable and implantable devices detached or corroded, which eventually causes device malfunction.[590] Furthermore, inadequate regulation of heat while wearing wearable electronic devices can lead to thermal discomfort and tissue damage. Therefore, strategies for bridging electronic devices with biosystems with high safety are required for reliable operations during desired periods, such as disease diagnosis or medical treatment. (Figure 17). This section introduces bridging strategies for efficient interfaces to the living body in mechanical, chemical, biochemical, and thermal aspects (Tables 6 and 7).

4.1. Mechanical Interface

Securing tissue-like mechanical properties is essential for the stable operation of wearable and implantable devices integrated with biosystems that constantly repeat dynamic mechanical contraction and relaxation. Human body, for instance, has a stretchability of ∼30% in the case of skin,[615] and the heart undergoes volume changes of 8−13% throughout the cardiac cycles.[616] In addition, the human body has soft mechanical properties with low Young's modulus depending on the area while widely used electronic materials show much higher ranges of modulus (Figure 18).[4] When conventional rigid electronic devices are attached or inserted into the living body, they can directly damage the biotissue due to the difference in mechanical modulus, and side effects such as foreign body reactions or immune responses can occur. This is not only dangerous in terms of human safety but also leads to the failure of electronic devices due to inflammatory encapsulation.[4] To resolve these problems, various structural and material studies have been actively conducted to design electronic devices with advanced mechanical properties including stretchability and softness to cope with repetitive mechanical deformation and the soft nature of living tissues. In this section, we review strategies to match the mechanical properties of devices to biological systems by using transparent electronic materials.

4.1.1. Stretchability. *4.1.1.1. Structural Engineering.* Inorganic electronic materials have been verified for their

https://doi.org/10.1021/acs.chemrev.3c00139
Chem. Rev. 2023, 123, 9982−10078

Table 6. Various Engineering Strategies for Improving Mechanical Stretchability of Electrode Materials for Human−Machine Bridging

engineering strategy	materials	stretchability	cycle test	electrical properties	transparency	ref
Structural Engineering						
ultrathin thickness	graphene	tensile strain, 12%; compression, 31%	bending cycles >150	pristine (696.5 Ω sq^{-1}), Au-doped (354.5 Ω sq^{-1}), and AgNW-coated (98.8 Ω sq^{-1})	>80%	591
ultrathin thickness	PEDOT:PSS	tensile strain: 2700%	bending cycles >45000	sheet resistance <350 Ω/sq	>92%	592
ultrathin thickness	microcracked Au	tensile strain: 350%	stretching cycles 5000 (100% strain)	resistivity: from 6.33×10^{-7} (0%) to 4.46×10^{-6} (100%) and 8.70×10^{-6} Ω m (200%)		593
prestrain	Ag	tensile strain: 30%	stretching cycles >600 (10%, 20% strain)	sheet resistance: 12−69 Ω sq^{-1}	17.66%	594
prestrain	AgNW	tensile strain: 180%	stretching cycles >5000 (50% strain)	sheet resistance: 26.8 Ω sq^{-1}	91.80%	595
prestrain	GO	tensile strain: 400%	stretching cycles >5000 (400% strain)	sheet resistance: 260 Ω sq^{-1}	70%	596
serpentine	ITO	tensile strain: 200%		device resistance: 10^5 Ω		597
serpentine	graphene	tensile strain: 106%		sheet resistance: 480 Ω sq^{-1}	90%	6
serpentine	AgNF	tensile strain: 60%	stretching cycles: 500	sheet resistance: 9.0 Ω sq^{-1}	90%	7
auxetic	graphene	maximum tensile strain: *x*, 13.7%; *y*, 8.8%			87.8% (@ 800 nm)	598
auxetic	AgNW (Kirigami)	tensile strain: 400%	stretching cycles >10000 (400% strain)	sheet resistance: 0−50 Ω sq^{-1}	80%	599
Materials Engineering						
percolation network	AgNW	tensile strain: 460%	stretching cycles: 100 (100% strain)	9−70 Ω sq^{-1}	90−96%	8
percolation network	AgNW/CNT	tensile strain: 460%	bending cycles >10000, large twisting >540 degrees, complete folding 6 times	sheet resistance from infinity to 24−27 Ω sq^{-1}	80−93%	281
percolation network	nanotrough networks	tensile strain: 70%	stretching cycle: 15000 (50% strain)	sheet resistance: 3.8 Ω sq^{-1}	90%	600
plasticizing networks	PEDOT:PSS	tensile strain: 800%	stretching cycles: 1000 (100% strain)	conductivity: 3100 S cm^{-1} under 0% strain and over 4100 S cm^{-1} under 100%	96%	601
plasticizing networks	PEDOT:PSS	tensile strain: 188%	stretching cycles >1000 (10% strain), resistance change 2%, > 1000 (20% strain)	sheet resistance: 260 Ω sq^{-1}	95%	602
plasticizing networks	PEDOT:PSS	no crack formation under 100% strain	stretching cycles: 500 (100% strain)	conductivity: 2700 S cm^{-1} (0%)−6000 S cm^{-1} (100%)	94%	603
nanoconfinement	semiconducting polymer	tensile strain: 100%	stretching cycles: 100 (100% strain)	mobility: 1.32 cm^2 V^{-1} s^{-1}		10
nanoconfinement	semiconducting polymer	tensile strain: 100%	stretching cycles: 1000 (50% strain)	mobility: 1.50 cm^2 V^{-1} s^{-1}		575

https://doi.org/10.1021/acs.chemrev.3c00139
Chem. Rev. 2023, 123, 9982−10078

Table 7. Various Engineering Strategies for Improving Softness of Electrode Materials for Human-Machine Bridging

materials	Young's modulus	stretchability	electrical properties	transparency	ref
Electrically Conductive Elastomer					
PEDOT:PSS, elastomer	56.1−301.0 kPa	tensile strain 700%	electrical conductivity: 1−37 S cm^{-1}	70−95%	604
EGaIn, elastomer	89 kPa	tensile strain 769%		semitransparent	605
Ionic Conductive Elastomer					
electrolyte salt (LiTFSI)/monomer (BA)/cross-linker (PEGDA)		tensile strain 1100%	electrical conductivity: 1.27×10^{-7} S cm^{-1}	98%	606
AAm/MA	0.04 MPa (AAm/MA = 1/2), 0.87 MPa (AAm/MA = 2/1)	tensile strain: 450%	ionic conductivity: 4.0×10^{-4} S cm^{-1}	95.1%	607
Electrically Conductive Hydrogels					
PVA/PAAm/PPy hydrogel	tensile strength 0.2 MPa, compression strength 1.5 MPa	tensile strain: 500%, stretching cycles: 2000 (100% strain)	electrical conductivity: 0.3 S m^{-1}	94.2%	608
PEDOT/PAAm hydrogels	8−400 kPa	tensile strain >100%, stretching cycles: 10 (100% strain)	electric conductivity: 23 ± 5.6 S m^{-1}		609
pure PEDOT hydrogels	24 ± 5.4 kPa (using AFM)	tensile strain: 20%, stretching cycles: 10000 (20% strain)	electric conductivity: 47.4 ± 1.2 S cm^{-1}		610
pure PEDOT hydrogels	1.1 MPa	tensile strain >35%	electric conductivity: 28 S cm^{-1}		611
pure PEDOT hydrogels	57 MPa	tensile strain: 20%, stretching cycles: 5000 (15% strain)	electric conductivity: 670 S cm^{-1}		612
Ionic Conductive Hydrogels					
PAAm hydrogel containing LiCl salts	12 kPa	areal strain: 1000%, tensile strain: 1000%, stretching cycle: 100 (200% strain)	ionic conductivity: 1 S m^{-1}	98%	613
NaCl containing polyacrylamide hydrogel	10^5 N m^{-2}	areal strain: 167%	sheet resistance: 10^2 Ω sq^{-1}	98.9%	614

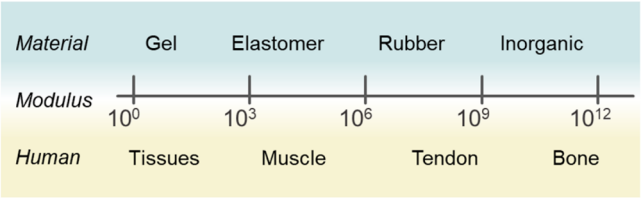

Figure 18. Elastic modulus of various electronic materials and biological tissues.

high electrical properties which enabled fast response to biosignals. However, due to their inherent rigidity, it is not mechanically matched with biological tissue, so electrical breakages occur during the repetitive deformation of living bodies, making their excellent performance useless. To maintain the high electrical properties of inorganic materials even interfaced with soft biological systems, ultrathin nanomembranes have been developed.[617,618] By thinning inorganic materials down to hundreds of nanometers, the elastic modulus and stiffness are greatly reduced but also can ensure high transparency simultaneously. The silicon nanomembrane showed a gradual increase in elongation when it is fabricated down to 25 nm. It also showed a notable decrease in Young's modulus, where bulk silicon has 180 GPa of modulus but drops to 3.25 GPa when it is thinned down to the nanoscale.[617] Single crystalline GaN nanomembrane also showed high compliance to human skin when it is fabricated down to 200 nm.[618] This concept can also be applied to organic materials such as graphene,[591,619] conducting polymers,[620] elastomers,[592,593] and hydrogels.[621] For example, microcracked gold-coated ultrathin PDMS conductors show superior stretchability to thick ones by demonstrating 300% stretchability and recovering electrical properties (Figure 19A).[593] A thin layer of gold was evaporated on the ultrathin thickness of the PDMS membrane with controlled cracked morphology for high stretchability. Due to ultrathin properties, it could be conformally attached to various biological tissues such as human skin and mouse nerves (Figure 19B,C). High gas permeability and adhesion to tissues also allowed long-term safe operation of bioelectronic applications.

Stretchability can be further enhanced by applying prestrain to the stretchable substrate where the electronic materials are deposited. Polymer substrate is prestretched before the deposition of materials such as metal, semiconductor, and graphene. By releasing after deposition, periodic wavy wrinkle structures are created and the structures are flattened under the strain to retain strain-insensitive characteristics.[594−596,622,623] If the thickness of deposited electronic materials on the prestrained substrate is reduced to the nanoscale, combined with the thickness-dependent mechanical property, better strain-insensitive properties can be designed. Transparent and stretchable electrodes can be fabricated by depositing ultrathin metals on prestretched PDMS. It shows 20% of stretchability with tunable electrical and optical properties.[594] This process can also be applied to percolation network-based transparent electronics such as AgNW,[595] GO,[596] and CNT.[622] AgNW percolation networks were prestrained for buckled structure for higher stretchability and subsequently treated with various solvents to reduce the instability of the buckled structure (Figure 19D). Rather than forming out-of-plane buckling of conventional prestrained AgNW percolation networks, solvent treatment rearranged the wavy AgNW networks more energetically favorable for uniform load transfer (Figure 19E).[595] Water as solvent showed the most desirable optical and electrical properties by showing a large area (25 cm × 20 cm) of the stretchable and transparent conductor with 91.8% of transmittance in the visible range and 26.8 Ω sq^{-1} of sheet resistance (Figure 19F). The fabricated transparent conductor showed much higher stretchability of over 50% than

https://doi.org/10.1021/acs.chemrev.3c00139
Chem. Rev. 2023, 123, 9982−10078

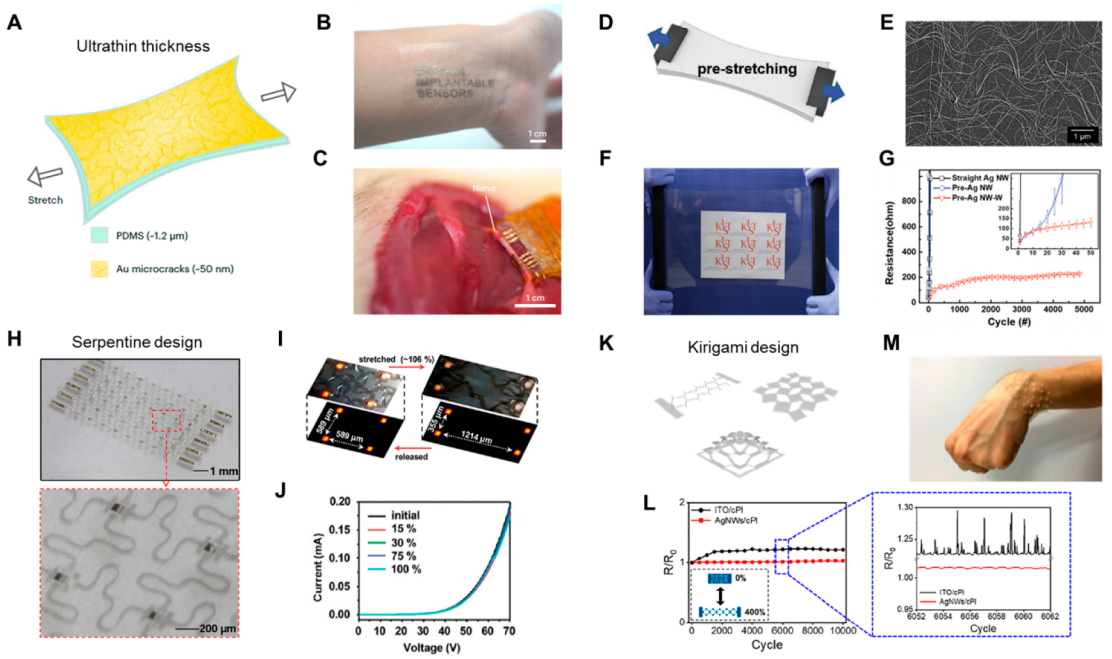

Figure 19. Structural engineering. (A) Schematic illustration of the ultrathin thickness of the stretchable elastic conductor. (B,C) Optical images of stretchable ultrathin electronics interfacing with human skin and rat nerves. Reproduced with permission from ref 593. Copyright 2022 Springer Nature. (D) Schematic illustration of prestrain methods for high stretchability. (E) SEM image of wrinkled AgNW percolation networks. (F) Optical image of the large area of prestrained AgNW transparent conductor. (G) The transmittance of prestrained AgNW percolation networks. Reproduced with permission from ref 595. Copyright 2020 Wiley-VCH. (H,I) Optical images of stretchable serpentine graphene electronics. (J) *I*–*V* curves of μLED under various strains. Reproduced from ref 6. Copyright 2011 American Chemical Society. (K) Schematic illustration of stretchable Kirigami conductor. (L) Change in resistance of Kirigami conductor under cyclic mechanical deformation. (M) Optical image of conformal contact of Kirigami conductor on human skin. Reproduced from ref 599. Copyright 2019 American Chemical Society.

straight AgNW percolation networks. As a result of solvent treatment for reducing the instability of buckling, prestrained AgNW showed better stability under the cyclic stretching test than the nontreated counterpart (Figure 19G).

For the hyperstretchability of brittle electronic materials, the geometry has been structurally designed. Periodically connected arc-shape termed "serpentine design" is broadly adopted for nonlinear response to applied strain which can be highly stretched without giving critical strain to brittle materials.[597] The stretchability of such designs can be systemically decided by the radius, periods, and line width of the arcs. Ultrathin inorganic materials are normally deposited on polymer substrates and laser-machined for designed geometry. Various electronic materials, including ultrathin metals,[5] carbon-based materials,[6] metal nanomaterials,[7] and conducting polymers,[601] are reported in serpentine shape for stable electrical connection under strain. Although CVD-grown graphene has been popularly utilized for e-skin applications due to its low flexural rigidity, it stayed at the level of flexible applications. For hyper stretchability, transparent graphene electrodes and interconnections were designed as serpentine geometry and transferred on a stretchable PDMS substrate for strain-insensitive electrical properties (Figure 19H).[6] μLED devices were assembled with the transparent circuit of graphene with high deformability which stably operated μLEDs under 106% of tensile strain (Figure 19I). The high electrical conductivity of transparent graphene under mechanical deformation was proved by measuring *I*–*V* characteristics that showed no clear difference (Figure 19J). Furthermore, if these geometries are fractally designed, electrical interconnections can be filled with high density in small spaces, making it possible to manufacture arrays of sensors or electrodes.[624] However, typical serpentine design can only be stretched in a single direction with a positive Poisson's ratio. Because living bodies are stretched in bidirection, more complex and elaborately designed structures are being studied. "Auxetic structure", or structure with negative Poisson's ratio, can be stretched in both directions when biaxially strained.[598,625,626] Recently, various studies have been carried out to attach auxetic-designed electronics to various biological tissues such as organs[626] and skins.[599] Simple laser cutting of 2D electronics can also impart auxetic structures termed "Kirigami structure" (Figure 19K). For transparent applications (over 80% of transmittance in the visible spectrum), AgNW percolation networks were embedded in a colorless PI substrate which is not stretchable. Then, AgNW embedded conductors are laser-machined as Kirigami structure for hyperstretchability (400% of strain with negligible mechanical hysteresis) (Figure 19L). By controlling cutting length, pitch, and periods, the response to mechanical deformation is freely tuned. Through the high stretchability of the Kirigami AgNW conductor, it is easily attached to curvilinear human skins and stably recorded biosignals for wearable electronics applications (Figure 19M).[599]

4.1.1.2. Materials Engineering. The structural design parameters for stretchability are also correlated with the optical and electrical properties of transparent electronics. For example, in the case of wrinkle structures by prestrain methods, optical clearance can be deteriorated due to light refraction induced by periodic wrinkles. For serpentine design, when a large arc radius is used for high stretchability, the length of the interconnection becomes long, which makes electrical

https://doi.org/10.1021/acs.chemrev.3c00139
Chem. Rev. 2023, 123, 9982−10078

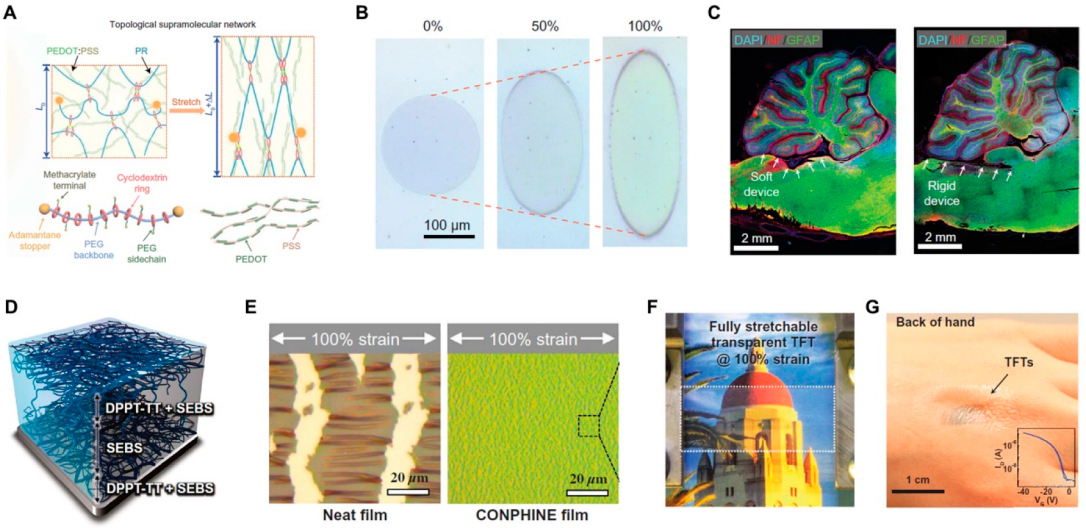

Figure 20. Materials engineering. (A) Schematic illustration of supramolecular chain engineering for high stretchability of PEDOT:PSS. (B) Optical images of stretchable transparent PEDOT:PSS under tensile strain. (C) Conformal contact of stretchable PEDOT conductor on the mouse brain. Reproduced with permission from ref 603. Copyright 2022 American Association for the Advancement of Science. (D) Schematic illustration of stretchable organic semiconductor fabricated by nanoconfinement effect. (E) Optical image of organic semiconductor films under tensile strain. (F),(G) Optical image of the high transparency of organic semiconductors and conformal contact to human skin. Reproduced with permission from ref 10. Copyright 2017 American Association for the Advancement of Science.

resistance too high. In addition, although the serpentine structure is made into fractals, it is hard to fabricate high-density sensors or electrode arrays in confined spaces due to inevitably possessing large spaces for curved patterns. Material engineering has resolved these limitations by developing creative electronic materials that are intrinsically stretchable that do not require structural engineering. Conductive percolation networks introduced in the previous chapters are representative of intrinsically stretchable transparent materials.[8,153,281] When highly conductive metals are synthesized into nanomaterials (e.g., nanoparticles and nanowires) and percolated into the mesh-like structure, optical properties can be ensured due to voids through which light can transmit, and simultaneously the mesh can be stretched up can recover its shape under cyclic tensile stress.[8,153] AgNW percolation networks decorated with CNT change can endure over 200% of strain with strain-invariant electrical properties.[281] Nanofiber-based percolation networks can also be easily stretched because their backbones are made with elastic polymers and also form mesh-like percolation structures.[600,627,628] Metalized nanofiber web also showed high transmittance of 90% in the visible range and sheet resistance of 3.8 Ω sq^{-1} and could be stretched over 70%.[600] During mechanical deformation, electrical disconnections normally occur at the junctions between the percolation backbones, and by performing post-treatments that weld the junctions, strengthened stretchable electronics can be developed.

Among various intrinsically stretchable electronic materials, conducting and semiconducting polymers are attracting the most attention due to their dual ionic and electronic conductivity, which is an important advantage for communicating with biological tissues. Their soft mechanical properties bridge the gap between rigid electronic devices and soft biological tissues. In the case of conducting polymers, electrochemical performances are superior to metallic materials due to 3D percolative morphology and ionic conducting polymer chains, and high transparency can be obtained when coated with thin thicknesses. PEDOT:PSS has attracted the most attention among various conducting polymers due to its excellent electrical conductivity and biocompatibility. However, it is easily electrically broken when only a little strain is applied. Furthermore, due to the unique chain structure surrounding the hydrophilic PSS-rich domain surrounding the hydrophobic PEDOT-rich domain, it was fragmented in physiological environments, resulting in device failures.[629] To resolve these limitations, plasticizing methods have been developed to modify the chain structure by mixing various types of additives such as ionic liquids and polar solvents.[9,601,602] With the charge screening effect, additives break the ionic bonds between the PEDOT-rich domains and the PSS-rich domains to separate conductive PEDOT-rich domains and soft PSS-rich domains. Mixed additives act as efficient dopants for the PEDOT-rich domain to induce morphological change in polymer chains. Plasticized PEDOT:PSS reported 4100 S cm^{-1} under 100% of strain with high transparency over 75%.[601] Recently, a more elaborate and elegant design of additives for PEDOT:PSS is developed for high stretchability and electrical conductivity. They designed a polyrotaxane structure-based cross-linkable supramolecular additive (Figure 20A).[603] The additives could slide along the polymer blend's chains, enhancing stretchability. The electrical conductivity was further enhanced by treating H_2SO_4 which reached one of the highest electrical conductivity of 6000 S cm^{-1} even under 100% of tensile strain (Figure 20B). Through soft mechanical properties of modified PEDOT:PSS, it could conformally be interfaced with the brain tissue of a mouse, whereas rigid devices showed a distinct gap between the device and tissues (Figure 20C). High resolution of photolithography patterning was possible for stretchable PEDOT:PSS that can further increase transparency through grid formations.

Semiconducting polymers have also been developed for the soft semiconducting component in wearable devices to replace inorganic semiconductors, but their charge carrier mobility is drastically dropped when tensile strain is applied. Through the

https://doi.org/10.1021/acs.chemrev.3c00139
Chem. Rev. 2023, 123, 9982−10078

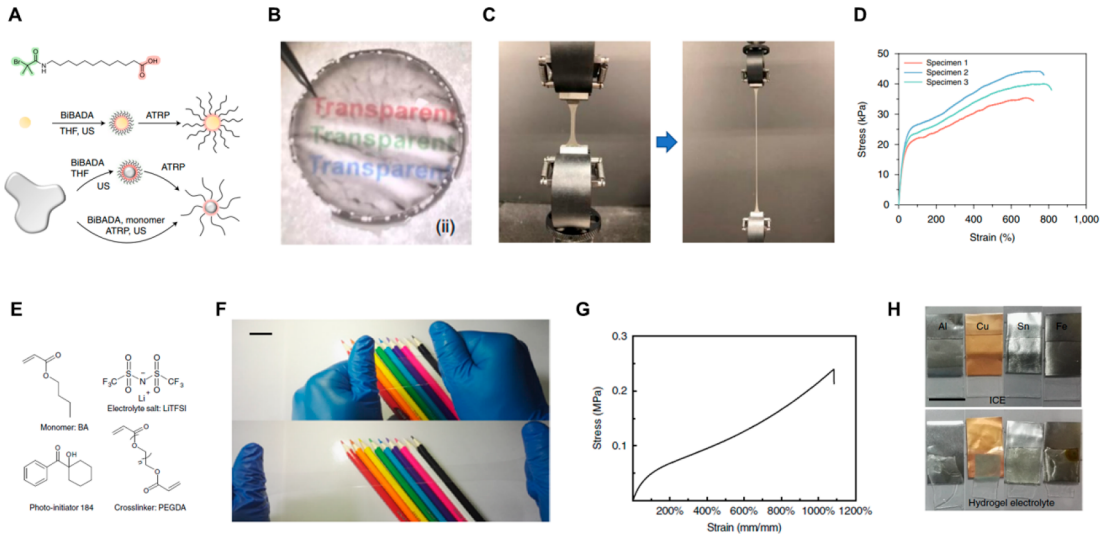

Figure 21. Conductive elastomer. (A) Schematic illustration of surface-initiated atom transfer radical polymerization with liquid metal and various polymer matrices. (B) Optical image of transparent liquid metal-based conductive elastomer. (C,D) High stretchability of liquid metal-based conductive elastomer. Reproduced with permission from ref 605. Copyright 2019 Springer Nature. (E) Molecular structure of transparent ionic conductive elastomer. (F) Optical image of highly transparent ionic conductive elastomer. (G) Stress−strain curve of transparent conductive elastomer. (H) Strong adhesion of ionic conductive elastomer to various substrates. Reproduced with permission from ref 606. Copyright 2018 Springer Nature under the CC BY 4.0 license http://creativecommons.org/licenses/by/4.0/.

nanoconfinement effect, semiconducting polymer nanofibrils are infiltrated in easily deformable elastomers (Figure 20D). High mobility was maintained due to the stable connections between nanofibrils and soft elastomeric matrix which can endure stresses.[10,575,630] Developed stretchable semiconductors with poly(2,5-bis(2-octyldodecyl)-3,6-di(thiophen-2-yl)-diketopyrrolo[3,4-*c*]pyrrole-1,4-dione-*alt*-thieno[3,2-*b*]-thiophen) as semiconducting polymer and polystyrene-*block*-poly(ethylene-*ran*-butylene)-*block*-polystyrene (SEBS) as elastomeric matrix showed high biaxial stretchability of 100% strain with little change of mobility (Figure 20E).[10] Due to its thin thickness of nanoconfined stretchable semiconductors, it showed great potential to be utilized for transparent wearable soft electronics (Figure 20F,G). Charge carrier mobility can be further enhanced through the directional alignment of nanofibrils by solution shearing processes. Stretchable semiconductors with poly-[2,5-bis(7-decylnonadecyl)pyrrolo[3,4-*c*]pyrrole-1,4-(2*H*,5*H*)-dione-(*E*)-(1,2-bis(5-(thiophen-2-yl)-selenophen-2-yl)ethene) (DPPDTSE) as semiconducting polymer and SEBS as the elastomeric matrix was solution sheared for directional alignment of DPPDTSE nanofibrils inside SEBS.[575] It showed enhanced stretchability and charge carrier mobility along the stretching direction simultaneously.

4.1.2. Softness. *4.1.2.1. Soft Layer Coating.* Although various strategies have been developed for stretchable electronics, still conventional materials over 1 GPa of Young's modulus (e.g., metals, stiff polymers) are widely applied to biological tissues, which have the potential danger of immune responses in long-term operations. Coating soft materials on rigid electronic devices can resolve the mechanical mismatch with soft biological tissues most intuitively and simply. Transparent microelectrode arrays that interface with neural tissues to record electrophysiological signals and obtain optical images simultaneously are usually made of rigid inorganic materials such as ITO. By coating soft conducting polymer, PEDOT:PSS on metal electrodes, it can reduce mechanical mismatch with soft tissues without deteriorating the electrical properties of the microelectrode array.[631] It rather enhances the signal-to-noise ratio of neural signals due to the higher electrochemical properties of conducting polymers than metal electrodes. Through the high electrochemical stability of conducting polymers in physiological environments, chronic recording of biosignals and optical imaging of tissues is possible.

Compared to conducting polymers that are selectively coated on metal electrodes, hydrogels are coated on entire devices for better soft interfaces with biological tissues.[632−634] Hydrogels are hydrophilic polymer networks infiltrated with high amounts of water inside. Through the highly porous morphology of hydrogels, it can contain high amounts of water (over 80%) which is advantageous for continuously supplying nutrition to interfacing tissues. This high content of water can make biological tissues feel soft enough when hydrogels are interfaced with them. Young's modulus of reported hydrogels ranges from a few kPa to hundreds of kPa depending on polymer types.[635] A variety of polymers are studied to fabricate soft hydrogels including synthetic polymers and natural polymers. Synthetic polymers such as PVA and poly(acrylic acid) (PAA) are widely reported as soft transparent hydrogels for bioelectronics interfacing.[636] It has the advantage of mass production with uniform quality, and the physical properties can be easily tuned with other polymer networks. Meanwhile, natural polymers such as gelatin and collagen are more compatible with biological systems due to their similar composition with them. However, the quality of manufactured products is relatively not uniform because they are naturally driven, which is inadequate for reliable and precise electronics applications. By coating hydrogels on electronics, it can block charge transfer with biological systems which hinder signal transfer. This can be resolved by the additional coating of conducting polymers selectively on electrode sites.[637]

4.1.2.2. Conductive Elastomer. Soft-layer coated rigid electronic systems must have unavoidable heterogeneous contacts between soft and rigid materials. Inherently different

https://doi.org/10.1021/acs.chemrev.3c00139
Chem. Rev. 2023, 123, 9982−10078

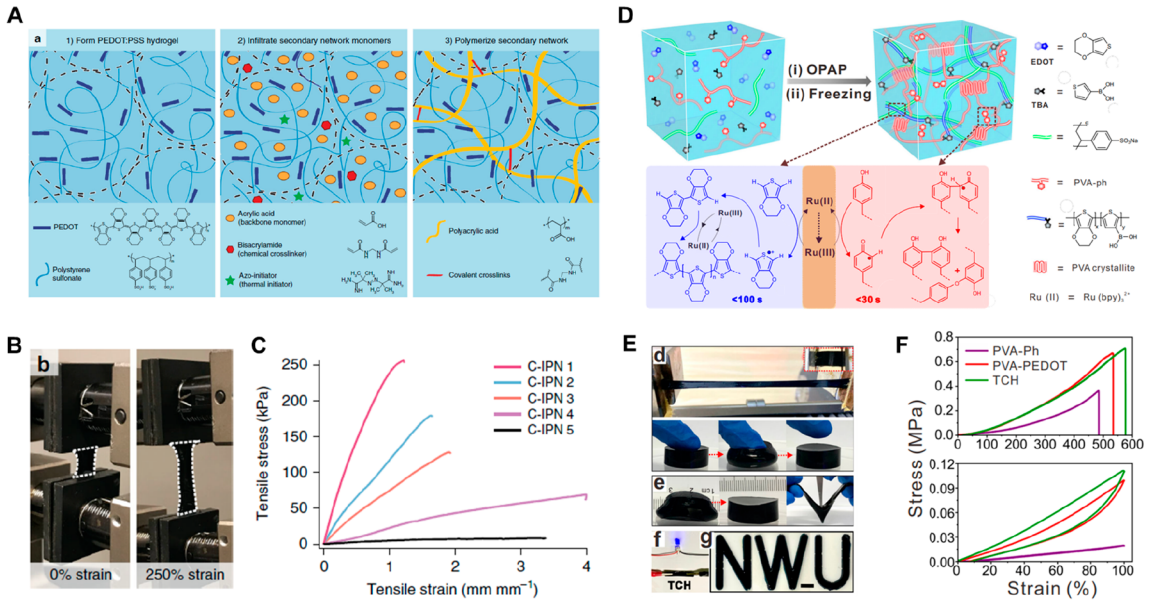

Figure 22. Conductive hydrogels. (A) Schematic illustration of interpenetrating networks of conductive hydrogels using PEDOT:PSS and PAA networks. (B) Optical image of conductive hydrogels under 250% of tensile strain. (C) Stress−strain curves of conductive hydrogels varying compositions of PEDOT:PSS and PAA contents. Reproduced with permission from ref 609. Copyright 2018 Springer Nature under the CC BY 4.0 license http://creativecommons.org/licenses/by/4.0/. (D) Schematic illustration of highly tough and stretchable conductive hydrogels by orthogonal photochemical reactions. (E) Optical images of highly tough and stretchable conductive hydrogels. (F) Stress−strain curve of conductive hydrogels. Reproduced with permission from ref 653. Copyright 2021 Springer Nature under the CC BY 4.0 license http://creativecommons.org/licenses/by/4.0/.

properties of these heterojunctions are mechanically vulnerable when electronic devices are exposed to cyclic strain interfaced with shape-changing biological systems. Also, in physiological environments, the adhesion properties of soft materials to rigid parts are relatively weak resulting in interfacial delamination. To prevent these latent risks, highly soft and conductive elastomers are developed to replace rigid electronic materials. Electrically conductive elastomer is one of the most promising materials which can reduce mechanical mismatch with soft tissues and additional soft layer coatings are unnecessary. Various nanomaterials, including metal nanomaterials, graphene, and CNT, are embedded in elastomeric matrices for transparent conductive elastomers.[604,638−643] The softness of conductive elastomer composite is controlled by the mass ratio of conductive filler to elastomeric matrices. By increasing the ratio, the mechanical properties get harder while the electrical properties become higher. Optical properties are also correlated with fractions of conductive fillers which get darker when the fraction gets too high due to their unique colorations. Because typical trade-offs are applied to composite design, it is essential to find reasonable percolation density while ensuring high transparency to use for transparent and wearable electronics.

For the past decade, among various conductive fillers, liquid metal attracted the greatest attention for the stretchable and soft interconnection of wearable electronics. Through its liquid-like physical properties, it possesses high electrical conductivity under large mechanical deformations. However, these liquid-like properties hinder its wide usability as electrical conductors on soft substrates due to its mechanical instability. Therefore, a lot of studies tried to fill liquid metals inside microchannels, which inevitably increases the thickness of devices sacrificing conformability to biological systems. Recently, liquid metal-based composites are developed to resolve these limitations. To fabricate soft composite, liquid metals are normally smashed into small particles through ultrasonication and blended with mechanical backbones such as polymer matrices[605,644,645] or metal nanowires.[646,647] For example, the surface of liquid metal nanoparticles was functionalized for uniform blending with polymer matrix and surface-initiated atom transfer radical polymerization (Figure 21A).[605] Through surface modification, a uniform blending of nanoparticles was possible for various polymer matrices. By controlling the density of liquid metal nanoparticles, a semitransparent liquid metal composite was successfully fabricated (Figure 21B). The mechanical property of the composite was also tunable by varying types of polymer matrice where the softest composite showed 89 kPa of elastic modulus and 769% of elongation (Figure 21C,D). However, due to its intrinsic coloration, the transparency of liquid metal was poor. Together with composite techniques, high-resolution grid patterning is an alternative approach to utilizing liquid metal as transparent conductors. Photolithography,[645] laser sintering,[646,647] and 3D printing[644] are recently reported to fabricate micropatterned liquid metal composites. Liquid metal composite fabricated by lithography showed over 500% of strain without loss of its electrical conductivity. Laser-sintered liquid metal and AgNW composite also showed high failure strain of up to 1358% and 3D printed liquid metal composite reported 230% of stretchability,[644] which are all stretchable enough for human-interfaced electronics. By selecting highly soft polymer matrices, Young's modulus of liquid metal composites showed below 1 MPa.[645] However, because the patterning resolution is still quite low to fabricate highly transparent electronics, more precise patterning techniques are required in the future.

As described above, because conductive fillers generally have their innate colors, transparency must be sacrificed to increase

https://doi.org/10.1021/acs.chemrev.3c00139
Chem. Rev. 2023, 123, 9982−10078

electrical properties. On the other hand, the ionically conductive elastomer (ICE) is a soft material that can secure high transparency of over 90%. Electrolytes in ICE play as charge carriers transported along the polymer chains. ICE, which contains lithium bis(trifluoromethane sulfonimide) as electrolyte salt and butyl acrylate as monomer and polyethylene glycol diacrylate (PEGDA) as cross-linker, was reported (Figure 21E).[606] It showed high stretchability of over 1000% of strain while maintaining its transparency over 90% (Figure 21F,G). It was also highly attachable to various surfaces which is crucial for long-term operation on human skin showing high interfacial toughness of 150 J m^{-2} (Figure 21H). ICE using polymerizable deep eutectic solvent (PDES) monomers could also achieve highly soft mechanical properties.[606,607,648,649] Photoinitiated copolymerization of acrylic amide (Aam)/choline chloride (ChCl) and maleic acid (MA)/ChCl PDES monomers form highly soft and transparent poly(AAm/ChCl-*co*-MA/ChCl) networks which also can transport charges. By controlling AAm/MA ratio, Young's modulus of ICE was lowered to 0.04 MPa, similar to biological tissues. It also has a high stretchability of over 400% of strain with 95% of transparency.[607]

4.1.2.3. Conductive Hydrogels. Although conductive elastomers are highly stretchable and durable for biointerfacing materials, it is hard to contain enough water in physiological environments which is distinct from biological systems. On the other hand, biological tissues contain high amounts of water and transmit biosignals through ion transmissions in wet physiological environments. Therefore, wet and conductive hydrogels are the next promising choice for soft biointerfacing electronic materials. Hydrogel coating techniques on rigid materials are introduced to reduce mechanical mismatch with biotissues in the previous section. This section describes hydrogels that can transport charge carriers inside their polymer backbones through electrically or ionically conductive components. Similar to conductive elastomers, electrically conductive fillers such as graphene[650] and metal nanomaterials[651] are incorporated with nonconductive hydrogel networks. Gold nanorod-incorporated gelatin-based conductive hydrogels reported 1.3 kPa of Young's modulus even with high contents of nanorods.[651] By combining biocompatible gold nanorod and gelatin, the conductive hydrogels are highly biocompatible and match with soft biological tissues. Conducting polymers also attracted great attention as conducting fillers to fabricate conductive hydrogels. Unlike metal nanomaterials and carbon materials that highly increase Young's modulus of conductive hydrogels with increasing the contents, conducting polymer-based hydrogels can secure highly soft hydrogels even with high contents.[608,609,652] Soft and conductive hydrogels were fabricated by forming interpenetrating networks of PEDOT:PSS and PAA (Figure 22A).[609] With PAA backbones that can greatly relieve mechanical stress, conductive hydrogels showed high stretchability with over 250% of strain (Figure 22B). Furthermore, PEDOT:PSS as soft conductive fillers showed great performance with 23 S cm^{-1} of electrical conductivity and 8−400 kPa of elastic modulus (Figure 22C). Recent studies have reported a conductive hydrogel that is not only stretchable and soft but also extremely tough.[653] Here, the phenol-coupling reaction and the polymerization of PEDOT were orthogonally photoreacted by visible light. The key components of the hydrogel precursor are tyramine-modified PVA (PVA-Ph), EDOT monomer, and thiopheneboronic acid (TBA) for rapid gelation of conductive hydrogels response to visible light (Figure 22D). When visible light was applied to the precursor by controlling the ratio components, PVA-Ph, which quickly became the mechanical backbone, was gelated by phenol coupling, and then EDOT was polymerized to form PEDOT. TBA strongly strengthened the PVA network and PEDOT. Depending on the composition ratio, the mechanical properties, as well as the time of photochemical reaction, could be controlled, and toughness over 2000 kJ m^{-3} and stretchability over 500% were achieved through the strong interconnection of PVA and PEDOT networks (Figure 22E,F). However, because a large fraction of electrically nonconductive polymer networks, the electrical conductivity of conductive hydrogels with extremely soft mechanical properties by employing mechanical backbones showed conductivity below 1 S cm^{-1}.

Recently, conductive hydrogels fabricated by pure conducting polymers emerged with their superior electrical properties to composite hydrogels, especially for PEDOT:PSS. When ionic liquid is added to the PEDOT:PSS aqueous solution, it breaks the ionic bond between the PEDOT-rich domain and the PSS-rich domain through the charge screening effect and induces phase separation.[610] Subsequent thermal annealing of the separated PEDOT:PSS system greatly strengthens the interconnections between the PEDOT-rich domains. By immersing phase-separated and annealed PEDOT:PSS, it can be transformed into conductive hydrogels maintaining strong interconnections between polymer chains and swelling high amounts of water without losing its electrical properties. Fabricated conductive hydrogels retain tissue-like elastic modulus of 32 kPa and high electrical conductivity of 47 S cm^{-1}. High boiling point polar solvents such as DMSO can also induce similar phenomena to ionic liquids to fabricate conductive hydrogels.[611,654] DMSO-mixed PEDOT-based conductive hydrogels were also applied for 3D printing for complex structures of bioelectronic applications by showing enough mechanical robustness in wet conditions.[654] The electrical conductivity of pure conducting polymer hydrogels was extraordinarily high due to the absence of electrically insulating polymer backbones with 40 S cm^{-1} of conductivity but still soft enough with 2 MPa of elastic modulus.[611] However, developed conductive hydrogels are difficult to use as transparent biointerfacing electronics due to their low transparency which requires grid-patterning techniques. Various patterning methods to pattern conductive hydrogels are reported, but only several results showed relatively high resolutions of patterns.[610,612,654,655] Conventional photolithography could fabricate the highest resolution of conductive hydrogels by incorporating UV-curable agents in polymer chains which succeed in sub 10 μm of line width.[610] However, it required over 10 steps of complex fabrication flow with expensive vacuum systems. Three-dimensional printing is a promising patterning tool to pattern paste-like PEDOT but showed only 30 μm of line resolution, which is not enough for transparent grid patterns.[654] Recently, the laser annealing process to induce phase separation and annealing enabled facile yet high-resolution conductive hydrogels. This process could fabricate 6 μm of PEDOT hydrogels with 670 S cm^{-1} of high electrical conductivity.[612]

Similar to the ionically conductive elastomer, hydrogel backbone also allows ion transportation along the polymer chains. Compared to conductive elastomers, ionically conductive hydrogels can contain higher contents of ionically conductive electrolytes inside. Ionic salts are dissolved in

https://doi.org/10.1021/acs.chemrev.3c00139
Chem. Rev. 2023, 123, 9982−10078

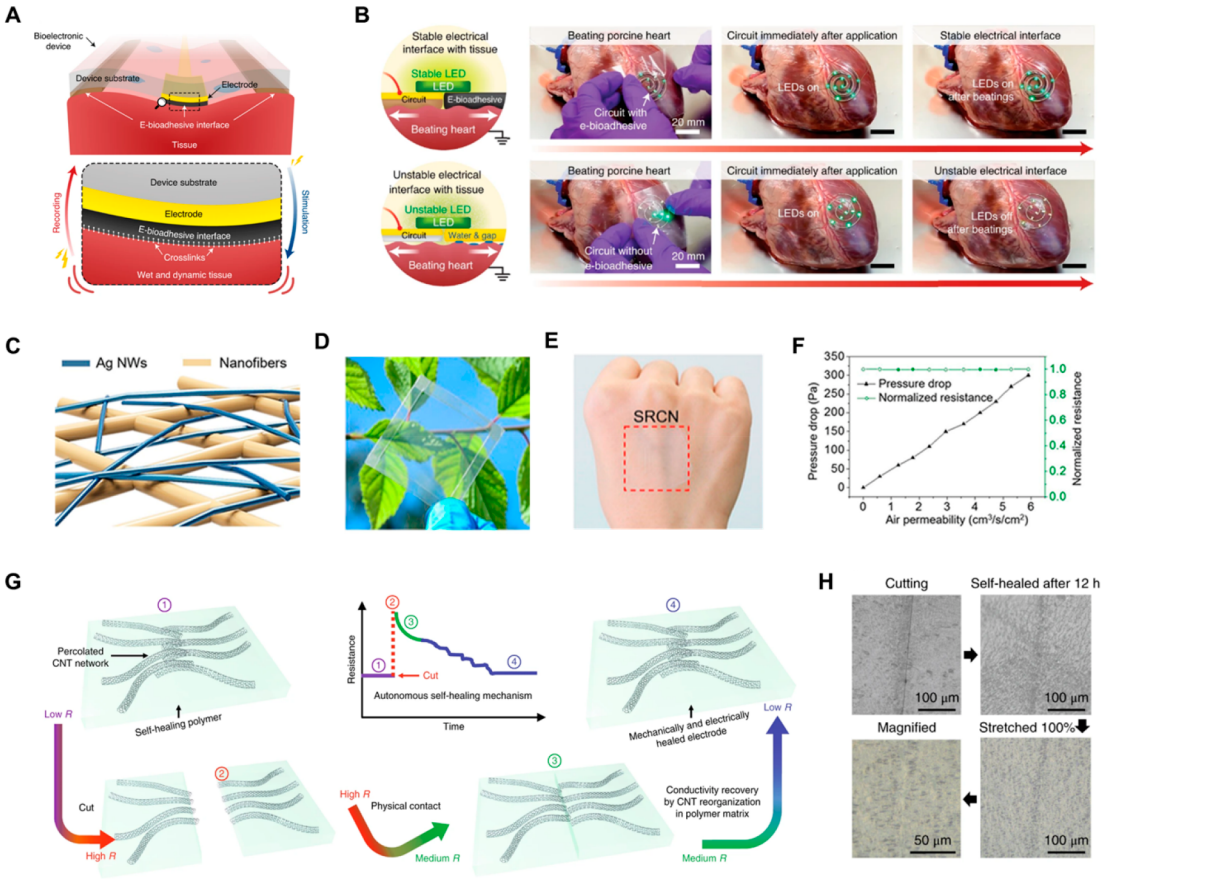

Figure 23. Long-term stability. (A) Schematic illustration of high adhesion of graphene-based adhesive layer on biological tissues. (B) The adhesive layer enabled the stable operation of bioelectronic devices on the heart. Reproduced with permission from ref 658. Copyright 2020 Springer Nature. (C) Schematic illustration of a gas and mass permeable conductor using nanofiber networks and AgNW. (D), (E) Optical images of transparent permeable conductors and stable contact with human skin. (F) Air permeability of the assembled conductor. Reproduced from ref 667. Copyright 2018 American Chemical Society. (G) Schematic illustration of self-healable CNT electronics. (H) Optical image of the healing process of stretchable CNT electronics. Reproduced with permission from ref 679. Copyright 2018 Springer Nature.

electrolytes and stored in conductive hydrogels. It has a highly soft elastic modulus with hundreds of kPa and transparent optical properties. It is normally applied for e-skin applications due to its high level of ionic concentration.[613,614,656,657] Therefore, it is promising to combine both ionic and electric conductivity in single materials with low concentrations of ionic salts. With ensured biocompatibility, it might be possible to transmit biosignals with a high sign-to-noise ratio.

4.1.3. Long-Term Stability. *4.1.3.1. Adhesion.* The human body contains 70% of water and continues life activities through repetitive chemical metabolism. In the case of the skin, sweat, and wastes are continuously secreted according to temperature, humidity, and metabolic state. Inside our bodies, biofluids constantly circulate in various physiological environments. Here, most electronic devices lose their mechanical adhesion to biological tissues due to interfacial waters between devices and tissues.[658] To solve this, various invasive devices such as the Utah arrays and Michigan arrays have been developed, but it is difficult to interact with normal biological tissues due to damages applied to the biosystem, and device failure occurs due to fibrotic encapsulation on the device in prolonged usage.[4] Therefore, it is required to develop techniques to give strong wet adhesion to noninvasive devices.

Employing adhesive layers between the device and the biological system is the most straightforward strategy to ensure long-term stability (Figure 23A). Various types of adhesives have emerged such as paste-like adhesives or tape-like thin film adhesives.[659] To utilize as an intermediate adhesive layer for transparent electronics, thin film types of adhesive are more appropriate. Film adhesives are made of PAA grafted with *N*-hydroxysuccinimide ester and biopolymers such as gelatin.[660] The dry state of the thin adhesive film can absorb interfacial water from biological systems due to carboxylic acid groups for fast cross-linking to the surface. Additional covalent cross-linking by amine groups enhances adhesion stability. Water-swollen adhesive layer transforms into a thin layer of hydrogel with high contents of water. This thin adhesive hydrogel layer was inserted between the electrical sensor and porcine heart for stable recording of the heart beating. This concept of the adhesive layer is further developed by incorporating conductive filler such as graphene. Graphene-incorporated adhesive layer enabled a strong biodevice interface by recording 2 weeks of in vivo cardiac recording with a high signal-to-noise ratio (Figure 23B).[658] Rather than employing additional adhesive layers, endowing self-adhesion to conductive materials has also emerged. Conductive composite made of PVA as elastic networks, PEDOT:PSS as conductive filler was modified by adopting biocompatible supramolecular solvents. Supramolecular solvents contain citric acid and cyclodextrin which enable strong adhesion to biological tissues due to a large number of hydroxyl groups. It showed strong adhesion to the surface of

https://doi.org/10.1021/acs.chemrev.3c00139
Chem. Rev. 2023, 123, 9982−10078

the swine liver and stable electromyogram (EMG) recording performance attached to human skin.[604]

Maintaining device functionality critically depends on functional layers such as electrodes and sensors. As we discussed before, conducting polymers are normally coated on metal electrodes for a high signal-to-noise ratio. Conducting polymers are also utilized as sensing layers of organic electrochemical transistors due to their fast response to ion species in physiological environments. However, due to its weak interfacial bonding, it easily delaminated from the surface of metal layers. To improve interfacial bonding, functional groups such as carboxylic, and amine groups are introduced on the target surfaces.[661,662] After modifying surfaces, deposited conducting polymers showed strong wet adhesion after 1 h of ultrasonication.[662] Thin adhesive layers are also employed on the target surfaces.[663,664] Hydrophilic PU was introduced as an adhesive layer for conducting polymer which also showed stable electrochemical properties even after 10000 cycles of cyclic voltammetry and 1 h of ultrasonication.[664] Mechanical surface modifications also enhanced wet stability and adhesions to metallic materials. By increasing the roughness of surfaces, conducting polymers were tightly interlocked to metallic materials for adhesion enhancements.[665,666]

4.1.3.2. Permeability. Gas permeability is a practical requirement in wearable electronics, especially for long-term monitoring of biosignals. Typical polymers used in wearable electronics such as PI or PDMS have low gas permeability. This inhibits the evaporation of biofluids which can induce skin irritations. Moreover, the discharged biofluids act as interfacial waters between the device and skins which results in interfacial delaminations. In the case of implanted devices, if sold devices are covering organs, it blocks the supply of nutrients and oxygens. To solve these problems, device types that effectively exchange mass or gas in both dry and wet environments are being developed with ensuring transparency in the visible range.[539,593,667−675] Electrospun transparent nanofibers were integrated with transparent AgNW percolation networks for e-skin applications (Figure 23C). Fabricated e-skin devices showed high transparency of 84.9% in the visible range and 8.2 Ω sq^{-1} of sheet resistance (Figure 23D,E). With their spaces for gas permeation, at 300 Pa of pressure drop, 6 cm^3 $s^{-1}cm^{-2}$ was achieved which is similar to fabrics (Figure 23F).[667] Thin gold layers were also deposited on electrospun nanomesh for transparent and gas-permeable conductors.[539,668,669] Transparent and conductive contact lenses were developed by depositing a thin Au layer and conducting polymer on polyacrylonitrile nanofiber.[668] The resultant device showed transparency of over 80% in the visible range. Through high permeability, in vivo rabbit eyes wearing transparent and conductive lenses showed little signs of irritation for 12 h. Gold-based nanomesh with high optical transparency was reported using natural polymer backbones.[669] Chitosan was utilized as transparent nanofiber backbones for permeable electronics. Chitosan nanomesh has excellent optical transparency of 94.8% with high sweat permeability of 1.91 kg m^{-2} d^{-1}. By combining gold nanomesh with chitosan meshes, it still retained a high optical transparency of over 80%.

Creating pores in materials also allows high gas permeability and conformal contact with biological tissues. Through a simple breath figure method, the highly porous stretchable film is fabricated for good gas permeability and sweat evaporation. Porous films showed high transparency of 61% and good vapor permeability of 23 mg cm^{-2} h^{-1}. They assembled AgNW with porous polymer films for electrophysiological sensing that could be stably stretched up to 45% of strain.[670] Punching holes to stretchable geometry such as auxetic structure also enabled sweat-permeable skin electronics. By designing dual scale of hole patterns in auxetic structure, vapor permeability was greatly enhanced compared to conventional electronics designs resulting in fast dehydration of interfacial sweat between the device and skin tissue. Through high sweat permeability, skin irritation was clearly reduced after 1 week of lamination. Stable monitoring in various health conditions was possible with hole-patterned devices due to stable interfacial contact with skin tissues.[671]

Mass permeability is an important parameter for biosignal recording through the movement of ion species in the area where implantable electronics are interfaced. For long-term monitoring, maintaining the ion concentration of the physiological environment to natural states is essential not only for biosafety but also for stable signal recording. Furthermore, in drug release for medical treatment, efficient mass transportation must be possible to achieve sufficient therapeutic effects. Highly porous electronics are required for these applications, among them, hydrogel-based electronics made of hydrophilic polymer networks are the most promising material design. PEDOT-incorporated PAAm hydrogel is synthesized and fabricated in ultrathin form factor. Ultrathin porous conductive hydrogel enabled efficient mass transfer with high amounts of oxygen penetration and reduced electrochemical impedance compared to thick hydrogels.[672] Due to ultrathin thickness, it also can ensure optical transparency which has the potential for transparent and soft implantable devices.

4.1.3.3. Self-Healing. Soft electronic devices interfaced with living bodies are exposed to unexpected mechanical impacts or accidental damages that require tedious repair or replacement work. In the case of implantable electronics, they also suffer from severe fatigue due to constant body movement during long-term operation. This fatigue problem can develop into sudden fractures during long-term implantation, resulting in a malfunction of the device. In this situation, to repair the implantable device, secondary surgery is required, which is highly dangerous for patients. Incorporating robust rigid materials in the soft matrix can enhance durability to resolve these issues. However, it inevitably results in relatively high stiffness of mechanical properties that induce mechanical mismatches with biological systems. To overcome cumbersome requirements for safe interfacing with biological tissues, self-healable electronics have emerged with the breakthrough idea.[607,676−682]

Self-healing properties are contributed by mixed play of extrinsic and intrinsic self-healing properties. For extrinsic self-healing, microencapsulated healing agents and catalysts are dispersed in polymer matrices. Monomers are loaded in microcapsules, and the catalysts are uniformly dispersed in the matrix. When cracks break the microcapsules of healing agents, polymerization of released monomer agents occurs with aid of neighboring catalysts at the crack sites for recovery.[676] This recovery autonomously starts with crack generation without external intervention. Until now, the extrinsic methods are closer to commercialization because they can disperse healing agents and catalysts in various polymer matrices with existing blending techniques. However, because the healing agents cannot be reused, it has limitations of difficulty to heal the area once broken.

https://doi.org/10.1021/acs.chemrev.3c00139
Chem. Rev. 2023, 123, 9982−10078

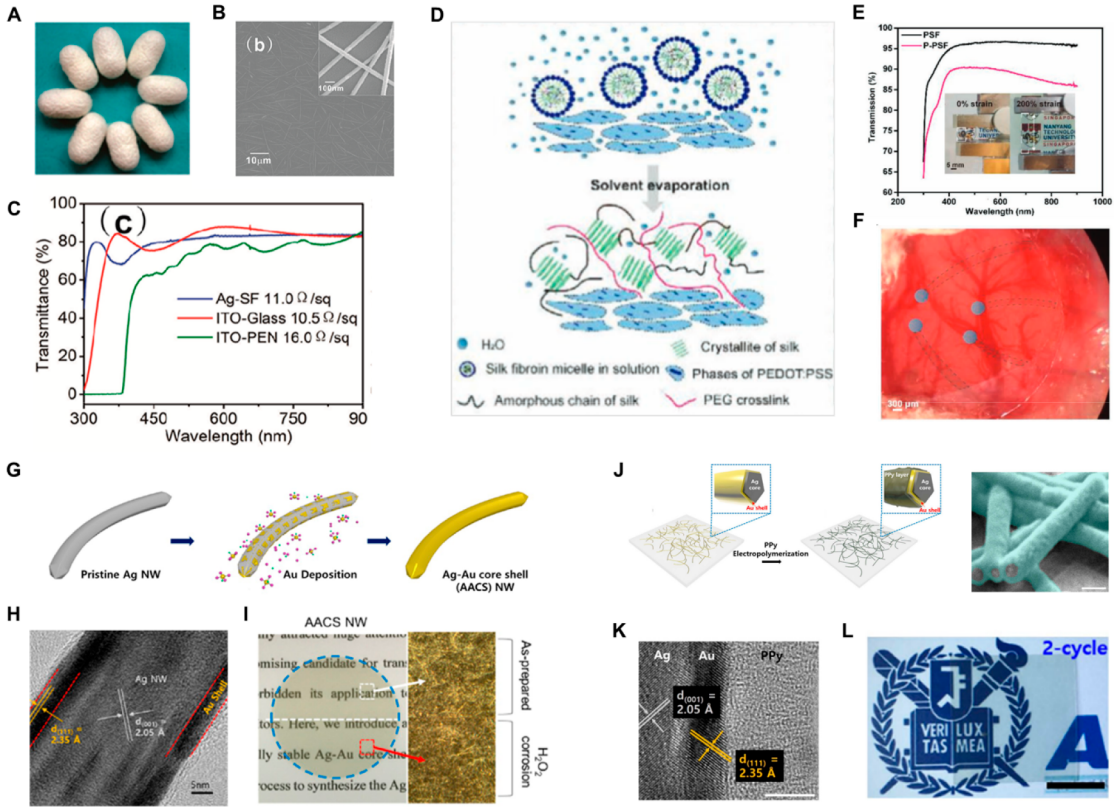

Figure 24. Biocompatibility. (A) Optical image of silk used for stretchable and biocompatible substrates. (B) SEM image of AgNW percolation networks on silk substrate. (C) Transmittance of silk-based AgNW conductor. Reproduced from ref 687. Copyright 2014 American Chemical Society. (D) Schematic illustration of PEGDE-reinforced silk-based electronics. (E) Transmittance of PEGDE and silk conductors. (F) Optical image of stable contact of silk electronics on the mouse brain. Reproduced with permission from ref 688. Copyright 2021 Wiley-VCH. (G) Schematic illustration of core−shell nanowire synthesis. (H) TEM image of synthesized Ag−Au core−shell nanowire. (I) Optical image of core−shell nanowire under corrosive environment. Reproduced from ref 695. Copyright 2016 American Chemical Society. (J) Schematic illustration and SEM image of Ag−Au−PPy core−shell nanowires. (K) TEM image of Ag−Au−Ppy core−shell nanowire. (L) Optical image of transparent core−shell nanowires. Reproduced with permission from ref 697. Copyright 2017 Springer Nature under the CC BY 4.0 license http://creativecommons.org/licenses/by/4.0/.

Intrinsic self-healing polymers attracted more attention due to their highly soft mechanical properties which resemble biological tissues. It utilizes various types of dynamic interactions of polymer chains for reconfiguration to recover crack spots. Dynamic interactions such as hydrogen bonding, dipole−dipole interaction, and imine bonds were used for recovery dynamics for intrinsic self-healing methods.[677] Transparent self-healing polymers were developed by utilizing highly reversible ion−dipole interactions. Amorphous elastomers with high dipole moments can strongly interact with cations in the ionic liquids for the active reconstruction of polymer chains. This stretchable self-healing polymer recovers its mechanical and electrical properties to 99.1% after 24 h healing at 50 °C.[678] Conducting filler-incorporated self-healing polymers are also of great interest in bioelectronic devices. Because the electrode or sensing layers are the core elements of electronic devices, protecting these elements is essentially required for long-term operation. Therefore, nanomaterials such as CNT networks embedded self-healing polymers are developed for safe biointerfacing functional layers (Figure 23G).[679] Electrical properties recovered after 12 h of healing process after cutting. After the healing process, it could be stretched up to 100% of the strain (Figure 23H). Depending on the concentration of nanomaterials loading in self-healing polymer, it showed relatively transparent optical properties which can potentially be used for transparent self-healing electronics.

Maintaining robustness before and after the healing processes is very challenging. Recently, a transparent elastomer that maintains extremely high toughness even after self-healing has been reported.[682] By employing TPU containing polytetramethylene ether glycol as the soft shape memory segment, and isophorone diisocyanate with asymmetric alicyclic structure as the hard segment, remarkable mechanical properties with the self-healing property were achieved. Toughness reached 26.9 MJ m^{-3} and 75% of mechanical properties were recovered compared to the virgin sample after 2 h of the healing process. The highly tough elastomer developed is expected to be very promising as a packaging material for transparent and wearable electronics because it has excellent optical properties.

4.2. Biochemical Interface

There exist plenty of biofluids continuously generated from biological systems that make physiological biochemical interfaces with wearable electronic devices. It is important to ensure the stability of the biochemical interface from biological and device perspectives to operate in desired durations. Even though the characteristics of the device are good on the electrical, mechanical, and optical sides, it is not desirable as an interfacing device if it is chronically dangerous (e.g., cytotoxicity) to the biological system.[683] From the device

https://doi.org/10.1021/acs.chemrev.3c00139
Chem. Rev. 2023, 123, 9982−10078

point of view, metallic materials show high electrical properties but in wet physiological environments, they face oxidation and corrosion problems[684] that lead to severe degradation of electrical performances. Therefore, interfacing soft electronic devices with ensuring the safety of the biological system and reliability of the devices are practical missions to conquer for scientists and engineers. In this section, we broadly introduce pioneering works to develop safe biochemical interfaces with biological systems by dividing them into biocompatibility and biodegradability.

4.2.1. Biocompatibility. *4.2.1.1. Natural Biopolymer.* Various polymers have been utilized as soft interfacing materials with biological systems such as PDMS, SEBS, and PI.[469] High biocompatibility is required for these materials because it contacts the largest area with biological tissues compared with electrodes and sensing parts. However, although these elastomers do not cause side reactions such as cytotoxicity, their mechanical properties are not soft enough, and their inherent properties are different from those of hydrophilic cell tissues. Hydrogels have been developed to solve this problem, but synthetic polymer networks (e.g., PAA and PVA) are still broadly used that have different compositions from natural tissues.[632] As a way to have highly similar compositions to biological tissues, studies have emerged to use materials originating from the natural biological system as building blocks for electronic devices. Natural biopolymers are derived from a variety of animals or plants and have the advantages of abundance in nature and safety for implantation due to their similar compositions to tissues.

Natural biopolymers are largely divided into proteins (e.g., silk, collagen, and gelatin) and polysaccharides (e.g., alginate, agarose, cellulose, and chitosan). For detailed composition and characteristics of each biopolymer, reviews on the classification of natural biopolymers are recommended.[685,686] Natural polymers have been tried to replace synthetic polymer-based electronic components such as transparent substrates, conductors, and sensing layers.[687−692] Especially, silk showed promising mechanical and optical properties for transparent substrate (Figure 24A). Common solution processes are enabled for silk films and assembled with metallic nanowires for transparent conductors with 80% of transmittance in the visible range and 11 Ω sq^{-1} of sheet resistance (Figure 24B,C).[687] However, their mechanical properties are still unstable to be fully compatible with various fabrication techniques such as thermal annealing for conductivity enhancement of conductive nanomaterials. Therefore, various chemical cross-linking agents are introduced to strengthen the mechanical properties of natural polymer-based electronic systems, or composites with synthetic polymers have been considered for practical use (Figure 24D). Highly transparent (over 85% of transmittance) and biocompatible silk-based hydrogel was strengthened by cross-linking with poly(ethylene glycol) diglycidyl (PEGDE) ether for high stretchability and stability in physiological environments (Figure 24E).[688] By combining natural silk polymer with synthetic PEGDE, stretchability was enhanced to 400% in wet conditions, and stability was maintained for 4 months in PBS. Transparent silk hydrogel was assembled with transparent PEDOT:PSS electrodes for fully transparent implantable neural signal recording devices. With its high optical and electrical properties and biocompatibility, it stably recorded neural signals with visual information simultaneously (Figure 24F).

Natural polymer solutions are also homogeneously blended with conductive fillers such as metal nanomaterials,[691] carbon materials,[689] and conducting polymers.[688] For example, biocompatible Au nanowires are incorporated into alginate hydrogel scaffolds.[691] Nanowire decoration in alginate hydrogel reduced electrochemical impedance on the overall frequency range and mechanical properties are highly matched to soft biological tissues (3.5 kPa of the compressive modulus). However, in the case of these composites, there is a limit in that the transparency is significantly lowered when fillers are added for sufficient electrical conductivity. Therefore, highly transparent ionic conductive organohydrogel have emerged using natural biopolymers.[692] Gelatin hydrogels are simply dipped into sodium citrate-containing solutions. Sodium ions strengthened the mechanical properties of organohydrogel through multiple cross-linking inside polymer networks but also highly increased ionic conductivity. Fabricated ionic conductive biopolymer-based organohydrogels were utilized as biointerfacing strain sensors.

4.2.1.2. Biocompatible Protective Layer. The most promising materials to fabricate transparent and wearable electronic devices are metal-based nanomaterials with high electrical conductivity. Among them, linear nanowires are more effective to form percolation networks than any other nanostructures, thus securing high transparency as well as mechanical stretchability. However, AgNWs, which are representative metal nanowires, are easily oxidated in physiological environments, and Ag ion exhibits cytotoxicity to tissues.[693] In the case of CuNWs, they have similar electrical conductivity to Ag and are much cheaper, but the problem of cytotoxicity to tissue as well as severe oxidation problem remains the same.[694] In order to keep the excellent electrical properties of these highly conductive metal nanowires and to utilize them safely in biological systems, synthesis methods have emerged to cap highly stable protective layers on the surface of nanowires that can ensure biocompatibility and electrical stability simultaneously in physiological environments. In this section, we introduce recent studies that successfully protected Ag and CuNWs with highly stable capping materials.

Au is highly biocompatible, electrically conductive, and stable in physiological environments. However, synthesizing pure Au nanowires for percolation networks is too costly. Therefore, core−shell metal nanowires have emerged to solve biocompatibility and oxidation issues at the same time. Ag−Au core−shell nanowires are developed to fabricate transparent percolation networks (Figure 24G).[599,693,695,696] Galvanic corrosion is prevented by precisely controlling the pH of the reaction solution and injection speed. A 30 nm thickness of AgNW is coated with 5 nm thickness of Au shell (Figure 24H).[695] These core−shell nanowires showed high stability in electrochemical environments that endured their electrical properties in corrosive solutions (Figure 24I). Transparent electrodes fabricated by Ag−Au core−shell nanowire networks showed 85% of high transparency with 42.3 Ω sq^{-1} of sheet resistance. Through percolation networks structure, transparent electrodes could also be stretched up to 60% of strain. Ag−Au core−shell nanowires have also blended with elastomer to fabricate highly biocompatible conductive elastomer composites.[693] To disperse core−shell nanowires in toluene-based elastomer solutions, ligand exchange of core−shell nanowires is introduced. Developed core−shell nanowire composite showed high biocompatibility and stability in

https://doi.org/10.1021/acs.chemrev.3c00139
Chem. Rev. 2023, 123, 9982−10078

physiological environments compared to AgNW composites by preventing oxidation and ion bleaching. Soft biocompatible composite electrodes have 266% of optimized stretchability and 41850 S cm^{-1} of electrical conductivity. By controlling the amount of introduced nanowire density, this composite is expected to be used as a transparent conductor.

Capping additional conducting polymer shell on Ag−Au core−shell nanowire have also emerged.[697] Because metallic Ag−Au core−shell nanowires have inherently low electrochemical properties compared to conducting polymer, an additional conducting polymer layer with high electrochemical properties can be a good supplement for biosignal transmission where the ions play important roles. Conducting polymer, PPy is directly electropolymerized on Ag−Au core−shell nanowires (Figure 24K). Transparent stretchable supercapacitors were fabricated through Ag−Au−PPy core−shell nanowire percolation networks. Depending on the cycles of electropolymerizations, percolation networks showed 62−85% transmittance (Figure 24L). PPy coating highly increased the surface area of percolation networks which enhanced the areal capacitance of devices.

CuNWs are attracting attention as transparent wearable electronics based on affordable percolation networks due to their low cost and high conductivity. Therefore, the synthesis of the Au capping layer on the CuNWs can significantly reduce the fabrication cost compared to expensive Ag−Au core−shell nanowires if their conductivity and stability are secured. Recently, Cu−Au core−shell nanowires with enhanced biocompatibility and stability have been developed.[694] To conformally coat the Au layer without losing the mass of Cu, galvanic corrosion is prevented by sodium sulfite and diethylhydroxylamine. The Ligand exchange of CuNWs played an important role in the penetration of Au ions to form a thin Au shell. Thin Au shells with 5 to 10 nm thicknesses were successfully formed on 80−120 nm thickness of CuNWs. Developed Cu−Au core−shell nanowires maintained their electrical properties under harsh environments (80 °C, 80% of relative humidity) and physiological environments while CuNWs instantly lose their electrical conductivity. Moreover, through enhanced biocompatibility, Cu−Au core−shell nanowires showed 95% of cell viability while most cells are dead in CuNWs. Developed Cu−Au nanowire was fabricated as percolation networks and applied for biointerfacing electronics to read ECG signals.

4.2.2. Biodegradability. In contrast to wearable electronics that record superficial bioinformation from skins, implantable devices can obtain versatile biosignals from deep tissues that provide more accurate information on human health.[698] Furthermore, by interacting with organs, they have important functions to give medical treatments such as electrical stimuli or drug treatments for sudden disorders. These devices are inserted into the bodies through surgery and the incision is safely sutured which requires recovery. However, current implantable electronic devices are not robust enough and accidental mechanical impacts or chronic fatigue under continuously moving organs might damage the devices that result in loss of functionality. Moreover, it is not necessary to maintain implantable devices when the intended functions are finished. Here, secondary surgeries are required to take out those electronic devices which give high burdens and risks to patients. Therefore, electronic devices have emerged with the concept of "biodegradability" which can control their device lifetime in the body, eliminating the risk of secondary surgery. In this section, we introduce electronic devices that can be biodegraded safely in terms of materials and degradation rates.

4.2.2.1. Biodegradable Materials. When implanting biodegradable electronics, immune responses in biological systems highly depends on degradation kinetics and byproduct which require careful selection of candidate materials. Detailed degradation kinetics and effects on biological systems can be obtained in the following review article.[686] It is necessary to rationally design the combinations of degradable materials regarding their potential effects on biological systems. Meanwhile, biodegradable electronics are also required to have enough mechanical robustness and electrical properties to extract biosignals for intended durations. Recent advancements fulfilled these cumbersome requirements that successfully demonstrated biodegradable electronics.[669,699−704] Natural biopolymers such as proteins and polysaccharides have been used as biodegradable soft substrates or matrices for conducting fillers. Owing to natural abundance and similar chemical compositions to biological tissues, natural polymers can ensure high biocompatibility with little immune response. Furthermore, the byproducts of the enzymatic degradation process of natural polymers are nontoxic such as peptides or amino acids.[705] Plenty of synthetic polymers have also been widely developed for biodegradable electronics, but poly(α-esters) groups including poly(glycolide) (PGA), polylactic acid (PLA), and their copolymers poly(lactide-*co*-glycolide) (PLGA) showed the most practical applications from the sutures to electronics devices. Compared to natural biopolymers, synthetic biopolymers have the disadvantage of eliciting an immune response due to the accumulation of their degradation products,[706] which can lead to the fibrotic encapsulation of implanted devices and the subsequent loss of functionality. Despite this limitation, synthetic polymers possess a significant advantage in that they can be mass-produced with uniform quality through the existing manufacturing system. Therefore, while further research is necessary to better understand and address the immune response induced by synthetic biopolymers, their ability to be produced on a large scale with consistent quality makes them an attractive option for the development of biodegradable medical devices and implants. For conducting materials, metals based on Mg, Zn, and Fe that naturally exist in our body were mainly used.[707] Au is a typical biocompatible and conductive metal but is not suitable for biodegradable electronics due to its insoluble properties in physiological environments and increase in fabrication cost. On the other hand, Mg, Zn, Fe, Mo, and W are easily dissolved in physiological environments with relatively high electrical conductivity. However, because high amounts of these metals can bring excessive byproducts such as metal ions, hydroxide ions, and hydrogen gas that can induce side effects to biological systems, careful material design of devices are required.

Among various studies on biodegradable electronics, few groups reported practical demonstrations of biodegradable electronics with high optical transparency. Natural biopolymers are fabricated into highly transparent substrates and assembled with metallic nanowires for transparent conductors.[699] Fish gelatin was obtained from fish scale and after multiple purification processes, it was dispersed in water. Then, fish gelation solution was cast for film fabrication that showed high transmittance of over 91%. Then AgNW percolation networks were assembled for gelatin-based transparent conductors that showed 22.4 Ω sq^{-1} of sheet resistance with 82.3% of

https://doi.org/10.1021/acs.chemrev.3c00139
Chem. Rev. 2023, 123, 9982−10078

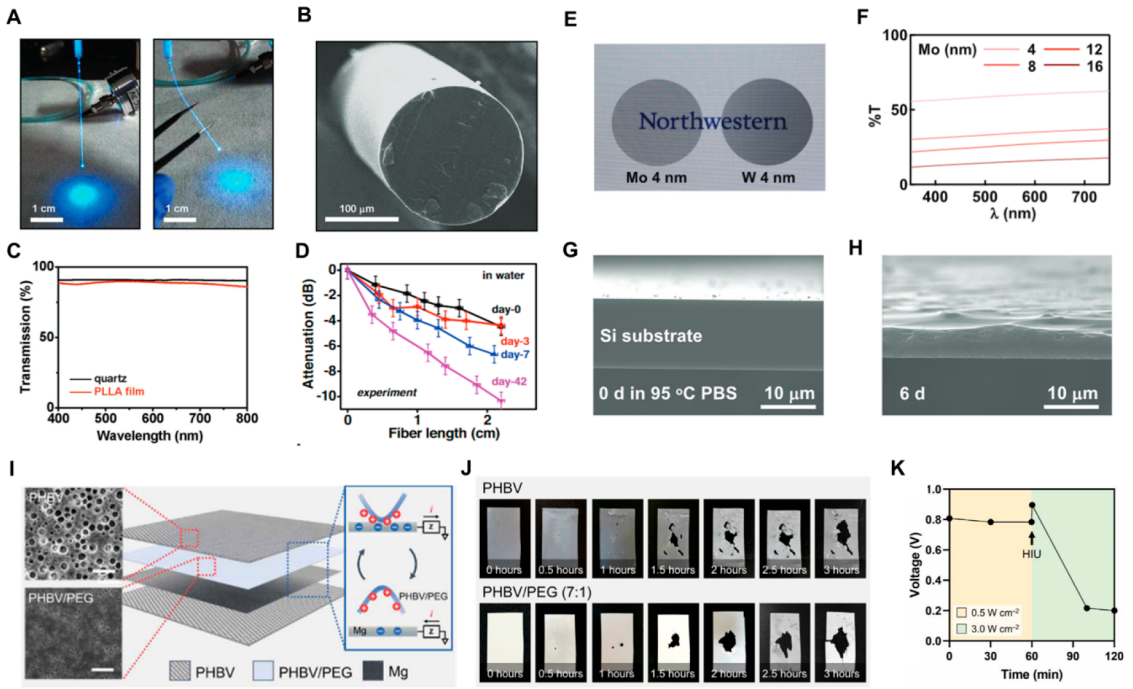

Figure 25. Biodegradability. (A) Optical image of biodegradable and transparent optical fiber fabricated by PLLA. (B) SEM image of transparent PLLA fiber. (C) Transmittance of PLLA optical fibers. (D) Biodegradation of PLLA fiber in water. Reproduced with permission from ref 700. Copyright 2017 Wiley-VCH. (E) Optical image of biodegradable and transparent conductors. (F) The transmittance of biodegradable conductors varying thicknesses. (G,H) SEM images of biodegraded electronics for 6 days. Reproduced with permission from ref 701. Copyright 2019 Wiley-VCH. (I) Schematic illustration of actively triggered biodegradable electronics using ultrasound. (J) Optical images of degraded electronics by ultrasound. (K) The output voltage of energy device under different power of ultrasound. Reproduced with permission from ref 710. Copyright 2022 American Association for the Advancement of Science under the CC BY-NC 4.0 license https://creativecommons.org/licenses/by-nc/4.0/.

transmittance and then degraded within 24 days in nature. Chitosan membrane was also used as a transparent substrate with over 94% of transparency for biodegradable electronics.[669] Then transparent chitosan substrates were assembled with Au nanofibers with 84% of transmittance at 800 nm wavelength and 25.8 Ω sq^{-1} at 80% of strain. Au nanofiber-assembled chitosan conductors were completely degraded in acidic solutions for 1 h, in enzyme solutions for 30 h, and in hydrogen peroxide solutions for 30 h. A synthetic polymer, poly(L-lactic acid) (PLLA) was fabricated into transparent and biodegradable optical fibers for the optical neural interface (Figure 25A).[700] Transparent PLLA fibers were fabricated by thermal drawing process and the diameter of obtained fiber was about 220 μm and transparency reached 95% in the visible range (Figure 25B, 25C). Fabricated optical fiber could deliver a 473 nm LED with loss coefficients of 1.64 dB cm^{-1} in the air and 1.87 dB cm^{-1} in water. After more than 40 days, loss coefficients increased to 4.75 in the air and 4.90 dB cm^{-1} in the water (Figure 25D). Through high biocompatibility and biodegradability, optical fibers were implanted in the brain of the mouse for light stimulus applications. For biodegradable conductors, Mo and W were deposited through pulsed laser deposition in ultrathin thickness (Figure 25E).[701] With 4 nm of thickness, Mo, and W showed transparency of about 60% in the visible range and 1 kΩ of sheet resistance (Figure 25F). With an ultrathin ZnO layer, transparent Mo and W were assembled into LED devices. Degradation of each metal showed 25 nm d^{-1} for W and 8 nm d^{-1} for Mo in PBS solution at 37 °C (Figure 25G, 25H).

4.2.2.2. Degradation Rate. In general, degradation in the body begins immediately with implantation and proceeded with time, so it is ideal to completely degrade the implanted electronics when the intended functions are finished. Therefore, precise design of degradation rate is crucial for biodegradable electronic devices for the safety of patients. To control the degradation rates of biodegradable electronics, critical variables on materials have been modified for natural biopolymers, synthetic polymers, and biodegradable metals.[707−711] Degradation rates of natural polymers can be tuned by controlling the density, and pore size of resultants polymer networks. Silk fibroin was studied by controlling its density and porosity and showed much slower degradation rates for high density of polymer networks and smaller pore sizes in them.[708] Similar behavior is shown for synthetic polymers such as PLA, scaffolds with small pore sizes showed slow hydrolysis while large pore sizes resulted in fast degradations.[709] In the case of synthetic polymers, the degradation rates can also be modified through design parameters such as crystallinity, MW, and copolymers. For biodegradable metals, degradation rates can be controlled by designing various types of metal alloys where each has different degradation rates in physiological environments. Engineering mechanical structures of metals can also affect the degradation rates such as porosity, grain size, and composite structure with nonmetallic materials.[707]

Meanwhile, despite the reasonable design of degradation rates, unexpected situations of removing devices can happen which require acceleration of degradation or even direct destruction of devices. To fulfill these requirements, active triggering methods to accelerate the degradation rates have emerged using ultrasound (Figure 25I).[710,711] Moderate ultrasound can deliver mechanical energy to implanted devices

https://doi.org/10.1021/acs.chemrev.3c00139
Chem. Rev. 2023, 123, 9982−10078

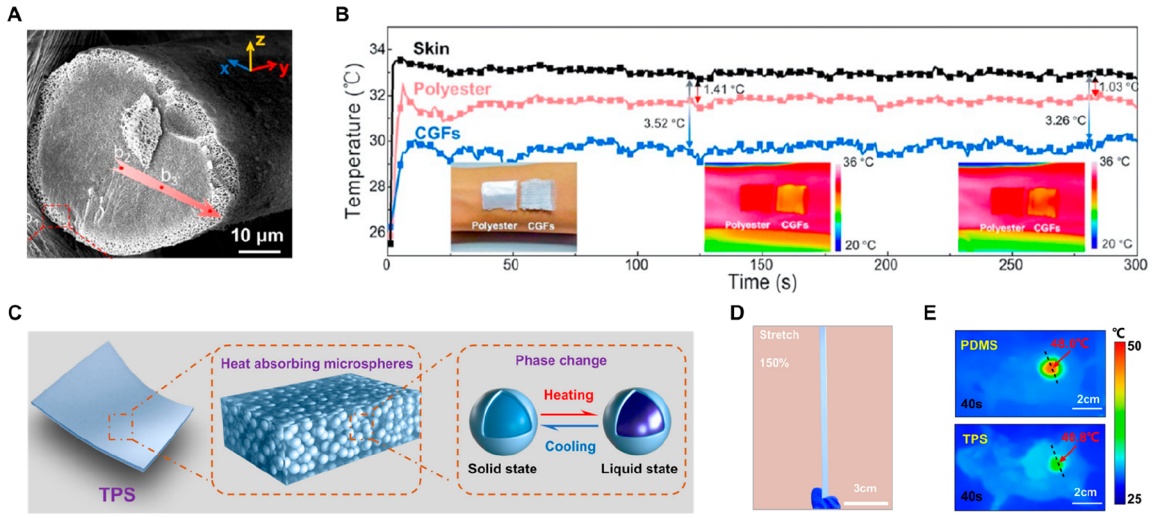

Figure 26. Thermal protection layer. (A) SEM cross-sectional image porous aerogel fiber that have graded structures inside. (B) The temperature response to the thermal protection layer. Reproduced from ref 713. Copyright 2022 American Chemical Society. (C) Schematic illustration of PCM microsphere embedded PDMS composite (D) Digital image of highly stretchable thermal protection layer. (E) Thermal images of mouse skin under normal PDMS and thermal protection layer after heating. Reproduced with permission from ref 716. Copyright 2022 Springer Nature under the CC BY 4.0 license http://creativecommons.org/licenses/by/4.0/.

without secondary surgeries with certified biocompatibility. By designing compositions of biodegradable materials, poly(3-hydroxybutyrate-*co*-3-hydroxyvalerate) combined with Mg electrode, transient triboelectric energy devices were fabricated. Ex vivo demonstration of biodegradable electronics under porcine tissue showed that with low-energy of ultrasound (0.5 W cm^{-2}), the device generated electrical energy stably, but when the power overcome the triggering threshold (3.0 W cm^{-2}), the degradation started, and finished in 120 min (Figure 25J,K).[710] Ultrasound first triggered the mechanical disintegration of biodegradable materials enabling high surface areas for subsequent hydrolytic degradation processes.

4.3. Thermal Interface

4.3.1. Thermal Protective Layer. When wearing wearable electronics for extended periods, continuous operation can lead to heat generation and excessive device temperatures. From the device point of view, such occurrences can cause performance degradation, including the warpage of the functional layers due to thermal deformation. More critically, there are risks of thermal burns to the biological tissue due to prolonged wearing of overheated devices.[712] Therefore, to ensure the safe use of wearable electronics in daily life, efficient and smart thermal management is required. Additionally, for the optical imperceptibility of the device system discussed in this review article, transparency should also be incorporated. However, achieving both high transparency and effective thermal management remains a challenge, with limited research focusing on maintaining consistent transparency while implementing thermal management. Thus, the main focus of this review will be on presenting pertinent research regarding thermal management, even if it means sacrificing optical properties.

Highly porous aerogels, known for their low thermal conductivity facilitated by air as a medium, have been widely recognized as thermal protective layers. However, they still face limitations in terms of mechanical strength and flexibility, which hinder their application as heat protection layers for wearable electronics during overheating conditions. Therefore, the development of a thermally insulating material that is mechanically flexible and possesses an appropriately low thermal conductivity is crucial for efficient thermal insulation in wearable electronics. Recently, wearable textiles made of aerogel have been reported, to exhibit impressive mechanical strength and thermal insulation properties. Unlike previous cellulose-based aerogels, which suffered from mechanical fragility, this aerogel incorporates a graded structure within its fibers, with dense internal regions and porous outer regions (Figure 26A).[713] This design enables the achievement of excellent mechanical properties. The fabrication of this structure employed a strategy of flow-assisted dynamic dual-cross-linking within a microfluidic chip, resulting in a thermal conductivity of 0.023 W m^{-1} K^{-1} and fabricated showed 3 °C lower than skin temperature without aerogel textiles (Figure 26B). In terms of mechanical characteristics, it demonstrated a fracture strength of 71.83 MPa, and even in a wet state, recorded a fracture strain of 105% and a fracture strength of 0.36 MPa. This remarkable combination of mechanical and thermal properties makes it a promising material for use as a thermal insulation layer in wearable electronics. Aramid nanofiber-decorated with SiO_2 nanoparticle composites have also been reported, ensuring mechanical properties through the 3D nanofiber networks while achieving very low thermal conductivity through SiO_2 nanoparticles.[714] These materials could be fabricated in textile form for application in wearable electronics, and they recorded a thermal conductivity of 0.034 W m^{-1} K^{-1} and a compressive strength of 1.1 MPa.

Phase change materials (PCMs) are suitable materials for thermal protection layers due to their excellent heat absorption capacity. However, for them to be used as protective layers in wearable electronics, sufficient flexibility must be ensured. Therefore, the development of materials that are both inherently flexible and capable of efficiently absorbing or releasing heat is required. Soft thermal protection layer consisting of PDMS composite incorporated by Ag flakes as heat diffusive component and a hydrogel matrix containing sodium acetate as heat storing component was reported.[715] It could effectively protect the skin using the high heat storage

https://doi.org/10.1021/acs.chemrev.3c00139
Chem. Rev. 2023, 123, 9982−10078

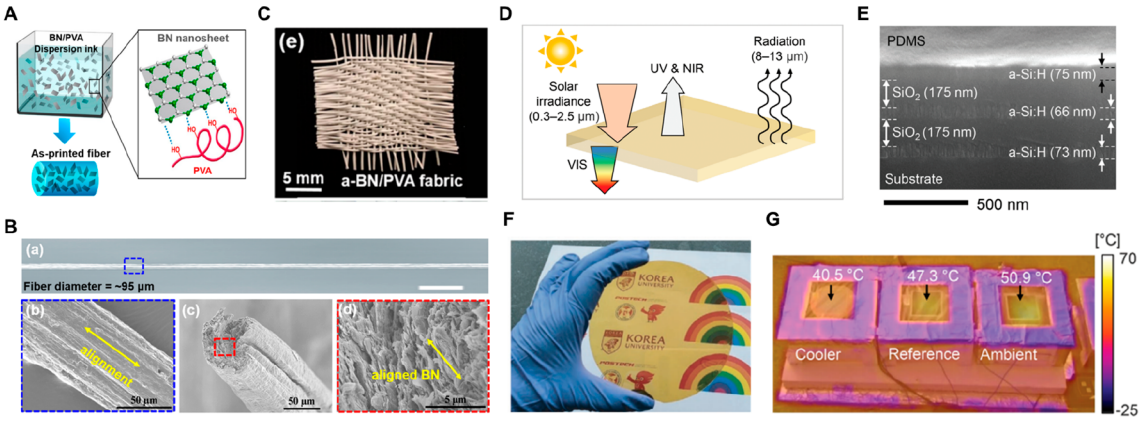

Figure 27. Heat dissipation layer. (A) Schematic illustration of heat conduction composite with PVA and BN nanosheet. (B) Aligned BN nanosheet in composite fiber. (C) Digital image of heat conductive fiber in textiles. Reproduced from ref 717. Copyright 2017 American Chemical Society. (D) Schematic illustration of the visibly transparent radiative cooler. (E) SEM images of multilayers of the radiative cooler. (F) Digital image of the transparent radiative cooler. (G) IR camera image measured outdoors. Reproduced with permission from ref 719. Copyright 2021 Wiley-VCH.

capacity of the phase-changing sodium acetate-based hydrogel matrix when wearable devices overheat. In normal conditions, the excellent thermal conductivity of the Ag flakes allows for the diffusion of heat. Additionally, the softness of the hydrogel matrix enables convenient application to various parts of the body. PDMS composite incorporated with PCM microspheres could also serve as an efficient thermal protective layer for wearable electronic applications.[716] When wearable electronics are overheated, the *n*-eicosane microspheres, which are PCM mixed with PDMS, undergo a phase change, absorbing heat and protecting the skin (Figure 26C). Due to its soft mechanical properties, it can stretch reliably up to 150% strain, making it highly suitable for wearable electronics applications (Figure 26D). PCM containing PDMS composite successfully lowered the surface temperature of the mouse to 40.8 °C while PDMS showed 48.0 °C (Figure 26E).

4.3.2. Heat Dissipation from the Human Body. Wearable electronics, worn directly on the body, face thermal discomfort due to prolonged use, physical activity, and humid conditions. Both the human body and wearable devices can serve as heat sources, therefore, effective thermal management is necessary, requiring materials with built-in heat regulation capabilities to ensure comfort, performance, and durability in daily life use of wearable electronics. In this section, we aim to discuss research focused on enhancing three modes of heat transfer (conduction, convection, and radiation) passively through materials. First, to induce efficient conduction from the curvilinear human body, it is reasonable to design composites by incorporating thermally conductive fillers into a soft polymer matrix. Commonly used polymer matrices include PDMS, TPU, and PVA, while a prominent filler is boron nitride (BN).[712] Metallic fillers can also effectively dissipate heat from sources, but they can critically disturb the wireless communications of wearable electronic devices. On the other hand, BN possesses high thermal conductivity and electrical insulation properties, making it highly suitable for use in the thermal regulation layer of wearable electronics. A recent study reported composites, consisting of BN and polymer that exhibit superior thermal conductivity when aligned in a specific direction compared to random alignments (Figure 27A).[717] Composite materials composed of BN and PVA can achieve directional alignment through 3D printing, resulting in excellent directional thermal conductivity (Figure 27B).

When these composites designed for heat conduction are fabricated in the form of textiles, they can more effectively dissipate heat in the convection mode (Figure 27C). Wearable electronics can also generate sweat during long-term use or intense physical activity. Therefore, it is necessary to have a material structure that not only manages heat but also facilitates sweat evaporation. By utilizing 3D printing to create textile structures using the aforementioned heat conduction materials, it is possible to achieve exceptional cooling performance with a thermal conductivity of 0.078 W m^{-1} K^{-1}, which is more than 2.22 times higher than that of commercial textiles. Electrospinning can enhance convective heat transfer at a smaller scale. A study involving the electrospinning of a composite of PVA and BN nanoplatelets, followed by the deposition of AgNW through spray coating and hot pressing, demonstrated a highly desirable thermal conductivity of 10.9 W m^{-1} K^{-1} and a low electrical conductivity of 10^{-12} S cm^{-1}, making it suitable for wearable electronics' thermal management layer.[718] Additionally, the porous nature of the nanofiber mat is expected to provide significant advantages in convective heat transfer.

When wearing electronics for outdoor activities, the heat source includes the human body and the device, along with additional solar heating. In this case, through material design, by enhancing solar reflectivity and thermal radiation through the long-wave infrared atmospheric window, a passive cooling effect can be achieved. It is commonly used to lower the temperature of confined spaces and its cooling performance is generally lower compared to other heat transfer mechanisms. However, composites designed for conduction often have inherent colors that make it difficult to maintain transparent optical properties. Conversely, the layer involved in radiative cooling can be made transparent, making it suitable as a transparent thermal regulation layer of wearable electronics. Furthermore, considering that the human body maintains homeostasis and even slight differences in body temperature are closely related to physical condition, radiative cooling can be a highly attractive cooling method. A recent study developed a radiative cooling material that partially transmits visible light while reflecting light in the NIR range (0.74−1.4

https://doi.org/10.1021/acs.chemrev.3c00139
Chem. Rev. 2023, 123, 9982−10078

μm) and radiates heat in the atmospheric window (Figure 27D).[719] This cooler is composed of a multilayer structure with alternating layers of dielectric materials, specifically amorphous silicon, and SiO_2. On top of these layers, PDMS was stacked as the radiative emitter to complete the composition (Figure 27E). By using dielectric layers instead of metal layers, the cooler used in this study is expected to be suitable for wearable electronics without interfering with wireless communication, and they can also be applied on soft and flexible substrates. Their optical properties are highly favorable compared to other thermal regulation materials, making them very promising as a heat dissipation layer for transparent and wearable electronics (Figure 27F). The fabricated cooler was able to lower the temperature inside the device by 14.4 °C compared to regular PDMS (Figure 27G).

5. ELECTRICAL DEVICES

Understanding nanomaterials, engineering strategies, and human−electronics bridging described in previous sections have expanded the development of transparent wearable electronics. This section summarizes various transparent wearable devices such as sensors, energy devices, actuators, displays, filters, and heaters.

5.1. Sensors

The wearable sensor captures and interprets stimuli related to human activity, making it an objective indicator of human and electronic device status. Although commercially available wearable electronic devices can detect heart rate, blood oxygen saturation, and body movements, the intrinsically rigid components hinder stable attachment to the skin, leading to compromised sensing performance and real-time monitoring. Consequently, numerous studies have investigated strategies to replace sensors with flexible and stretchable forms that can ensure stable attachment. Advancements in cognitive technology through vision sensors necessitate the preservation of visual data and prevention of visual information infringement, particularly when wearable sensors are attached to joints, muscles, or skin. This aids in delivering delicate judgment by integrating multiple data sets from visual information and wearable sensor signals.[720] The electrical properties requirements for wearable sensors vary based on their operational principles, necessitating thoughtful design considerations. In this section, we discuss recent advancements in the development of sensors for transparent wearable electronics (Table 8).

5.1.1. Physical Sensors. *5.1.1.1. Mechanical Sensors.* The majority of wearable mechanical sensors function by detecting changes in electrical properties due to the structural deformation of the sensing material. The tracking of body motion, such as hand gestures, limb movement, facial expression, and external sensations, has been an area of interest for a considerable period of time.[744−748] Humans possess more than 650 muscles and over 100 joints, and even a simple expression like frowning involves more than 70 facial muscles. Therefore, the ultimate objective for future wearable mechanical stimulus sensors is to achieve high sensitivity with high stability. However, this presents a challenge, as these two characteristics have a trade-off relationship, and it is challenging to achieve both simultaneously, for example, GF of greater than 50 and a maximum strain of over 100%.[749] To achieve a high level of mechanical sensitivity, it is necessary for the structure of the sensing material to undergo significant changes, even at low levels of strain. At the same time, to ensure that the sensing material remains stable during deformation, it must be securely attached to the stretchable substrate to prevent any damage or fatigue. In order to satisfy both of the high GF with a wide strain range, various sensing mechanisms such as a resistive type,[750,751] a capacitive type,[752,753] a piezoelectric type,[754,755] and a triboelectric type[756,757] have been employed.

Resistive-type mechanical sensors operate by detecting variations in resistance due to deformation. This mechanism enables the use of simple read-out circuits, low-cost fabrications, and improved mechanical robustness. The typical approach involves forming a percolation network using conductive materials such as CNT,[758] graphene,[746] and metal nanowires[759] as a sensing channel. Transparent resistive-type wearable sensors do not demand high electrical conductivity. It is more crucial, in this case, to design for enhanced mechanical stability and appropriate resistivity. Transparent wearable sensors should be designed to be comfortably worn on any body part, implying the need for high stretchability. A design that minimizes distortion from environmental factors, while remaining sensitive to the targeted stimulus, is imperative. A resistance value that is too low diminishes sensitivity, while a resistance value that is too high renders the sensor susceptible to noise.

When the sensor is subjected to strain, the electrical resistance increases due to the loosening of the electrical connections between the sensing materials. During mechanical deformation, the geometry of the conductive path, contact resistance between nanomaterials, and connection/disconnection between nanomaterials change.[760] The percolation feature of nanomaterials is a key factor for optical and mechanical characteristics, influencing resistivity, transparency, and sensing performance.[761] Wearable sensors based on the percolation network exhibit high responses to mechanical deformation at low percolation densities while preserving high transparency. Nonetheless, a trade-off between sensitivity and stretchability exists, as the network forms a bottleneck at low mechanical deformation, potentially leading to disconnection.[762]

One of the solutions to this issue is enhancing mechanical stability through the application of a protective layer that ensures network connectivity under mechanical deformation.[763] A PU−PEDOT:PSS/SWCNT/PU−PEDOT:PSS structure was proposed in which PU−PEDOT:PSS and SWCNTs are stacked on stretchable PDMS.[721] SWCNTs are partially embedded in the lower soft PU−PEDOT: PSS and protected by the upper PU−PEDOT:PSS layer. The developed sensor had a transmittance of 63%, GF 62.3 at 2.5% strain and stretchability of more than 100%, and there was little performance change after 20% 1000 cycles. As another approach, a combination of different dimensions of nanowires improves transparency, conductivity, and stretchability compared to a single type of nanowire electrode.[722] After drop casting AgNWS on PDMS, the AuNWs were subjected to Langmuir−Blodgett transfer several times to fabricate a sensor. Very thin AuNWs smoothly connect relatively large AgNWs and show a trade-off between stretchability and sensitivity depending on the number of transfers of AuNWs. At 66.7% transparency, the AgNWs/AuNWs hybrid-based strain sensor offers a GF of 236.6 in the strain region within 5%. At a transmittance of 58.7%, the maximum strain is improved to 70%, but the GF is reduced to 5.

https://doi.org/10.1021/acs.chemrev.3c00139
Chem. Rev. 2023, 123, 9982−10078

Table 8. Electrical, Mechanical, and Optical Properties of Transparent Wearable Sensor Devices

material	sensitivity	mechanical stability	transparency	ref
PU−PEDOT:PSS/SWCNT/PU−PEDOT:PSS	GF: 62.3 (maximum, at 2.5% strain) GF: 8.7−62.3 (1.6−3.5% strain range)	tensile strain, 100%; stretching cycles, 1000 (20% strain)	63%	721
AuNW/AgNW hybrid nanowire networks	GF: 236.6 (0−5% strain, 1 layer of Au) GF: 27.0 (0−40% strain, 4 layers of Au) GF: 5.0 (0−70% strain, 6 layers of Au)	tensile strain, 70%; stretching cycles, 1000 (10% strain)	58.7−66.7%	722
ionic liquid (ethylene glycol/sodium chloride)	GF: 2−3.6 (strain: 25−250%)	tensile strain, 830%; stretching cycles, 3000 (300% strain)		723
zwitterionic [2-(methacryloyloxy ethyl]dimethyl-(3-sulfopropyl) ammonium hydroxide (SBMA) 2-hydroxyethyl methacrylate (HEMA) laponite XLG nanosheets	GF: 1.8	Tensile strain: 2000%		724
egg white and NaOH hydrogel	GF: 0.86 (0−80% strain range) GF: 0.21 (80−200% strain range)	tensile strain, 200%; stretching cycles, 10000 (100% strain)	99.8%	725
PEG diacrylate 1-ethyl-3-methylimidazolium tricyanomethanide 2-hydroxy-2-methylpropiophenone	pressure, 3.1 nF kPa^{-1} (below 5 kPa); pressure, 1−13 kPa	bending radius of curvature: 50 mm	99%	726
scrylamide (AAm) base hydrogel	15% capacitance decrease by light touch from 20 mm above the surface of the sensor to light touch	stretching cycles: 500000 (10% strain)	90%	727
CVD graphene	6.55% kPa^{-1} (pressure range: 0−16 kPa) 1.15% kPa^{-1} (pressure range: 16−30 kPa)	bending radius of curvature: 8 mm (500 cycles)	>70%	728
motion sensing: SWCNT/polylactic acid (PLA) composite-piezoelectric polymer electrotactile stimulator: AgNW/graphene electrode: Au doped CVD graphene	pressure: 0.8 mV kPa^{-1}	electrotactile stimulator: tensile strain 30% bending radius of curvature: 0.38 cm	∼80%	591
PDMS/boron nitride nanosheet	piezoelectric charged constant: 50 pC N^{-1} push force: 40−80 kg		65−81%	729
fluorinated ethylene propylene (FEP)/polyvinyl butyral (PVB)/FEP	piezoelectric charged constant: 930 pC N^{-1}		>80%	730
PDMS/ITO coated PET			75%	731
AgNF/PDMS		stretching cycles: 12000 (100% strain)	>70%	627

https://doi.org/10.1021/acs.chemrev.3c00139
Chem. Rev. 2023, 123, 9982−10078

Table 8. continued

material	sensitivity	mechanical stability	transparency	ref
1-ethyl-3-methylimidazolium bis(trifluoromethylsulfonyl)imide	23.3 V kPa^{-1} (before 20 kPa) 3−6 V kPa^{-1} (beyond 20 kPa)	tensile strain: 1500% for iTPU	5%	732
temperature sensor, rGO/PU; strain sensor, AgNW/PEDOT:PSS/PU; electrode, PEDOT:PSS/PU	temperature: ∼1.34% /°C temperature: 30−80 °C GF: 1 (2−5.8% tensile strain) GF: 1.5 (2−5.8% compressive strain)	tensile strain, 70%; stretching cycles, 10000 (30% strain)	75%	733
strain sensor: AgNF/AgNW hybrid nanostructure temperature sensor: PEDOT:PSS	temperature: 0.03%/°C in 30−45 °C strain: 1.78×10^{-3} kPa^{-1} (below 350 kPa) and 9.65×10^{-3} kPa^{-1} (above 350 kPa)	tensile strain, 90%; stretching cycles, 15000 (70% strain)	89.05%	734
temperature sensor: acrylamide (AAm), acrylic acid (AAc) based hydrogel electrode: AgNW/Ag flakes	temperature: -0.0289 $°C^{1-}$ (below ∼24 °C) and -0.0127 $°C^{1-}$ (above ∼24 °C) in the temperature range of 15−40 °C	Tensile strain: 150%	7−96% (thermoresponsive) at 600 nm wavelength	735
AgNW/Triton X treated PDMS	GF: 1.4 (0−5% strain) GF: 13 (10−20% strain)	tensile strain, 400%; stretching cycles, 10000 (15% strain)	AgNW, 75%; PDMS, 84.7%	736
AgNW/cPI with Kirigami structure		stretching cycles: 10000 (400% strain)	80%	599
graphene/PEDOT:PSS on SEBS substrate		tensile strain: 40%	85%	737
sensing layer: PEDOT:PSS electrode: Au grid	light stimulation: 17−150 mW mW	compression strain: 50%	60%	549
graphene	electrical stimulation current: 50−300 μA (charge density: 116.07−174.10 μC cm^{-2})		90%	738
PEDOT:PSS doped with ethylene glycol	response: 105−722 μV (power 0.05−2 mW) light stimulation power: 0.05−2 mW (density: 5.78−231.09 mW mm^{-2})		85%	739
graphene/AgNW GOD-pyrene functionalized graphene	glucose: minimum 0.4 μM pressure: 2.64 MHz mm Hg^{1-}	stretching cycles: 5000 (25% strain), 10000 (20% strain)	>91%	460
P-type doped SWCNT	0.13 μA μM^{-1} cm^{-2}		80%	740
inkjet printed thin film optode ink (chromoionophore I, potassium tetrakis[3,5-bis (trifluoromethyl)phenyl]borate, sodium ionophore IV)	Na^+: 100 μM of NaCl (in 35 μL solution)			741

https://doi.org/10.1021/acs.chemrev.3c00139
Chem. Rev. 2023, 123, 9982−10078

Table 8. continued

material	sensitivity	mechanical stability	transparency	ref
nano-Au/CNT/PDMS (Rs: 350 Ω/sq) nanostructured Au (clusters)	H_2O_2: 8 nM (S/N ratio: 3)	stretching cycles: 100 (50% strain)	~65%	742
sensing layer: graphene electrode: WO_3/Au/WO_3	conductance: 39.73 μA V^{-1} 0.763 μA mM^{-1} folding: 150°	tensile strain: 0.324% radius of curvature: 175 μm shrinking: ~50%	graphene: 2.7% PET substrate: 98% electrode: 81%	743

Resistive-type pressure sensor utilizes the change of the contact architecture as a sensing principle.[764] The sensing properties are directly influenced by the geometrical design of the conductive materials used in the sensor. Adjusting the nanomicro scale morphology by controlling the parameters of laser sintering was suggested.[506] Localized heat by laser irradiation instantaneously melts AgNPs to form Marangoni flow. This geometrical perturbation tends to minimize energy. However, energy equilibrium is not reached when the laser scans too fast, and melted AgNPs are solidified and structurally fixed. The surface morphology of the sintered electrode can be controlled through the laser parameters. Afterward, a transparent AgNW electrode was placed vertically on the AgNP electrode to fabricate a pressure sensor whose contact area varies depending on the pressure (Figure 28A). Compared to the flat shape, the regular wave structure had a larger contact area variation depending on the pressure, and a broader range of pressure (10−100 kPa) was detected (Figure 28B).

Another strategy is to utilize intrinsically transparent conductive materials such as ionic gel or hydrogel.[723−725,765] Low modulus and self-healing properties are beneficial properties for wearable mechanical sensors. For example, self-healable ionically conductive zwitterionic nanocomposite hydrogels ([2-(methacryloyloxy) ethyl]dimethyl-(3-sulfopropyl) ammonium hydroxide (SBMA) and 2-hydroxyethyl methacrylate (HEMA) copolymers) can be elongated to 2000% at fracture stress of 0.27 MPa. This hydrogel skin strain sensor shows a GF of 1.8 (Figure 28C, 28D).[724] Mechanical deformation only changes the arrangement of the crossed-linked polymer and inert liquid, so the ionic conductive hydrogel does not affect the ionic transportation characteristics. Therefore, like a common bulk conductor, the electrical conductivity is inversely proportional to the length and directly proportional to the cross-sectional area. According to Poisson's ratio, the geometrical transformation in the three-dimensional determines the resistance change.[766] It exhibits much higher stretchability than the percolation network-based mechanism.[767]

The capacitive-type mechanical sensor has a sandwich structure with a dielectric layer between two electrode layers. Stress modifies the gap between the electrodes at both ends of the dielectric layer and causes changes in capacitance. Compressed by strain or pressure, it narrows the two electrodes and increases the capacitance. The capacitive-type mechanical sensors have higher linearity and lower hysteresis than the resistance type. These characteristics are important because extra calculations are not required according to strain and deformation directions.[768] The transparent capacitive type mechanical sensor can be manufactured by replacement to transparent electrodes (e.g., CNT,[642,769] graphene,[728] ITO,[726] metal nanowires,[770−772] and conductive hydrogel[727]) and the dielectric layer.

Theoretically, the capacitive-type mechanical sensor cannot have a GF higher than 1, and the signal range is very low (pF), making it vulnerable to external interference.[726] Iontronic film is a capacitive pressure sensing material that provides high unit area capacitance by forming an electrical double layer on the electrolytic−electronic interface. The composite of the highly conductive ionic liquid 1-ethyl-3-methylimidazolium tricyanomethanide [EMIM][TCM] and the photoinitiator PEG diacrylate and the photoinitiator 2-hydroxy-2-methylpropiophenone (HOMPP) is placed between two spaced ITO electrodes (Figure 28E).[726] The transparent iontronic

https://doi.org/10.1021/acs.chemrev.3c00139
Chem. Rev. 2023, 123, 9982−10078

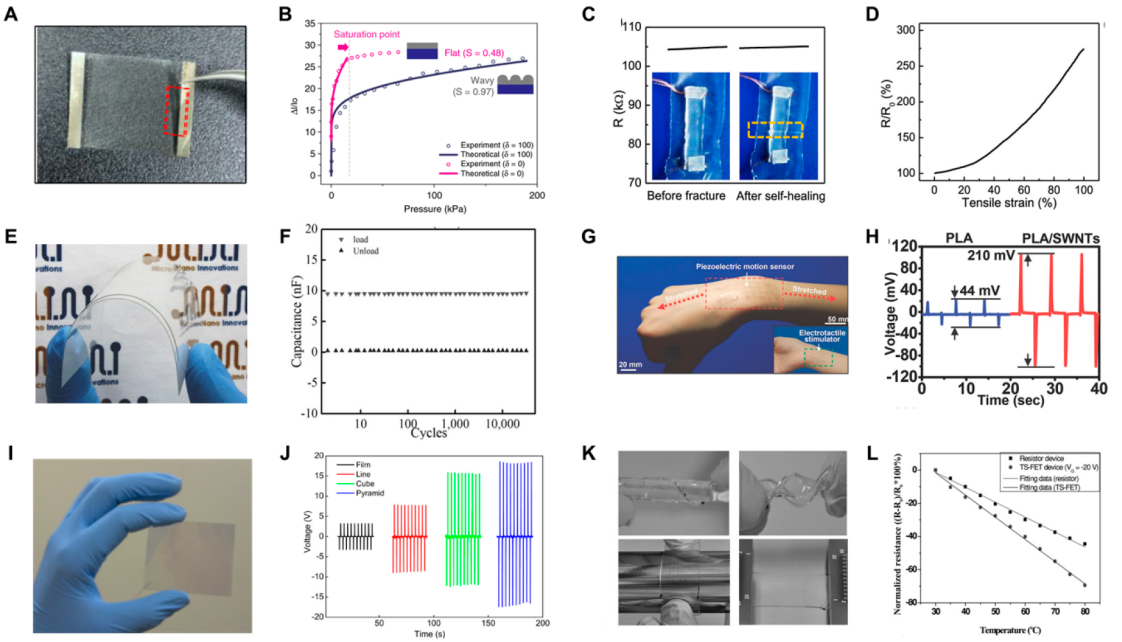

Figure 28. Physical sensors. (A) Optical image of a free-standing transparent electrode. (B) The variation in the electrical current by the different surface morphologies Reproduced with permission from ref 506. Copyright 2019 Springer Nature. (C) The change in the resistance of an L4S90 hydrogel before and after self-healing. (D) The relationship between the resistance ratio and strain. Reproduced from ref 724. Copyright 2019 American Chemical Society. (E) Thin, transparent iontronic film on the electrode substrate. (F) The capacitive values measured from the device when subjected to repetitive cycles of external pressure, exceeding 30 000 cycles. Reproduced with permission from ref 726. Copyright 2015 Wiley-VCH. (G) The transparent piezoelectric motion sensor conforming to the contours of a human wrist. (H) The voltage output of sensors with PLA and SWNT-embedded PLA. Reproduced with permission from ref 591. Copyright 2014 Wiley-VCH. (I) Optical image of micropatterned PDMS triboelectric sensor. (J) The output voltage of a PDMS thin film sensor with different micropatterns. Reproduced from ref 731. Copyright 2012 American Chemical Society. (K) Optical images of a stretchable and conformable gated temperature sensor. (L) A comparison of the temperature responses of a gated sensor and a resistor sensor. Reproduced with permission from ref 733. Copyright 2015 Wiley-VCH.

capacitive pressure sensor (transmittance 77%) showed high sensitivity (3.1 nF kPa) and large unit-area capacitance (5.4 μF cm^2) and maintained its performance even after 30 000 testing cycles (Figure 28F).

The piezoelectric sensor and triboelectric sensors are other strategies for sensing mechanical stimuli. Such types require low power because it measures the charges generated by converting mechanical energy into electrical energy. The transparent piezoelectric mechanical sensor has a structure in which a transparent piezoelectric layer (e.g., ZnO,[773] BN,[729] PVDF,[730,774] and P(VDF-TrFE)[775]) is sandwiched between two transparent electrode layers. The dipoles are aligned after applying high voltage to both ends and maintained even when the voltage is removed.[776] When the external stress is applied, the electric dipole moment generates piezo potential. The electrical charge accumulates on both electrodes by stress, and the piezoelectric mechanical sensor creates an electrical current. When the stress is released, it makes a reversed current in the opposite direction.

Flexible, transparent piezoelectric polymers show low piezoelectric coefficients, so their performance can be improved by infiltrating conductive fillers.[777] The structure in which the PLA/SWNT composite was sandwiched between graphene electrodes showed higher piezoelectricity depending on the structural deformation than when pristine PLA was used as the piezoelectric layer (Figure 28G).[591] SWNTs with a relatively high modulus than PLA increase the local strain of the piezoelectric layer and maximize the charge generation. As a result, the current and voltage are more than five times greater than the pristine state, with a slope of −0.8 mV kPa^{-1} by the applied pressure (Figure 28H). The serpentine structure transparent wearable piezoelectric pressure sensor effectively detects dynamic human body movements by showing different signal patterns according to the pressed, stretched, and compressed states.

The triboelectricity generated at the contact region of dissimilar materials is another operation principle for mechanical sensors. By anchoring it with a transparent electrode, transparent triboelectric mechanical sensors have been demonstrated.[627,731,732,778] When two materials with different electronegativities come in contact, opposite electricity is generated on each surface, and a dipole moment is formed when they are separated.[732] Accordingly, the accumulating charge establishes the electric potential, and as a result, the electric current flows. Triboelectricity can be induced by various operation mechanisms (contact, sliding, single electrode, and freestanding triboelectric layer modes). Material selection and geometrical structure affect the degree of friction and polarization and are studied to improve performance.[779]

The friction effect is improved through the transparent micropatterned PDMS film so that even slight pressure and vibration can be detected (Figure 28I).[731] Fabricating micropatterns such as lines, cubes, and pyramids through an etching process on a Si wafer mold to cast and peel off PDMS. After transfer to ITO-coated PET, a transparent triboelectric self-powered pressure sensor was demonstrated (transmittance 50%). Among them, the PDMS film with a pyramid pattern effectively induced surface charge and generated more triboelectricity (a peak voltage of 18 V and a current of 0.7

https://doi.org/10.1021/acs.chemrev.3c00139
Chem. Rev. 2023, 123, 9982−10078

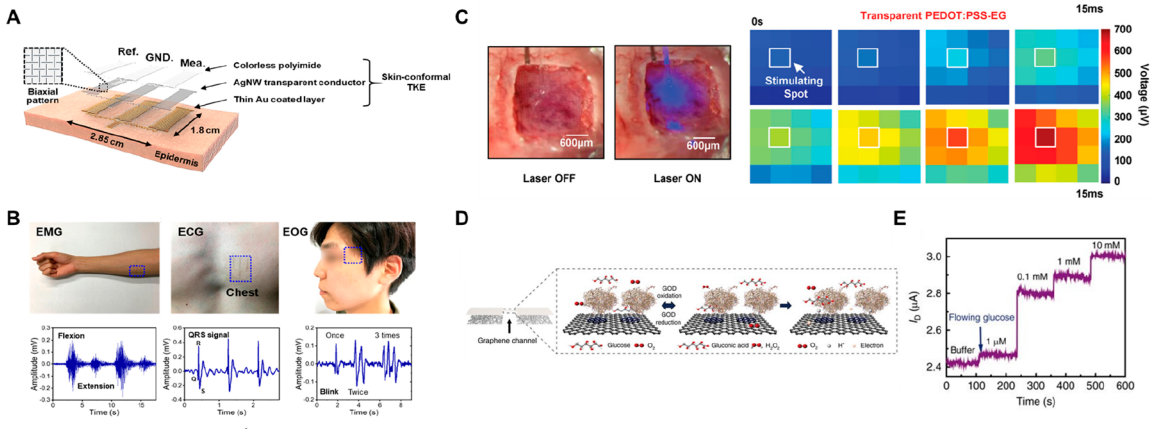

Figure 29. Physiological sensors. (A) Schematic illustration of transparent Kirigami electrophysiological sensor. (B) Capturing various electrophysiology signals (EMG, ECG, and EOG). Reproduced from ref 599. Copyright 2019 American Chemical Society. (C) Optical images and electrophysiological mapping of the PEDOT:PSS-EG electrode applied by a blue laser. Reproduced with permission from ref 739. Copyright 2021 Wiley-VCH under the CC BY-NC 4.0 license https://creativecommons.org/licenses/by-nc/4.0/. (D) Schematic illustration of glucose detection. (E) The current values at the glucose concentration from 1 mM to 10 mM. Reproduced with permission from ref 460. Copyright 2017 Springer Nature under the CC BY 4.0 license http://creativecommons.org/licenses/by/4.0/.

μA) (Figure 28J). The air gap between the microstructures improved the friction, showed an electricity generation more than five times larger than the flat film, and showed a low-end detection limit (13 mPa).

5.1.1.2. Temperature Sensors. Body temperature is vital for health monitoring and all medical diagnoses. Healthy humans maintain a constant body temperature with a very narrow range (around 36.5 °C with 3 degrees °C of differentiation). If the body temperature is out of this range, it can be suspected as a critical sign of health abnormalities such as shock, infection, and inflammatory reaction.[780] Therefore, body temperature sensors require high resolution, fast response time, and long-term continuous measurement. However, due to rigidity, conventional thermometers cannot accomplish long-term continuous measurements. The wearable temperature sensor conforms to the skin to deliver fast heat transfer. The thin active material layer has a low heat capacity and quickly reaches thermal equilibrium.[304]

Most wearable temperature sensors utilize intrinsic electrical resistance change according to the temperature coefficient of resistance. Metal has a positive temperature coefficient of resistance, whose resistance increases linearly as the temperature increases. Transparent Cu nanomesh showed 0.00272 $°C^{-1}$, which has a minor change than bulk Cu due to reduced electron−phonon coupling.[781] Also, metal oxide[304] and hydrogel[735,782,783] have a negative temperature coefficient of resistance because carrier mobility increases as the temperature increases. Transparent PEDOT:PSS is a transparent, temperature-sensitive material showing a linear change in temperature near body temperature (0.03% $°C^{-1}$).[734] Because such materials typically respond to mechanical strain, the wearable temperature sensor should minimize the sensor's electrical properties change according to the skin's deformation.[784] Therefore, the sensing signal must be precisely structurally designed and deconvoluted.

Alternatively, a gated structure can improve thermal responsivity. PEDOT:PSS/PU composite was used as an elastomeric conductor for the source, drain, and gate, and R-GO/PU nanocomposite was used as a temperature-responsive channel to fabricate a transparent, stretchable gated temperature sensor.[733] All made of transparent materials with PDMS substrate showed 70% transparency in the visible region (Figure 28K). As the temperature rises, the transport by means of hopping across the barrier at the RGO junction increases, increasing the conductivity of the channel. As a result, the resistance changes by 1.34% $°C^{-1}$, which shows a higher sensitivity than the resistive type made of the same sensing material (Figure 28L) (0.9% $°C^{-1}$). This sensor shows only a slight resistance change even at 30% strain 10 000 cycles.

5.1.2. Physiological Sensors. *5.1.2.1. Electrophysiological Sensors.* The human body performs functions through chemical and electrical signaling between cells. Humans continuously emit electrophysiological signals for the activities of organs and tissues. Nerve cells, cardiomyocytes, skeletal muscle cells, and endocrine gland cells generate electrical action potentials that can propagate to distant organs or stimulate microscopic tissues. As representative examples, measuring EMG, electrocardiogram (ECG), and electroencephalogram (EEG) is valuable for health status validation and pathological diagnosis (e.g., muscle fatigue, myocardial infarction, and brain tumors).[5,694,785] These are easily disrupted by external noise, leading to inaccurate measurements, hence higher conductivity of transparent electrodes ensures effective data acquisition.[599,736,737]

Gold, one of the promising biocompatible and highly conductive skin electrode materials, improves stability through thin overlayer coating on other electrode materials.[599] After embedding AgNWs in ultrathin cPI, a transparent kirigami E-skin was fabricated by partial laser cutting (Figure 29A). Afterward, the exposed AgNWs were selectively replaced with Au thin layer by galvanic replacement to enhance biocompatibility and enable them to be directly attached to the skin. The resistance change is within 5% of hysteresis at 400% strain, and high reversibility is shown even after 10 000 cycles. It was used as an electrophysiological sensor capable of detecting EMG, ECG, and EOG (Figure 29B).

The implantable biosensors attach to soft organs, tissues, and nerves and capture physiological signals. To prevent inflammation, electronic materials with high biocompatibility and low modulus are suitable for the neural interface.[786] Therefore, chemically stable gold,[549,787] graphenes,[738,788,789] and conducting polymers[739,790] are utilized as transparent

https://doi.org/10.1021/acs.chemrev.3c00139
Chem. Rev. 2023, 123, 9982−10078

Table 9. Electrical, Mechanical, and Optical Properties of Transparent Wearable Energy Storages

material	energy density, power density	voltage, current	charging performance	transparency	mechanical stability	ref
Supercapacitor						
CNT networks (working electrode), PET (substrate), Ag/AgCl (counter electrode), H_2SO_4 (electrolyte)	areal capacitance, 10^{-4} F cm^{-2}; stored energy, 10^{-4} J			13−97%		798
bilayer graphene/redox-active layer/bilayer graphene sandwich structure (electrode), (PVA)-H_2SO_4 gel (electrolyte)	areal capacitance: 101 μF cm^{-2}		1000 cyclic test	75%	bending cycles 1000 times (radius 5 mm)	799
Ag/Au/polypyrrole core−shell nanowire networks (electrode), PVA/H_3PO_4 gel (electrolyte)	areal capacitance: 580, 320 μF cm^{-2} at current density 5.8, 35 μA cm^{-2}		CV shape maintain at 1 V s^{-1} rate	86% (Ag.Ag core−shell NW networks), 73% and 64% (supercapacitors with 2 and 3 coating cycles)	bending cycles >800 times (retained 93% capacitance), stretching cycles 10000 times (30% strain)	697
Ti_3C_2Tx films (electrode), PVA/H_2SO_4 gel (electrolyte)	areal capacitance, 1.6 mF cm^{-2}; energy density, 0.05 μWh cm^{-2} (at power density 2.4 μW cm^{-2})		no capacitance decay over 20000 cycles	72%		800
NiO/MnO_2 (positive electrode), Fe_2O_3 (negative electrode), PVA/KOH gel (electrolyte), PET/ITO (substrate)	areal capacitance, 48.1 mF cm^{-2}; energy density, 9.62 μWh cm^{-2} (at power density 28.9 μW cm^{-2})	voltage window: 1.2 V	capacitance retains 90% after 10000 cycles	59%	maintaining CV shape under bending angle from 0 to 150°	801
AgNW/PET/graphene (current collector, electrode), PVA/H_3PO_4 gel (electrolyte)	areal capacitance: 0.3 mF cm^{-2}		capacitance retains 98% after 10000 cycles	65%	slight increase of areal capacitance under bending radius from 10 to 30 mm	802
Ni micromesh/NiCoP (positive electrode), nickel micromesh/nitrogen-doped porous carbon (negative electrode), PVA/KOH gel (electrolyte)	specific capacity, 11.1 μAh cm^{-2}; energy density, 8.0 μWh cm^{-2}; power density, 980 μW cm^{-2}	voltage window: 0−1.4 V	capacitance retains 97.6% after 50000 cycles	80.2% (electrode only), 57.1% (the full device with packaging), 67.5% (full device without packaging)	stable under bending radius from 2 to 12 mm	803
Mxene quantum dots/laser rGO (electrode), PVA/H_2SO_4 gel (electrolyte), PET (substrate)	areal capacitance, 10.42, 15.2, 23.1, 39.8, and 64.6 mF cm^{-2}; energy density, 2.04 × 10^{-3} mWh cm^{-2}; power density, 129.4 μW cm^2	voltage window: 1.2 V	capacitance retains 97.6% after 12000 cycles	>90%	stable under a bending angle from 0 to 180°	804
Battery						
$LiMn_2O_4$ nanorods (cathode), $Li_4Ti_5O_{12}$ nanopowder (anode), PVDF-HFP with $LiClO_4$ in EC/DEC (electrolyte gel), gold (current collector)	areal capacity: 20, 10, 5 Wh L^{-1}	discharge voltage 2.4 V, current density <10 μA cm^{-2} at 2 mV s^{-1}	discharge capacity: 100 mAh g^{-1} (remains over 80 mAh g^{-1} after 15 cycles)	57% (full cell with packaging)	bending cycles: 100 (radius 2 cm)	805
Ti/Pt (bottom current collector), $LiCoO_2$ (positive electrode), LiPON (electrolyte), Si (negative electrode), Ti (top current collector)		4.2−3 V	discharge capacity: 0.15−0.6 mAh, average capacity loss of 0.08% after 100 cycles	17−60%		806
Zn/Ni/Ag nanofiber (anode), porous PANi/THE (cathode), PVA/$ZnCl_2$ gel (electrolyte)	areal capacity 174.82 mAh m^{-2}(at 0.013 A cm^{-2}), areal energy density, 113.6 mWh m^{-2} (at 168.8 mW m^{-2}); volumetric energy density, 378.8 Wh m^{-3} (at power density 562.7 W m^{-3})	discharge voltage: 0.3−1.6 V	coloration stability, optical contrast loss of 11% under 500 cycles	80%	bending cycles: 10000 (radius 2 mm)	807
AuNWs (bote current collector), PAM hydrogel (electrolyte), Zn (anode), α-MnO_2 (cathode)	capacity, 176.5 mAh g^{-1}; energy density, 261 mWh g^{-1}	1−1.8 V	Coulombic efficiency: 91.2% after 120 cycles and 50% strain	72.6% (without strain), 64.7% (with 50% strain)	stretching cycles: 120 (50% strain)	808

https://doi.org/10.1021/acs.chemrev.3c00139
Chem. Rev. 2023, 123, 9982−10078

Table 10. Electrical, Mechanical, and Optical Properties of Transparent Wearable Energy Harvesters

material	power density, energy density	voltage, current	transparency	flexibility	ref
Piezoelectric					
PES (substrate), PdAu or ITO (top electrode), ZnO nanorods (piezomaterials)		current density, 1 μA cm^{-2} (at load 0.9 kgf, ITO); current density, 10 μA cm^{-2} (at load 0.9 kgf, PdAu)	70%		809
PET (substrate), ITO (electrode), GQDs/PVDF-HFP (piezomaterials)		6 V, 25 nA (at load 1 kgf)		80, 100 mV (hand movement, breathing condition)	810
ITO/PET (substrate, bottom electrode), Zn_2SiO_4 nanorods/NR-PDMS (piezomaterials), graphene (top electrode)	piezoelectric charge coefficient: 117 p.m. V^{-1}, average energy conversion efficiency, 29.10%	5.5 V, 0.50 μA cm^{-2} (at load 0.15 kgf)		2.35 V, 13 nA cm^{-2} (bending condition)	811
PVDF-TrFE/SWCNTs (piezo-materials), Cr/Au (electrode)	power density: 20 mW cm^{-3} (at load resistance 1 MΩ), no notable decrease in energy harvesting capability under 10000 cycles	maximum 2.0 V (recycled device) at input impedance 20 MΩ (finger pinching), maximum 1.2 μA (recycled device) at input impedance 10 kΩ (finger pinching)		bendable	812
h-BN/ZnO nanorods array/h-BN sandwich, Cu paper (electrode), ZnO nanorods array/PDMS (piezomaterials), CuNWs (electrode), PET (substrate)	power density: 169 mW cm^{-3} (at load resistance 30 MΩ, with h-BN), 0.1313 mW cm^{-3}	5 V, short-current: 18 μA (bending, with h-BN sandwiched ZnO nanoarray), 2.1 V, 0.5 μA	46%	bendable	813
Triboelectric					
silicon rubber/PVA gel (ionic current collector), VHB (substrate)	power density: 40 μW cm^{-2}(at load resistance 1 MΩ, ∼10 N, 4 Hz)	open-circuit voltage, 50 V, current: 6.5 μA cm^{-2}; charge transfer density, 17 nC cm^{-2} (10 N, 4 Hz)	92%	tensile strain, 700%; stretching cycles, 500	681
PDMS or VHB (elastomer), PAAm hydrogel/LiCl (ionic conductor, electrode), PDMS or VHB (elastomer)	power density: 35 mW cm^{-2} (at load resistance 70 MΩ, 100 kPa, 1.5 Hz)	open-circuit voltage, 145 V, current 1.5 μA cm^{-2}; charge, 47 nC (100 kPa, 1.5 Hz)	96.2%	tensile strain: 1160%	814
ionogel (electrode, friction layer 1), PDMS (friction layer 2), ionogel (electrode, friction layer 1), PDMS (packaging)	maximum sensitivity: 1.76 V N^{-1} (range 0.1−1 N, at strain 50%)	open-circuit voltage, 0.3 V; current, 2.3 nA (0.1 N, 1 Hz, contact area diameter 11.5 mm)	83%	tensile strain: 80% (no change in sensitivity)	815
PDMS/zwitterionic network hydrogel (ionic conductor), PDMS	power density: 209 mW cm^{-2} (at load resistance 30 MΩ)	open-circuit voltage, 123 V; current, 5.1 μA; charge, 42 nC (contact area 40 × 50 mm^2)	98.1%	areal strain: 1600%	816
PVC gel (active material, conducting layer)	power density: 8.7 μW cm^{-2} (at load resistance 500 MΩ)	open-circuit voltage, 24.7 V; current, 0.83 μA (50 kPa, 5 Hz, contact area 20 × 20 mm^2)	91%	tensile strain: 250%,	817
Thermoelectric					
Cu iodide (thermoelectric materials), Au (electrode), PET (substrate)	thermoelectric figure of merit ZT, 0.23 (at 300 K); power density, 2.4 mW cm^{-2} (at del T: 50 K)	power output: 8.2 nW (at del T: 10.8K)	60−85%	bending cycles: 400, (resistance change <0.2% under bending angle of 90°	818
donor-doped ZnO/mica (thermoelectric materials)	power factor: 1 × 10^{-4} W m^{-1} K^{-2}			bending cycles: 100 (radius 14 mm, without crack and change in Seebeck coefficient)	819
CuI (thermoelectric materials, p-type), gallium doped ZnO (thermoelectric materials, n-type), ITO (conductive electrode for series connection), Kapton (substrate)	thermoelectric figure of merit ZT, 0.29; power factor, 4.7 × 10^{-4} W m^{-1} K^{-2}	short-circuit current, 0.29 μA; maximum output voltage, 0.43 mV, (at del T: 5 °C); power output, 0.41 nW (at del T: 20 °C)	>70% (CuI film, p-type), >80% (GZO, n-type)	CuI film-bending cycle, 100 (resistance change <10%); GZO film-cracks in films at bending	820

https://doi.org/10.1021/acs.chemrev.3c00139
Chem. Rev. 2023, 123, 9982−10078

neural interface materials. Simultaneous integration with electrophysiological recordings and neural activity modulation is beneficial for comprehensively understanding the neural system and developing remedies for disease. Optical stimulation is prospective for the modulation method of bioactivity due to high temporal and spatial controllability.[791] Accordingly, neural interface sensors must ultimately be optically imperceptible. The opaque neural interface material blocks not only external light, greatly hindering light stimulation, but also generates unwanted current by light. Metal electrodes have free electrons by the external photoelectric effect at wavelengths with light energy above the threshold.[792] These problems significantly affect results because it is challenging to distinguish between electrophysiological signals and noise.

PEDOT:PSS was used as a transparent neural interface electrode, reducing the gap between electrodes and biological tissue with low electrochemical impedance.[739] After patterning the PR in the form of an electrode array on the PET substrate, PEDOT:PSS is spin-coated. After that, dipping in EG after lifting off by ultrasound in an acetone solution reduced the electrochemical impedance. The completed transparent conductive sensor array (transmittance 85%) effectively captures the neural signal in response to optogenetic stimulation of the genetically engineered mouse. Unlike the Au electrode, the transparent conducting polymer electrode did not produce any photoelectric artifact under laser irradiation (Figure 29C).

5.1.2.2. Biochemical Sensors. Biochemicals such as electrolytes (e.g., Na^+, K^+, Ca^-, and Cl^-), metabolites (e.g., glucose, uric acid, lactic acid, and ascorbic acid), and nitrogenous compounds play essential roles in the human body for maintaining homeostasis and performing the functions of nerves. When concentrations of biochemical are out of balance, it can be considered a health problem. In situ measuring biochemical compounds in the body will be very important in future portable health monitoring.[793] Currently, urine and blood are evaluated for medical diagnosis. However, these methods need direct bodily extraction, potentially risky and a considerable barrier to real-time monitoring. In addition, such methods are expensive and challenging to manufacture mobile devices. Therefore, other body fluids (sweat, saliva, tears), which can be obtained easily, are promising replacements for real-time monitoring electronics.[460,794,795] However, body fluids contain many biochemical molecules with low concentrations and are easily contaminated by uncontrollable external factors. Thus, choosing appropriate biomarkers and developing suitable sensors for diagnosis and prediction is challenging. Biomarkers must be sufficient in bodily fluids and not react with other molecules. Biochemical sensors must capture the concentration range of markers in body fluid with high resolution and respond quickly. Biosensors detect changes in electrochemical properties caused by oxidation, reduction, and redox of the adhesion surface through binding with active molecules. Transparent sensing materials, including CNT,[740,742] graphene,[459,460,743] and ion-selective optodes,[741] have been successfully used to fabricate transparent biochemical sensors.

Glucose is an essential biomarker in the diagnosis and treatment of diabetes. A FET-based transparent sensor was proposed for noninvasive monitoring by forming a graphene channel between graphene/AgNWs electrodes (91% transparency).[460] Graphene is functionalized by selectively linking glucose oxidase (GOD) to the graphene surface via $\pi-\pi$ stacking (Figure 29D). GOD oxidizes glucose to gluconic acid and reduces H_2O to H_2O_2. Hydrogen peroxide generates oxygen, protons, and electrons, increasing the channel's concentrations of charge carriers and drain current (Figure 29E). The signal-to-noise ratio was 7.34 at a glucose concentration of 1 μM under zero gate bias. It had a detection limit of 0.4 μM and sensitively detected the normal tear glucose concentration range.

5.2. Energy Devices

The wearable energy device plays a crucial role in wearable electronics by converting external stimuli into electrical signals and supplying them to the electrical device. With the advancement of wearable technology, more sophisticated functions are being integrated into smaller platforms. A high-capacity energy storage device and a high-efficiency energy harvester are necessary to ensure long-lasting usage with minimal charging time. In this respect, the demand for high-performance and sustainable energy devices is increasing urgently. Furthermore, with the development of transparent wearable electronic devices, transparent wearable energy devices are sought after due to their potential to seamlessly integrate into other transparent wearable electronics such as displays[796,797] and touchpads.[130,585] It can be achieved by innovative transparent electrode material design, allowing the devices to blend in visually with the surrounding environment. Transparent wearable energy devices can enhance the aesthetic appeal of wearable electronics and provide a more immersive user experience. This section discusses transparent wearable energy devices categorized by energy storage and energy harvester (Tables 9 and 10).

5.2.1. Energy Storages. Transparent energy storage devices are essential to ensure the total device maintains its transparency when coupled with other components. Currently, these storage devices present the most significant obstacle in the development of transparent wearable electronics. Thus, transparent electrodes exhibiting high conductivity are crucial for superior electrochemical performance. Unlike transparent electrodes for other components, these electrodes also require significant capacitive properties. Given that volumetric capacitance is proportional to thickness, there is a trade-off between electrical properties and transparency.[798,821] Electrical properties tend to decrease rapidly as transparency increases in the high transparency range. Also, low conductivity makes it easier to reach the cutoff voltage, which lowers the total amount of energy, power delivery, lifetime, and efficiency, so high-performance electrodes have been developed. In this respect, most energy storage devices have been developed with a transparency of 50−80%.

5.2.1.1. Supercapacitors. The supercapacitor, the representative energy storage device type, consists of an electrode, current collector, and electrolyte. The reactions on the electrode surface store electrical energy, resulting in a high power density, quick charge and discharge times, and a long lifetime.[822] With the advancement of transparent electrode materials such as ITO,[801,823] graphene,[799,802] metal,[697,803,824] PEDOT:PSS,[496,825] and MXenes,[800,804] transparent supercapacitors have been reported.

The performance of energy storage devices is greatly influenced by the size of the electrode's surface area. A common approach for increasing the surface area is the formation of a percolation network using nanomaterials.[826]

https://doi.org/10.1021/acs.chemrev.3c00139
Chem. Rev. 2023, 123, 9982−10078

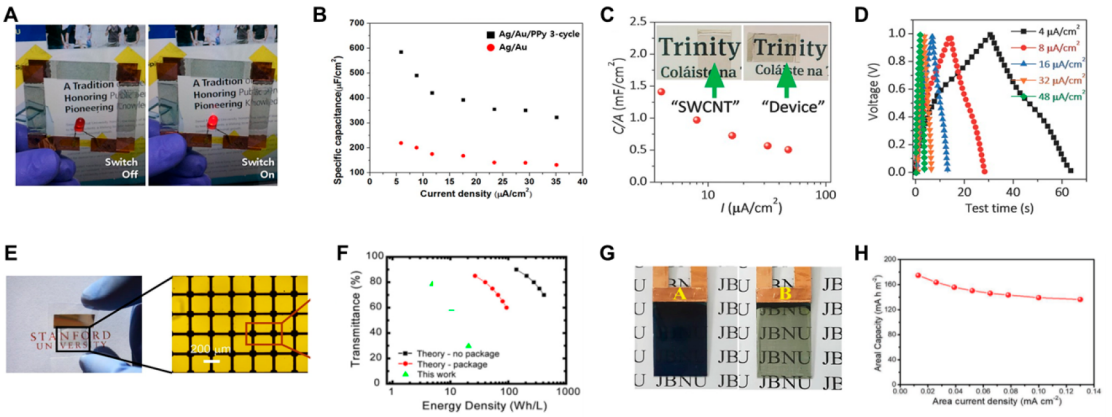

Figure 30. Energy storages. (A) A series-connected supercapacitor. (B) The areal capacitance of Ag/Au, Ag/Au/ppy supercapacitor as a function of the current density. Reproduced with permission from ref 697. Copyright 2017 Springer Nature under the CC BY 4.0 license http://creativecommons.org/licenses/by/4.0/. (C) Areal capacitance at various current densities and photographs of SWCNT film and the asymmetric device. (D) Galvanostatic charge−discharge at different current densities of the asymmetric device. Reproduced with permission from ref 800. Copyright 2017 Wiley-VCH. (E) Optical image and SEM image of a transparent and flexible battery electrode. (F) The optical transparency versus energy density. (10Wh/L at 60% transmittance) Reproduced with permission from ref 805. Copyright 2011 National Academy of Sciences. (G) Image of an FE-ZiB device in the (left) charged state at 1.6 V and (right) discharged state at 0.3 V. (H) Areal capacity under various area current densities. Reproduced with permission from ref 807. Copyright 2021 Wiley-VCH.

Due to the high surface area of the percolation network of 1D material, it showed higher performance than the film type.[697] Ag@Au core−shell nanowires allow for lowering the consumption of expensive Au and improving electrochemical stability. Then, through electropolymerization, a Ag/Au/polypyrrole core−shell nanowire network was utilized for the transparent supercapacitor electrode (73% at 550 nm) (Figure 30A). After that, the supercapacitor was fabricated by coating PVA H_3PO_4 gel electrolyte and showed a performance of 580 μFcm^{-2} at the current density of 5.8 μAcm^{-2} (Figure 30B). These electrochemical properties were maintained even after 5000 cycles of bending with a radius of curvature of 5 mm.

The mechanism of charge storage in supercapacitors is dependent on the electrode material. Carbon and graphene-based materials store energy through electrical double-layer capacitance, which is based on the desorption of electrostatic charge at the electrode−electrolyte interface. Metal oxides, conducting polymers, and metal carbides store energy through pseudocapacitance, which is based on faradaic electron charge transfer between the electrode and electrolyte.[827] This transfer is caused by reversible faradaic redox, electrosorption, or intercalation processes. The use of asymmetric supercapacitors, which incorporate electrical double-layer capacitance electrodes and pseudocapacitance electrodes, has improved energy density and specific capacitance.[828]

MXenes, a class of transparent pseudocapacitive materials, have shown promising results in high electrical conductivity and electrochemical performance.[829] Parallel aligned MXenes-($Ti_3C_2T_x$) to substrate exhibit high volumetric capacitance characteristics (676 F cm^{-3}) with the electrical conductivity of 5736 S cm^{-1} at 93% transparency.[800] An SWCNT electrode was used as the opposite electrode for a transparent asymmetric supercapacitor (Figure 30C). As a result, the asymmetric design shows relatively inferior rate performance compared to a symmetric supercapacitor. However, the areal capacitance is improved (1.4 mF cm^{-2} at 4 μA cm^{-2}), and the current density is improved by 12 times (Figure 30D). Asymmetric supercapacitors have high coulomb efficiency with a gradual increase in capacitance due to the enhanced active site region between MXene sheets during 20000 cycles.

5.2.1.2. Batteries. The lithium-ion battery, which utilizes Li-ion as the charge carrier, is a popular energy storage solution widely used in electronics. This type of battery is characterized by its high energy density and lack of memory effect from repetitive charging and discharging.[830] The lithium-ion battery includes cathode and anode active material, cathode, and anode current collector, electrolyte, and separator. During the redox reaction at the electrode, Li-ion from the electrode diffuses into the electrolyte to reach the counter-electrode for charge compensation. Recently, researchers have developed a flexible version of the lithium-ion battery that uses thin film technology.[831] This design replaces traditional components with flexible layers, resulting in improved mechanical stability. However, the transparent wearable lithium-ion battery is still limited, and further development is needed to enhance its electrochemical performance.[805,806]

As the representative work, the transparent anode $LiMn_2O_4$ and cathode $Li_4Ti_5O_{12}$ were patterned in a grid structure (50 μm width) by the microfluidics-assisted method (Figure 30E).[805] By patterning the grid spacing with a width lower than the human resolution, it was possible to manufacture a transparent lithium-ion battery visually through the combination of transparent gel electrolyte and packaging material. As a result, the performance does not change even after bending, and an energy density of 10 Wh L^{-1} was obtained at 60% transparency (Figure 30F). Due to the grid shape, aligning multiple layers does not sacrifice transparency.

Nontoxicity is another crucial factor in wearable electronics like E-skin, implantable devices, and health monitoring systems. While traditional lithium-ion batteries contain highly toxic and flammable chemicals,[832] such as multivalent materials are being considered as alternative materials due to their low toxicity and environmental safety.[833] One such material is zinc, which has a high capacity density (5855 mA h cm^{-3}) and shows positive potential as a power source for wearable devices through the use of zinc ion batteries (ZIBs).[807,808,834] Ag, Ni, and Zn were sequentially coated on electrospun nanofiber for a

https://doi.org/10.1021/acs.chemrev.3c00139
Chem. Rev. 2023, 123, 9982−10078

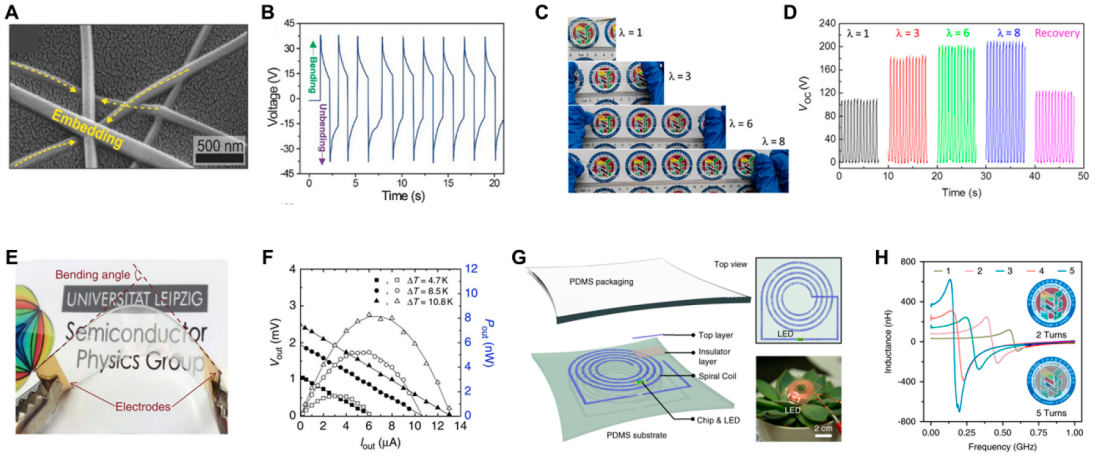

Figure 31. Energy harvesters. (A) SEM image of the AgNWs embedded into the PET film. (B) The open-circuit voltage during repeated bending and unbending. Reproduced with permission from ref 586. Copyright 2016 Wiley-VCH. (C) Digital images of a different stretched state of triboelectric nanogenerator. (D) The output voltage of triboelectric nanogenerator. Reproduced with permission from ref 814. Copyright 2017 American Association for the Advancement of Science under the CC BY-NC 4.0 license https://creativecommons.org/licenses/by-nc/4.0/. (E) A CuI thin film on PET. (F) Output voltage and output power of a CuI-based thermoelectric energy harvester. Reproduced with permission from ref 818. Copyright 2017 Springer Nature under the CC BY 4.0 license http://creativecommons.org/licenses/by/4.0/. (G) Schematic illustration of wireless power devices. (H) Inductance variation versus frequency of various multiturn spiral coils. Reproduced with permission from ref 843. Copyright 2020 Springer Nature under the CC BY 4.0 license http://creativecommons.org/licenses/by/4.0/.

Zn@Ni@AgNFs nanofiber network and used as an anode for transparent flexible ZIB.[807] As a result, color and transparency distinguished the discharged state (50% transparency, 0.3 V) and the charged state (dark blue-violet, 1.6 V) (Figure 30G). ZIB exhibited a high volumetric energy density of 378.8 W h m^{-3} at a power density of 562.7 W m^{-3} and a high areal capacity of 174.8 mA h m^{-2} at 0.013 m A cm^{-2} and maintained its performance even under mechanical strain (Figure 30H).

5.2.2. Energy Harvesters. Energy storage requires recharging or replacement over time, which can be inconvenient and costly. An ideal alternative would be to convert external stimuli directly into electrical signals, eliminating the need for charging or discharging. Humans constantly generate energy through movement, heat production, and biological processes, with estimates ranging from 0.8 to 60 W.[835] This presents an opportunity to harness this energy to power wearable devices through energy harvesting systems. By converting human movement into electrical current, energy harvesting systems can supplement or even replace traditional energy storage systems. It is imperative for transparent wearable energy harvesters to employ transparent electrodes of high conductivity for the efficient collection of electrical signals. This aids in effectively capturing the electrical signals generated by the devices and mitigating energy leakage during transmission. Moreover, ensuring close contact between the energy harvesting layers is crucial to optimally harness the energy. This approach offers the potential for a more convenient and sustainable solution for powering wearable electronics.

5.2.2.1. Piezoelectric Energy Harvesters. The energy generated by body movement can be converted into electrical current using the piezoelectric and triboelectric principles.[836] This principle can be utilized to convert the kinetic and vascular dynamic signals generated by body movement into electrical energy. In the piezoelectric method, a piezoelectric nanogenerator generates a piezoelectric potential from an external force.[837] The charges induced through electrodes on the ends of the piezoelectric material (e.g., ZnO,[809,813] Zn_2SiO_4,[811] $BaTiO_3$,[838] MOS_2,[839] PVDF-TRFE,[812] and PVDF-HFP[810]) are then harvested as current pulses.

In order to avoid performance degradation under repeated deformation, the conductivity of the transparent electrodes and the adhesion force between electrode material and substrate are critical issues.[840] Radiation of the UV flash lamp on AgNWs electrode achieves high transparency and electrical conductivity (5 Ω sq^{-1} at 90% transmittance) by local junction welding (Figure 31A).[586] Moreover, surface plasmon polaritons partially melt PET and dramatically improve adhesion energy (30.7 Jm^{-2}) with AgNWs. This electrode−substrate interlocking prevents delamination, so the transparent energy harvesting device used as a single crystalline $Pb(Mg_{1/3}Nb_{2/3})$-O_3−$PbTiO_3$ (PMN−PT) piezoelectric layer showed excellent mechanical stability and harvesting performance. This device exhibited an output voltage of 38 V and a current density of 6.8 μAcm^{-2} and maintained harvesting performance even under 100 000 cycles at a bending radius of 4.75 mm (Figure 31B).

5.2.2.2. Triboelectric Energy Harvesters. Triboelectric energy harvesting is highly effective for generating electrical energy from mechanical movement, even in small devices. Triboelectric nanogenerators are robust, cost-effective, and generate high voltage, making them an attractive option for powering wearable devices. This method works by harvesting the electrostatic force generated through the contact and separation of dissimilar materials. The contact between the materials creates opposite charges on each surface, generating a current when the two surfaces are separated. The performance of triboelectric nanogenerators is greatly influenced by the material's electron affinity, surface roughness, and pressure.[731] Triboelectric nanogenerators have four operating modes, including contact, sliding, single electrode, and freestanding triboelectric layer modes. They can be used as a power source for self-powered sensors and complex electronic device sensor platforms.[681,814−817]

A transparent and stretchable triboelectric nanogenerator was fabricated by using elastomer (PDMS or VHB 9469) and ionic hydrogel PAAm hydrogel containing lithium chloride

https://doi.org/10.1021/acs.chemrev.3c00139
Chem. Rev. 2023, 123, 9982−10078

Table 11. Mechanical and Optical Properties of Transparent Soft Actuator Devices

material (structure)	operation stimulus	actuation	actuation force, energy, speed, strain	transparency	ref
SFA					
PAAM-alginate hydrogel	pressure	bending	2 N (constrained actuator, under hydraulic pressure 20 kPa), strain 300%, responsive time <1 s	95%	855
PEGgel/P(HEMA-*co*-AAc	pressure	bending	fracture strain: 12−4336%	>95%	856
DEA					
SWCNT/prestrained VHB 4910	voltage	elongation (areal)	5 kV, area strain 200%		857
CuNW/VHB	voltage	elongation (areal)	4.8 kV, area strain 200%	13% (rest), 58% (actuated to 200%, 4.8 kV)	858
biaxially oriented polypropylene(BOPP)/FR3 liquid dielectric/ polyacrylamide hydrogel (swollen with an aqueous LiCl)	voltage	contraction/ elongations	10 kV(50 Hz), 0.02 N, strain 10%, strain rate 900% s^{-1}		859
VHB 4905/conductive fluid/water (ionic solution)/two DEAf from three layers for bidirectional actuators	voltage	bending (bidirectional)	10 kV, maximum curvature: 12.5 ± 0.4 m^{-1}	97% (active area), 90% (border)	860
AgNW/PEDOT:PSS/WPU (PEDOT:PSS waterborne PU)/VHB	voltage	elongation, expansion/ contraction	12 kV (2 Hz), area strain 146%, 0.4 s (expansion) and 0.24 s (contraction) at 5 kV (2 Hz)	87−89%	861
PEDOT:PSS/WPU/PDMS lens/VHB 4910	voltage	elongation	10 kV, change in focal length (209%)	80.30%	862
SMP					
multiphase copolyester urethane network (PPD−PCL)	temperature	programming	reversible strain 21%, switching temperature 27 °C (A→B), 38 °C (B→A)		863
smart hydrogel (polyacrylamide/alginate-PBA)	moisture, multivalent cation and PH (shape memory, Ca^{2+} inside the gel)	programming	average relative strain >15(mm/mm)		864
liquid crystal elastomer/Cu (heating wire)/PI	electric potential	programming	1−3 V, actuation strain 41% (contraction), surface temperature 20−120 °C, lifting load 3.92 N		865
self-cracking aluminum mesh/TSMPI	electric potential	programming	12 V, reverted to the original shape in 13 s, transition temperature 230 °C	∼83%	866
NAGAm/MBA or NAGAM/PEGDA hydrogels	temperature/PH	programming	shape deformation at 70 °C, PH 1.2→5.9, elongation 600−1000%	>90%	867

https://doi.org/10.1021/acs.chemrev.3c00139
Chem. Rev. 2023, 123, 9982−10078

(LiCl)) as the electrification material and electrode material, respectively.[814] This triboelectric nanogenerator exhibits 1160% stretchability and 96.2% transmittance (Figure 31C). It has a single-electrode operation mechanism that discharges electric charge to an externally grounded electrode through contact and separation with an external dielectric film in the form of an elastomer-wrapping ionic hydrogel. It showed a maximum open circuit voltage of 145 V and an instantaneous areal power density of 35 mW m^{-2} (Figure 31D). The performance was maintained even after 5000 contacts and 20 000 cycles of stretching.

5.2.2.3. Thermoelectric Energy Harvesters. Body heat can be harnessed as an alternative source of electrical energy using a thermoelectric generator. This device, when attached to the skin, generates a voltage by leveraging the temperature differential between the skin-facing surface and the exterior surface.[841] While the limited temperature difference between the skin and ambient air limits the maximum power density that can be achieved, the thermoelectric generator has the advantage of providing a steady output of electricity. A temperature gradient between the two sides of a semiconductor material can be utilized to generate electricity through the thermoelectric effect. The difference in temperature causes the holes in the transparent N-type semiconducting material (e.g., Bi_2Te_3[842] and ZnO:GA[819]) and electrons in the transparent P-type semiconducting material (e.g., CuI[818,820]) to migrate to the colder side, thus creating a flow of electricity between the two electrodes. To improve energy harvesting efficiency, exploring appropriate materials with a high Seebeck coefficient, high electrical conductivity, and low thermal conductivity is required.

Typically, N-type semiconducting materials possess higher Seebeck coefficients and greater transparency compared to P-type semiconductors. To achieve more efficient energy harvesting, developing P-type transparent thermoelectric materials is essential (band gap >3 eV). Polycrystalline P-type γ-CuI thin films deposited on PET and glass by reactive sputtering showed superior performance compared to other P-type semiconducting materials.[818] It showed high transparency (60−85% at 410−2000 nm of wavelength) and a high Seeback coefficient and has high thermoelectric performance even at room temperature, making it highly applicable for transparent wearable thermoelectric devices (Figure 31E). Such a thin film only shows a resistance change of 0.2%, even at 400 cycles with a compressive bending angle of 90 °C. Furthermore, the transparent single-leg thermoelectric module showed 0.10 mW cm^{-2} at ΔT = 10.8 K, similar to Bi_2Te_3/Sb_2Te_3 (Figure 31F).

5.2.2.4. Radio Frequency Energy Harvesters. As another strategy, wireless power transmission is a preferred technology for battery-free wearable electronics due to its higher reliability and controllability, and it also offers the potential for data transportation.[618,843] The stretchable and transparent energy transfer between two coils holds promise for attachable wearable devices,[844] optical lenses,[459] and wearable glasses.[845] This technology has proven effective in supplying energy to a variety of wearable applications, such as complex integrated circuits and smart lenses. Currently, wireless charging of cell phone watches and mobile devices is achieved through electromagnetic induction, which exhibits a high efficiency at short distances. Despite improving the stability against electromagnetic interference, this method's efficiency drops quickly with increasing distance. Utilizing magnetic resonance between two coils with matching resonant frequencies offers a more effective solution for maintaining high efficiency over longer distances, making it a future technology for wearable electronics. Through the design of Ag nanofibers (AgNFs), a stretchable transparent spiral coil capable of wireless power transfer was suggested (Figure 31G).[843] The design and structural deformation of the coil affects the quality factor, radio frequency properties, and electrical properties (inductance, resistance, capacitance) of the coil (Figure 31H). The five-turn stretchable spiral coil showed an excellent transmission capability of 15% at 10 MHz in magnetic resonant coupling mode, even under 100% tensile state.

5.3. Soft Actuators

Wearable robotics are rapidly gaining popularity in various fields, such as human augmentation and medical rehabilitation.[846,847] Conventional rigid robots are precise and powerful in performing repetitive tasks. However, they lack the ability to adapt to unpredictable situations and operate safely in human activities. In this context, soft robotics, composed of soft matter, has emerged as a promising alternative to rigid robots. Soft actuators' mechanical properties are similar to biological organs and muscles, allowing them to perform distinctive functions that are impossible with rigid robots.[848,849]

Soft actuators have the unique ability to reach a force equilibrium state without complicated control actively and can be stably worn in dynamic environments. The human−machine interface has been greatly improved through multilateral studies on soft materials and working principles, leading to an expansion of various application fields such as haptic reproduction,[850] implantable drug delivery,[851,852] and assistive robotics.[853,854] Furthermore, transparent soft actuators hold immense significance in the field of soft robotics, attributed to their unique characteristics and potential applications. Primarily, they offer an aesthetically agreeable and unobtrusive solution, merging seamlessly into attire or attaching directly to the body without drawing attention. Integration of soft actuators with additional sensors can enhance controllability, and the combination with vision sensors could potentially yield superior performance.[854] Hence, the advent of the transparent soft actuator is likely to pioneer a new trajectory in the future. The actuation capability, encompassing power, strain, strain rate, and operation mechanism, holds significant importance when evaluating soft actuators. It must transmit large forces and maintain their mechanical properties under repeated deformation. However, the development of optically imperceptible soft robotics is still in its early stages due to the inferior mechanical properties of transparent materials. In this section, we will discuss the principles of soft fluidic actuators, dielectric actuators, and shape memory polymers, which are developed with various transparent materials, such as elastomeric materials, liquid crystal elastomers, and hydrogels (Table 11).

5.3.1. Soft Fluidic Actuators. Soft fluidic actuators (SFAs) have been widely researched in wearable robotics. By applying fluidic pressure to the chamber embedded within a soft and elastic material, the material can be mechanically stretched, resulting in the production of mechanical movements.[868] SFAs have many advantages compared to other operating principles. Complex movement by simple operation, SFAs make large deformation with simple fabrication such as soft lithography, delivering high force.[869,870] Actuating force and direction are modulated through the magnitude and direction of the fluid pressure. Asymmetric modeling of the stiffness of the chamber enables various motions (e.g.,

https://doi.org/10.1021/acs.chemrev.3c00139
Chem. Rev. 2023, 123, 9982−10078

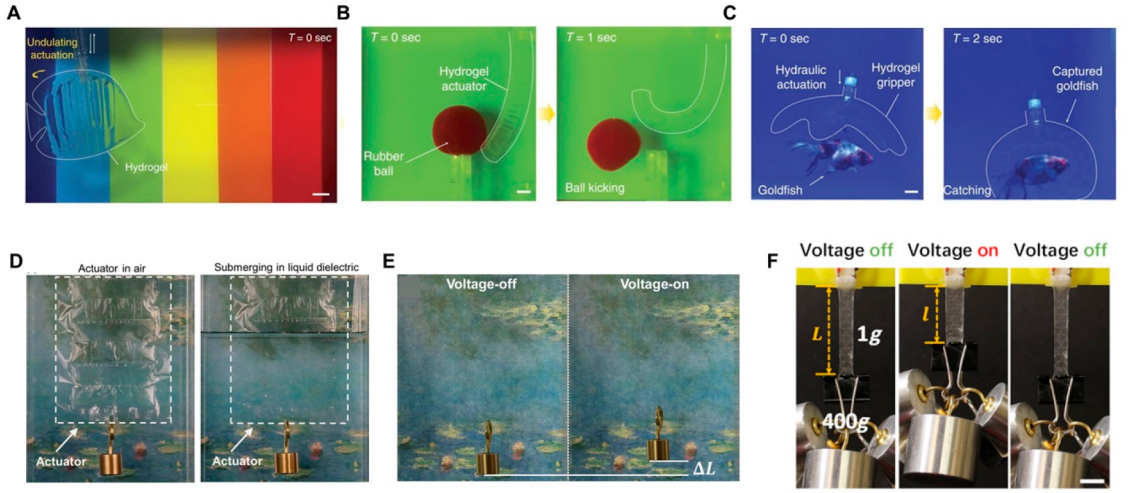

Figure 32. Actuators. Various applications of hydrogel actuators and robots. (A) Forward fish-like swimming robotic fish. (B) A hydrogel actuator kicking a rubber-ball in water. (C) A hydrogel gripper. Reproduced with permission from ref 855. Copyright 2017 Springer Nature under the CC BY 4.0 license http://creativecommons.org/licenses/by/4.0/. (D) A Peano-HASEL actuator and the submerged portion of the actuator are nearly invisible. (E) Submerged actuator lifting 10 g weight under 8 kV. Reproduced with permission from ref 859. Copyright 2018 American Association for the Advancement of Science. (F) An LCE artificial muscle film lifting an object of 400 g. Reproduced with permission from ref 865. Copyright 2019 American Association for the Advancement of Science under the CC BY-NC 4.0 license https://creativecommons.org/licenses/by-nc/4.0/.

bending,[871,872] elongation,[873] and twisting.[874] A combination of actuators can induce multi-DOF motion.[875] Elastomeric materials must be simulated through sophisticated theoretical modeling due to their nonlinear mechanical behavior.[874]

The properties of the chamber material greatly influence the force transmission and deformation of the fluidic soft actuator. Low-cost and light, semitransparent, or transparent dragon skin,[876] Ecoflex,[877] PDMS,[878] and hydrogel[855,856] are used as chamber materials. Ecoflex, which has a low modulus, shows large deformations even with low-pressure inflow but is more disadvantageous in terms of force transmission. Through soft lithography, a soft pneumatic robot with a difference in strain between the top and bottom was demonstrated by using translucent Ecoflex and transparent PDMS as the upper and lower layers, respectively.[879] The Ecoflex layer, which has a relatively lower modulus than the PDMS layer, stretches more even at low stress and enables bending. The exact mechanism consists of five actuators, one main body, and four limbs, and a pneumatic channel independently controls each actuator. A crawling group undulation gait was achieved by continuously operating each component in a different sequence (13m h^{-1}).

Most wearable soft actuators are composed of opaque materials, as highly transparent soft materials have poor mechanical properties compared to other opaque materials. Therefore, there is a need to develop transparent soft materials with higher mechanical properties. Hydrogel is intrinsically transparent, allowing the building of transparent actuators with a bulkier and thicker layer than flexible silicone elastomers. PAAm-alginate hydrogel is used for a hydraulic soft actuator with fast response (<1 s) and high force (<1 N).[855] Hydraulics soft actuators generate more force than pneumatics soft actuators. Because PAAm-alginate hydrogel is composed of more than 90% water, its optical properties are very similar to water. This way, under the water, optically and sonically, camouflaged swimming fish, a bending actuator, and a gripper were fabricated (Figure 32A–C). Due to the robustness of the hydrogel, it could operate over 1000 multiple cycles.

5.3.2. Dielectric Elastomer Actuators. Another method is the dielectric elastomer actuators (DEAs), operated by electricity. The electrically driven actuators show large and fast responses obtained with low current, have high controllability, and are easy to interface with other electrical devices.[880−883] When an electrical potential difference is applied to both stretchable electrodes on both ends of the dielectric elastomer, positive charges on one side and negative charges on the other are accumulated to form an electric field and generate a Coulomb attraction that compresses both ends.[884] Due to the elastomer's low modulus, the deformation occurs until the mechanical stress and the Coulomb attraction are in equilibrium. Strain and strain rate can be controlled according to the applied voltage, and the soft elastomer returns most of the input energy as mechanical strain energy, not capacitive energy. For high deformation, thin electrodes are required. Because the electrodes must be stretched together, interference by the electrodes must be minimized for large deformation. Metal nanowire,[858] CNT,[857] and conductive hydrogel[861,862] have been used for the electrode of optically imperceptible actuators. Prestretched VHB tape was used as a dielectric layer, and it was confirmed that the area of the dielectric elastomer widened when voltage was applied to the electrodes. Compared to other methods, it can produce high power while maintaining transparency, which has high potential in transparent wearable soft robotics.

However, the manufacturing process for complicated geometry is difficult, and there is a risk of leakage due to a high voltage (kV) requirement. Complex structural transformations were achieved through submerged actuators in which both electrodes were fluids.[860] The interface between the fluid electrode and the dielectric elastomer improved light transmittance compared to the air−elastomer interface, so it maintained high transparency in water (active area, 97%; border area, 90%). When an external voltage is applied to one of the two independent fluid electrodes surrounded by three layers of elastomer, maxwell pressure compressed the dielectric layer. As a result, the chamber is tensioned and bent. By

https://doi.org/10.1021/acs.chemrev.3c00139
Chem. Rev. 2023, 123, 9982−10078

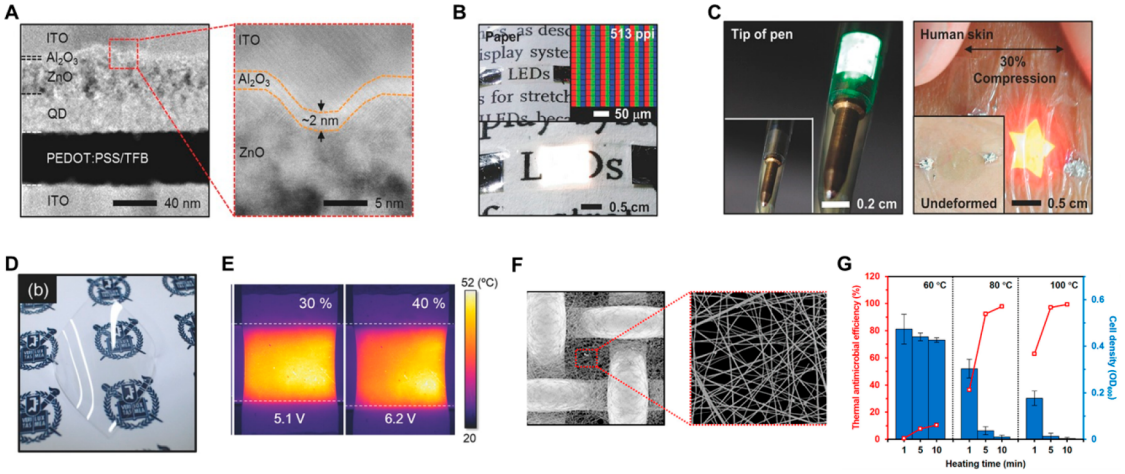

Figure 33. Display, heater, air filter. (A) Cross-sectional scanning TEM image of the Tr-QLED. (B) The array is patterned by the intaglio transfer printing method (513 pixels in^{-1}). (C) Digital image of transparent flexible Tr-QLED. Reproduced with permission from ref 797. Copyright 2017 Wiley-VCH. (D) Digital image of AgNWs transparent stretchable heater. (E) Temperature distribution under various strains with adjusted voltage to maintain constant temperatures (50 °C). Reproduced with permission from ref 153. Copyright 2015 Wiley-VCH. (F) SEM images of CuNWs on nylon mesh. (G) Bacterial growth and corresponding thermal antimicrobial efficiencies. Reproduced from ref 912. Copyright 2022 American Chemical Society.

connecting three elastomers in an aligned form and controlling each individually, movements similar to those of leptocephali were fabricated.

A hydraulically amplified self-healing electrostatic (HASEL) actuator that utilizes a DEA and a hydraulic principle has been presented.[859] This soft actuator achieves higher deformation and greater force. It is manufactured simply by filling the PAM hydrogel fluid dielectric into an inextensible but flexible thin chamber and then patterning the electrode with conductive hydrogel electrodes on the outside. The electrode, which is half the size of the chamber, pushes the fluid inside to generate contraction when electricity is applied (Figure 32D,E). It showed 10% contraction, 50 Hz, and 900% s^{-1} strain rate, and the power to lift 200 times its weight, and it could drive complex movements through rational design.

5.3.3. Shape Memory Polymers. Shape memory polymers (SMPs) are materials that can temporarily hold a specific shape and revert to their original form in response to external stimuli. These properties allow SMPs to produce motions such as bending and twisting through stimuli. Unlike traditional actuator mechanisms, SMPs have the potential to be used in untethered robotics. The configurations of SMPs can be fixed via physical or chemical triggering, allowing them to temporarily retain their deformed state in the absence of external stimuli. Upon application of an additional external stimulus to remove the internal fixing energy, the SMPs return to their original shape.[863,866,867] For example, liquid crystal elastomer (LCE) undergoes a change in length in response to temperature owing to its ability to transition between different phases based on temperature, causing a variation in molecular configuration. When the LCE molecules are aligned, the application of heat triggers a noticeable and reversible contraction in the direction of alignment, resulting from the changes in molecular configuration attributed to the thermal response.

A thermally controllable actuator was fabricated by arranging the internal mesogen by irradiating UV light on a sandwich type.[885] A stretchable heat wire was inserted between two layers of loosely cross-linked LCE films. The increased temperature by joule heating of the hot wire caused a phase transition from the nematic state to the isotropic state, enabling contraction in the longitudinal direction. The film-type actuator was controllable with a low voltage of 3 V, homogeneous contraction within 40% was achieved, and the lightweight of the 1 g of soft actuator lifted 3.92 N (Figure 32F). In addition, the tubular actuator manufactured by rolling the film form can be bent in the desired direction through independent control of the heater. It can be manufactured as a gripper or untethered soft robot.

Transparent soft actuators have also been presented that utilize various external triggers as the actuation principle. The soft hydrogel actuator composed of PAM precursors and polymer chains of alginate-PBA is multiresponsive to moisture, multivalent cations, and pH.[864] Hydrogel has a shape memory property in which the volume changes reversibly and significantly depending on the water content. Because the PDMS film does not deform in external triggers, an asymmetric bilayer of hydrogel and PDMS is bent by dehydration. This mechanism enables complex actuating, such as flowering with simple stimulation through the structural design of the bilayer actuator. In addition, alginate is combined with multivalent cations to improve the water absorption of the hydrogel so that structural changes are possible even with the influx of ions such as Ca^{2+}.

5.4. Others

5.4.1. Display. Display conveying software information in a visual form or serving as a medium for people to give commands to software, significantly impacting the human lifestyle. Personal, flexible displays and head-mounted displays can be purchased in the market. Accordingly, developing a transparent and flexible new format with high wearability and convenience is expected. It will play an important role in the metaverse, IoT. Transparent top electrodes, such as metal oxide,[886−888] metal,[889,890] and graphene,[891] have been effectively utilized to manufacture transparent flexible displays, including OLEDs,[892,893] QLEDs,[797,894] and PeLEDs.[895] A transparent flexible display requires the background on the opposite side to be seen without obstruction, and high intensity and clear security are required when emitting light.

https://doi.org/10.1021/acs.chemrev.3c00139
Chem. Rev. 2023, 123, 9982−10078

Transparent displays necessitate exceptionally high transparency (>90%) and high conductivity (<50 Ω sq^{-1}) in top and bottom electrodes.[896] Transparency is particularly crucial for the top electrodes due to the susceptibility of underlying materials to environmental conditions such as oxygen exposure, humidity, plasma interactions, and temperature fluctuations. These constraints can cause the performance of transparent devices to lag behind their opaque counterparts. Furthermore, characterizing the morphology of transparent electrodes is significant in stacking multiple thin layers. For instance, a network of metal nanowires demonstrates superior transparency and conductivity. However, due to its uneven surface, it may intrude on the underlying layer and cause potential damage.

Among light-emitting materials, colloidal quantum dots (QDs) have been investigated as promising candidates for thin-film displays due to their exceptional luminous efficiency and versatility in tuning colors. For example, electron transport layers composed of an ultrathin alumina layer with ZnO nanoparticle assembly and transparent quantum dot light-emitting diodes (Tr-QLEDs) achieve high optical and mechanical properties (Figure 33A).[797] Electron transport layers improve active layer stability and balance carrier injection. This device showed more than 84% transparency in the visible spectrum range and a total performance of 73 000 cd m^{-2} and was patterned with red, green, and blue Tr-QLED with high resolution (513 pixels in^{-1}) (Figure 33B). In addition, with an ultrathin film structure of 2.7 μm, light emission was stable even in bending, folding, and stretching (Figure 33C). There was no degradation in performance even under 50% strain.

5.4.2. Heater. The heater is an indispensable component in many fields requiring thermal regulation. It can be applied to defogging of the display,[897,898] personal thermotherapy,[899] and heat preservation,[900] and it needs to be highly stretchable and transparent to adhere to curved target skin. When current flows, a transparent conductive electrode increases the temperature by Joule heating. Transparent flexible heaters have been demonstrated CNT,[901] graphene,[902] metal nanowire,[153,903] and conducting polymer.[904] Wearable heaters which operate with high power on the skin, necessitate designs for a moderate operating voltage range. Typically, these wearable heaters function at a few volts, ensuring an optimal power level while minimizing the risk of device damage and potential harm to the wearer. When excessively conductive materials are used, there is a risk of high currents traversing the nanomaterials, leading to damage due to electromigration. During this process, ions can migrate and induce the formation of voids or hillocks within the nanomaterials. Such structural irregularities can escalate the electrical resistance of the electrode, consequently undermining the device's performance. Conversely, wearable heater with too low conductivity electrodes requires a high-voltage power source for adequate output. This condition diminishes wearability and safety during operation, thereby restricting the device's practical utility.

As a representative example, a stretchable, transparent heater was fabricated by vacuum filtration of AgNW percolation networks on PDMS.[153] Depending on the AgNWs density, the electrical conductivity and transmittance were varied, and high heater characteristics were exhibited under transmittance >85% at 30 Ω sq^{-1} (Figure 33D). It showed a maximum temperature of over 80 °C at an applied voltage of 5 V. The stable operation was performed even under deformations such as 60% strain, bending, and twisting. Although the heat generation decreased due to resistance increasing under applied strain, it was possible to obtain a uniform temperature distribution by actively controlling the voltage (Figure 33E).

In order to maintain a high temperature for a long period, wearable heaters must improve their stability. Electrodes based on percolation networks have advantages in terms of high conductivity, transparency, and mechanical properties. However, the metallic nanowire network is vulnerable to high temperatures and high currents. The thermal instability of metallic nanowires can result in spheroidization, causing a loss of the percolating nature of the networks.[905] Additionally, electrical instability can occur when the networks are subjected to electrical stress.[906] Various techniques, such as core−shell nanowire and layer coating, have been proposed to improve stability against harsh environments.[763] The selective electrodeposition of GO nanosheets on AgNWs and pulsed laser irradiation greatly improved thermal stability.[907] The heater with a sheet resistance of 3.3 Ω sq^{-1} and transparency of 91% showed even at Joule heating temperature of 366 °C.

5.4.3. Air Filter. Particulate matter (PM) is composed of various toxic substances from soot, dust, and forest fires and, when inhaled, causes many diseases related to the cardiovascular and respiratory organs.[908] In particular, microparticles with a diameter of less than 2.5 μm (PM2.5) are more dangerous because they can easily penetrate the human body. In addition, fine particles play a role in mediating the spread of viruses and bacteria.[909] Air quality management in living spaces has become an essential factor. In particular, wearing a personal mask, which has become an essential element of daily life during the Covid pandemic, disturbs communication between people and screens the transmission of facial expressions and mouth movements. Therefore, a mask requires high wearability and optical transparency.

Conventional air filters have a thick thickness, which causes a pressure drop and degrades performance. Electrostatic precipitators typically entail the deposition of a conductive material onto a fiber filter, requiring a highly conductive substance to generate a robust electric field.[910,911] One notable challenge with wearable filters lies in the decrement of air permeability due to the accumulation of microparticles over time, which can significantly impair their performance. Consequently, attributes such as the maintenance of physical integrity and the potential for reusability emerge as pivotal considerations in the design of wearable filters. Furthermore, it is essential to ensure the preservation of conductivity even after repeated wash cycles. In particular, Cu-based air filters can inhibit the secondary transmission of microbes due to their intrinsic bactericidal properties. CuNW air filter is fabricated by partially filling the pores by vacuum filtration of CuNWs on a flexible nylon mesh (Figure 33F).[912] In addition to mechanizing air pollutants, electrostatic filtration performance was enhanced. (PM0.3 conditions, 68.4−93.4%) In addition, Joule heating greatly enhanced the sterilization of *Escherichia coli* and *Geobacter anodireducens* (Figure 33G). The proposed filter could be integrated with a commercial mask with 70% transparency.

6. APPLICATIONS

The performance of individual electronic components, integration technology, and the development of data analysis are accelerating wearable electronics to the systematic level.[913] This section describes usage possibilities for health monitoring,

https://doi.org/10.1021/acs.chemrev.3c00139
Chem. Rev. 2023, 123, 9982−10078

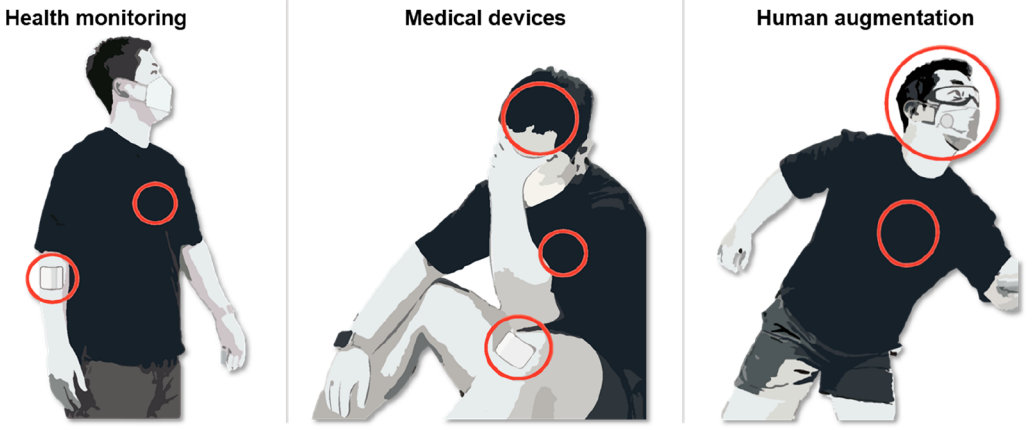

Figure 34. Various wearable electronics applications.

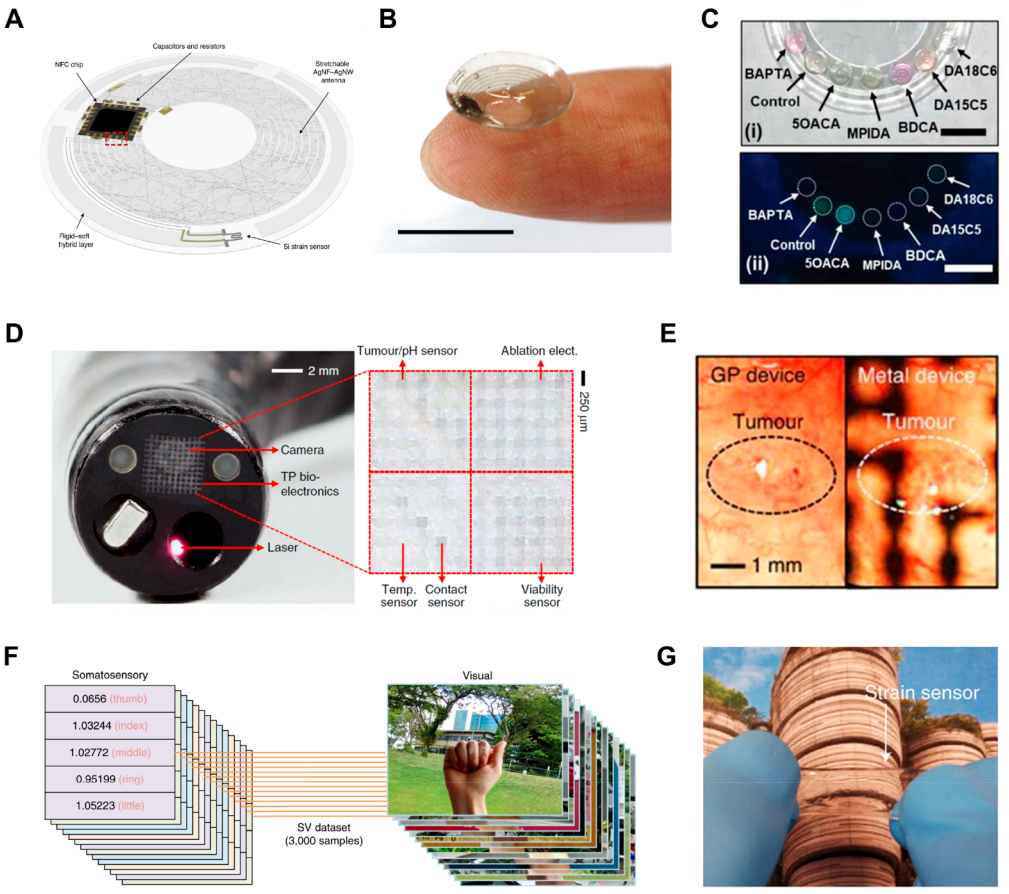

Figure 35. Transparent wearable electronics applications. (A) Schematic illustration of an integrated system including strain sensor, antenna, NFC chip, and interconnects. (B) Digital image of smart contact lens. Reproduced with permission from ref 919. Copyright 2021 Springer Nature. (C) Digital image of multiplexed scleral lens with fluorescent probes. Reproduced with permission from ref 920. Copyright 2019 Wiley-VCH under the CC BY 4.0 license http://creativecommons.org/licenses/by/4.0/. (D) Digital image of a multifunctional endoscope system. (E) Digital image of tumor captured by transparent bioelectronic devices, and control metal devices. Reproduced with permission from ref 922. Copyright 2015 Springer Nature under the CC BY 4.0 license http://creativecommons.org/licenses/by/4.0/. (F) Illustration of the data sets for multimodal fusion. (G) Digital image of stretchable transparent strain sensor. Reproduced with permission from ref 720. Copyright 2020 Springer Nature.

medical treatment, and human augmentation in which various electrical components are organically functioning (Figure 34).

6.1. Health Monitoring

The increasing demand for health monitoring is expected to revolutionize the role of portable electronic devices, positioning them as critical tools for remote medical services, early health issue detection, and preventative diagnostics. Recent advancements in physical[914−916] and physiological[748,913,917,918] sensors have made precise detection of human activity and health status possible, allowing for a more comprehensive understanding of individual health. Furthermore, the growth in wireless transmission capabilities has been a vital factor in the evolution of wearable health monitoring devices. Smart contact

https://doi.org/10.1021/acs.chemrev.3c00139
Chem. Rev. 2023, 123, 9982−10078

lenses serve as an innovative solution for noninvasive, continuous monitoring of both physical and chemical biomarkers. Tears, which contain a diverse array of electrolytes, provide a noninvasive, readily accessible source of biomarkers. The challenge with smart contact lenses lies in ensuring high transparency to not obstruct the wearer's vision while integrating various electrical components and ensuring the biocompatibility of materials used. As such, significant strides in research have been made in developing biocompatible materials, integrating technology that preserves the wearer's vision.

Recent research has successfully developed a transparent, wearable smart contact lens to aid glaucoma patients by monitoring intraocular pressure (IOP).[919] The lens is constructed from PET and integrates a strain sensor, wireless antenna, and an NFC chip (Figure 35A,B). The strain sensor, an ultrathin boron-doped single crystalline silicon layer, is strategically placed on a rigid-soft hybrid substrate, enabling it to detect very minor changes in IOP. The system also includes a stretchable AgNF-AgNW antenna and an NFC chip with embedded passive elements, interconnected by direct patterning of a stretchable material. A temperature sensor embedded within the NFC chip calibrates the IOP value and wirelessly transmits this data to a mobile device. The lens has been successfully tested in practice on a rabbit's eye, with results recorded wirelessly. Human trials further confirmed that wearing the smart contact lens caused no noticeable discomfort.

The acquisition of complex signals is vital for precise diagnosis. Advances in integration technologies are poised to enhance compact platforms, allowing for the sensing of multiple biomarkers in small devices.[913] This progress may lead to more sophisticated diagnostic capabilities. Notably, multiplexed scleral lens sensors have been developed to quantitatively monitor pH and various electrolytes (Na^+, K^+, Ca^{2+}, Mg^{2+}, and Zn^{2+}) (Figure 35C).[920] These are made by incorporating multiple fluorescent probes into laser-engraved microfluidic channels. The optical measurements of the colorimetric changes of these sensors enable the extraction of quantitative results for individual sensors. This technology has facilitated the assessment of dry eye disease severity without the need for an internal power source.

6.2. Medical Devices

Wearable medical devices present an innovative approach for managing and treating various health conditions. By using biometric signals for continuous patient monitoring and treatment, they provide a more effective solution than traditional methods. This approach could potentially reduce reliance on regular medical appointments and enable more responsive treatment plans. With the integration of cutting-edge technology, wearable medical devices are capable of detecting changes in a patient's condition and adapting treatments accordingly.[921] Aligning the detected health issue with the targeted treatment location is crucial. In this regard, transparent wearable electronics show significant promise. They can facilitate precise monitoring and treatment by leveraging visual information, providing a more accurate representation of the patient's condition and treatment requirements.

Providing transparency to sensors can preserve visual information on interfacing biological tissues for multimodal optical imaging purposes. Transparent sensor arrays are integrated with a commercial endoscope system (Figure 35D).[922] For the transparent sensors, typical transparent electronic materials (graphene, AgNW, and IrO_x) were combined for excellent performance, and the transparency of the final device reached about 80% at the visible range. The sensor array developed in this way was attached to the camera of the endoscope for comprehensive and accurate diagnosis of the tumor by combining optical imaging and sensor data (e.g., pH and temperature). Also, within the endoscope, the laser system for photothermal therapy that can be coupled with nanoparticles is combined. Because the transparent sensor does not block the camera of the endoscope, it was possible to readily observe the area to be irradiated by the laser and to perform precise treatment treatments (Figure 35E). The smart endoscope system combined with a transparent sensor was demonstrated to accurately diagnose and treat cancer through optical imaging and comprehensive signal interpretation through sensing data.

6.3. Human Augmentation

Wearable electronics have increasingly become an integral part of our daily lives, offering vital information about our health and activity levels and enhancing human capabilities beyond their inherent abilities. Recent advances in wearable robotics, sensors, and artificial intelligence have paved the way for wearable electronics to generate artificial senses and improve overall human performance. A standout development in this domain is the wearable cognitive system, a device that operates like human cognition, demonstrating the immense potential for various applications. The advent of intelligent wearable electronics has been enabled by the integration of mechanical sensors and machine learning algorithms, endowing these devices with the ability to recognize tasks and perceive materials.[923] Such wearable cognitive systems, that couple state-of-the-art technology with human-like abilities in a compact device, are a highly sought-after advancement in this field.[696,924,925]

The collection of high-quality data to improve cognitive abilities is a significant focus of current research. Vision data, being a pivotal factor in decision-making processes, can be substantially enhanced by the use of transparent wearable sensors. These sensors play a crucial role in collecting signals from the same location without interfering with vision data. A recent study has shown that the multimodal fusion of vision data with data from wearable transparent strain sensors can significantly increase recognition accuracy (Figure 35F).[720] To gather somatosensory information, a strain sensor was fabricated using a SWCNT sensing layer, PDMS substrate, and PAA adhesive layer. This sensor exhibited 89% transparency and 100% stretchability, which allowed for a conformable attachment to the skin (Figure 35G). The collected vision and somatosensory data were processed through the following steps: a sectional convolutional neural network (CNN) was used for visual processing, a multilayer neural network was employed for somatosensory information processing, and a sparse neural network fused the visual and somatosensory information. As a result, this multimodal fusion approach could classify hand gestures with an impressive accuracy of 100%. Furthermore, this method maintained a high accuracy rate of 96.7%, even in the dark, where visual information is typically less accurate.

In addition, the creation of virtual sensory information technology has seen significant progress with the growth of

https://doi.org/10.1021/acs.chemrev.3c00139
Chem. Rev. 2023, 123, 9982−10078

interest in the metaverse. Currently, these technologies are limited to generating visual and auditory information through rigid devices. Although humans heavily rely on spatial and temporal cutaneous sensations, the generation of haptic sensations is still in its infancy stage.[926] The technology of reconstructing haptic sensations is vital in enabling a realistic artificial feeling in the next-generation virtual world.[584,927,928] The integration of optical and mechanical imperceptibility has the potential to significantly enhance user experiences by providing a more immersive environment. Research has been presented on the integration of a transparent touch display with a haptic actuator.[929] In this study, a dielectric elastomer microactuators (DEMA) array was fabricated, utilizing a AgNW electrode with a multiple three-dimensional structure. Each actuator in this expands vertically, thus producing a localized force. This DEMA array was integrated with both a tactile sensing layer and a display layer, resulting in the construction of a transparent, dual-functioning device. This device exhibits a total thickness of less than 200 μm and a transparency of 90%. This system allows for the simultaneous transmission of visual and haptic information directly onto the skin.

7. CHALLENGE AND FUTURE WORKS

The continued innovation of transparent electronic materials and processing techniques discussed in this review has led to the emergence of a new class of electronics with novel optical properties that were not achievable in previous wearable devices. While recent regulatory approvals for wearable and implantable devices have encouraged progress in this field, numerous challenges remain to be overcome (Figure 36).

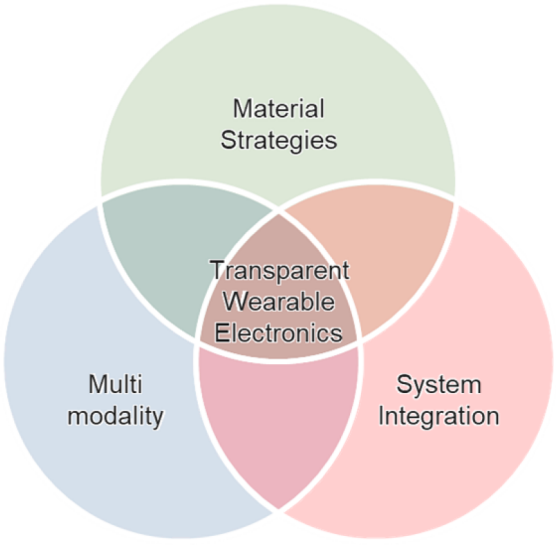

Figure 36. Challenges of transparent wearable electronics.

One of the key challenges in developing transparent and wearable electronics is the urgent need for highly transparent materials with high electrical and mechanical properties. Imparting the three required characteristics simultaneously will be one of the ultimate goals for researchers in transparent wearable electronics and related fields. From the perspective of electrical properties, progress has been made in developing electrode materials with high transparency and conductivity. Although several studies have achieved high transparency of over 90% and high conductivity below 5 Ω sq^{-1} simultaneously, the electrical properties still fall short of those of rigid materials such as bulk metals. The electrical conductivity of transparent electronics significantly impacts the performance of electrical components such as displays, energy devices, and interconnects, so further improvements are needed.

Another concern due to a higher resistance than bulk conducting materials, is the possibility of overheating in operation. Even in the most highly conductive structure, the AgNW percolation network, the high junction resistance can lead to localized overheating due to partial heating. In the most severe scenarios, this can lead to the breakdown of the device and injury to organs and delicate skin. In this regard, studies on thermal management are needed for transparent wearable electronics applications, and techniques such as the development of thermal storage and radiative cooling technology will be used for safe working.

Validation of the process to form the transparent electrode is also a critical step, as it directly affects the performance of the entire device and can reduce its efficiency, lifetime, and reliability. During the formation of the upper conductive layer by vacuum deposition or a solution-based process, these processes can damage the existing lower layer. Achieving scalability and uniformity in these processes also remains a hurdle, requiring further development of processing techniques. In addition, because integrating multiple sensors enables more accurate decision-making in health monitoring and medical applications, the development of more diverse transparent active materials is needed. Although much research has been investigated on the electrical properties of transparent active materials, achieving great functionality for wearable applications remains challenging due to the need for more material options. Exploring a broad range of transparent active materials is becoming more critical for complex and sophisticated features.

In addition, the mechanical properties of highly transparent materials are essential for maintaining conformal attachment on biological tissues, necessitating the development of materials with superior transparency, electrical conductivity, and softness. In this respect, polymer-based materials, such as conducting or semiconducting polymers and their hydrogels, have been proposed as promising alternatives for simultaneously achieving these three characteristics. However, they still have a long way to go. Advances in the mechanical properties of transparent packaging materials, such as modulus, stretchability, and toughness, are also necessary. Soft robotics has emerged as a promising solution for supporting human physical movements and enhancing musculoskeletal abilities, with a high potential for daily life, exercise, and rehabilitation. The rational design of soft robotics has allowed attachment to body parts (e.g., the waist, legs, arms, and hands).[853,930,931] However, previous research has been limited to using translucent materials due to the weak mechanical properties of transparent polymeric materials. As the integration of wearable robotics and vision sensors is verified to improve controllability, wearable robotics need to be replaced by transparent packaging materials with high mechanical performance.

Integration of multiple components is another challenge in developing transparent wearable electronics applications. This requires designing intelligent wearable systems that perform independent functions while avoiding device interference and reducing power consumption. Various commercial chips are

https://doi.org/10.1021/acs.chemrev.3c00139
Chem. Rev. 2023, 123, 9982−10078

currently used for complex system integrations to drive wearable electronics. In fact, surpassing the electrical performance of these rigid chips and batteries is extremely difficult. Therefore, a hybrid system of commercialized chips and flexible electronics, or a simplified system to replace chips, could be a potential solution for future transparent wearable electronics applications.

We recommend reading about the recent advancement of systemized biointerfacing electronics.[618] The combination of multiple sensors, advanced data processing, and wireless communication technology is crucial for a comprehensive personal health monitoring system. The integrated circuit configuration of multiple sensors and commercial chips demonstrated a fully integrated system capable of simultaneous measurement and in situ analysis of body signals. In addition, the future research direction is to go toward wireless a chip-less sensor system that can collect various biosignals by stacking thin materials. In this regard, to read biosignals without multiple chips, a single sensor must be designed to carry out multiple functions called multimodality. Current multimodal sensor systems are composed of stacked sensors that individually sense signals or parallelly arranged sensors. To measure signals more elegantly, reading multiple signals through multiple operating mechanisms of a single sensor can drastically reduce the complexity of the integrated system and allow a high density of sensor arrays in a small area. However, in the case of these sensors, various signals are inevitably coupled, and the introduction of AI is expected to decouple and separate signals into meaningful results precisely. We have been pioneering these single-sensor and deep-learning-integrated systems to measure precise biosignals from the wrist of humans and separate them into a single movement of fingers.[696,748]

For practical use, proactive and in-depth research into the issues that can occur when wearing electronics is necessary. Long-term stability is another critical requirement for wearable and implantable electronics. The materials used in the devices must be robust and have high adhesion in wet physiological conditions as well as dry conditions to ensure stable attachment to the packaging materials and biological tissues. While interfacial adhesive layers have been introduced to prevent unwanted delamination from substrates or tissues, further development is required to ensure robustness and high adhesion to packaging materials and biological tissues. Molecular engineering may offer a solution for developing self-adhesive materials that can maintain adhesion even in wet environments. Biocompatibility is a major factor that determines the approval or regulation of the use and commercialization of wearable and implantable electronics. Various techniques have been attempted, such as the engineering configuration of materials and encapsulation with biocompatible materials. Natural polymers may offer a promising solution due to their similarity with biological tissues. However, their mechanical properties still have room to be improved. Combinations of natural polymers with synthetic polymers will be a consensual direction for biocompatible and green electronic fabrications.

Despite the challenges, transparent and soft wearable electronics offer an ideal research direction for merging wearable electronics with humans to provide extreme physical and mental comfort and blend into everyday life. As AI technology advances, optical information becomes increasingly valuable. For future industries such as the XR industry, the ultimate goal would be to blur the distinction between the virtual world and the real world, and transparent wearable electronics could offer ideal routes for various interesting applications ranging from simple entertainment to medical treatments such as telesurgery and teletherapy by overcoming geographical limitations.

In conclusion, while progress has been made in the development of transparent and wearable electronics, many challenges remain. Further material development, long-term stability, and system integration are critical requirements for the advancement of this field. However, transparent and soft wearable electronics offer a promising research direction for the integration of wearable electronics with humans, blurring the distinction between the virtual world and the real world and offering numerous applications in the future.[3]

AUTHOR INFORMATION

Corresponding Author

Seung Hwan Ko − *Applied Nano and Thermal Science Lab, Department of Mechanical Engineering, Seoul National University, Seoul 08826, Korea; Institute of Engineering Research/Institute of Advanced Machinery and Design (SNU-IAMD), Seoul National University, Seoul 08826, South Korea;* orcid.org/0000-0002-7477-0820; Email: maxko@snu.ac.kr

Authors

Daeyeon Won − *Applied Nano and Thermal Science Lab, Department of Mechanical Engineering, Seoul National University, Seoul 08826, Korea*

Junhyuk Bang − *Applied Nano and Thermal Science Lab, Department of Mechanical Engineering, Seoul National University, Seoul 08826, Korea*

Seok Hwan Choi − *Applied Nano and Thermal Science Lab, Department of Mechanical Engineering, Seoul National University, Seoul 08826, Korea;* orcid.org/0009-0009-4049-562X

Kyung Rok Pyun − *Applied Nano and Thermal Science Lab, Department of Mechanical Engineering, Seoul National University, Seoul 08826, Korea*

Seongmin Jeong − *Applied Nano and Thermal Science Lab, Department of Mechanical Engineering, Seoul National University, Seoul 08826, Korea*

Youngseok Lee − *Applied Nano and Thermal Science Lab, Department of Mechanical Engineering, Seoul National University, Seoul 08826, Korea*

Complete contact information is available at: https://pubs.acs.org/10.1021/acs.chemrev.3c00139

Author Contributions

[§]Daeyeon Won, Junhyuk Bang, and Seok Hwan Choi contributed equally to this work. CRediT: **Daeyeon Won** conceptualization, visualization, writing-original draft, writing-review & editing; **Junhyuk Bang** visualization, writing-original draft, writing-review & editing; **Seok Hwan Choi** software, visualization, writing-original draft, writing-review & editing; **Kyung Rok Pyun** writing-original draft, writing-review & editing; **Seongmin Jeong** writing-original draft, writing-review & editing; **Youngseok Lee** writing-original draft, writing-review & editing; **Seung Hwan Ko** conceptualization, funding acquisition, project administration, resources, supervision, writing-original draft, writing-review & editing.

https://doi.org/10.1021/acs.chemrev.3c00139
Chem. Rev. 2023, 123, 9982−10078

Notes

The authors declare no competing financial interest.

Biographies

Daeyeon Won is a Ph.D. candidate in the Department of Mechanical Engineering at Seoul National University. He earned his B.S. degree in the Department of Mechanical Engineering and Civil Engineering from Korea University. His research focuses on the advanced fabrication processes for soft and stretchable bioelectronics.

Junhyuk Bang is a Ph.D. candidate in the Department of Mechanical Engineering at Seoul National University. He earned his B.S. degree in the Department of Naval Architecture and Ocean Engineering from Seoul National University. His research focuses on the advanced fabrication of soft sensors.

Seok Hwan Choi is a Ph.D. candidate in the Department of Mechanical Engineering at Seoul National University. He earned his B.S. degree in the Department of Mechanical Engineering from Sungkyunkwan University. His research focuses on fabricating soft actuators and electronic devices based on functional polymers.

Kyung Rok Pyun is a Ph.D. candidate in the Department of Mechanical Engineering at Seoul National University. He earned his B.S. degree in the Department of Mechanical Engineering from Sungkyunkwan University and his M.S. degree from Seoul National University. His research focuses on soft sensor systems for wearable electronics.

Seongmin Jeong is a Ph.D. candidate in the Department of Mechanical Engineering at Seoul National University. He earned his B.S. degree in the Department of Mechanical Engineering from Yonsei University and his M.S. degree from Seoul National University. His research focuses on nanofiber-based wearable electronics.

Youngseok Lee is a Ph.D. candidate in the Department of Mechanical Engineering at Seoul National University. He earned his B.S. degree in the Department of Mechanical Engineering from Seoul National University. His research focuses on the fabrication process for bioelectronics.

Seung Hwan Ko is a Professor of Mechanical Engineering and Principal Investigator of the ANTS lab (http://ants.snu.ac.kr) at Seoul National University and Associate Head of the Institute of Engineering Research at Seoul National University. He received his B.S. in the Department of Mechanical Engineering from Yonsei University and his M.S. degree from Seoul National University. Then, he earned his Ph.D. degree in the Department of Mechanical Engineering at the University of California, Berkeley. ANTS lab is actively developing soft materials, fabrication processes, and wearable and bioelectronic devices to address the current bottlenecks of current research fields. The current major research interest of the ANTS lab is to develop soft electronic devices with high transparency for powerful applications by utilizing visual information.

ACKNOWLEDGMENTS

This study was supported by the National Research Foundation of Korea (grant number 2021R1A2B5B03001691).

REFERENCES

(1) Ray, T. R.; Choi, J.; Bandodkar, A. J.; Krishnan, S.; Gutruf, P.; Tian, L.; Ghaffari, R.; Rogers, J. A. Bio-Integrated Wearable Systems: A Comprehensive Review. *Chem. Rev.* **2019**, *119*, 5461−5533.

(2) Ates, H. C.; Nguyen, P. Q.; Gonzalez-Macia, L.; Morales-Narvaez, E.; Guder, F.; Collins, J. J.; Dincer, C. End-to-end design of wearable sensors. *Nat. Rev. Mater.* **2022**, *7*, 887−907.

(3) Pyun, K. R.; Rogers, J. A.; Ko, S. H. Materials and devices for immersive virtual reality. *Nat. Rev. Mater.* **2022**, *7*, 841−843.

(4) Feiner, R.; Dvir, T. Tissue-electronics interfaces: from implantable devices to engineered tissues. *Nat. Rev. Mater.* **2018**, *3*, 17076.

(5) Webb, R. C.; Bonifas, A. P.; Behnaz, A.; Zhang, Y.; Yu, K. J.; Cheng, H.; Shi, M.; Bian, Z.; Liu, Z.; Kim, Y. S.; et al. Ultrathin conformal devices for precise and continuous thermal characterization of human skin. *Nat. Mater.* **2013**, *12*, 938−944.

(6) Kim, R. H.; Bae, M. H.; Kim, D. G.; Cheng, H.; Kim, B. H.; Kim, D. H.; Li, M.; Wu, J.; Du, F.; Kim, H. S.; et al. Stretchable, transparent graphene interconnects for arrays of microscale inorganic light emitting diodes on rubber substrates. *Nano Lett.* **2011**, *11*, 3881−3886.

(7) Jiang, C.; Li, Q.; Fan, S.; Guo, Q.; Bi, S.; Wang, X.; Cao, X.; Liu, Y.; Song, J. Hyaline and stretchable haptic interfaces based on serpentine-shaped silver nanofiber networks. *Nano Energy* **2020**, *73*, 104782.

(8) Lee, P.; Lee, J.; Lee, H.; Yeo, J.; Hong, S.; Nam, K. H.; Lee, D.; Lee, S. S.; Ko, S. H. Highly stretchable and highly conductive metal electrode by very long metal nanowire percolation network. *Adv. Mater.* **2012**, *24*, 3326−3332.

(9) Savagatrup, S.; Chan, E.; Renteria-Garcia, S. M.; Printz, A. D.; Zaretski, A. V.; O'Connor, T. F.; Rodriquez, D.; Valle, E.; Lipomi, D. J. Plasticization of PEDOT:PSS by Common Additives for Mechanically Robust Organic Solar Cells and Wearable Sensors. *Adv. Funct. Mater.* **2015**, *25*, 427−436.

(10) Xu, J.; Wang, S.; Wang, G. N.; Zhu, C.; Luo, S.; Jin, L.; Gu, X.; Chen, S.; Feig, V. R.; To, J. W.; et al. Highly stretchable polymer semiconductor films through the nanoconfinement effect. *Science* **2017**, *355*, 59−64.

(11) Ge, M.; Cao, C.; Biesold, G. M.; Sewell, C. D.; Hao, S. M.; Huang, J.; Zhang, W.; Lai, Y.; Lin, Z. Recent Advances in Silicon-Based Electrodes: From Fundamental Research toward Practical Applications. *Adv. Mater.* **2021**, *33*, 2004577.

(12) Kim, K.; Park, Y. G.; Hyun, B. G.; Choi, M.; Park, J. U. Recent Advances in Transparent Electronics with Stretchable Forms. *Adv. Mater.* **2019**, *31*, 1804690.

(13) Scheideler, W.; Subramanian, V. Printed flexible and transparent electronics: enhancing low-temperature processed metal oxides with 0D and 1D nanomaterials. *Nanotechnology* **2019**, *30*, 272001.

(14) Sahu, D. R.; Lin, S.-Y.; Huang, J.-L. ZnO/Ag/ZnO multilayer films for the application of a very low resistance transparent electrode. *Appl. Surf. Sci.* **2006**, *252*, 7509−7514.

(15) Dhar, A.; Alford, T. L. High quality transparent TiO2/Ag/TiO2 composite electrode films deposited on flexible substrate at room temperature by sputtering. *APL Mater.* **2013**, *1*, 012102.

(16) Hong, K.; Kim, K.; Kim, S.; Lee, I.; Cho, H.; Yoo, S.; Choi, H. W.; Lee, N.-Y.; Tak, Y.-H.; Lee, J.-L. Optical properties of WO3/Ag/WO3 multilayer as transparent cathode in top-emitting organic light emitting diodes. *J. Phys. Chem. C* **2011**, *115*, 3453−3459.

(17) Choi, K. H.; Kim, J. Y.; Lee, Y. S.; Kim, H. J. ITO/Ag/ITO multilayer films for the application of a very low resistance transparent electrode. *Thin Solid Films* **1999**, *341*, 152−155.

(18) Kao, P.-C.; Hsieh, C.-J.; Chen, Z.-H.; Chen, S.-H. Improvement of MoO3/Ag/MoO3 multilayer transparent electrodes for organic solar cells by using UV−ozone treated MoO3 layer. *Sol. Energy Mater. Sol. Cells* **2018**, *186*, 131−141.

(19) Lee, H. J.; Kang, J. W.; Hong, S. H.; Song, S. H.; Park, S. J. MgxZn1-xO/Ag/MgxZn1-xO Multilayers As High-Performance Transparent Conductive Electrodes. *ACS Appl. Mater. Interfaces* **2016**, *8*, 1565−1570.

(20) Sahu, D. R.; Lin, S.-Y.; Huang, J.-L. Investigation of conductive and transparent Al-doped ZnO/Ag/Al-doped ZnO multilayer coatings by electron beam evaporation. *Thin Solid Films* **2008**, *516*, 4728−4732.

https://doi.org/10.1021/acs.chemrev.3c00139
Chem. Rev. 2023, 123, 9982−10078

(21) Logeeswaran, V. J.; Kobayashi, N. P.; Islam, M. S.; Wu, W.; Chaturvedi, P.; Fang, N. X.; Wang, S. Y.; Williams, R. S. Ultrasmooth silver thin films deposited with a germanium nucleation layer. *Nano Lett.* **2009**, *9*, 178−182.
(22) Wróbel, P.; Stefaniuk, T.; Trzcinski, M.; Wronkowska, A. A.; Wronkowski, A.; Szoplik, T. Ge wetting layer increases ohmic plasmon losses in Ag film due to segregation. *ACS Appl. Mater. Interfaces* **2015**, *7*, 8999−9005.
(23) Hautcoeur, J.; Castel, X.; Colombel, F.; Benzerga, R.; Himdi, M.; Legeay, G.; Motta-Cruz, E. Transparency and electrical properties of meshed metal films. *Thin Solid Films* **2011**, *519*, 3851−3858.
(24) Im, J. H.; Kang, K.-T.; Lee, S. H.; Hwang, J. Y.; Kang, H.; Cho, K. H. Bulk-like Al/Ag bilayer film due to suppression of surface plasmon resonance for high transparent organic light emitting diodes. *Org. Electron.* **2016**, *33*, 116−120.
(25) Hu, L.; Kim, H. S.; Lee, J. Y.; Peumans, P.; Cui, Y. Scalable coating and properties of transparent, flexible, silver nanowire electrodes. *ACS Nano* **2010**, *4*, 2955−2963.
(26) Layani, M.; Magdassi, S. Flexible transparent conductive coatings by combining self-assembly with sintering of silver nanoparticles performed at room temperature. *J. Mater. Chem.* **2011**, *21*, 15378−15382.
(27) Hong, S.; Yeo, J.; Kim, G.; Kim, D.; Lee, H.; Kwon, J.; Lee, H.; Lee, P.; Ko, S. H. Nonvacuum, maskless fabrication of a flexible metal grid transparent conductor by low-temperature selective laser sintering of nanoparticle ink. *ACS Nano* **2013**, *7*, 5024−5031.
(28) Han, S.; Hong, S.; Ham, J.; Yeo, J.; Lee, J.; Kang, B.; Lee, P.; Kwon, J.; Lee, S. S.; Yang, M. Y.; et al. Fast plasmonic laser nanowelding for a Cu-nanowire percolation network for flexible transparent conductors and stretchable electronics. *Adv. Mater.* **2014**, *26*, 5808−5814.
(29) Chu, H. C.; Chang, Y. C.; Lin, Y.; Chang, S. H.; Chang, W. C.; Li, G. A.; Tuan, H. Y. Spray-Deposited Large-Area Copper Nanowire Transparent Conductive Electrodes and Their Uses for Touch Screen Applications. *ACS Appl. Mater. Interfaces* **2016**, *8*, 13009−13017.
(30) Kwon, J.; Cho, H.; Suh, Y. D.; Lee, J.; Lee, H.; Jung, J.; Kim, D.; Lee, D.; Hong, S.; Ko, S. H. Flexible and Transparent Cu Electronics by Low-Temperature Acid-Assisted Laser Processing of Cu Nanoparticles. *Adv. Mater. Technol.* **2017**, *2*, 1600222.
(31) Jung, J.; Cho, H.; Choi, S. H.; Kim, D.; Kwon, J.; Shin, J.; Hong, S.; Kim, H.; Yoon, Y.; Lee, J.; et al. Moire-Free Imperceptible and Flexible Random Metal Grid Electrodes with Large Figure-of-Merit by Photonic Sintering Control of Copper Nanoparticles. *ACS Appl. Mater. Interfaces* **2019**, *11*, 15773−15780.
(32) Gong, S.; Zhao, Y.; Yap, L. W.; Shi, Q.; Wang, Y.; Bay, J. A. P. B.; Lai, D. T. H.; Uddin, H.; Cheng, W. Fabrication of Highly Transparent and Flexible NanoMesh Electrode via Self-assembly of Ultrathin Gold Nanowires. *Adv. Electron. Mater.* **2016**, *2*, 1600121.
(33) Kister, T.; Maurer, J. H. M.; Gonzalez-Garcia, L.; Kraus, T. Ligand-Dependent Nanoparticle Assembly and Its Impact on the Printing of Transparent Electrodes. *ACS Appl. Mater. Interfaces* **2018**, *10*, 6079−6083.
(34) Novoselov, K. S.; Geim, A. K.; Morozov, S. V.; Jiang, D.; Zhang, Y.; Dubonos, S. V.; Grigorieva, I. V.; Firsov, A. A. Electric field effect in atomically thin carbon films. *Science* **2004**, *306*, 666−669.
(35) Li, X.; Cai, W.; An, J.; Kim, S.; Nah, J.; Yang, D.; Piner, R.; Velamakanni, A.; Jung, I.; Tutuc, E.; et al. Large-area synthesis of high-quality and uniform graphene films on copper foils. *Science* **2009**, *324*, 1312−1314.
(36) Bi, H.; Huang, F.; Liang, J.; Xie, X.; Jiang, M. Transparent conductive graphene films synthesized by ambient pressure chemical vapor deposition used as the front electrode of CdTe solar cells. *Adv. Mater.* **2011**, *23*, 3202−3206.
(37) Wang, S. M.; Pei, Y. H.; Wang, X.; Wang, H.; Meng, Q. N.; Tian, H. W.; Zheng, X. L.; Zheng, W. T.; Liu, Y. C. Synthesis of graphene on a polycrystalline Co film by radio-frequency plasma-enhanced chemical vapour deposition. *J. Phys. D: Appl. Phys.* **2010**, *43*, 455402.
(38) Zhang, Q.; Zhou, W.; Xia, X.; Li, K.; Zhang, N.; Wang, Y.; Xiao, Z.; Fan, Q.; Kauppinen, E. I.; Xie, S. Transparent and Freestanding Single-Walled Carbon Nanotube Films Synthesized Directly and Continuously via a Blown Aerosol Technique. *Adv. Mater.* **2020**, *32*, 2004277.
(39) Nasibulin, A. G.; Kaskela, A.; Mustonen, K.; Anisimov, A. S.; Ruiz, V.; Kivisto, S.; Rackauskas, S.; Timmermans, M. Y.; Pudas, M.; Aitchison, B.; et al. Multifunctional free-standing single-walled carbon nanotube films. *ACS Nano* **2011**, *5*, 3214−3221.
(40) Jung, D.; Lee, K. H.; Kim, D.; Burk, D.; Overzet, L. J.; Lee, G. S. Highly Conductive Flexible Multi-Walled Carbon Nanotube Sheet Films for Transparent Touch Screen. *Jpn. J. Appl. Phys.* **2013**, *52*, 03BC03.
(41) Jang, H.-S.; Jeon, S. K.; Nahm, S. H. The manufacture of a transparent film heater by spinning multi-walled carbon nanotubes. *Carbon* **2011**, *49*, 111−116.
(42) Wang, X.; Zhi, L.; Mullen, K. Transparent, conductive graphene electrodes for dye-sensitized solar cells. *Nano Lett.* **2008**, *8*, 323−327.
(43) Geng, J.; Liu, L.; Yang, S. B.; Youn, S.-C.; Kim, D. W.; Lee, J.-S.; Choi, J.-K.; Jung, H.-T. A Simple Approach for Preparing Transparent Conductive Graphene Films Using the Controlled Chemical Reduction of Exfoliated Graphene Oxide in an Aqueous Suspension. *J. Phys. Chem. C* **2010**, *114*, 14433−14440.
(44) Li, Z.; Ye, B.; Hu, X.; Ma, X.; Zhang, X.; Deng, Y. Facile electropolymerized-PANI as counter electrode for low cost dye-sensitized solar cell. *Electrochem. Commun.* **2009**, *11*, 1768−1771.
(45) Tai, Q.; Chen, B.; Guo, F.; Xu, S.; Hu, H.; Sebo, B.; Zhao, X. Z. In situ prepared transparent polyaniline electrode and its application in bifacial dye-sensitized solar cells. *ACS Nano* **2011**, *5*, 3795−3799.
(46) Pei, Q.; Zuccarello, G.; Ahlskog, M.; Inganäs, O. Electrochromic and highly stable poly(3,4-ethylenedioxythiophene) switches between opaque blue-black and transparent sky blue. *Polymer* **1994**, *35*, 1347−1351.
(47) Yan, J.; Sun, C.; Tan, F.; Hu, X.; Chen, P.; Qu, S.; Zhou, S.; Xu, J. Electropolymerized poly(3,4-ethylenedioxythiophene):poly(styrene sulfonate) (PEDOT:PSS) film on ITO glass and its application in photovoltaic device. *Sol. Energy Mater. Sol. Cells* **2010**, *94*, 390−394.
(48) Kaiser, M. R.; Han, Z.; Wang, J. Electro-polymerized polypyrrole film for fabrication of flexible and slurry-free polypyrrole-sulfur-polypyrrole sandwich electrode for the lithium-sulfur battery. *J. Power Sources* **2019**, *437*, 226925.
(49) Bu, C.; Tai, Q.; Liu, Y.; Guo, S.; Zhao, X. A transparent and stable polypyrrole counter electrode for dye-sensitized solar cell. *J. Power Sources* **2013**, *221*, 78−83.
(50) Bi, Y. G.; Liu, Y. F.; Zhang, X. L.; Yin, D.; Wang, W. Q.; Feng, J.; Sun, H. B. Ultrathin Metal Films as the Transparent Electrode in ITO-Free Organic Optoelectronic Devices. *Adv. Opt. Mater.* **2019**, *7*, 1800778.
(51) Lu, X.; Zhang, Y.; Zheng, Z. Metal-Based Flexible Transparent Electrodes: Challenges and Recent Advances. *Adv. Electron. Mater.* **2021**, *7*, 2001121.
(52) Cetinkaya, C.; Cokduygulular, E.; Guzelcimen, F.; Kinaci, B. Functional optical design of thickness-optimized transparent conductive dielectric-metal-dielectric plasmonic structure. *Sci. Rep.* **2022**, *12*, 8822.
(53) Powell, C. J.; Jablonski, A. Evaluation of Calculated and Measured Electron Inelastic Mean Free Paths Near Solid Surfaces. *J. Phys. Chem. Ref. Data* **1999**, *28*, 19−62.
(54) Gall, D. Electron mean free path in elemental metals. *J. Appl. Phys.* **2016**, *119*, 085101.
(55) Luo, E. Z.; Heun, S.; Kennedy, M.; Wollschlager, J.; Henzler, M. Surface roughness and conductivity of thin Ag films. *Phys. Rev. B: Condens. Matter* **1994**, *49*, 4858−4865.
(56) Rossnagel, S. M. Thin film deposition with physical vapor deposition and related technologies. *J. Vac. Sci. Technol., A* **2003**, *21*, S74−S87.
(57) Yun, J. Ultrathin Metal films for Transparent Electrodes of Flexible Optoelectronic Devices. *Adv. Funct. Mater.* **2017**, *27*, 1606641.

https://doi.org/10.1021/acs.chemrev.3c00139
Chem. Rev. 2023, 123, 9982−10078

(58) Kaiser, N. Review of the fundamentals of thin-film growth. *Appl. Opt.* **2002**, *41*, 3053−3060.
(59) Bauer, E. Phänomenologische theorie der kristallabscheidung an oberflächen. i, Z. *Kristallogr.−Cryst. Mater.* **1958**, *110*, 372−394.
(60) Sangiorgi, R.; Muolo, M. L.; Chatain, D.; Eustathopoulos, N. Wettability and Work of Adhesion of Nonreactive Liquid Metals on Silica. *J. Am. Ceram. Soc.* **1988**, *71*, 742−748.
(61) Campbell, C. T. Ultrathin metal films and particles on oxide surfaces: structural, electronic and chemisorptive properties. *Surf. Sci. Rep.* **1997**, *27*, 1−111.
(62) Yang, X.; Gao, P.; Yang, Z.; Zhu, J.; Huang, F.; Ye, J. Optimizing ultrathin Ag films for high performance oxide-metal-oxide flexible transparent electrodes through surface energy modulation and template-stripping procedures. *Sci. Rep.* **2017**, *7*, 44576.
(63) Han, H.; Theodore, N. D.; Alford, T. L. Improved conductivity and mechanism of carrier transport in zinc oxide with embedded silver layer. *J. Appl. Phys.* **2008**, *103*, 013708.
(64) Choi, H. W.; Theodore, N. D.; Alford, T. L. ZnO−Ag−MoO3 transparent composite electrode for ITO-free, PEDOT: PSS-free bulk-heterojunction organic solar cells. *Sol. Energy Mater. Sol. Cells* **2013**, *117*, 446−450.
(65) Kim, J. H.; Lee, H.-K.; Na, J.-Y.; Kim, S.-K.; Yoo, Y.-Z.; Seong, T.-Y. Dependence of optical and electrical properties on Ag thickness in TiO2/Ag/TiO2 multilayer films for photovoltaic devices. *Ceram. Int.* **2015**, *41*, 8059−8063.
(66) Dima, I.; Popescu, B.; Iova, F.; Popescu, G. Influence of the silver layer on the optical properties of the TiO2/Ag/TiO2 multilayer. *Thin Solid Films* **1991**, *200*, 11−18.
(67) Kim, K.; Hong, K.; Koo, B.; Lee, I.; Lee, J.-L. Transparency controllable silver-based electrode for flexible optoelectronics. *Appl. Phys. Lett.* **2013**, *102*, 081118.
(68) Guillén, C.; Herrero, J. ITO/metal/ITO multilayer structures based on Ag and Cu metal films for high-performance transparent electrodes. *Sol. Energy Mater. Sol. Cells* **2008**, *92*, 938−941.
(69) Bender, M.; Seelig, W.; Daube, C.; Frankenberger, H.; Ocker, B.; Stollenwerk, J. Dependence of film composition and thicknesses on optical and electrical properties of ITO−metal−ITO multilayers. *Thin Solid Films* **1998**, *326*, 67−71.
(70) Abachi, T.; Cattin, L.; Louarn, G.; Lare, Y.; Bou, A.; Makha, M.; Torchio, P.; Fleury, M.; Morsli, M.; Addou, M.; et al. Highly flexible, conductive and transparent MoO 3 /Ag/MoO 3 multilayer electrode for organic photovoltaic cells. *Thin Solid Films* **2013**, *545*, 438−444.
(71) Lopéz, I. P.; Cattin, L.; Nguyen, D. T.; Morsli, M.; Bernède, J. C. Dielectric/metal/dielectric structures using copper as metal and MoO3 as dielectric for use as transparent electrode. *Thin Solid Films* **2012**, *520*, 6419−6423.
(72) Cho, H.; Yun, C.; Park, J.-W.; Yoo, S. Highly flexible organic light-emitting diodes based on ZnS/Ag/WO3 multilayer transparent electrodes. *Org. Electron.* **2009**, *10*, 1163−1169.
(73) Kermani, H.; Fallah, H. R.; Hajimahmoodzadeh, M. Design and fabrication of nanometric ZnS/Ag/MoO3 transparent conductive electrode and investigating the effect of annealing process on its characteristics. *Physica E* **2013**, *47*, 303−308.
(74) Dhar, A.; Alford, T. L. Optimization of Nb2O5/Ag/Nb2O5 multilayers as transparent composite electrode on flexible substrate with high figure of merit. *J. Appl. Phys.* **2012**, *112*, 103113.
(75) Chen, D.; Fan, G.; Zhu, W.; Yang, H.; Xi, H.; He, F.; Lin, Z.; Zhang, J.; Zhang, C.; Hao, Y. Highly efficient bifacial CsPbIBr2 solar cells with a TeO2/Ag transparent electrode and unsymmetrical carrier transport behavior. *Dalton Trans.* **2020**, *49*, 6012−6019.
(76) Martinez-Cercos, D.; Paulillo, B.; Maniyara, R. A.; Rezikyan, A.; Bhattacharyya, I.; Mazumder, P.; Pruneri, V. Ultrathin Metals on a Transparent Seed and Application to Infrared Reflectors. *ACS Appl. Mater. Interfaces* **2021**, *13*, 46990−46997.
(77) Ko, R. H.; Khalatpour, A.; Clark, J. K. D.; Kherani, N. P. Ultrasmooth ultrathin Ag films by AlN seeding and Ar/N2 sputtering for transparent conductive and heating applications. *APL Mater.* **2018**, *6*, 121112.
(78) Formica, N.; Mantilla-Perez, P.; Ghosh, D. S.; Janner, D.; Chen, T. L.; Huang, M.; Garner, S.; Martorell, J.; Pruneri, V. An indium tin oxide-free polymer solar cell on flexible glass. *ACS Appl. Mater. Interfaces* **2015**, *7*, 4541−4548.
(79) Ji, C.; Liu, D.; Zhang, C.; Jay Guo, L. Ultrathin-metal-film-based transparent electrodes with relative transmittance surpassing 100. *Nat. Commun.* **2020**, *11*, 3367.
(80) Song, J. K.; Son, D.; Kim, J.; Yoo, Y. J.; Lee, G. J.; Wang, L.; Choi, M. K.; Yang, J.; Lee, M.; Do, K.; et al. Wearable Force Touch Sensor Array Using a Flexible and Transparent Electrode. *Adv. Funct. Mater.* **2017**, *27*, 1605286.
(81) Jeong, E.; Zhao, G.; Yu, S. M.; Lee, S.-G.; Bae, J.-S.; Park, J.; Rha, J.; Lee, G.-H.; Yun, J. Minimizing optical loss in ultrathin Ag films based on Ge wetting layer: Insights on Ge-mediated Ag growth. *Appl. Surf. Sci.* **2020**, *528*, 146989.
(82) Hautcoeur, J.; Colombel, F.; Castel, X.; Himdi, M.; Motta Cruz, E. Optically transparent monopole antenna with high radiation efficiency manufactured with silver grid layer (AgGL). *Electron. Lett.* **2009**, *45*, 1014−1015.
(83) Fukuda, K.; Lim, S. H. N.; Anders, A. Coalescence of magnetron-sputtered silver islands affected by transition metal seeding (Ni, Cr, Nb, Zr, Mo, W, Ta) and other parameters. *Thin Solid Films* **2008**, *516*, 4546−4552.
(84) Stefaniuk, T.; Wrobel, P.; Trautman, P.; Szoplik, T. Ultrasmooth metal nanolayers for plasmonic applications: surface roughness and specific resistivity. *Appl. Opt.* **2014**, *53*, B237−B241.
(85) Hoogvliet, J. C.; van Bennekom, W. P. Gold thin-film electrodes: an EQCM study of the influence of chromium and titanium adhesion layers on the response. *Electrochim. Acta* **2001**, *47*, 599−611.
(86) Todeschini, M.; Bastos da Silva Fanta, A.; Jensen, F.; Wagner, J. B.; Han, A. Influence of Ti and Cr Adhesion Layers on Ultrathin Au Films. *ACS Appl. Mater. Interfaces* **2017**, *9*, 37374−37385.
(87) Schubert, S.; Meiss, J.; Müller-Meskamp, L.; Leo, K. Improvement of Transparent Metal Top Electrodes for Organic Solar Cells by Introducing a High Surface Energy Seed Layer. *Adv. Energy Mater.* **2013**, *3*, 438−443.
(88) Formica, N.; Ghosh, D. S.; Carrilero, A.; Chen, T. L.; Simpson, R. E.; Pruneri, V. Ultrastable and atomically smooth ultrathin silver films grown on a copper seed layer. *ACS Appl. Mater. Interfaces* **2013**, *5*, 3048−3053.
(89) Faraday, M. X. The Bakerian Lecture.—Experimental relations of gold (and other metals) to light. *Philos. Trans. R. Soc. London, Ser. A* **1857**, *14*, 512−539.
(90) Turkevich, J.; Stevenson, P. C.; Hillier, J. A study of the nucleation and growth processes in the synthesis of colloidal gold. *Discuss. Faraday Soc.* **1951**, *11*, 55−75.
(91) Frens, G. Controlled nucleation for the regulation of the particle size in monodisperse gold suspensions. *Nature physical science* **1973**, *241*, 20−22.
(92) Piella, J.; Bastús, N. G.; Puntes, V. Size-Controlled Synthesis of Sub-10-nanometer Citrate-Stabilized Gold Nanoparticles and Related Optical Properties. *Chem. Mater.* **2016**, *28*, 1066−1075.
(93) Aslan, K.; Pérez-Luna, V. H. Surface Modification of Colloidal Gold by Chemisorption of Alkanethiols in the Presence of a Nonionic Surfactant. *Langmuir* **2002**, *18*, 6059−6065.
(94) Lin, S.-Y.; Tsai, Y.-T.; Chen, C.-C.; Lin, C.-M.; Chen, C.-h. Two-Step Functionalization of Neutral and Positively Charged Thiols onto Citrate-Stabilized Au Nanoparticles. *J. Phys. Chem. B* **2004**, *108*, 2134−2139.
(95) Lee, P. C.; Meisel, D. Adsorption and surface-enhanced Raman of dyes on silver and gold sols. *J. Phys. Chem.* **1982**, *86*, 3391−3395.
(96) Steinigeweg, D.; Schlucker, S. Monodispersity and size control in the synthesis of 20−100 nm quasi-spherical silver nanoparticles by citrate and ascorbic acid reduction in glycerol-water mixtures. *Chem. Commun.* **2012**, *48*, 8682−8684.
(97) Dadosh, T. Synthesis of uniform silver nanoparticles with a controllable size. *Mater. Lett.* **2009**, *63*, 2236−2238.

https://doi.org/10.1021/acs.chemrev.3c00139
Chem. Rev. 2023, 123, 9982−10078

(98) Velikov, K. P.; Zegers, G. E.; van Blaaderen, A. Synthesis and Characterization of Large Colloidal Silver Particles. *Langmuir* **2003**, *19*, 1384−1389.
(99) Creighton, J. A.; Blatchford, C. G.; Albrecht, M. G. Plasma resonance enhancement of Raman scattering by pyridine adsorbed on silver or gold sol particles of size comparable to the excitation wavelength. *J. Chem. Soc., Faraday Trans. 2* **1979**, *75*, 790−798.
(100) Kurihara, L. K.; Chow, G. M.; Schoen, P. E. Nanocrystalline metallic powders and films produced by the polyol method. *Nanostruct. Mater.* **1995**, *5*, 607−613.
(101) Jacob, J. A.; Kapoor, S.; Biswas, N.; Mukherjee, T. Size tunable synthesis of silver nanoparticles in water−ethylene glycol mixtures. *Colloids Surf., A* **2007**, *301*, 329−334.
(102) Yin, Y.; Li, Z.-Y.; Zhong, Z.; Gates, B.; Xia, Y.; Venkateswaran, S. Synthesis and characterization of stable aqueous dispersions of silver nanoparticles through the Tollens process. *J. Mater. Chem.* **2002**, *12*, 522−527.
(103) Pastoriza-Santos, I.; Liz-Marzán, L. M. Binary cooperative complementary nanoscale interfacial materials. Reduction of silver nanoparticles in DMF. Formation of monolayers and stable colloids. *Pure Appl. Chem.* **2000**, *72*, 83−90 83.
(104) Pastoriza-Santos, I.; Liz-Marzán, L. M. Formation of PVP-Protected Metal Nanoparticles in DMF. *Langmuir* **2002**, *18*, 2888−2894.
(105) Kyrychenko, A.; Pasko, D. A.; Kalugin, O. N. Poly(vinyl alcohol) as a water protecting agent for silver nanoparticles: the role of polymer size and structure. *Phys. Chem. Chem. Phys.* **2017**, *19*, 8742−8756.
(106) Pencheva, D.; Bryaskova, R.; Kantardjiev, T. Polyvinyl alcohol/silver nanoparticles (PVA/AgNps) as a model for testing the biological activity of hybrid materials with included silver nanoparticles. *Mater. Sci. Eng., C* **2012**, *32*, 2048−2051.
(107) Kim, D.; Jeong, S.; Moon, J. Synthesis of silver nanoparticles using the polyol process and the influence of precursor injection. *Nanotechnology* **2006**, *17*, 4019−4024.
(108) Luo, C.; Zhang, Y.; Zeng, X.; Zeng, Y.; Wang, Y. The role of poly(ethylene glycol) in the formation of silver nanoparticles. *J. Colloid Interface Sci.* **2005**, *288*, 444−448.
(109) Shameli, K.; Bin Ahmad, M.; Jazayeri, S. D.; Sedaghat, S.; Shabanzadeh, P.; Jahangirian, H.; Mahdavi, M.; Abdollahi, Y. Synthesis and characterization of polyethylene glycol mediated silver nanoparticles by the green method. *Int. J. Mol. Sci.* **2012**, *13*, 6639−6650.
(110) Mott, D.; Galkowski, J.; Wang, L.; Luo, J.; Zhong, C. J. Synthesis of size-controlled and shaped copper nanoparticles. *Langmuir* **2007**, *23*, 5740−5745.
(111) Song, X.; Sun, S.; Zhang, W.; Yin, Z. A method for the synthesis of spherical copper nanoparticles in the organic phase. *J. Colloid Interface Sci.* **2004**, *273*, 463−469.
(112) Songping, W.; Shuyuan, M. Preparation of micron size copper powder with chemical reduction method. *Mater. Lett.* **2006**, *60*, 2438−2442.
(113) Chang, S. J.; Tung, C. A.; Chen, B. W.; Chou, Y. C.; Li, C. C. Synthesis of non-oxidative copper nanoparticles. *RSC Adv.* **2013**, *3*, 24005−24008.
(114) Wu, S. Preparation of fine copper powder using ascorbic acid as reducing agent and its application in MLCC. *Mater. Lett.* **2007**, *61*, 1125−1129.
(115) Xiong, J.; Wang, Y.; Xue, Q.; Wu, X. Synthesis of highly stable dispersions of nanosized copper particles using l-ascorbic acid. *Green Chem.* **2011**, *13*, 900−904.
(116) Chen, J. P.; Lim, L. L. Key factors in chemical reduction by hydrazine for recovery of precious metals. *Chemosphere* **2002**, *49*, 363−370.
(117) Saikova, S. V.; Vorob'ev, S. A.; Nikolaeva, R. B.; Mikhlin, Y. L. Conditions for the formation of copper nanoparticles by reduction of copper(II) ions with hydrazine hydrate solutions. *Russ. J. Gen. Chem.* **2010**, *80*, 1122−1127.
(118) Shenoy, U. S.; Shetty, A. N. A Simple Solution Phase Synthesis of Copper Nanofluid Using Single-step Glucose Reduction Method. *Synth. React. Inorg. Met.-Org. Chem.* **2013**, *43*, 343−348.
(119) Li, S.; Chen, Y.; Huang, L.; Pan, D. Large-scale synthesis of well-dispersed copper nanowires in an electric pressure cooker and their application in transparent and conductive networks. *Inorg. Chem.* **2014**, *53*, 4440−4444.
(120) Park, B. K.; Jeong, S.; Kim, D.; Moon, J.; Lim, S.; Kim, J. S. Synthesis and size control of monodisperse copper nanoparticles by polyol method. *J. Colloid Interface Sci.* **2007**, *311*, 417−424.
(121) Lee, Y.-J.; Kim, K.; Shin, I.-S.; Shin, K. S. Antioxidative metallic copper nanoparticles prepared by modified polyol method and their catalytic activities. *J. Nanopart. Res.* **2020**, *22*, 8.
(122) Zhang, W. C.; Wu, X. L.; Chen, H. T.; Gao, Y. J.; Zhu, J.; Huang, G. S.; Chu, P. K. Self-organized formation of silver nanowires, nanocubes and bipyramids via a solvothermal method. *Acta Mater.* **2008**, *56*, 2508−2513.
(123) Jiang, X.; Xie, Y.; Lu, J.; Zhu, L.; He, W.; Qian, Y. Oleate vesicle template route to silver nanowires. *J. Mater. Chem.* **2001**, *11*, 1775−1777.
(124) Tung, H.-T.; Chen, I.-G.; Song, J.-M.; Yen, C.-W. Thermally assisted photoreduction of vertical silver nanowires. *J. Mater. Chem.* **2009**, *19*, 2386−2391.
(125) Xu, X. J.; Fei, G. T.; Wang, X. W.; Jin, Z.; Yu, W. H.; Zhang, L. D. Synthetic control of large-area, ordered silver nanowires with different diameters. *Mater. Lett.* **2007**, *61*, 19−22.
(126) Sun, Y.; Gates, B.; Mayers, B.; Xia, Y. Crystalline Silver Nanowires by Soft Solution Processing. *Nano Lett.* **2002**, *2*, 165−168.
(127) Sun, Y.; Xia, Y. Large-Scale Synthesis of Uniform Silver Nanowires Through a Soft, Self-Seeding, Polyol Process. *Adv. Mater.* **2002**, *14*, 833−837.
(128) Sun, Y.; Yin, Y.; Mayers, B. T.; Herricks, T.; Xia, Y. Uniform Silver Nanowires Synthesis by Reducing AgNO3 with Ethylene Glycol in the Presence of Seeds and Poly(Vinyl Pyrrolidone). *Chem. Mater.* **2002**, *14*, 4736−4745.
(129) Lee, J. H.; Lee, P.; Lee, D.; Lee, S. S.; Ko, S. H. Large-Scale Synthesis and Characterization of Very Long Silver Nanowires via Successive Multistep Growth. *Cryst. Growth Des.* **2012**, *12*, 5598−5605.
(130) Moon, H.; Won, P.; Lee, J.; Ko, S. H. Low-haze, annealing-free, very long Ag nanowire synthesis and its application in a flexible transparent touch panel. *Nanotechnology* **2016**, *27*, 295201.
(131) Sun, Y.; Mayers, B.; Herricks, T.; Xia, Y. Polyol Synthesis of Uniform Silver Nanowires: A Plausible Growth Mechanism and the Supporting Evidence. *Nano Lett.* **2003**, *3*, 955−960.
(132) Ma, J.; Zhan, M. Rapid production of silver nanowires based on high concentration of AgNO3 precursor and use of FeCl3 as reaction promoter. *RSC Adv.* **2014**, *4*, 21060−21071.
(133) Lin, J.-Y.; Hsueh, Y.-L.; Huang, J.-J.; Wu, J.-R. Effect of silver nitrate concentration of silver nanowires synthesized using a polyol method and their application as transparent conductive films. *Thin Solid Films* **2015**, *584*, 243−247.
(134) Yang, H.; Chen, T.; Wang, H.; Bai, S.; Guo, X. One-pot rapid synthesis of high aspect ratio silver nanowires for transparent conductive electrodes. *Mater. Res. Bull.* **2018**, *102*, 79−85.
(135) Jeevika, A.; Ravi Shankaran, D. Seed-free synthesis of 1D silver nanowires ink using clove oil (Syzygium Aromaticum) at room temperature. *J. Colloid Interface Sci.* **2015**, *458*, 155−159.
(136) Luo, L. B.; Yu, S. H.; Qian, H. S.; Zhou, T. Large-scale fabrication of flexible silver/cross-linked poly(vinyl alcohol) coaxial nanocables by a facile solution approach. *J. Am. Chem. Soc.* **2005**, *127*, 2822−2823.
(137) Chang, Y.; Lye, M. L.; Zeng, H. C. Large-scale synthesis of high-quality ultralong copper nanowires. *Langmuir* **2005**, *21*, 3746−3748.
(138) Rathmell, A. R.; Bergin, S. M.; Hua, Y. L.; Li, Z. Y.; Wiley, B. J. The growth mechanism of copper nanowires and their properties in flexible, transparent conducting films. *Adv. Mater.* **2010**, *22*, 3558−3563.

https://doi.org/10.1021/acs.chemrev.3c00139
Chem. Rev. 2023, 123, 9982−10078

(139) Jin, M.; He, G.; Zhang, H.; Zeng, J.; Xie, Z.; Xia, Y. Shape-controlled synthesis of copper nanocrystals in an aqueous solution with glucose as a reducing agent and hexadecylamine as a capping agent. *Angew. Chem., Int. Ed.* **2011**, *50*, 10560−10564.
(140) Cui, F.; Dou, L.; Yang, Q.; Yu, Y.; Niu, Z.; Sun, Y.; Liu, H.; Dehestani, A.; Schierle-Arndt, K.; Yang, P. Benzoin Radicals as Reducing Agent for Synthesizing Ultrathin Copper Nanowires. *J. Am. Chem. Soc.* **2017**, *139*, 3027−3032.
(141) Yokoyama, S.; Motomiya, K.; Jeyadevan, B.; Tohji, K. Environmentally friendly synthesis and formation mechanism of copper nanowires with controlled aspect ratios from aqueous solution with ascorbic acid. *J. Colloid Interface Sci.* **2018**, *531*, 109−118.
(142) Shi, Y.; Li, H.; Chen, L.; Huang, X. Obtaining ultra-long copper nanowires via a hydrothermal process. *Sci. Technol. Adv. Mater.* **2005**, *6*, 761−765.
(143) Zhang, D.; Wang, R.; Wen, M.; Weng, D.; Cui, X.; Sun, J.; Li, H.; Lu, Y. Synthesis of ultralong copper nanowires for high-performance transparent electrodes. *J. Am. Chem. Soc.* **2012**, *134*, 14283−14286.
(144) Seo, M.; Kim, J. S.; Lee, J. G.; Kim, S. B.; Koo, S. M. The effect of silver particle size and organic stabilizers on the conductivity of silver particulate films in thermal sintering processes. *Thin Solid Films* **2016**, *616*, 366−374.
(145) Ding, J.; Liu, J.; Tian, Q.; Wu, Z.; Yao, W.; Dai, Z.; Liu, L.; Wu, W. Preparing of Highly Conductive Patterns on Flexible Substrates by Screen Printing of Silver Nanoparticles with Different Size Distribution. *Nanoscale Res. Lett.* **2016**, *11*, 412.
(146) Mo, L.; Guo, Z.; Yang, L.; Zhang, Q.; Fang, Y.; Xin, Z.; Chen, Z.; Hu, K.; Han, L.; Li, L. Silver Nanoparticles Based Ink with Moderate Sintering in Flexible and Printed Electronics. *Int. J. Mol. Sci.* **2019**, *20*, 2124.
(147) Langley, D.; Giusti, G.; Mayousse, C.; Celle, C.; Bellet, D.; Simonato, J. P. Flexible transparent conductive materials based on silver nanowire networks: a review. *Nanotechnology* **2013**, *24*, 452001.
(148) Khanarian, G.; Joo, J.; Liu, X. Q.; Eastman, P.; Werner, D.; O'Connell, K.; Trefonas, P. The optical and electrical properties of silver nanowire mesh films. *J. Appl. Phys.* **2013**, *114*, 024302.
(149) Niu, Z.; Cui, F.; Kuttner, E.; Xie, C.; Chen, H.; Sun, Y.; Dehestani, A.; Schierle-Arndt, K.; Yang, P. Synthesis of Silver Nanowires with Reduced Diameters Using Benzoin-Derived Radicals to Make Transparent Conductors with High Transparency and Low Haze. *Nano Lett.* **2018**, *18*, 5329−5334.
(150) De, S.; Higgins, T. M.; Lyons, P. E.; Doherty, E. M.; Nirmalraj, P. N.; Blau, W. J.; Boland, J. J.; Coleman, J. N. Silver Nanowire Networks as Flexible, Transparent, Conducting Films: Extremely High DC to Optical Conductivity Ratios. *ACS Nano* **2009**, *3*, 1767−1774.
(151) Lee, J.; Lee, P.; Lee, H.; Lee, D.; Lee, S. S.; Ko, S. H. Very long Ag nanowire synthesis and its application in a highly transparent, conductive and flexible metal electrode touch panel. *Nanoscale* **2012**, *4*, 6408−6414.
(152) Lee, J.; Lee, P.; Lee, H. B.; Hong, S.; Lee, I.; Yeo, J.; Lee, S. S.; Kim, T.-S.; Lee, D.; Ko, S. H. Room-Temperature Nanosoldering of a Very Long Metal Nanowire Network by Conducting-Polymer-Assisted Joining for a Flexible Touch-Panel Application. *Adv. Funct. Mater.* **2013**, *23*, 4171−4176.
(153) Hong, S.; Lee, H.; Lee, J.; Kwon, J.; Han, S.; Suh, Y. D.; Cho, H.; Shin, J.; Yeo, J.; Ko, S. H. Highly stretchable and transparent metal nanowire heater for wearable electronics applications. *Adv. Mater.* **2015**, *27*, 4744−4751.
(154) Lee, C.; Wei, X.; Kysar, J. W.; Hone, J. Measurement of the elastic properties and intrinsic strength of monolayer graphene. *Science* **2008**, *321*, 385−388.
(155) Orlita, M.; Faugeras, C.; Plochocka, P.; Neugebauer, P.; Martinez, G.; Maude, D. K.; Barra, A. L.; Sprinkle, M.; Berger, C.; de Heer, W. A.; et al. Approaching the dirac point in high-mobility multilayer epitaxial graphene. *Phys. Rev. Lett.* **2008**, *101*, 267601.
(156) Bae, S.; Kim, H.; Lee, Y.; Xu, X.; Park, J. S.; Zheng, Y.; Balakrishnan, J.; Lei, T.; Kim, H. R.; Song, Y. I.; et al. Roll-to-roll production of 30-in. graphene films for transparent electrodes. *Nat. Nanotechnol.* **2010**, *5*, 574−578.
(157) Zhao, J.; Pei, S.; Ren, W.; Gao, L.; Cheng, H. M. Efficient preparation of large-area graphene oxide sheets for transparent conductive films. *ACS Nano* **2010**, *4*, 5245−5252.
(158) Morozov, S. V.; Novoselov, K. S.; Katsnelson, M. I.; Schedin, F.; Elias, D. C.; Jaszczak, J. A.; Geim, A. K. Giant intrinsic carrier mobilities in graphene and its bilayer. *Phys. Rev. Lett.* **2008**, *100*, 016602.
(159) Blake, P.; Brimicombe, P. D.; Nair, R. R.; Booth, T. J.; Jiang, D.; Schedin, F.; Ponomarenko, L. A.; Morozov, S. V.; Gleeson, H. F.; Hill, E. W.; et al. Graphene-based liquid crystal device. *Nano Lett.* **2008**, *8*, 1704−1708.
(160) Gee, C.-M.; Tseng, C.-C.; Wu, F.-Y.; Chang, H.-P.; Li, L.-J.; Hsieh, Y.-P.; Lin, C.-T.; Chen, J.-C. Flexible transparent electrodes made of electrochemically exfoliated graphene sheets from low-cost graphite pieces. *Displays* **2013**, *34*, 315−319.
(161) Hernandez, Y.; Nicolosi, V.; Lotya, M.; Blighe, F. M.; Sun, Z.; De, S.; McGovern, I. T.; Holland, B.; Byrne, M.; Gun'Ko, Y. K.; et al. High-yield production of graphene by liquid-phase exfoliation of graphite. *Nat. Nanotechnol.* **2008**, *3*, 563−568.
(162) Lotya, M.; Hernandez, Y.; King, P. J.; Smith, R. J.; Nicolosi, V.; Karlsson, L. S.; Blighe, F. M.; De, S.; Wang, Z.; McGovern, I. T.; et al. Liquid phase production of graphene by exfoliation of graphite in surfactant/water solutions. *J. Am. Chem. Soc.* **2009**, *131*, 3611−3620.
(163) Parviz, D.; Das, S.; Ahmed, H. S.; Irin, F.; Bhattacharia, S.; Green, M. J. Dispersions of non-covalently functionalized graphene with minimal stabilizer. *ACS Nano* **2012**, *6*, 8857−8867.
(164) Nuvoli, D.; Valentini, L.; Alzari, V.; Scognamillo, S.; Bon, S. B.; Piccinini, M.; Illescas, J.; Mariani, A. High concentration few-layer graphene sheets obtained by liquid phase exfoliation of graphite in ionic liquid. *J. Mater. Chem.* **2011**, *21*, 3428−3431.
(165) Khan, U.; O'Neill, A.; Lotya, M.; De, S.; Coleman, J. N. High-concentration solvent exfoliation of graphene. *Small* **2010**, *6*, 864−871.
(166) Leon, V.; Quintana, M.; Herrero, M. A.; Fierro, J. L.; de la Hoz, A.; Prato, M.; Vazquez, E. Few-layer graphenes from ball-milling of graphite with melamine. *Chem. Commun.* **2011**, *47*, 10936−10938.
(167) Paton, K. R.; Varrla, E.; Backes, C.; Smith, R. J.; Khan, U.; O'Neill, A.; Boland, C.; Lotya, M.; Istrate, O. M.; King, P.; et al. Scalable production of large quantities of defect-free few-layer graphene by shear exfoliation in liquids. *Nat. Mater.* **2014**, *13*, 624−630.
(168) Bourlinos, A. B.; Georgakilas, V.; Zboril, R.; Steriotis, T. A.; Stubos, A. K.; Trapalis, C. Aqueous-phase exfoliation of graphite in the presence of polyvinylpyrrolidone for the production of water-soluble graphenes. *Solid State Commun.* **2009**, *149*, 2172−2176.
(169) Botas, C.; Álvarez, P.; Blanco, P.; Granda, M.; Blanco, C.; Santamaría, R.; Romasanta, L. J.; Verdejo, R.; López-Manchado, M. A.; Menéndez, R. Graphene materials with different structures prepared from the same graphite by the Hummers and Brodie methods. *Carbon* **2013**, *65*, 156−164.
(170) Chen, J.; Yao, B.; Li, C.; Shi, G. An improved Hummers method for eco-friendly synthesis of graphene oxide. *Carbon* **2013**, *64*, 225−229.
(171) Hermanova, S.; Zarevucka, M.; Bousa, D.; Pumera, M.; Sofer, Z. Graphene oxide immobilized enzymes show high thermal and solvent stability. *Nanoscale* **2015**, *7*, 5852−5858.
(172) Shin, H. J.; Kim, K. K.; Benayad, A.; Yoon, S. M.; Park, H. K.; Jung, I. S.; Jin, M. H.; Jeong, H. K.; Kim, J. M.; Choi, J. Y.; et al. Efficient Reduction of Graphite Oxide by Sodium Borohydride and Its Effect on Electrical Conductance. *Adv. Funct. Mater.* **2009**, *19*, 1987−1992.
(173) Park, S.; An, J.; Potts, J. R.; Velamakanni, A.; Murali, S.; Ruoff, R. S. Hydrazine-reduction of graphite- and graphene oxide. *Carbon* **2011**, *49*, 3019−3023.

https://doi.org/10.1021/acs.chemrev.3c00139
Chem. Rev. 2023, 123, 9982−10078

(174) Alam, S. N.; Sharma, N.; Kumar, L. Synthesis of graphene oxide (GO) by modified hummers method and its thermal reduction to obtain reduced graphene oxide (rGO). *Graphene* **2017**, *6*, 1−18.
(175) Larciprete, R.; Fabris, S.; Sun, T.; Lacovig, P.; Baraldi, A.; Lizzit, S. Dual path mechanism in the thermal reduction of graphene oxide. *J. Am. Chem. Soc.* **2011**, *133*, 17315−17321.
(176) Guo, H.; Peng, M.; Zhu, Z.; Sun, L. Preparation of reduced graphene oxide by infrared irradiation induced photothermal reduction. *Nanoscale* **2013**, *5*, 9040−9048.
(177) Voiry, D.; Yang, J.; Kupferberg, J.; Fullon, R.; Lee, C.; Jeong, H. Y.; Shin, H. S.; Chhowalla, M. High-quality graphene via microwave reduction of solution-exfoliated graphene oxide. *Science* **2016**, *353*, 1413−1416.
(178) Eigler, S.; Enzelberger-Heim, M.; Grimm, S.; Hofmann, P.; Kroener, W.; Geworski, A.; Dotzer, C.; Rockert, M.; Xiao, J.; Papp, C.; et al. Wet chemical synthesis of graphene. *Adv. Mater.* **2013**, *25*, 3583−3587.
(179) Butz, B.; Dolle, C.; Halbig, C. E.; Spiecker, E.; Eigler, S. Highly Intact and Pure Oxo-Functionalized Graphene: Synthesis and Electron-Beam-Induced Reduction. *Angew. Chem., Int. Ed.* **2016**, *55*, 15771−15774.
(180) Zheng, Q.; Ip, W. H.; Lin, X.; Yousefi, N.; Yeung, K. K.; Li, Z.; Kim, J. K. Transparent conductive films consisting of ultralarge graphene sheets produced by Langmuir-Blodgett assembly. *ACS Nano* **2011**, *5*, 6039−6051.
(181) Ning, J.; Hao, L.; Jin, M.; Qiu, X.; Shen, Y.; Liang, J.; Zhang, X.; Wang, B.; Li, X.; Zhi, L. A Facile Reduction Method for Roll-to-Roll Production of High Performance Graphene-Based Transparent Conductive Films. *Adv. Mater.* **2017**, *29*, 1605028.
(182) Kim, K. S.; Zhao, Y.; Jang, H.; Lee, S. Y.; Kim, J. M.; Kim, K. S.; Ahn, J. H.; Kim, P.; Choi, J. Y.; Hong, B. H. Large-scale pattern growth of graphene films for stretchable transparent electrodes. *Nature* **2009**, *457*, 706−710.
(183) Somani, P. R.; Somani, S. P.; Umeno, M. Planer nano-graphenes from camphor by CVD. *Chem. Phys. Lett.* **2006**, *430*, 56−59.
(184) Vlassiouk, I.; Fulvio, P.; Meyer, H.; Lavrik, N.; Dai, S.; Datskos, P.; Smirnov, S. Large scale atmospheric pressure chemical vapor deposition of graphene. *Carbon* **2013**, *54*, 58−67.
(185) Li, X.; Magnuson, C. W.; Venugopal, A.; Tromp, R. M.; Hannon, J. B.; Vogel, E. M.; Colombo, L.; Ruoff, R. S. Large-area graphene single crystals grown by low-pressure chemical vapor deposition of methane on copper. *J. Am. Chem. Soc.* **2011**, *133*, 2816−2819.
(186) Woehrl, N.; Ochedowski, O.; Gottlieb, S.; Shibasaki, K.; Schulz, S. Plasma-enhanced chemical vapor deposition of graphene on copper substrates. *AIP Adv.* **2014**, *4*, 047128.
(187) Cui, L.; Chen, X.; Liu, B.; Chen, K.; Chen, Z.; Qi, Y.; Xie, H.; Zhou, F.; Rummeli, M. H.; Zhang, Y.; et al. Highly Conductive Nitrogen-Doped Graphene Grown on Glass toward Electrochromic Applications. *ACS Appl. Mater. Interfaces* **2018**, *10*, 32622−32630.
(188) Wei, D.; Peng, L.; Li, M.; Mao, H.; Niu, T.; Han, C.; Chen, W.; Wee, A. T. Low temperature critical growth of high quality nitrogen doped graphene on dielectrics by plasma-enhanced chemical vapor deposition. *ACS Nano* **2015**, *9*, 164−171.
(189) Ajayan, P. M.; Schadler, L. S.; Braun, P. V. *Nanocomposite Science and Technology*; John Wiley & Sons, 2006.
(190) Iijima, S. Helical microtubules of graphitic carbon. *Nature* **1991**, *354*, 56−58.
(191) Ebbesen, T. W.; Ajayan, P. M. Large-scale synthesis of carbon nanotubes. *Nature* **1992**, *358*, 220−222.
(192) Iijima, S.; Ichihashi, T. Single-shell carbon nanotubes of 1-nm diameter. *Nature* **1993**, *363*, 603−605.
(193) Zhang, D.; Ryu, K.; Liu, X.; Polikarpov, E.; Ly, J.; Tompson, M. E.; Zhou, C. Transparent, conductive, and flexible carbon nanotube films and their application in organic light-emitting diodes. *Nano Lett.* **2006**, *6*, 1880−1886.
(194) Yang, G.-W.; Gao, G.-Y.; Wang, C.; Xu, C.-L.; Li, H.-L. Controllable deposition of Ag nanoparticles on carbon nanotubes as a catalyst for hydrazine oxidation. *Carbon* **2008**, *46*, 747−752.
(195) Bhaviripudi, S.; Mile, E.; Steiner, S. A., 3rd; Zare, A. T.; Dresselhaus, M. S.; Belcher, A. M.; Kong, J. CVD synthesis of single-walled carbon nanotubes from gold nanoparticle catalysts. *J. Am. Chem. Soc.* **2007**, *129*, 1516−1517.
(196) Hutchison, J. L.; Kiselev, N. A.; Krinichnaya, E. P.; Krestinin, A. V.; Loutfy, R. O.; Morawsky, A. P.; Muradyan, V. E.; Obraztsova, E. D.; Sloan, J.; Terekhov, S. V.; et al. Double-walled carbon nanotubes fabricated by a hydrogen arc discharge method. *Carbon* **2001**, *39*, 761−770.
(197) Hofmann, S.; Blume, R.; Wirth, C. T.; Cantoro, M.; Sharma, R.; Ducati, C.; Hävecker, M.; Zafeiratos, S.; Schnoerch, P.; Oestereich, A.; et al. State of Transition Metal Catalysts During Carbon Nanotube Growth. *J. Phys. Chem. C* **2009**, *113*, 1648−1656.
(198) Lee, C. J.; Park, J.; Yu, J. A. Catalyst effect on carbon nanotubes synthesized by thermal chemical vapor deposition. *Chem. Phys. Lett.* **2002**, *360*, 250−255.
(199) Lee, C. J.; Park, J.; Kim, J. M.; Huh, Y.; Lee, J. Y.; No, K. S. Low-temperature growth of carbon nanotubes by thermal chemical vapor deposition using Pd, Cr, and Pt as co-catalyst. *Chem. Phys. Lett.* **2000**, *327*, 277−283.
(200) Tang, S.; Zhong, Z.; Xiong, Z.; Sun, L.; Liu, L.; Lin, J.; Shen, Z. X.; Tan, K. L. Controlled growth of single-walled carbon nanotubes by catalytic decomposition of CH4 over Mo/Co/MgO catalysts. *Chem. Phys. Lett.* **2001**, *350*, 19−26.
(201) Guo, T.; Nikolaev, P.; Thess, A.; Colbert, D. T.; Smalley, R. E. Catalytic growth of single-walled manotubes by laser vaporization. *Chem. Phys. Lett.* **1995**, *243*, 49−54.
(202) Thess, A.; Lee, R.; Nikolaev, P.; Dai, H.; Petit, P.; Robert, J.; Xu, C.; Lee, Y. H.; Kim, S. G.; Rinzler, A. G.; et al. Crystalline Ropes of Metallic Carbon Nanotubes. *Science* **1996**, *273*, 483−487.
(203) Terrones, M.; Grobert, N.; Olivares, J.; Zhang, J. P.; Terrones, H.; Kordatos, K.; Hsu, W. K.; Hare, J. P.; Townsend, P. D.; Prassides, K.; et al. Controlled production of aligned-nanotube bundles. *Nature* **1997**, *388*, 52−55.
(204) Kazeimzadeh, F.; Malekfar, R.; Houshiar, M., The effect of graphitic target density on carbon nanotube synthesis by pulsed laser ablation method. In*6th International Biennial Conference on Ultrafine Grained and Nanostructured Materials (UFGNSM 2017)*, 2018.
(205) Chrzanowska, J.; Hoffman, J.; Małolepszy, A.; Mazurkiewicz, M.; Kowalewski, T. A.; Szymanski, Z.; Stobinski, L. Synthesis of carbon nanotubes by the laser ablation method: Effect of laser wavelength. *Phys. Status Solidi B* **2015**, *252*, 1860−1867.
(206) Kokai, F.; Takahashi, K.; Kasuya, D.; Yudasaka, M.; Iijima, S. Growth dynamics of single-wall carbon nanotubes and nanohorn aggregates by CO2 laser vaporization at room temperature. *Appl. Surf. Sci.* **2002**, *197*, 650−655.
(207) Roch, A.; Jost, O.; Schultrich, B.; Beyer, E. High-yield synthesis of single-walled carbon nanotubes with a pulsed arc-discharge technique. *Phys. Status Solidi B* **2007**, *244*, 3907−3910.
(208) Mubarak, N. M.; Abdullah, E. C.; Jayakumar, N. S.; Sahu, J. N. An overview on methods for the production of carbon nanotubes. *J. Ind. Eng. Chem.* **2014**, *20*, 1186−1197.
(209) Hernadi, K.; Fonseca, A.; Nagy, J. B.; Bernaerts, D.; Lucas, A. A. Fe-catalyzed carbon nanotube formation. *Carbon* **1996**, *34*, 1249−1257.
(210) Fan, S.; Chapline, M. G.; Franklin, N. R.; Tombler, T. W.; Cassell, A. M.; Dai, H. Self-oriented regular arrays of carbon nanotubes and their field emission properties. *Science* **1999**, *283*, 512−514.
(211) Satishkumar, B. C.; Govindaraj, A.; Rao, C. N. R. Bundles of aligned carbon nanotubes obtained by the pyrolysis of ferrocene−hydrocarbon mixtures: role of the metal nanoparticles produced in situ. *Chem. Phys. Lett.* **1999**, *307*, 158−162.
(212) Sen, R.; Govindaraj, A.; Rao, C. Metal-filled and hollow carbon nanotubes obtained by the decomposition of metal-containing free precursor molecules. *Chem. Mater.* **1997**, *9*, 2078−2081.

https://doi.org/10.1021/acs.chemrev.3c00139
Chem. Rev. 2023, 123, 9982−10078

(213) Wei, B. Q.; Vajtai, R.; Jung, Y.; Ward, J.; Zhang, R.; Ramanath, G.; Ajayan, P. M. Microfabrication technology: organized assembly of carbon nanotubes. *Nature* **2002**, *416*, 495−496.
(214) Nikolaev, P.; Bronikowski, M. J.; Bradley, R. K.; Rohmund, F.; Colbert, D. T.; Smith, K. A.; Smalley, R. E. Gas-phase catalytic growth of single-walled carbon nanotubes from carbon monoxide. *Chem. Phys. Lett.* **1999**, *313*, 91−97.
(215) Kong, J.; Cassell, A. M.; Dai, H. Chemical vapor deposition of methane for single-walled carbon nanotubes. *Chem. Phys. Lett.* **1998**, *292*, 567−574.
(216) Huang, Z. P.; Xu, J. W.; Ren, Z. F.; Wang, J. H.; Siegal, M. P.; Provencio, P. N. Growth of highly oriented carbon nanotubes by plasma-enhanced hot filament chemical vapor deposition. *Appl. Phys. Lett.* **1998**, *73*, 3845−3847.
(217) Öncel, Ç.; Yürüm, Y. Carbon Nanotube Synthesis via the Catalytic CVD Method: A Review on the Effect of Reaction Parameters. *Fullerenes Nanotubes Carbon Nanostruct.* **2006**, *14*, 17−37.
(218) Li, Y.; Mann, D.; Rolandi, M.; Kim, W.; Ural, A.; Hung, S.; Javey, A.; Cao, J.; Wang, D.; Yenilmez, E.; et al. Preferential Growth of Semiconducting Single-Walled Carbon Nanotubes by a Plasma Enhanced CVD Method. *Nano Lett.* **2004**, *4*, 317−321.
(219) Qin, L. C.; Zhou, D.; Krauss, A. R.; Gruen, D. M. Growing carbon nanotubes by microwave plasma-enhanced chemical vapor deposition. *Appl. Phys. Lett.* **1998**, *72*, 3437−3439.
(220) Alexandrescu, R.; Crunteanu, A.; Morjan, R. E.; Morjan, I.; Rohmund, F.; Falk, L. K. L.; Ledoux, G.; Huisken, F. Synthesis of carbon nanotubes by CO2-laser-assisted chemical vapour deposition. *Infrared Phys. Technol.* **2003**, *44*, 43−50.
(221) Yun, Y.; Shanov, V.; Tu, Y.; Subramaniam, S.; Schulz, M. J. Growth mechanism of long aligned multiwall carbon nanotube arrays by water-assisted chemical vapor deposition. *J. Phys. Chem. B* **2006**, *110*, 23920−23925.
(222) Chiang, C. K.; Fincher, C. R.; Park, Y. W.; Heeger, A. J.; Shirakawa, H.; Louis, E. J.; Gau, S. C.; MacDiarmid, A. G. Electrical Conductivity in Doped Polyacetylene. *Phys. Rev. Lett.* **1977**, *39*, 1098−1101.
(223) Shirakawa, H.; Louis, E. J.; MacDiarmid, A. G.; Chiang, C. K.; Heeger, A. J. Synthesis of electrically conducting organic polymers: halogen derivatives of polyacetylene, (CH) x. *J. Chem. Soc., Chem. Commun.* **1977**, 578−580.
(224) Mokhtar, S. M. A.; Alvarez de Eulate, E.; Yamada, M.; Prow, T. W.; Evans, D. R. Conducting polymers in wearable devices. *Med. Devices Sens.* **2021**, *4*, No. e10160.
(225) MacDiarmid, A. G. Polyaniline and polypyrrole: Where are we headed? *Synth. Met.* **1997**, *84*, 27−34.
(226) Beygisangchin, M.; Abdul Rashid, S.; Shafie, S.; Sadrolhosseini, A. R.; Lim, H. N. Preparations, Properties, and Applications of Polyaniline and Polyaniline Thin Films-A Review. *Polymers* **2021**, *13*, 2003.
(227) Saeb, M. R.; Zarrintaj, P.; Khandelwal, P.; Chauhan, N. P. S. *Synthetic Route of Polyaniline (I): Conventional Oxidative Polymerization*; Elsevier, 2019.
(228) Kumari Jangid, N.; Jadoun, S.; Kaur, N. RETRACTED: A review on high-throughput synthesis, deposition of thin films and properties of polyaniline. *Eur. Polym. J.* **2020**, *125*, 109485.
(229) Stejskal, J.; Sapurina, I.; Trchová, M.; Konyushenko, E. N. Oxidation of Aniline: Polyaniline Granules, Nanotubes, and Oligoaniline Microspheres. *Macromolecules* **2008**, *41*, 3530−3536.
(230) Bláha, M.; Varga, M.; Prokeš, J.; Zhigunov, A.; Vohlídal, J. Effects of the polymerization temperature on the structure, morphology and conductivity of polyaniline prepared with ammonium peroxodisulfate. *Eur. Polym. J.* **2013**, *49*, 3904−3911.
(231) Majeed, A. H.; Mohammed, L. A.; Hammoodi, O. G.; Sehgal, S.; Alheety, M. A.; Saxena, K. K.; Dadoosh, S. A.; Mohammed, I. K.; Jasim, M. M.; Salmaan, N. U.; et al. A Review on Polyaniline: Synthesis, Properties, Nanocomposites, and Electrochemical Applications. *Int. J. Polym. Sci.* **2022**, *2022*, 1−19.
(232) Li, G.-R.; Feng, Z.-P.; Zhong, J.-H.; Wang, Z.-L.; Tong, Y.-X. Electrochemical Synthesis of Polyaniline Nanobelts with Predominant Electrochemical Performances. *Macromolecules* **2010**, *43*, 2178−2183.
(233) Wang, P.-C.; Yu, J.-Y. Dopant-dependent variation in the distribution of polarons and bipolarons as charge-carriers in polypyrrole thin films synthesized by oxidative chemical polymerization. *React. Funct. Polym.* **2012**, *72*, 311−316.
(234) Wallace, G. G.; Teasdale, P. R.; Spinks, G. M.; Kane-Maguire, L. A. *Conductive Electroactive Polymers: Intelligent Materials Systems*; CRC Press, 2002.
(235) Deljoo Kojabad, Z.; Shojaosadati, S. A. Chemical synthesis of polypyrrole nanostructures: Optimization and applications for neural microelectrodes. *Mater. Des.* **2016**, *96*, 378−384.
(236) Wysocka-Żołopa, M.; Winkler, K. Electrochemical synthesis and properties of conical polypyrrole structures. *Electrochim. Acta* **2017**, *258*, 1421−1434.
(237) Tan, Y.; Ghandi, K. Kinetics and mechanism of pyrrole chemical polymerization. *Synth. Met.* **2013**, *175*, 183−191.
(238) Pang, A. L.; Arsad, A.; Ahmadipour, M. Synthesis and factor affecting on the conductivity of polypyrrole: a short review. *Polym. Adv. Technol.* **2021**, *32*, 1428−1454.
(239) Zhao, P.; Tang, Q.; Zhao, X.; Tong, Y.; Liu, Y. Highly stable and flexible transparent conductive polymer electrode patterns for large-scale organic transistors. *J. Colloid Interface Sci.* **2018**, *520*, 58−63.
(240) Gupta, N. D.; Maity, S.; Chattopadhyay, K. K. Field emission enhancement of polypyrrole due to band bending induced tunnelling in polypyrrole-carbon nanotubes nanocomposite. *J. Ind. Eng. Chem.* **2014**, *20*, 3208−3213.
(241) Sri Utami, R.; Puspasari, I.; Shyuan, L. K.; Mohamed, A. B.; Alva, S. Effect of process parameters on the synthesis of polypyrrole by the Taguchi method. *Malaysian J. Anal. Sci.* **2016**, *20*, 660−669.
(242) Machida, S.; Miyata, S.; Techagumpuch, A. Chemical synthesis of highly electrically conductive polypyrrole. *Synth. Met.* **1989**, *31*, 311−318.
(243) Paramo-Garcia, U.; Ibanez, J. G.; Batina, N. AFM Analysis of Polypyrrole Films Synthesized in the Presence of Selected Doping Agents. *Int. J. Electrochem. Sci.* **2013**, *8*, 2656−2669.
(244) Wang, J.; Xu, Y.; Yan, F.; Zhu, J.; Wang, J. Template-free prepared micro/nanostructured polypyrrole with ultrafast charging/discharging rate and long cycle life. *J. Power Sources* **2011**, *196*, 2373−2379.
(245) Liao, J.; Wu, S.; Yin, Z.; Huang, S.; Ning, C.; Tan, G.; Chu, P. K. Surface-dependent self-assembly of conducting polypyrrole nanotube arrays in template-free electrochemical polymerization. *ACS Appl. Mater. Interfaces* **2014**, *6*, 10946−10951.
(246) Genies, E. M.; Bidan, G.; Diaz, A. F. Spectroelectrochemical study of polypyrrole films. *J. Electroanal. Chem. Interfacial Electrochem.* **1983**, *149*, 101−113.
(247) Ko, J. M.; Rhee, H. W.; Park, S. M.; Kim, C. Y. Morphology and Electrochemical Properties of Polypyrrole Films Prepared in Aqueous and Nonaqueous Solvents. *J. Electrochem. Soc.* **1990**, *137*, 905−909.
(248) Jonas, F.; Schrader, L. Conductive modifications of polymers with polypyrroles and polythiophenes. *Synth. Met.* **1991**, *41*, 831−836.
(249) Jonas, F.; Krafft, W. New polythlophene dispersions, their preparation and their use. European Patent EP0440957B1, 1991.
(250) Ha, Y. H.; Nikolov, N.; Pollack, S. K.; Mastrangelo, J.; Martin, B. D.; Shashidhar, R. Towards a Transparent, Highly Conductive Poly(3,4-ethylenedioxythiophene). *Adv. Funct. Mater.* **2004**, *14*, 615−622.
(251) Jiang, Y.; Liu, T.; Zhou, Y. Recent Advances of Synthesis, Properties, Film Fabrication Methods, Modifications of Poly(3,4-ethylenedioxythiophene), and Applications in Solution-Processed Photovoltaics. *Adv. Funct. Mater.* **2020**, *30*, 2006213.
(252) Heywang, G.; Jonas, F. Poly(alkylenedioxythiophene)s—new, very stable conducting polymers. *Adv. Mater.* **1992**, *4*, 116−118.

https://doi.org/10.1021/acs.chemrev.3c00139
Chem. Rev. 2023, 123, 9982−10078

(253) Jiang, C.; Chen, G.; Wang, X. High-conversion synthesis of poly(3,4-ethylenedioxythiophene) by chemical oxidative polymerization. *Synth. Met.* **2012**, *162*, 1968−1971.
(254) Ayub, A. N.; Ismail, N. A.; Aizamddin, M. F.; Bonnia, N. N.; Sulaiman, N. S.; Nadzri, N. I. M.; Mahat, M. M. Effects of Organic Solvent Doping on the Structural and Conductivity Properties of PEDOT: PSS Fabric. *J. Phys. Conf. Ser.* **2022**, *2169*, 012008.
(255) Corradi, R.; Armes, S. P. Chemical synthesis of poly(3,4-ethylenedioxythiophene). *Synth. Met.* **1997**, *84*, 453−454.
(256) Im, S. G.; Kusters, D.; Choi, W.; Baxamusa, S. H.; van de Sanden, M. C.; Gleason, K. K. Conformal coverage of poly(3,4-ethylenedioxythiophene) films with tunable nanoporosity via oxidative chemical vapor deposition. *ACS Nano* **2008**, *2*, 1959−1967.
(257) Zotti, G.; Zecchin, S.; Schiavon, G.; Louwet, F.; Groenendaal, L.; Crispin, X.; Osikowicz, W.; Salaneck, W.; Fahlman, M. Electrochemical and XPS Studies toward the Role of Monomeric and Polymeric Sulfonate Counterions in the Synthesis, Composition, and Properties of Poly(3,4-ethylenedioxythiophene). *Macromolecules* **2003**, *36*, 3337−3344.
(258) Culebras, M.; Gómez, C. M.; Cantarero, A. Enhanced thermoelectric performance of PEDOT with different counter-ions optimized by chemical reduction. *J. Mater. Chem. A* **2014**, *2*, 10109−10115.
(259) Poverenov, E.; Li, M.; Bitler, A.; Bendikov, M. Major Effect of Electropolymerization Solvent on Morphology and Electrochromic Properties of PEDOT Films. *Chem. Mater.* **2010**, *22*, 4019−4025.
(260) Gueye, M. N.; Carella, A.; Faure-Vincent, J.; Demadrille, R.; Simonato, J.-P. Progress in understanding structure and transport properties of PEDOT-based materials: A critical review. *Prog. Mater. Sci.* **2020**, *108*, 100616.
(261) Huang, J.; Miller, P. F.; de Mello, J. C.; de Mello, A. J.; Bradley, D. D. C. Influence of thermal treatment on the conductivity and morphology of PEDOT/PSS films. *Synth. Met.* **2003**, *139*, 569−572.
(262) Davis, R.; Predeep, P. UV-ozone treatment of PEDOT: PSS for improved charge transport in organic photovoltaics. *AIP Conf. Proc.* **2020**, *2287*, 020017.
(263) Xia, Y.; Zhang, H.; Ouyang, J. Highly conductive PEDOT:PSS films prepared through a treatment with zwitterions and their application in polymer photovoltaic cells. *J. Mater. Chem.* **2010**, *20*, 9740−9747.
(264) Kim, J. Y.; Jung, J. H.; Lee, D. E.; Joo, J. Enhancement of electrical conductivity of poly(3,4-ethylenedioxythiophene)/poly(4-styrenesulfonate) by a change of solvents. *Synth. Met.* **2002**, *126*, 311−316.
(265) Shi, H.; Liu, C.; Jiang, Q.; Xu, J. Effective Approaches to Improve the Electrical Conductivity of PEDOT:PSS: A Review. *Adv. Electron. Mater.* **2015**, *1*, 1500017.
(266) Shi, H.; Liu, C.; Xu, J.; Song, H.; Lu, B.; Jiang, F.; Zhou, W.; Zhang, G.; Jiang, Q. Facile fabrication of PEDOT:PSS/polythiophenes bilayered nanofilms on pure organic electrodes and their thermoelectric performance. *ACS Appl. Mater. Interfaces* **2013**, *5*, 12811−12819.
(267) Zhang, X.; Wu, J.; Wang, J.; Zhang, J.; Yang, Q.; Fu, Y.; Xie, Z. Highly conductive PEDOT:PSS transparent electrode prepared by a post-spin-rinsing method for efficient ITO-free polymer solar cells. *Sol. Energy Mater. Sol. Cells* **2016**, *144*, 143−149.
(268) Murali, G.; Reddy Modigunta, J. K.; Park, Y. H.; Lee, J. H.; Rawal, J.; Lee, S. Y.; In, I.; Park, S. J. A Review on MXene Synthesis, Stability, and Photocatalytic Applications. *ACS Nano* **2022**, *16*, 13370−13429.
(269) Gogotsi, Y.; Anasori, B. The Rise of MXenes. *ACS Nano* **2019**, *13*, 8491−8494.
(270) Anasori, B.; Gogotsi, Û. G. Introduction to 2D Transition Metal Carbides and Nitrides (MXenes)*2D Metal Carbides and Nitrides (MXenes)*; Springer: Cham, 2019; p 3
(271) Naguib, M.; Kurtoglu, M.; Presser, V.; Lu, J.; Niu, J.; Heon, M.; Hultman, L.; Gogotsi, Y.; Barsoum, M. W. Two-dimensional nanocrystals produced by exfoliation of Ti3 AlC2. *Adv. Mater.* **2011**, *23*, 4248−4253.
(272) Sun, W.; Shah, S. A.; Chen, Y.; Tan, Z.; Gao, H.; Habib, T.; Radovic, M.; Green, M. J. Electrochemical etching of Ti2AlC to Ti2CTx (MXene) in low-concentration hydrochloric acid solution. *J. Mater. Chem. A* **2017**, *5*, 21663−21668.
(273) Yang, S.; Zhang, P.; Wang, F.; Ricciardulli, A. G.; Lohe, M. R.; Blom, P. W. M.; Feng, X. Fluoride-Free Synthesis of Two-Dimensional Titanium Carbide (MXene) Using A Binary Aqueous System. *Angew. Chem., Int. Ed.* **2018**, *57*, 15491−15495.
(274) Handoko, A. D.; Fredrickson, K. D.; Anasori, B.; Convey, K. W.; Johnson, L. R.; Gogotsi, Y.; Vojvodic, A.; Seh, Z. W. Tuning the Basal Plane Functionalization of Two-Dimensional Metal Carbides (MXenes) To Control Hydrogen Evolution Activity. *ACS Appl. Energy Mater.* **2018**, *1*, 173−180.
(275) Iqbal, A.; Shahzad, F.; Hantanasirisakul, K.; Kim, M. K.; Kwon, J.; Hong, J.; Kim, H.; Kim, D.; Gogotsi, Y.; Koo, C. M. Anomalous absorption of electromagnetic waves by 2D transition metal carbonitride Ti3CNTx (MXene). *Science* **2020**, *369*, 446−450.
(276) Riazi, H.; Anayee, M.; Hantanasirisakul, K.; Shamsabadi, A. A.; Anasori, B.; Gogotsi, Y.; Soroush, M. Surface Modification of a MXene by an Aminosilane Coupling Agent. *Adv. Mater. Interfaces* **2020**, *7*, 1902008.
(277) Dillon, A. D.; Ghidiu, M. J.; Krick, A. L.; Griggs, J.; May, S. J.; Gogotsi, Y.; Barsoum, M. W.; Fafarman, A. T. Highly Conductive Optical Quality Solution-Processed Films of 2D Titanium Carbide. *Adv. Funct. Mater.* **2016**, *26*, 4162−4168.
(278) Guo, T.; Zhou, D.; Deng, S.; Jafarpour, M.; Avaro, J.; Neels, A.; Heier, J.; Zhang, C. Rational Design of Ti3C2Tx MXene Inks for Conductive, Transparent Films. *ACS Nano* **2023**, *17*, 3737−3749.
(279) Liu, Z.; Ji, H.; Wang, S.; Zhao, W.; Huang, Y.; Feng, H.; Wei, J.; Li, M. Enhanced Electrical and Mechanical Properties of a Printed Bimodal Silver Nanoparticle Ink for Flexible Electronics. *Phys. Status Solidi A* **2018**, *215*, 1800007.
(280) Suh, Y. D.; Jung, J.; Lee, H.; Yeo, J.; Hong, S.; Lee, P.; Lee, D.; Ko, S. H. Nanowire reinforced nanoparticle nanocomposite for highly flexible transparent electrodes: borrowing ideas from macrocomposites in steel-wire reinforced concrete. *J. Mater. Chem. C* **2017**, *5*, 791−798.
(281) Lee, P.; Ham, J.; Lee, J.; Hong, S.; Han, S.; Suh, Y. D.; Lee, S. E.; Yeo, J.; Lee, S. S.; Lee, D.; et al. Highly Stretchable or Transparent Conductor Fabrication by a Hierarchical Multiscale Hybrid Nanocomposite. *Adv. Funct. Mater.* **2014**, *24*, 5671−5678.
(282) Lee, M. S.; Lee, K.; Kim, S. Y.; Lee, H.; Park, J.; Choi, K. H.; Kim, H. K.; Kim, D. G.; Lee, D. Y.; Nam, S.; et al. High-performance, transparent, and stretchable electrodes using graphene-metal nanowire hybrid structures. *Nano Lett.* **2013**, *13*, 2814−2821.
(283) Li, L.; Li, W.; Jiu, J.; Suganuma, K. Efficient assembly of high-performance reduced graphene oxide/silver nanowire transparent conductive film based on in situ light-induced reduction technology. *Appl. Surf. Sci.* **2018**, *459*, 732−740.
(284) Kim, S.; Kim, S. Y.; Kim, J.; Kim, J. H. Highly reliable AgNW/PEDOT:PSS hybrid films: efficient methods for enhancing transparency and lowering resistance and haziness. *J. Mater. Chem. C* **2014**, *2*, 5636−5643.
(285) Ahsan Saeed, M.; Hyeon Kim, S.; Baek, K.; Hyun, J. K.; Youn Lee, S.; Won Shim, J. PEDOT:PSS: CuNW-based transparent composite electrodes for high-performance and flexible organic photovoltaics under indoor lighting. *Appl. Surf. Sci.* **2021**, *567*, 150852.
(286) Liu, Z.; Parvez, K.; Li, R.; Dong, R.; Feng, X.; Mullen, K. Transparent conductive electrodes from graphene/PEDOT:PSS hybrid inks for ultrathin organic photodetectors. *Adv. Mater.* **2015**, *27*, 669−675.
(287) Song, K.; Noh, J.; Jun, T.; Jung, Y.; Kang, H. Y.; Moon, J. Fully flexible solution-deposited zno thin-film transistors. *Adv. Mater.* **2010**, *22*, 4308−4312.
(288) Chen, X.; Zhang, G.; Wan, J.; Guo, T.; Li, L.; Yang, Y.; Wu, H.; Liu, C. Transparent and Flexible Thin-Film Transistors with High

https://doi.org/10.1021/acs.chemrev.3c00139
Chem. Rev. 2023, 123, 9982−10078

Performance Prepared at Ultralow Temperatures by Atomic Layer Deposition. *Adv. Electron. Mater.* **2019**, *5*, 1800583.
(289) Zhang, Y.; Mei, Z.; Cui, S.; Liang, H.; Liu, Y.; Du, X. Flexible Transparent Field-Effect Diodes Fabricated at Low-Temperature with All-Oxide Materials. *Adv. Electron. Mater.* **2016**, *2*, 1500486.
(290) Park, K.; Lee, D.-K.; Kim, B.-S.; Jeon, H.; Lee, N.-E.; Whang, D.; Lee, H.-J.; Kim, Y. J.; Ahn, J.-H. Stretchable, Transparent Zinc Oxide Thin Film Transistors. *Adv. Funct. Mater.* **2010**, *20*, 3577−3582.
(291) Lee, C. Y.; Lin, M. Y.; Wu, W. H.; Wang, J. Y.; Chou, Y.; Su, W. F.; Chen, Y. F.; Lin, C. F. Flexible ZnO transparent thin-film transistors by a solution-based process at various solution concentrations. *Semicond. Sci. Technol.* **2010**, *25*, 105008.
(292) Benamara, M.; Massoudi, J.; Dahman, H.; Dhahri, E.; El Mir, L.; Ly, A.; Debliquy, M.; Lahem, D. High response to sub-ppm level of NO 2 with 50% RH of ZnO sensor obtained by an auto-combustion method. *J. Mater. Sci.: Mater. Electron.* **2020**, *31*, 14249−14260.
(293) Narayana, A.; Bhat, S. A.; Fathima, A.; Lokesh, S. V.; Surya, S. G.; Yelamaggad, C. V. Green and low-cost synthesis of zinc oxide nanoparticles and their application in transistor-based carbon monoxide sensing. *RSC Adv.* **2020**, *10*, 13532−13542.
(294) Selvaraj, B.; Balaguru Rayappan, J. B.; Jayanth Babu, K. Influence of calcination temperature on the growth of electrospun multi-junction ZnO nanowires: A room temperature ammonia sensor. *Mater. Sci. Semicond. Process.* **2020**, *112*, 105006.
(295) Mativenga, M.; Choi, M. H.; Choi, J. W.; Jang, J. Transparent flexible circuits based on amorphous-indium−gallium−zinc−oxide thin-film transistors. *IEEE Electron Device Lett.* **2011**, *32*, 170−172.
(296) Oh, H.; Cho, K.; Park, S.; Kim, S. Electrical characteristics of bendable a-IGZO thin-film transistors with split channels and top-gate structure. *Microelectron. Eng.* **2016**, *159*, 179−183.
(297) Kim, J.; Kim, J.; Jo, S.; Kang, J.; Jo, J. W.; Lee, M.; Moon, J.; Yang, L.; Kim, M. G.; Kim, Y. H.; et al. Ultrahigh Detective Heterogeneous Photosensor Arrays with In-Pixel Signal Boosting Capability for Large-Area and Skin-Compatible Electronics. *Adv. Mater.* **2016**, *28*, 3078−3086.
(298) Carlos, E.; Leppäniemi, J.; Sneck, A.; Alastalo, A.; Deuermeier, J.; Branquinho, R.; Martins, R.; Fortunato, E. Printed, highly stable metal oxide thin-film transistors with ultra-thin high-κ oxide dielectric. *Adv. Electron. Mater.* **2020**, *6*, 1901071.
(299) Zhang, B.; Bao, N.; Wang, T.; Xu, Y.; Dong, Y.; Ni, Y.; Yu, P.; Wei, Q.; Wang, J.; Guo, L.; et al. High-performance room temperature NO2 gas sensor based on visible light irradiated In2O3 nanowires. *J. Alloys Compd.* **2021**, *867*, 159076.
(300) Wang, X.-X.; Li, H.-Y.; Guo, X. Flexible and transparent sensors for ultra-low NO2 detection at room temperature under visible light illumination. *J. Mater. Chem. A* **2020**, *8*, 14482−14490.
(301) Gao, L.; Cheng, Z.; Xiang, Q.; Zhang, Y.; Xu, J. Porous corundum-type In2O3 nanosheets: Synthesis and NO2 sensing properties. *Sens. Actuators, B* **2015**, *208*, 436−443.
(302) Yang, J.; Wang, B.; Zhang, Y.; Ding, X.; Zhang, J. Low-temperature combustion synthesis and UV treatment processed p-type Li: NiO x active semiconductors for high-performance electronics. *J. Mater. Chem. C* **2018**, *6*, 12584−12591.
(303) Liu, A.; Zhu, H.; Guo, Z.; Meng, Y.; Liu, G.; Fortunato, E.; Martins, R.; Shan, F. Solution Combustion Synthesis: Low-Temperature Processing for p-Type Cu:NiO Thin Films for Transparent Electronics. *Adv. Mater.* **2017**, *29*, 1701599.
(304) Shin, J.; Jeong, B.; Kim, J.; Nam, V. B.; Yoon, Y.; Jung, J.; Hong, S.; Lee, H.; Eom, H.; Yeo, J.; et al. Sensitive Wearable Temperature Sensor with Seamless Monolithic Integration. *Adv. Mater.* **2020**, *32*, 1905527.
(305) Liu, N.; Kim, P.; Kim, J. H.; Ye, J. H.; Kim, S.; Lee, C. J. Large-area atomically thin MoS2 nanosheets prepared using electrochemical exfoliation. *ACS Nano* **2014**, *8*, 6902−6910.
(306) Zhao, J.; Chen, W.; Meng, J.; Yu, H.; Liao, M.; Zhu, J.; Yang, R.; Shi, D.; Zhang, G. Integrated Flexible and High-Quality Thin Film Transistors Based on Monolayer MoS2. *Adv. Electron. Mater.* **2016**, *2*, 1500379.
(307) Park, J.; Choudhary, N.; Smith, J.; Lee, G.; Kim, M.; Choi, W. Thickness modulated MoS2 grown by chemical vapor deposition for transparent and flexible electronic devices. *Appl. Phys. Lett.* **2015**, *106*, 012104.
(308) Li, N.; Wang, Q.; Shen, C.; Wei, Z.; Yu, H.; Zhao, J.; Lu, X.; Wang, G.; He, C.; Xie, L.; et al. Large-scale flexible and transparent electronics based on monolayer molybdenum disulfide field-effect transistors. *Nat. Electron.* **2020**, *3*, 711−717.
(309) Park, M.; Park, Y. J.; Chen, X.; Park, Y. K.; Kim, M. S.; Ahn, J. H. MoS2 -Based Tactile Sensor for Electronic Skin Applications. *Adv. Mater.* **2016**, *28*, 2556−2562.
(310) Zhao, Y.; Song, J. G.; Ryu, G. H.; Ko, K. Y.; Woo, W. J.; Kim, Y.; Kim, D.; Lim, J. H.; Lee, S.; Lee, Z.; et al. Low-temperature synthesis of 2D MoS2 on a plastic substrate for a flexible gas sensor. *Nanoscale* **2018**, *10*, 9338−9345.
(311) Rhyee, J. S.; Kwon, J.; Dak, P.; Kim, J. H.; Kim, S. M.; Park, J.; Hong, Y. K.; Song, W. G.; Omkaram, I.; Alam, M. A.; et al. High-Mobility Transistors Based on Large-Area and Highly Crystalline CVD-Grown MoSe2 Films on Insulating Substrates. *Adv. Mater.* **2016**, *28*, 2316−2321.
(312) Pataniya, P. M.; Bhakhar, S. A.; Tannarana, M.; Zankat, C.; Patel, V.; Solanki, G. K.; Patel, K. D.; Jha, P. K.; Late, D. J.; Sumesh, C. K. Highly sensitive and flexible pressure sensor based on two-dimensional MoSe2 nanosheets for online wrist pulse monitoring. *J. Colloid Interface Sci.* **2021**, *584*, 495−504.
(313) Guo, S.; Yang, D.; Zhang, S.; Dong, Q.; Li, B.; Tran, N.; Li, Z.; Xiong, Y.; Zaghloul, M. E. Development of a Cloud-Based Epidermal MoSe2 Device for Hazardous Gas Sensing. *Adv. Funct. Mater.* **2019**, *29*, 1900138.
(314) Cho, B.; Kim, A. R.; Kim, D. J.; Chung, H. S.; Choi, S. Y.; Kwon, J. D.; Park, S. W.; Kim, Y.; Lee, B. H.; Lee, K. H.; et al. Two-Dimensional Atomic-Layered Alloy Junctions for High-Performance Wearable Chemical Sensor. *ACS Appl. Mater. Interfaces* **2016**, *8*, 19635−19642.
(315) Guo, R.; Han, Y.; Su, C.; Chen, X.; Zeng, M.; Hu, N.; Su, Y.; Zhou, Z.; Wei, H.; Yang, Z. Ultrasensitive room temperature NO2 sensors based on liquid phase exfoliated WSe2 nanosheets. *Sens. Actuators, B* **2019**, *300*, 127013.
(316) Yang, C.; Xie, J.; Lou, C.; Zheng, W.; Liu, X.; Zhang, J. Flexible NO2 sensors based on WSe2 nanosheets with bifunctional selectivity and superior sensitivity under UV activation. *Sens. Actuators, B* **2021**, *333*, 129571.
(317) Liao, K. C.; Ismail, A. G.; Kreplak, L.; Schwartz, J.; Hill, I. G. Designed organophosphonate self-assembled monolayers enhance device performance of pentacene-based organic thin-film transistors. *Adv. Mater.* **2010**, *22*, 3081−3085.
(318) Giri, G.; Verploegen, E.; Mannsfeld, S. C.; Atahan-Evrenk, S.; Kim, D. H.; Lee, S. Y.; Becerril, H. A.; Aspuru-Guzik, A.; Toney, M. F.; Bao, Z. Tuning charge transport in solution-sheared organic semiconductors using lattice strain. *Nature* **2011**, *480*, 504−508.
(319) Niazi, M. R.; Li, R.; Qiang Li, E.; Kirmani, A. R.; Abdelsamie, M.; Wang, Q.; Pan, W.; Payne, M. M.; Anthony, J. E.; Smilgies, D. M.; et al. Solution-printed organic semiconductor blends exhibiting transport properties on par with single crystals. *Nat. Commun.* **2015**, *6*, 8598.
(320) Sugiyama, M.; Jancke, S.; Uemura, T.; Kondo, M.; Inoue, Y.; Namba, N.; Araki, T.; Fukushima, T.; Sekitani, T. Mobility enhancement of DNTT and BTBT derivative organic thin-film transistors by triptycene molecule modification. *Org. Electron.* **2021**, *96*, 106219.
(321) Xie, W.; Willa, K.; Wu, Y.; Hausermann, R.; Takimiya, K.; Batlogg, B.; Frisbie, C. D. Temperature-independent transport in high-mobility dinaphtho-thieno-thiophene (DNTT) single crystal transistors. *Adv. Mater.* **2013**, *25*, 3478−3484.
(322) Nawaz, A.; Kumar, A.; Hümmelgen, I. A. Ultra-high mobility in defect-free poly(3-hexylthiophene-2,5-diyl) field-effect transistors through supra-molecular alignment. *Org. Electron.* **2017**, *51*, 94−102.

https://doi.org/10.1021/acs.chemrev.3c00139
Chem. Rev. 2023, 123, 9982−10078

(323) Sun, B.; Hong, W.; Yan, Z.; Aziz, H.; Li, Y. Record high electron mobility of 6.3 cm2V− 1s− 1 achieved for polymer semiconductors using a new building block. *Adv. Mater.* **2014**, *26*, 2636−2642.
(324) Kang, I.; Yun, H. J.; Chung, D. S.; Kwon, S. K.; Kim, Y. H. Record high hole mobility in polymer semiconductors via side-chain engineering. *J. Am. Chem. Soc.* **2013**, *135*, 14896−14899.
(325) Nomura, K.; Ohta, H.; Takagi, A.; Kamiya, T.; Hirano, M.; Hosono, H. Room-temperature fabrication of transparent flexible thin-film transistors using amorphous oxide semiconductors. *Nature* **2004**, *432*, 488−492.
(326) Yu, X.; Marks, T. J.; Facchetti, A. Metal oxides for optoelectronic applications. *Nat. Mater.* **2016**, *15*, 383−396.
(327) Petti, L.; Münzenrieder, N.; Vogt, C.; Faber, H.; Büthe, L.; Cantarella, G.; Bottacchi, F.; Anthopoulos, T. D.; Tröster, G. Metal oxide semiconductor thin-film transistors for flexible electronics. *Appl. Phys. Rev.* **2016**, *3*, 021303.
(328) Walsh, A.; Da Silva, J. L.; Wei, S.-H. Multi-component transparent conducting oxides: progress in materials modelling. *J. Phys.: Condens. Matter* **2011**, *23*, 334210.
(329) Saruhan, B.; Lontio Fomekong, R.; Nahirniak, S. Influences of semiconductor metal oxide properties on gas sensing characteristics. *Front. Sens.* **2021**, *2*, 657931.
(330) Guo, T.; Yao, M.-S.; Lin, Y.-H.; Nan, C.-W. A comprehensive review on synthesis methods for transition-metal oxide nanostructures. *CrystEngComm* **2015**, *17*, 3551−3585.
(331) Konenkamp, R.; Word, R. C.; Godinez, M. Ultraviolet electroluminescence from ZnO/polymer heterojunction light-emitting diodes. *Nano Lett.* **2005**, *5*, 2005−2008.
(332) Jose, R.; Thavasi, V.; Ramakrishna, S. Metal Oxides for Dye-Sensitized Solar Cells. *J. Am. Ceram. Soc.* **2009**, *92*, 289−301.
(333) Zhang, Y.-H.; Mei, Z.-X.; Liang, H.-L.; Du, X.-L. Review of flexible and transparent thin-film transistors based on zinc oxide and related materials. *Chin. Phys. B* **2017**, *26*, 047307.
(334) Hoffman, R. L.; Norris, B. J.; Wager, J. F. ZnO-based transparent thin-film transistors. *Appl. Phys. Lett.* **2003**, *82*, 733−735.
(335) Fortunato, E. M. C.; Barquinha, P. M. C.; Pimentel, A. C. M. B. G.; Gonçalves, A. M. F.; Marques, A. J. S.; Pereira, L. M. N.; Martins, R. F. P. Fully Transparent ZnO Thin-Film Transistor Produced at Room Temperature. *Adv. Mater.* **2005**, *17*, 590−594.
(336) Lim, S. J.; Kwon, S.-j.; Kim, H.; Park, J.-S. High performance thin film transistor with low temperature atomic layer deposition nitrogen-doped ZnO. *Appl. Phys. Lett.* **2007**, *91*, 183517.
(337) Lim, S.; Kim, J.-M.; Kim, D.; Kwon, S.; Park, J.-S.; Kim, H. Atomic layer deposition ZnO: N thin film transistor: the effects of N concentration on the device properties. *J. Electrochem. Soc.* **2010**, *157*, H214.
(338) Iwasaki, T.; Itagaki, N.; Den, T.; Kumomi, H.; Nomura, K.; Kamiya, T.; Hosono, H. Combinatorial approach to thin-film transistors using multicomponent semiconductor channels: An application to amorphous oxide semiconductors in In−Ga−Zn−O system. *Appl. Phys. Lett.* **2007**, *90*, 242114.
(339) Jeong, J. K.; Jeong, J. H.; Yang, H. W.; Park, J.-S.; Mo, Y.-G.; Kim, H. D. High performance thin film transistors with cosputtered amorphous indium gallium zinc oxide channel. *Appl. Phys. Lett.* **2007**, *91*, 113505.
(340) Kolodziejczak-Radzimska, A.; Jesionowski, T. Zinc Oxide-From Synthesis to Application: A Review. *Materials* **2014**, *7*, 2833−2881.
(341) Le, A. T.; Ahmadipour, M.; Pung, S.-Y. A review on ZnO-based piezoelectric nanogenerators: Synthesis, characterization techniques, performance enhancement and applications. *J. Alloys Compd.* **2020**, *844*, 156172.
(342) Hjiri, M.; Bahanan, F.; Aida, M. S.; El Mir, L.; Neri, G. High Performance CO Gas Sensor Based on ZnO Nanoparticles. *J. Inorg. Organomet. Polym. Mater.* **2020**, *30*, 4063−4071.
(343) Yu, Z.; Gao, J.; Xu, L.; Liu, T.; Liu, Y.; Wang, X.; Suo, H.; Zhao, C. Fabrication of Lettuce-Like ZnO Gas Sensor with Enhanced H2S Gas Sensitivity. *Crystals* **2020**, *10*, 145.
(344) Chen, Y.; Liu, B.; Liu, J.; Pei, C.; Zhao, H.; Shang, Y.; Yang, H. Enhancing gas-sensing property and sensing mechanism at molecule level of the hollow microspheres assembled with ZnO nanoflakes exposing {001} facets. *J. Mater. Sci.: Mater. Electron.* **2020**, *31*, 6118−6129.
(345) Tonezzer, M.; Lacerda, R. G. Zinc oxide nanowires on carbon microfiber as flexible gas sensor. *Physica E* **2012**, *44*, 1098−1102.
(346) Xu, Q.; Cheng, L.; Meng, L.; Wang, Z.; Bai, S.; Tian, X.; Jia, X.; Qin, Y. Flexible Self-Powered ZnO Film UV Sensor with a High Response. *ACS Appl. Mater. Interfaces* **2019**, *11*, 26127−26133.
(347) Xue, X.; Nie, Y.; He, B.; Xing, L.; Zhang, Y.; Wang, Z. L. Surface free-carrier screening effect on the output of a ZnO nanowire nanogenerator and its potential as a self-powered active gas sensor. *Nanotechnology* **2013**, *24*, 225501.
(348) Park, T.; Lee, K. E.; Kim, N.; Oh, Y.; Yoo, J.-K.; Um, M.-K. Aspect ratio-controlled ZnO nanorods for highly sensitive wireless ultraviolet sensor applications. *J. Mater. Chem. C* **2017**, *5*, 12256−12263.
(349) Subbiah, D. K.; Mani, G. K.; Babu, K. J.; Das, A.; Balaguru Rayappan, J. B. Nanostructured ZnO on cotton fabrics − A novel flexible gas sensor & UV filter. *J. Cleaner Prod.* **2018**, *194*, 372−382.
(350) Zheng, Z. Q.; Yao, J. D.; Wang, B.; Yang, G. W. Light-controlling, flexible and transparent ethanol gas sensor based on ZnO nanoparticles for wearable devices. *Sci. Rep.* **2015**, *5*, 11070.
(351) He, Q.; Li, X.; Zhang, J.; Zhang, H.; Briscoe, J. P−N junction-based ZnO wearable textile nanogenerator for biomechanical energy harvesting. *Nano Energy* **2021**, *85*, 105938.
(352) Forsh, E. A.; Abakumov, A. M.; Zaytsev, V. B.; Konstantinova, E. A.; Forsh, P. A.; Rumyantseva, M. N.; Gaskov, A. M.; Kashkarov, P. K. Optical and photoelectrical properties of nanocrystalline indium oxide with small grains. *Thin Solid Films* **2015**, *595*, 25−31.
(353) Tomita, T.; Yamashita, K.; Hayafuji, Y.; Adachi, H. The origin of n-type conductivity in undoped In2O3. *Appl. Phys. Lett.* **2005**, *87*, 051911.
(354) Rupprecht, G. Untersuchungen der elektrischen und lichtelektrischen Leitfhigkeit dnner Indiumoxydschichten. *Z. Angew. Phys.* **1954**, *139*, 504−517.
(355) Kim, H.; Gilmore, C. M.; Piqué, A.; Horwitz, J. S.; Mattoussi, H.; Murata, H.; Kafafi, Z. H.; Chrisey, D. B. Electrical, optical, and structural properties of indium−tin−oxide thin films for organic light-emitting devices. *J. Appl. Phys.* **1999**, *86*, 6451−6461.
(356) Ma, Z.; Li, Z.; Liu, K.; Ye, C.; Sorger, V. J. Indium-Tin-Oxide for High-performance Electro-optic Modulation. *Nanophotonics* **2015**, *4*, 198−213.
(357) Abdullah, I.; Emyr Macdonald, J.; Lin, Y.-H.; Anthopoulos, T. D.; Salahr, N. H.; Anwar Kakil, S.; Muhammadsharif, F. F. Bias stability of solution-processed In2O3 thin film transistors. *J. Phys.: Mater.* **2021**, *4*, 015003.
(358) Bierwagen, O. Indium oxide—a transparent, wide-band gap semiconductor for (opto)electronic applications. *Semicond. Sci. Technol.* **2015**, *30*, 024001.
(359) Prasad, K. R.; Koga, K.; Miura, N. Electrochemical Deposition of Nanostructured Indium Oxide: High-Performance Electrode Material for Redox Supercapacitors. *Chem. Mater.* **2004**, *16*, 1845−1847.
(360) Jia, H.; Zhang, Y.; Chen, X.; Shu, J.; Luo, X.; Zhang, Z.; Yu, D. Efficient field emission from single crystalline indium oxide pyramids. *Appl. Phys. Lett.* **2003**, *82*, 4146−4148.
(361) Katoh, R.; Furube, A.; Yoshihara, T.; Hara, K.; Fujihashi, G.; Takano, S.; Murata, S.; Arakawa, H.; Tachiya, M. Efficiencies of Electron Injection from Excited N3 Dye into Nanocrystalline Semiconductor (ZrO2, TiO2, ZnO, Nb2O5, SnO2, In2O3) Films. *J. Phys. Chem. B* **2004**, *108*, 4818−4822.
(362) Cheng, Z.; Song, L.; Ren, X.; Zheng, Q.; Xu, J. Novel lotus root slice-like self-assembled In2O3 microspheres: Synthesis and NO2-sensing properties. *Sens. Actuators, B* **2013**, *176*, 258−263.
(363) Jun, L.; Chen, Q.; Fu, W.; Yang, Y.; Zhu, W.; Zhang, J. Electrospun Yb-Doped In2O3 Nanofiber Field-Effect Transistors for

https://doi.org/10.1021/acs.chemrev.3c00139
Chem. Rev. 2023, 123, 9982−10078

Highly Sensitive Ethanol Sensors. *ACS Appl. Mater. Interfaces* **2020**, *12*, 38425−38434.
(364) Liu, Q.; Liu, Y.; Wu, F.; Cao, X.; Li, Z.; Alharbi, M.; Abbas, A. N.; Amer, M. R.; Zhou, C. Highly Sensitive and Wearable In2O3 Nanoribbon Transistor Biosensors with Integrated On-Chip Gate for Glucose Monitoring in Body Fluids. *ACS Nano* **2018**, *12*, 1170−1178.
(365) Abbas, S.; Kumar, M.; Ban, D.-K.; Yun, J.-H.; Kim, J. Transparent and Flexible In2O3 Thin Film for Multilevel Nonvolatile Photomemory Programmed by Light. *ACS Appl. Electron. Mater.* **2019**, *1*, 437−443.
(366) Cheng, Z.-X.; Dong, X.-B.; Pan, Q.-Y.; Zhang, J.-c.; Dong, X.-W. Preparation and characterization of In2O3 nanorods. *Mater. Lett.* **2006**, *60*, 3137−3140.
(367) Wen, J. G.; Lao, J. Y.; Wang, D. Z.; Kyaw, T. M.; Foo, Y. L.; Ren, Z. F. Self-assembly of semiconducting oxide nanowires, nanorods, and nanoribbons. *Chem. Phys. Lett.* **2003**, *372*, 717−722.
(368) Kar, S.; Santra, S.; Chaudhuri, S. Direct Synthesis of Indium Nanotubes from Indium Metal Source. *Cryst. Growth Des.* **2008**, *8*, 344−346.
(369) Absi, E.; Saleh, M.; Al-Hada, N. M.; Hamzah, K.; Alhawsawi, A. M.; Banoqitah, E. M. A review on preparation and characterization of silver/nickel oxide nanostructures and their applications. *Appl. Phys. A: Mater. Sci. Process.* **2021**, *127*, 871.
(370) Baksh, H.; Buledi, J. A.; Khand, N. H.; Solangi, A. R.; Mallah, A.; Sherazi, S. T.; Abro, M. I. Ultra-selective determination of carbofuran by electrochemical sensor based on nickel oxide nanoparticles stabilized by ionic liquid. *Monatsh. Chem.* **2020**, *151*, 1689−1696.
(371) Adhikary, J.; Chakraborty, P.; Das, B.; Datta, A.; Dash, S. K.; Roy, S.; Chen, J.-W.; Chattopadhyay, T. Preparation and characterization of ferromagnetic nickel oxide nanoparticles from three different precursors: application in drug delivery. *RSC Adv.* **2015**, *5*, 35917−35928.
(372) Deevi, K.; Immareddy, V. S. R. Synthesis and characterization of optically transparent nickel oxide nanoparticles as a hole transport material for hybrid perovskite solar cells. *J. Mater. Sci.: Mater. Electron.* **2019**, *30*, 6242−6248.
(373) Wang, L.; Hao, Y.; Zhao, Y.; Lai, Q.; Xu, X. Hydrothermal synthesis and electrochemical performance of NiO microspheres with different nanoscale building blocks. *J. Solid State Chem.* **2010**, *183*, 2576−2581.
(374) Li, Y.; Chu, J.; Duan, W.; Cai, G.; Fan, X.; Wang, X.; Wang, G.; Pei, Y. Analog and Digital Bipolar Resistive Switching in Solution-Combustion-Processed NiO Memristor. *ACS Appl. Mater. Interfaces* **2018**, *10*, 24598−24606.
(375) Lee, D.; Paeng, D.; Park, H. K.; Grigoropoulos, C. P. Vacuum-free, maskless patterning of Ni electrodes by laser reductive sintering of NiO nanoparticle ink and its application to transparent conductors. *ACS Nano* **2014**, *8*, 9807−9814.
(376) Sharma, R.; Acharya, A. D.; Shrivastava, S. B.; Shripathi, T.; Ganesan, V. Preparation and characterization of transparent NiO thin films deposited by spray pyrolysis technique. *Optik* **2014**, *125*, 6751−6756.
(377) Kim, S. K.; Seok, H. J.; Kim, D. H.; Choi, D. H.; Nam, S. J.; Kim, S. C.; Kim, H. K. Comparison of NiOx thin film deposited by spin-coating or thermal evaporation for application as a hole transport layer of perovskite solar cells. *RSC Adv.* **2020**, *10*, 43847−43852.
(378) Acuña, J. R. A.; Perez, I.; Sosa, V.; Gamboa, F.; Elizalde, J. T.; Farías, R.; Carrillo, D.; Enríquez, J. L.; Burrola, A.; Mani, P. Sputtering power effects on the electrochromic properties of NiO films. *Optik* **2021**, *231*, 166509.
(379) Salunkhe, P.; A V, M. A.; Kekuda, D. Investigation on tailoring physical properties of Nickel Oxide thin films grown by dc magnetron sputtering. *Mater. Res. Express* **2020**, *7*, 016427.
(380) Carbone, M. NiO-Based Electronic Flexible Devices. *Applied Sciences* **2022**, *12*, 2839.
(381) Teoh, L. G.; Li, K.-D. Synthesis and Characterization of NiO Nanoparticles by Sol−Gel Method. *Mater. Trans.* **2012**, *53*, 2135−2140.
(382) Song, X.; Gao, L. Facile Synthesis of Polycrystalline NiO Nanorods Assisted by Microwave Heating. *J. Am. Ceram. Soc.* **2008**, *91*, 3465−3468.
(383) Tonezzer, M.; Dang, L. T. T.; Tran, H. Q.; Iannotta, S. Multiselective visual gas sensor using nickel oxide nanowires as chemiresistor. *Sens. Actuators, B* **2018**, *255*, 2785−2793.
(384) Zhu, Z.; Wei, N.; Liu, H.; He, Z. Microwave-assisted hydrothermal synthesis of Ni(OH)2 architectures and their in situ thermal convention to NiO. *Adv. Powder Technol.* **2011**, *22*, 422−426.
(385) Farhadi, S.; Roostaei-Zaniyani, Z. Preparation and characterization of NiO nanoparticles from thermal decomposition of the [Ni(en)3](NO3)2 complex: A facile and low-temperature route. *Polyhedron* **2011**, *30*, 971−975.
(386) Huang, C. C.; Kao, Z. K.; Liao, Y. C. Flexible miniaturized nickel oxide thermistor arrays via inkjet printing technology. *ACS Appl. Mater. Interfaces* **2013**, *5*, 12954−12959.
(387) Choi, W.; Choudhary, N.; Han, G. H.; Park, J.; Akinwande, D.; Lee, Y. H. Recent development of two-dimensional transition metal dichalcogenides and their applications. *Mater. Today* **2017**, *20*, 116−130.
(388) Yao, J.; Yang, G. 2D group 6 transition metal dichalcogenides toward wearable electronics and optoelectronics. *J. Appl. Phys.* **2020**, *127*, 030902.
(389) Dong, R.; Kuljanishvili, I. Review Article: Progress in fabrication of transition metal dichalcogenides heterostructure systems. *J. Vac. Sci. Technol., B* **2017**, *35*, 030803.
(390) Manzeli, S.; Ovchinnikov, D.; Pasquier, D.; Yazyev, O. V.; Kis, A. 2D transition metal dichalcogenides. *Nat. Rev. Mater.* **2017**, *2*, 17033.
(391) Sung, S. H.; Schnitzer, N.; Brown, L.; Park, J.; Hovden, R. Stacking, strain, and twist in 2D materials quantified by 3D electron diffraction. *Phys. Rev. Mater.* **2019**, *3*, 064003.
(392) Gan, X.; Lee, L. Y. S.; Wong, K.-y.; Lo, T. W.; Ho, K. H.; Lei, D. Y.; Zhao, H. 2H/1T Phase Transition of Multilayer MoS2 by Electrochemical Incorporation of S Vacancies. *ACS Appl. Energy Mater.* **2018**, *1*, 4754−4765.
(393) Joe, D. J.; Park, E.; Kim, D. H.; Doh, I.; Song, H.-C.; Kwak, J. Y. Graphene and Two-Dimensional Materials-Based Flexible Electronics for Wearable Biomedical Sensors. *Electronics* **2023**, *12*, 45.
(394) Wang, Y.; Li, T.; Li, Y.; Yang, R.; Zhang, G. 2D-Materials-Based Wearable Biosensor Systems. *Biosensors* **2022**, *12*, 936.
(395) Velicky, M.; Donnelly, G. E.; Hendren, W. R.; McFarland, S.; Scullion, D.; DeBenedetti, W. J. I.; Correa, G. C.; Han, Y.; Wain, A. J.; Hines, M. A.; et al. Mechanism of Gold-Assisted Exfoliation of Centimeter-Sized Transition-Metal Dichalcogenide Monolayers. *ACS Nano* **2018**, *12*, 10463−10472.
(396) Oh, J. Y.; Lee, J. H.; Han, S. W.; Chae, S. S.; Bae, E. J.; Kang, Y. H.; Choi, W. J.; Cho, S. Y.; Lee, J.-O.; Baik, H. K.; et al. Chemically exfoliated transition metal dichalcogenide nanosheet-based wearable thermoelectric generators. *Energy Environ. Sci.* **2016**, *9*, 1696−1705.
(397) Castellanos-Gomez, A.; Agraït, N.; Rubio-Bollinger, G. Optical identification of atomically thin dichalcogenide crystals. *Appl. Phys. Lett.* **2010**, *96*, 213116.
(398) Castellanos-Gomez, A.; Navarro-Moratalla, E.; Mokry, G.; Quereda, J.; Pinilla-Cienfuegos, E.; Agraït, N.; van der Zant, H. S. J.; Coronado, E.; Steele, G. A.; Rubio-Bollinger, G. Fast and reliable identification of atomically thin layers of TaSe2 crystals. *Nano Res.* **2013**, *6*, 191−199.
(399) Novoselov, K. S.; Jiang, D.; Schedin, F.; Booth, T. J.; Khotkevich, V. V.; Morozov, S. V.; Geim, A. K. Two-dimensional atomic crystals. *Proc. Natl. Acad. Sci. U.S.A.* **2005**, *102*, 10451−10453.
(400) Zhang, Y.; Yao, Y.; Sendeku, M. G.; Yin, L.; Zhan, X.; Wang, F.; Wang, Z.; He, J. Recent Progress in CVD Growth of 2D Transition Metal Dichalcogenides and Related Heterostructures. *Adv. Mater.* **2019**, *31*, 1901694.
(401) Cohen, A.; Patsha, A.; Mohapatra, P. K.; Kazes, M.; Ranganathan, K.; Houben, L.; Oron, D.; Ismach, A. Growth-Etch Metal-Organic Chemical Vapor Deposition Approach of WS2 Atomic Layers. *ACS Nano* **2021**, *15*, 526−538.

https://doi.org/10.1021/acs.chemrev.3c00139
Chem. Rev. 2023, 123, 9982−10078

(402) Mattinen, M.; Leskelä, M.; Ritala, M. Atomic Layer Deposition of 2D Metal Dichalcogenides for Electronics, Catalysis, Energy Storage, and Beyond. *Adv. Mater. Interfaces* **2021**, *8*, 2001677.
(403) Huang, C.; Wu, S.; Sanchez, A. M.; Peters, J. J.; Beanland, R.; Ross, J. S.; Rivera, P.; Yao, W.; Cobden, D. H.; Xu, X. Lateral heterojunctions within monolayer MoSe2−WSe2 semiconductors. *Nat. Mater.* **2014**, *13*, 1096−1101.
(404) Ellmer, K. Preparation routes based on magnetron sputtering for tungsten disulfide (WS2) films for thin-film solar cells. *Phys. Status Solidi B* **2008**, *245*, 1745−1760.
(405) Kang, K.; Xie, S.; Huang, L.; Han, Y.; Huang, P. Y.; Mak, K. F.; Kim, C. J.; Muller, D.; Park, J. High-mobility three-atom-thick semiconducting films with wafer-scale homogeneity. *Nature* **2015**, *520*, 656−660.
(406) Eichfeld, S. M.; Hossain, L.; Lin, Y. C.; Piasecki, A. F.; Kupp, B.; Birdwell, A. G.; Burke, R. A.; Lu, N.; Peng, X.; Li, J.; et al. Highly scalable, atomically thin WSe2 grown via metal-organic chemical vapor deposition. *ACS Nano* **2015**, *9*, 2080−2087.
(407) Lee, Y.; Lee, J.; Bark, H.; Oh, I. K.; Ryu, G. H.; Lee, Z.; Kim, H.; Cho, J. H.; Ahn, J. H.; Lee, C. Synthesis of wafer-scale uniform molybdenum disulfide films with control over the layer number using a gas phase sulfur precursor. *Nanoscale* **2014**, *6*, 2821−2826.
(408) Liu, J.; Zeng, Z.; Cao, X.; Lu, G.; Wang, L. H.; Fan, Q. L.; Huang, W.; Zhang, H. Preparation of MoS2-polyvinylpyrrolidone nanocomposites for flexible nonvolatile rewritable memory devices with reduced graphene oxide electrodes. *Small* **2012**, *8*, 3517−3522.
(409) Choi, M.; Park, Y. J.; Sharma, B. K.; Bae, S. R.; Kim, S. Y.; Ahn, J. H. Flexible active-matrix organic light-emitting diode display enabled by MoS2 thin-film transistor. *Sci. Adv.* **2018**, *4*, No. eaas8721.
(410) Kim, S.; Han, J.; Kang, M.-A.; Song, W.; Myung, S.; Kim, S.-W.; Lee, S. S.; Lim, J.; An, K.-S. Flexible chemical sensors based on hybrid layer consisting of molybdenum disulphide nanosheets and carbon nanotubes. *Carbon* **2018**, *129*, 607−612.
(411) Radisavljevic, B.; Radenovic, A.; Brivio, J.; Giacometti, V.; Kis, A. Single-layer MoS2 transistors. *Nat. Nanotechnol.* **2011**, *6*, 147−150.
(412) Iqbal, M. W.; Iqbal, M. Z.; Khan, M. F.; Shehzad, M. A.; Seo, Y.; Park, J. H.; Hwang, C.; Eom, J. High-mobility and air-stable single-layer WS2 field-effect transistors sandwiched between chemical vapor deposition-grown hexagonal BN films. *Sci. Rep.* **2015**, *5*, 10699.
(413) Larentis, S.; Fallahazad, B.; Tutuc, E. Field-effect transistors and intrinsic mobility in ultra-thin MoSe2 layers. *Appl. Phys. Lett.* **2012**, *101*, 223104.
(414) Movva, H. C.; Rai, A.; Kang, S.; Kim, K.; Fallahazad, B.; Taniguchi, T.; Watanabe, K.; Tutuc, E.; Banerjee, S. K. High-Mobility Holes in Dual-Gated WSe2 Field-Effect Transistors. *ACS Nano* **2015**, *9*, 10402−10410.
(415) Yoon, J.; Park, W.; Bae, G. Y.; Kim, Y.; Jang, H. S.; Hyun, Y.; Lim, S. K.; Kahng, Y. H.; Hong, W. K.; Lee, B. H.; et al. Highly flexible and transparent multilayer MoS2 transistors with graphene electrodes. *Small* **2013**, *9*, 3185.
(416) Ostroverkhova, O. *Handbook of Organic Materials for Electronic and Photonic Devices*; Woodhead Publishing, 2019.
(417) Martin-Palma, R. J.; Martinez-Duart, J. M. *Nanotechnology for Microelectronics and Photonics*; Elsevier, 2017.
(418) Wang, J.; Ye, D.; Meng, Q.; Di, C. a.; Zhu, D. Advances in Organic Transistor-Based Biosensors. *Adv. Mater. Technol.* **2020**, *5*, 2000218−2000218.
(419) Lee, M. Y.; Lee, H. R.; Park, C. H.; Han, S. G.; Oh, J. H. Organic Transistor-Based Chemical Sensors for Wearable Bioelectronics. *Acc. Chem. Res.* **2018**, *51*, 2829−2838.
(420) Rivnay, J.; Inal, S.; Salleo, A.; Owens, R. M.; Berggren, M.; Malliaras, G. G. Organic electrochemical transistors. *Nat. Rev. Mater.* **2018**, *3*, 17086.
(421) Lin, Y.; Li, Y.; Zhan, X. Small molecule semiconductors for high-efficiency organic photovoltaics. *Chem. Soc. Rev.* **2012**, *41*, 4245−4272.
(422) Ren, A.; Wang, H.; Zhang, W.; Wu, J.; Wang, Z.; Penty, R. V.; White, I. H. Emerging light-emitting diodes for next-generation data communications. *Nat. Electron.* **2021**, *4*, 559−572.
(423) Chua, L. L.; Zaumseil, J.; Chang, J. F.; Ou, E. C.; Ho, P. K.; Sirringhaus, H.; Friend, R. H. General observation of n-type field-effect behaviour in organic semiconductors. *Nature* **2005**, *434*, 194−199.
(424) Zaumseil, J.; Friend, R. H.; Sirringhaus, H. Spatial control of the recombination zone in an ambipolar light-emitting organic transistor. *Nat. Mater.* **2006**, *5*, 69−74.
(425) Bürgi, L.; Turbiez, M.; Pfeiffer, R.; Bienewald, F.; Kirner, H. J.; Winnewisser, C. High-mobility ambipolar near-infrared light-emitting polymer field-effect transistors. *Adv. Mater.* **2008**, *20*, 2217−2224.
(426) Roelofs, W. S. C.; Mathijssen, S. G. J.; Bijleveld, J. C.; Raiteri, D.; Geuns, T. C. T.; Kemerink, M.; Cantatore, E.; Janssen, R. A. J.; de Leeuw, D. M. Fast ambipolar integrated circuits with poly-(diketopyrrolopyrrole- terthiophene). *Appl. Phys. Lett.* **2011**, *98*, 203301.
(427) Jurchescu, O. D.; Popinciuc, M.; van Wees, B. J.; Palstra, T. T. M. Interface-Controlled, High-Mobility Organic Transistors. *Adv. Mater.* **2007**, *19*, 688−692.
(428) Singh, T. B.; Meghdadi, F.; Günes, S.; Marjanovic, N.; Horowitz, G.; Lang, P.; Bauer, S.; Sariciftci, N. S. High-Performance Ambipolar Pentacene Organic Field-Effect Transistors on Poly(vinyl alcohol) Organic Gate Dielectric. *Adv. Mater.* **2005**, *17*, 2315−2320.
(429) Jurchescu, O. D.; Baas, J.; Palstra, T. T. M. Effect of impurities on the mobility of single crystal pentacene. *Appl. Phys. Lett.* **2004**, *84*, 3061−3063.
(430) Zeis, R.; Besnard, C.; Siegrist, T.; Schlockermann, C.; Chi, X.; Kloc, C. Field Effect Studies on Rubrene and Impurities of Rubrene. *Chem. Mater.* **2006**, *18*, 244−248.
(431) Anthony, J. E.; Brooks, J. S.; Eaton, D. L.; Parkin, S. R. Functionalized pentacene: improved electronic properties from control of solid-state order. *J. Am. Chem. Soc.* **2001**, *123*, 9482−9483.
(432) Sheraw, C. D.; Jackson, T. N.; Eaton, D. L.; Anthony, J. E. Functionalized Pentacene Active Layer Organic Thin-Film Transistors. *Adv. Mater.* **2003**, *15*, 2009−2011.
(433) Jurchescu, O. D.; Subramanian, S.; Kline, R. J.; Hudson, S. D.; Anthony, J. E.; Jackson, T. N.; Gundlach, D. J. Organic Single-Crystal Field-Effect Transistors of a Soluble Anthradithiophene. *Chem. Mater.* **2008**, *20*, 6733−6737.
(434) Kline, R. J.; Hudson, S. D.; Zhang, X.; Gundlach, D. J.; Moad, A. J.; Jurchescu, O. D.; Jackson, T. N.; Subramanian, S.; Anthony, J. E.; Toney, M. F.; et al. Controlling the Microstructure of Solution-Processable Small Molecules in Thin-Film Transistors through Substrate Chemistry. *Chem. Mater.* **2011**, *23*, 1194−1203.
(435) Minemawari, H.; Yamada, T.; Matsui, H.; Tsutsumi, J.; Haas, S.; Chiba, R.; Kumai, R.; Hasegawa, T. Inkjet printing of single-crystal films. *Nature* **2011**, *475*, 364−367.
(436) Ebata, H.; Izawa, T.; Miyazaki, E.; Takimiya, K.; Ikeda, M.; Kuwabara, H.; Yui, T. Highly soluble [1]benzothieno[3,2-b]-benzothiophene (BTBT) derivatives for high-performance, solution-processed organic field-effect transistors. *J. Am. Chem. Soc.* **2007**, *129*, 15732−15733.
(437) Uemura, T.; Nakayama, K.; Hirose, Y.; Soeda, J.; Uno, M.; Li, W.; Yamagishi, M.; Okada, Y.; Takeya, J. Band-like transport in solution-crystallized organic transistors. *Curr. Appl. Phys.* **2012**, *12*, S87−S91.
(438) Nakayama, K.; Hirose, Y.; Soeda, J.; Yoshizumi, M.; Uemura, T.; Uno, M.; Li, W.; Kang, M. J.; Yamagishi, M.; Okada, Y.; et al. Patternable solution-crystallized organic transistors with high charge carrier mobility. *Adv. Mater.* **2011**, *23*, 1626−1629.
(439) Lee, E. K.; Lee, M. Y.; Park, C. H.; Lee, H. R.; Oh, J. H. Toward Environmentally Robust Organic Electronics: Approaches and Applications. *Adv. Mater.* **2017**, *29*, 1703638.
(440) Yokota, T.; Kuribara, K.; Tokuhara, T.; Zschieschang, U.; Klauk, H.; Takimiya, K.; Sadamitsu, Y.; Hamada, M.; Sekitani, T.; Someya, T. Flexible low-voltage organic transistors with high thermal stability at 250 degrees C. *Adv. Mater.* **2013**, *25*, 3639−3644.
(441) Venkateshvaran, D.; Nikolka, M.; Sadhanala, A.; Lemaur, V.; Zelazny, M.; Kepa, M.; Hurhangee, M.; Kronemeijer, A. J.; Pecunia,

V.; Nasrallah, I.; et al. Approaching disorder-free transport in high-mobility conjugated polymers. *Nature* **2014**, *515*, 384−388.
(442) McCulloch, I.; Heeney, M.; Chabinyc, M. L.; DeLongchamp, D.; Kline, R. J.; Cölle, M.; Duffy, W.; Fischer, D.; Gundlach, D.; Hamadani, B.; et al. Semiconducting Thienothiophene Copolymers: Design, Synthesis, Morphology, and Performance in Thin-Film Organic Transistors. *Adv. Mater.* **2009**, *21*, 1091−1109.
(443) Ong, B. S.; Wu, Y.; Liu, P.; Gardner, S. High-performance semiconducting polythiophenes for organic thin-film transistors. *J. Am. Chem. Soc.* **2004**, *126*, 3378−3379.
(444) Goncalves, R.; Pereira, E. C.; Marchesi, L. F. The Overoxidation of poly(3-hexylthiophene) (P3HT) Thin Film: CV and EIS measurements. *Int. J. Electrochem. Sci.* **2017**, *12*, 1983−1991.
(445) Sarhan, A. A.; Bolm, C. Iron(III) chloride in oxidative C-C coupling reactions. *Chem. Soc. Rev.* **2009**, *38*, 2730−2744.
(446) Loewe, R. S.; Ewbank, P. C.; Liu, J.; Zhai, L.; McCullough, R. D. Regioregular, Head-to-Tail Coupled Poly(3-alkylthiophenes) Made Easy by the GRIM Method: Investigation of the Reaction and the Origin of Regioselectivity. *Macromolecules* **2001**, *34*, 4324−4333.
(447) Chen, T.-A.; Wu, X.; Rieke, R. D. Regiocontrolled Synthesis of Poly(3-alkylthiophenes) Mediated by Rieke Zinc: Their Characterization and Solid-State Properties. *J. Am. Chem. Soc.* **1995**, *117*, 233−244.
(448) Wang, Q.; Takita, R.; Kikuzaki, Y.; Ozawa, F. Palladium-catalyzed dehydrohalogenative polycondensation of 2-bromo-3-hexylthiophene: an efficient approach to head-to-tail poly(3-hexylthiophene). *J. Am. Chem. Soc.* **2010**, *132*, 11420−11421.
(449) Kline, R. J.; McGehee, M. D.; Kadnikova, E. N.; Liu, J.; Fréchet, J. M. J.; Toney, M. F. Dependence of Regioregular Poly(3-hexylthiophene) Film Morphology and Field-Effect Mobility on Molecular Weight. *Macromolecules* **2005**, *38*, 3312−3319.
(450) Zen, A.; Pflaum, J.; Hirschmann, S.; Zhuang, W.; Jaiser, F.; Asawapirom, U.; Rabe, J. P.; Scherf, U.; Neher, D. Effect of Molecular Weight and Annealing of Poly(3-hexylthiophene)s on the Performance of Organic Field-Effect Transistors. *Adv. Funct. Mater.* **2004**, *14*, 757−764.
(451) Rodriquez, D.; Kim, J. H.; Root, S. E.; Fei, Z.; Boufflet, P.; Heeney, M.; Kim, T. S.; Lipomi, D. J. Comparison of Methods for Determining the Mechanical Properties of Semiconducting Polymer Films for Stretchable Electronics. *ACS Appl. Mater. Interfaces* **2017**, *9*, 8855−8862.
(452) Kim, J.-S.; Kim, J.-H.; Lee, W.; Yu, H.; Kim, H. J.; Song, I.; Shin, M.; Oh, J. H.; Jeong, U.; Kim, T.-S.; et al. Tuning Mechanical and Optoelectrical Properties of Poly(3-hexylthiophene) through Systematic Regioregularity Control. *Macromolecules* **2015**, *48*, 4339−4346.
(453) Liu, X.; He, B.; Garzón-Ruiz, A.; Navarro, A.; Chen, T. L.; Kolaczkowski, M. A.; Feng, S.; Zhang, L.; Anderson, C. A.; Chen, J.; et al. Unraveling the Main Chain and Side Chain Effects on Thin Film Morphology and Charge Transport in Quinoidal Conjugated Polymers. *Adv. Funct. Mater.* **2018**, *28*, 1801874.
(454) Sugiyama, F.; Kleinschmidt, A. T.; Kayser, L. V.; Rodriquez, D.; Finn, M., 3rd; Alkhadra, M. A.; Wan, J. M.; Ramirez, J.; Chiang, A. S.; Root, S. E.; et al. Effects of flexibility and branching of side chains on the mechanical properties of low-bandgap conjugated polymers. *Polym. Chem.* **2018**, *9*, 4354−4363.
(455) Shin, M.; Oh, J. Y.; Byun, K. E.; Lee, Y. J.; Kim, B.; Baik, H. K.; Park, J. J.; Jeong, U. Polythiophene nanofibril bundles surface-embedded in elastomer: a route to a highly stretchable active channel layer. *Adv. Mater.* **2015**, *27*, 1255−1261.
(456) O'Connor, B.; Chan, E. P.; Chan, C.; Conrad, B. R.; Richter, L. J.; Kline, R. J.; Heeney, M.; McCulloch, I.; Soles, C. L.; DeLongchamp, D. M. Correlations between mechanical and electrical properties of polythiophenes. *ACS Nano* **2010**, *4*, 7538−7544.
(457) Yang, J.; Zhao, Z.; Wang, S.; Guo, Y.; Liu, Y. Insight into High-Performance Conjugated Polymers for Organic Field-Effect Transistors. *Chem.* **2018**, *4*, 2748−2785.
(458) Zou, X.; Cui, S.; Li, J.; Wei, X.; Zheng, M. Diketopyrrolopyrrole Based Organic Semiconductor Materials for Field-Effect Transistors. *Front. Chem.* **2021**, *9*, 671294.
(459) Park, J.; Kim, J.; Kim, S. Y.; Cheong, W. H.; Jang, J.; Park, Y. G.; Na, K.; Kim, Y. T.; Heo, J. H.; Lee, C. Y.; et al. Soft, smart contact lenses with integrations of wireless circuits, glucose sensors, and displays. *Sci. Adv.* **2018**, *4*, No. eaap9841.
(460) Kim, J.; Kim, M.; Lee, M. S.; Kim, K.; Ji, S.; Kim, Y. T.; Park, J.; Na, K.; Bae, K. H.; Kyun Kim, H.; et al. Wearable smart sensor systems integrated on soft contact lenses for wireless ocular diagnostics. *Nat. Commun.* **2017**, *8*, 14997.
(461) Araki, T.; Yoshida, F.; Uemura, T.; Noda, Y.; Yoshimoto, S.; Kaiju, T.; Suzuki, T.; Hamanaka, H.; Baba, K.; Hayakawa, H.; et al. Long-Term Implantable, Flexible, and Transparent Neural Interface Based on Ag/Au Core-Shell Nanowires. *Adv. Healthcare Mater.* **2019**, *8*, 1900130.
(462) Thunemann, M.; Lu, Y.; Liu, X.; Kilic, K.; Desjardins, M.; Vandenberghe, M.; Sadegh, S.; Saisan, P. A.; Cheng, Q.; Weldy, K. L.; et al. Deep 2-photon imaging and artifact-free optogenetics through transparent graphene microelectrode arrays. *Nat. Commun.* **2018**, *9*, 2035.
(463) Choi, S.-J.; Kim, S.-J.; Kim, I.-D. Ultrafast optical reduction of graphene oxide sheets on colorless polyimide film for wearable chemical sensors. *NPG Asia Mater.* **2016**, *8*, No. e315.
(464) Bell, C.; Nammari, A.; Uttamchandani, P.; Rai, A.; Shah, P.; Moore, A. L. Flexible electronics-compatible non-enzymatic glucose sensing via transparent CuO nanowire networks on PET films. *Nanotechnology* **2017**, *28*, 245502.
(465) Wang, T.; Guo, Y.; Wan, P.; Sun, X.; Zhang, H.; Yu, Z.; Chen, X. A flexible transparent colorimetric wrist strap sensor. *Nanoscale* **2017**, *9*, 869−874.
(466) Choi, S. J.; Kim, S. J.; Jang, J. S.; Lee, J. H.; Kim, I. D. Silver Nanowire Embedded Colorless Polyimide Heater for Wearable Chemical Sensors: Improved Reversible Reaction Kinetics of Optically Reduced Graphene Oxide. *Small* **2016**, *12*, 5826−5835.
(467) Spanu, A.; Mascia, A.; Baldazzi, G.; Fenech-Salerno, B.; Torrisi, F.; Viola, G.; Bonfiglio, A.; Cosseddu, P.; Pani, D. Parylene C-Based, Breathable Tattoo Electrodes for High-Quality Bio-Potential Measurements. *Front. Bioeng. Biotechnol.* **2022**, *10*, 820217.
(468) Liu, Z.; Zhao, Z.; Zeng, X.; Fu, X.; Hu, Y. Ultrathin, flexible and transparent graphene-based triboelectric nanogenerators for attachable curvature monitoring. *J. Phys. D: Appl. Phys.* **2019**, *52*, 314002.
(469) Hassan, M.; Abbas, G.; Li, N.; Afzal, A.; Haider, Z.; Ahmed, S.; Xu, X.; Pan, C.; Peng, Z. Significance of flexible substrates for wearable and implantable devices: Recent advances and perspectives. *Adv. Mater. Technol.* **2022**, *7*, 2100773.
(470) Chen, J.; Zheng, J.; Gao, Q.; Zhang, J.; Zhang, J.; Omisore, O.; Wang, L.; Li, H. Polydimethylsiloxane (PDMS)-Based Flexible Resistive Strain Sensors for Wearable Applications. *Applied Sciences* **2018**, *8*, 345.
(471) Lee, S.; Franklin, S.; Hassani, F. A.; Yokota, T.; Nayeem, M. O. G.; Wang, Y.; Leib, R.; Cheng, G.; Franklin, D. W.; Someya, T. Nanomesh pressure sensor for monitoring finger manipulation without sensory interference. *Science* **2020**, *370*, 966−970.
(472) Wolf, M. P.; Salieb-Beugelaar, G. B.; Hunziker, P. PDMS with designer functionalities—Properties, modifications strategies, and applications. *Prog. Polym. Sci.* **2018**, *83*, 97−134.
(473) Qi, D.; Zhang, K.; Tian, G.; Jiang, B.; Huang, Y. Stretchable Electronics Based on PDMS Substrates. *Adv. Mater.* **2021**, *33*, 2003155.
(474) Kalra, A.; Lowe, A.; Al-Jumaily, A. Mechanical behaviour of skin: a review. *J. Mater. Sci. Eng.* **2016**, *5*, 1000254.
(475) Kim, J.; Cho, D.-i.; Muller, R. S., Why is (111) silicon a better mechanical material for MEMS?, *Transducers' 01 Eurosensors XV: The 11th International Conference on Solid-State Sensors and Actuators June 10−14, 2001, Munich, Germany*, 2001.

https://doi.org/10.1021/acs.chemrev.3c00139
Chem. Rev. 2023, 123, 9982−10078

(476) Hopcroft, M. A.; Nix, W. D.; Kenny, T. W. What is the Young's Modulus of Silicon? *J. Microelectromech. Syst.* **2010**, *19*, 229−238.
(477) Ying, B.; Liu, X. Skin-like hydrogel devices for wearable sensing, soft robotics and beyond. *iScience* **2021**, *24*, 103174.
(478) Spencer, K. C.; Sy, J. C.; Ramadi, K. B.; Graybiel, A. M.; Langer, R.; Cima, M. J. Characterization of Mechanically Matched Hydrogel Coatings to Improve the Biocompatibility of Neural Implants. *Sci. Rep.* **2017**, *7*, 1952.
(479) Liu, Y.; Yang, T.; Zhang, Y.; Qu, G.; Wei, S.; Liu, Z.; Kong, T. Ultrastretchable and Wireless Bioelectronics Based on All-Hydrogel Microfluidics. *Adv. Mater.* **2019**, *31*, 1902783.
(480) Lin, S.; Yuk, H.; Zhang, T.; Parada, G. A.; Koo, H.; Yu, C.; Zhao, X. Stretchable Hydrogel Electronics and Devices. *Adv. Mater.* **2016**, *28*, 4497−4505.
(481) Gupta, P. K.; Raghunath, S. S.; Prasanna, D. V.; Venkat, P.; Shree, V.; Chithananthan, C.; Choudhary, S.; Surender, K.; Geetha, K.An update on overview of cellulose, its structure and applications. In *Cellulose*; IntechOpen, 2019; Vol. *201*, p 84727.
(482) Dulal, M.; Afroj, S.; Ahn, J.; Cho, Y.; Carr, C.; Kim, I. D.; Karim, N. Toward Sustainable Wearable Electronic Textiles. *ACS Nano* **2022**, *16*, 19755−19788.
(483) Zhao, G.; Lyu, X.; Lee, J.; Cui, X.; Chen, W.-N. Biodegradable and transparent cellulose film prepared eco-friendly from durian rind for packaging application. *Food Packag. Shelf Life* **2019**, *21*, 100345.
(484) Jiang, F.; Hsieh, Y. L. Chemically and mechanically isolated nanocellulose and their self-assembled structures. *Carbohydr. Polym.* **2013**, *95*, 32−40.
(485) Koga, H.; Saito, T.; Kitaoka, T.; Nogi, M.; Suganuma, K.; Isogai, A. Transparent, conductive, and printable composites consisting of TEMPO-oxidized nanocellulose and carbon nanotube. *Biomacromolecules* **2013**, *14*, 1160−1165.
(486) Isobe, N.; Kasuga, T.; Nogi, M. Clear transparent cellulose nanopaper prepared from a concentrated dispersion by high-humidity drying. *RSC Adv.* **2018**, *8*, 1833−1837.
(487) Kang, W.; Yan, C.; Foo, C. Y.; Lee, P. S. Foldable Electrochromics Enabled by Nanopaper Transfer Method. *Adv. Funct. Mater.* **2015**, *25*, 4203−4210.
(488) Kasuga, T.; Yagyu, H.; Uetani, K.; Koga, H.; Nogi, M. Cellulose Nanofiber Coatings on Cu Electrodes for Cohesive Protection against Water-Induced Short-Circuit Failures. *ACS Appl. Nano Mater.* **2021**, *4*, 3861−3868.
(489) Haacke, G. New figure of merit for transparent conductors. *J. Appl. Phys.* **1976**, *47*, 4086−4089.
(490) Juvaid, M. M.; Sarkar, S.; Gogoi, P. K.; Ghosh, S.; Annamalai, M.; Lin, Y. C.; Prakash, S.; Goswami, S.; Li, C.; Hooda, S.; et al. Direct Growth of Wafer-Scale, Transparent, p-Type Reduced-Graphene-Oxide-like Thin Films by Pulsed Laser Deposition. *ACS Nano* **2020**, *14*, 3290−3298.
(491) Kim, M.; Nabeya, S.; Han, S. M.; Kim, M. S.; Lee, S.; Kim, H. M.; Cho, S. Y.; Lee, D. J.; Kim, S. H.; Kim, K. B. Selective Atomic Layer Deposition of Metals on Graphene for Transparent Conducting Electrode Application. *ACS Appl. Mater. Interfaces* **2020**, *12*, 14331−14340.
(492) Song, J.; Kam, F. Y.; Png, R. Q.; Seah, W. L.; Zhuo, J. M.; Lim, G. K.; Ho, P. K.; Chua, L. L. A general method for transferring graphene onto soft surfaces. *Nat. Nanotechnol.* **2013**, *8*, 356−362.
(493) Song, M.; You, D. S.; Lim, K.; Park, S.; Jung, S.; Kim, C. S.; Kim, D.-H.; Kim, D.-G.; Kim, J.-K.; Park, J.; et al. Highly Efficient and Bendable Organic Solar Cells with Solution-Processed Silver Nanowire Electrodes. *Adv. Funct. Mater.* **2013**, *23*, 4177−4184.
(494) Jo, J. W.; Jung, J. W.; Lee, J. U.; Jo, W. H. Fabrication of highly conductive and transparent thin films from single-walled carbon nanotubes using a new non-ionic surfactant via spin coating. *ACS Nano* **2010**, *4*, 5382−5388.
(495) Badre, C.; Marquant, L.; Alsayed, A. M.; Hough, L. A. Highly Conductive Poly(3,4-ethylenedioxythiophene):Poly (styrenesulfonate) Films Using 1-Ethyl-3-methylimidazolium Tetracyanoborate Ionic Liquid. *Adv. Funct. Mater.* **2012**, *22*, 2723−2727.
(496) Higgins, T. M.; Coleman, J. N. Avoiding Resistance Limitations in High-Performance Transparent Supercapacitor Electrodes Based on Large-Area, High-Conductivity PEDOT:PSS Films. *ACS Appl. Mater. Interfaces* **2015**, *7*, 16495−16506.
(497) Scardaci, V.; Coull, R.; Lyons, P. E.; Rickard, D.; Coleman, J. N. Spray deposition of highly transparent, low-resistance networks of silver nanowires over large areas. *Small* **2011**, *7*, 2621−2628.
(498) Lyons, P. E.; De, S.; Elias, J.; Schamel, M.; Philippe, L.; Bellew, A. T.; Boland, J. J.; Coleman, J. N. High-Performance Transparent Conductors from Networks of Gold Nanowires. *J. Phys. Chem. Lett.* **2011**, *2*, 3058−3062.
(499) Wu, H.; Kong, D.; Ruan, Z.; Hsu, P. C.; Wang, S.; Yu, Z.; Carney, T. J.; Hu, L.; Fan, S.; Cui, Y. A transparent electrode based on a metal nanotrough network. *Nat. Nanotechnol.* **2013**, *8*, 421−425.
(500) Wu, H.; Hu, L.; Rowell, M. W.; Kong, D.; Cha, J. J.; McDonough, J. R.; Zhu, J.; Yang, Y.; McGehee, M. D.; Cui, Y. Electrospun metal nanofiber webs as high-performance transparent electrode. *Nano Lett.* **2010**, *10*, 4242−4248.
(501) Maurer, J. H.; Gonzalez-Garcia, L.; Reiser, B.; Kanelidis, I.; Kraus, T. Templated Self-Assembly of Ultrathin Gold Nanowires by Nanoimprinting for Transparent Flexible Electronics. *Nano Lett.* **2016**, *16*, 2921−2925.
(502) Khan, A.; Liang, C.; Huang, Y.-T.; Zhang, C.; Cai, J.; Feng, S.-P.; Li, W.-D. Template-Electrodeposited and Imprint-Transferred Microscale Metal-Mesh Transparent Electrodes for Flexible and Stretchable Electronics. *Adv. Eng. Mater.* **2019**, *21*, 1900723.
(503) Li, L.; Zhang, B.; Zou, B.; Xie, R.; Zhang, T.; Li, S.; Zheng, B.; Wu, J.; Weng, J.; Zhang, W.; et al. Fabrication of Flexible Transparent Electrode with Enhanced Conductivity from Hierarchical Metal Grids. *ACS Appl. Mater. Interfaces* **2017**, *9*, 39110−39115.
(504) Jin, Y.; Cheng, Y.; Deng, D.; Jiang, C.; Qi, T.; Yang, D.; Xiao, F. Site-selective growth of patterned silver grid networks as flexible transparent conductive film by using poly(dopamine) at room temperature. *ACS Appl. Mater. Interfaces* **2014**, *6*, 1447−1453.
(505) Paeng, D.; Yoo, J. H.; Yeo, J.; Lee, D.; Kim, E.; Ko, S. H.; Grigoropoulos, C. P. Low-cost facile fabrication of flexible transparent copper electrodes by nanosecond laser ablation. *Adv. Mater.* **2015**, *27*, 2762−2767.
(506) Kim, K. K.; Ha, I.; Won, P.; Seo, D. G.; Cho, K. J.; Ko, S. H. Transparent wearable three-dimensional touch by self-generated multiscale structure. *Nat. Commun.* **2019**, *10*, 2582.
(507) Kang, J.; Jang, Y.; Kim, Y.; Cho, S. H.; Suhr, J.; Hong, B. H.; Choi, J. B.; Byun, D. An Ag-grid/graphene hybrid structure for large-scale, transparent, flexible heaters. *Nanoscale* **2015**, *7*, 6567−6573.
(508) Jiang, J.; Bao, B.; Li, M.; Sun, J.; Zhang, C.; Li, Y.; Li, F.; Yao, X.; Song, Y. Fabrication of Transparent Multilayer Circuits by Inkjet Printing. *Adv. Mater.* **2016**, *28*, 1420−1426.
(509) Zhang, S.; Park, J. G.; Nguyen, N.; Jolowsky, C.; Hao, A.; Liang, R. Ultra-high conductivity and metallic conduction mechanism of scale-up continuous carbon nanotube sheets by mechanical stretching and stable chemical doping. *Carbon* **2017**, *125*, 649−658.
(510) Lee, Y.-Y.; Lee, J.-H.; Cho, J.-Y.; Kim, N.-R.; Nam, D.-H.; Choi, I.-S.; Nam, K. T.; Joo, Y.-C. Stretching-Induced Growth of PEDOT-Rich Cores: A New Mechanism for Strain-Dependent Resistivity Change in PEDOT:PSS Films. *Adv. Funct. Mater.* **2013**, *23*, 4020−4027.
(511) Huang, Y.; Rui, G.; Li, Q.; Allahyarov, E.; Li, R.; Fukuto, M.; Zhong, G. J.; Xu, J. Z.; Li, Z. M.; Taylor, P. L.; et al. Enhanced piezoelectricity from highly polarizable oriented amorphous fractions in biaxially oriented poly(vinylidene fluoride) with pure beta crystals. *Nat. Commun.* **2021**, *12*, 675.
(512) Kang, S.; Kim, T.; Cho, S.; Lee, Y.; Choe, A.; Walker, B.; Ko, S. J.; Kim, J. Y.; Ko, H. Capillary Printing of Highly Aligned Silver Nanowire Transparent Electrodes for High-Performance Optoelectronic Devices. *Nano Lett.* **2015**, *15*, 7933−7942.
(513) Giri, G.; DeLongchamp, D. M.; Reinspach, J.; Fischer, D. A.; Richter, L. J.; Xu, J.; Benight, S.; Ayzner, A.; He, M.; Fang, L.; et al. Effect of Solution Shearing Method on Packing and Disorder of

https://doi.org/10.1021/acs.chemrev.3c00139
Chem. Rev. 2023, 123, 9982−10078

Organic Semiconductor Polymers. *Chem. Mater.* **2015**, *27*, 2350−2359.
(514) Worfolk, B. J.; Andrews, S. C.; Park, S.; Reinspach, J.; Liu, N.; Toney, M. F.; Mannsfeld, S. C.; Bao, Z. Ultrahigh electrical conductivity in solution-sheared polymeric transparent films. *Proc. Natl. Acad. Sci. U.S.A.* **2015**, *112*, 14138−14143.
(515) Jung, D.; Lim, C.; Shim, H. J.; Kim, Y.; Park, C.; Jung, J.; Han, S. I.; Sunwoo, S. H.; Cho, K. W.; Cha, G. D.; et al. Highly conductive and elastic nanomembrane for skin electronics. *Science* **2021**, *373*, 1022−1026.
(516) Park, J. H.; Han, S.; Kim, D.; You, B. K.; Joe, D. J.; Hong, S.; Seo, J.; Kwon, J.; Jeong, C. K.; Park, H.-J.; et al. Plasmonic-Tuned Flash Cu Nanowelding with Ultrafast Photochemical-Reducing and Interlocking on Flexible Plastics. *Adv. Funct. Mater.* **2017**, *27*, 1701138.
(517) Liu, Y.; Zhang, J.; Gao, H.; Wang, Y.; Liu, Q.; Huang, S.; Guo, C. F.; Ren, Z. Capillary-Force-Induced Cold Welding in Silver-Nanowire-Based Flexible Transparent Electrodes. *Nano Lett.* **2017**, *17*, 1090−1096.
(518) Nevrela, J.; Micjan, M.; Novota, M.; Kovacova, S.; Pavuk, M.; Juhasz, P.; Kovac, J.; Jakabovic, J.; Weis, M. Secondary doping in poly(3,4-ethylenedioxythiophene):Poly(4-styrenesulfonate) thin films. *J. Polym. Sci., Part B: Polym. Phys.* **2015**, *53*, 1139−1146.
(519) Kim, N.; Kang, H.; Lee, J. H.; Kee, S.; Lee, S. H.; Lee, K. Highly conductive all-plastic electrodes fabricated using a novel chemically controlled transfer-printing method. *Adv. Mater.* **2015**, *27*, 2317−2323.
(520) Zhang, Y.; Ng, S. W.; Lu, X.; Zheng, Z. Solution-Processed Transparent Electrodes for Emerging Thin-Film Solar Cells. *Chem. Rev.* **2020**, *120*, 2049−2122.
(521) Hall, D. B.; Underhill, P.; Torkelson, J. M. Spin coating of thin and ultrathin polymer films. *Polym. Eng. Sci.* **1998**, *38*, 2039−2045.
(522) Tokuno, T.; Nogi, M.; Karakawa, M.; Jiu, J.; Nge, T. T.; Aso, Y.; Suganuma, K. Fabrication of silver nanowire transparent electrodes at room temperature. *Nano Res.* **2011**, *4*, 1215−1222.
(523) Becerril, H. A.; Mao, J.; Liu, Z.; Stoltenberg, R. M.; Bao, Z.; Chen, Y. Evaluation of solution-processed reduced graphene oxide films as transparent conductors. *ACS Nano* **2008**, *2*, 463−470.
(524) Vosgueritchian, M.; Lipomi, D. J.; Bao, Z. Highly Conductive and Transparent PEDOT:PSS Films with a Fluorosurfactant for Stretchable and Flexible Transparent Electrodes. *Adv. Funct. Mater.* **2012**, *22*, 421−428.
(525) Chang, H.; Wang, G.; Yang, A.; Tao, X.; Liu, X.; Shen, Y.; Zheng, Z. A Transparent, Flexible, Low-Temperature, and Solution-Processible Graphene Composite Electrode. *Adv. Funct. Mater.* **2010**, *20*, 2893−2902.
(526) Abdellah, A.; Fabel, B.; Lugli, P.; Scarpa, G. Spray deposition of organic semiconducting thin-films: Towards the fabrication of arbitrary shaped organic electronic devices. *Org. Electron.* **2010**, *11*, 1031−1038.
(527) Tenent, R. C.; Barnes, T. M.; Bergeson, J. D.; Ferguson, A. J.; To, B.; Gedvilas, L. M.; Heben, M. J.; Blackburn, J. L. Ultrasmooth, Large-Area, High-Uniformity, Conductive Transparent Single-Walled-Carbon-Nanotube Films for Photovoltaics Produced by Ultrasonic Spraying. *Adv. Mater.* **2009**, *21*, 3210−3216.
(528) Li, Z.; Jia, Y.; Wei, J.; Wang, K.; Shu, Q.; Gui, X.; Zhu, H.; Cao, A.; Wu, D. Large area, highly transparent carbon nanotube spiderwebs for energy harvesting. *J. Mater. Chem.* **2010**, *20*, 7236−7240.
(529) Pham, V. H.; Cuong, T. V.; Hur, S. H.; Shin, E. W.; Kim, J. S.; Chung, J. S.; Kim, E. J. Fast and simple fabrication of a large transparent chemically-converted graphene film by spray-coating. *Carbon* **2010**, *48*, 1945−1951.
(530) Kim, T.; Canlier, A.; Kim, G. H.; Choi, J.; Park, M.; Han, S. M. Electrostatic spray deposition of highly transparent silver nanowire electrode on flexible substrate. *ACS Appl. Mater. Interfaces* **2013**, *5*, 788−794.
(531) Gorkina, A. L.; Tsapenko, A. P.; Gilshteyn, E. P.; Koltsova, T. S.; Larionova, T. V.; Talyzin, A.; Anisimov, A. S.; Anoshkin, I. V.; Kauppinen, E. I.; Tolochko, O. V.; et al. Transparent and conductive hybrid graphene/carbon nanotube films. *Carbon* **2016**, *100*, 501−507.
(532) Jung, J.; Lee, H.; Ha, I.; Cho, H.; Kim, K. K.; Kwon, J.; Won, P.; Hong, S.; Ko, S. H. Highly Stretchable and Transparent Electromagnetic Interference Shielding Film Based on Silver Nanowire Percolation Network for Wearable Electronics Applications. *ACS Appl. Mater. Interfaces* **2017**, *9*, 44609−44616.
(533) Eda, G.; Fanchini, G.; Chhowalla, M. Large-area ultrathin films of reduced graphene oxide as a transparent and flexible electronic material. *Nat. Nanotechnol.* **2008**, *3*, 270−274.
(534) De, S.; King, P. J.; Lotya, M.; O'Neill, A.; Doherty, E. M.; Hernandez, Y.; Duesberg, G. S.; Coleman, J. N. Flexible, transparent, conducting films of randomly stacked graphene from surfactant-stabilized, oxide-free graphene dispersions. *Small* **2010**, *6*, 458−464.
(535) Aloui, W.; Ltaief, A.; Bouazizi, A. Transparent and conductive multi walled carbon nanotubes flexible electrodes for optoelectronic applications. *Superlattices Microstruct.* **2013**, *64*, 581−589.
(536) Huang, Z.-M.; Zhang, Y. Z.; Kotaki, M.; Ramakrishna, S. A review on polymer nanofibers by electrospinning and their applications in nanocomposites. *Compos. Sci. Technol.* **2003**, *63*, 2223−2253.
(537) Wang, Y.; Yokota, T.; Someya, T. Electrospun nanofiber-based soft electronics. *NPG Asia Mater.* **2021**, *13*, 22.
(538) Xu, J.; Liu, C.; Hsu, P. C.; Liu, K.; Zhang, R.; Liu, Y.; Cui, Y. Roll-to-Roll Transfer of Electrospun Nanofiber Film for High-Efficiency Transparent Air Filter. *Nano Lett.* **2016**, *16*, 1270−1275.
(539) Miyamoto, A.; Lee, S.; Cooray, N. F.; Lee, S.; Mori, M.; Matsuhisa, N.; Jin, H.; Yoda, L.; Yokota, T.; Itoh, A.; et al. Inflammation-free, gas-permeable, lightweight, stretchable on-skin electronics with nanomeshes. *Nat. Nanotechnol.* **2017**, *12*, 907−913.
(540) Kim, G. H.; Woo, H.; Kim, S.; An, T.; Lim, G. Highly-robust, solution-processed flexible transparent electrodes with a junction-free electrospun nanofiber network. *RSC Adv.* **2020**, *10*, 9940−9948.
(541) Lee, H. B.; Jin, W.-Y.; Ovhal, M. M.; Kumar, N.; Kang, J.-W. Flexible transparent conducting electrodes based on metal meshes for organic optoelectronic device applications: a review. *J. Mater. Chem. C* **2019**, *7*, 1087−1110.
(542) Chen, X.; Wu, X.; Shao, S.; Zhuang, J.; Xie, L.; Nie, S.; Su, W.; Chen, Z.; Cui, Z. Hybrid Printing Metal-mesh Transparent Conductive Films with Lower Energy Photonically Sintered Copper/tin Ink. *Sci. Rep.* **2017**, *7*, 13239.
(543) Zhou, L.; Xiang, H. Y.; Shen, S.; Li, Y. Q.; Chen, J. D.; Xie, H. J.; Goldthorpe, I. A.; Chen, L. S.; Lee, S. T.; Tang, J. X. High-performance flexible organic light-emitting diodes using embedded silver network transparent electrodes. *ACS Nano* **2014**, *8*, 12796−12805.
(544) Li, D.; Liu, X.; Chen, X.; Lai, W. Y.; Huang, W. A Simple Strategy towards Highly Conductive Silver-Nanowire Inks for Screen-Printed Flexible Transparent Conductive Films and Wearable Energy-Storage Devices. *Adv. Mater. Technol.* **2019**, *4*, 1900196.
(545) Overgaard, M. H.; Kühnel, M.; Hvidsten, R.; Petersen, S. V.; Vosch, T.; Nørgaard, K.; Laursen, B. W. Highly Conductive Semitransparent Graphene Circuits Screen-Printed from Water-Based Graphene Oxide Ink. *Adv. Mater. Technol.* **2017**, *2*, 1700011.
(546) Angmo, D.; Andersen, T. R.; Bentzen, J. J.; Helgesen, M.; Søndergaard, R. R.; Jørgensen, M.; Carlé, J. E.; Bundgaard, E.; Krebs, F. C. Roll-to-Roll Printed Silver Nanowire Semitransparent Electrodes for Fully Ambient Solution-Processed Tandem Polymer Solar Cells. *Adv. Funct. Mater.* **2015**, *25*, 4539−4547.
(547) Maurer, J. H. M.; González-García, L.; Backes, I. K.; Reiser, B.; Schlossberg, S. M.; Kraus, T. Direct Nanoimprinting of a Colloidal Self-Organizing Nanowire Ink for Flexible, Transparent Electrodes. *Adv. Mater. Technol.* **2017**, *2*, 1700034.
(548) Suh, Y. D.; Kwon, J.; Lee, J.; Lee, H.; Jeong, S.; Kim, D.; Cho, H.; Yeo, J.; Ko, S. H. Maskless Fabrication of Highly Robust, Flexible Transparent Cu Conductor by Random Crack Network Assisted Cu Nanoparticle Patterning and Laser Sintering. *Adv. Electron. Mater.* **2016**, *2*, 1600277.

https://doi.org/10.1021/acs.chemrev.3c00139
Chem. Rev. 2023, 123, 9982−10078

(549) Lee, W.; Kim, D.; Matsuhisa, N.; Nagase, M.; Sekino, M.; Malliaras, G. G.; Yokota, T.; Someya, T. Transparent, conformable, active multielectrode array using organic electrochemical transistors. *Proc. Natl. Acad. Sci. U.S.A.* **2017**, *114*, 10554−10559.
(550) Park, J. H.; Lee, D. Y.; Kim, Y. H.; Kim, J. K.; Lee, J. H.; Park, J. H.; Lee, T. W.; Cho, J. H. Flexible and transparent metallic grid electrodes prepared by evaporative assembly. *ACS Appl. Mater. Interfaces* **2014**, *6*, 12380−12387.
(551) Zheng, Y. Q.; Liu, Y.; Zhong, D.; Nikzad, S.; Liu, S.; Yu, Z.; Liu, D.; Wu, H. C.; Zhu, C.; Li, J.; et al. Monolithic optical microlithography of high-density elastic circuits. *Science* **2021**, *373*, 88−94.
(552) Hong, S.; Lee, H.; Yeo, J.; Ko, S. H. Digital selective laser methods for nanomaterials: From synthesis to processing. *Nano Today* **2016**, *11*, 547−564 547.
(553) Hong, S.; Yeo, J.; Lee, J.; Lee, H.; Lee, P.; Lee, S. S.; Ko, S. H. Selective Laser Direct Patterning of Silver Nanowire Percolation Network Transparent Conductor for Capacitive Touch Panel. *J. Nanosci. Nanotechnol.* **2015**, *15*, 2317−2323.
(554) Cao, L.; Yang, S.; Gao, W.; Liu, Z.; Gong, Y.; Ma, L.; Shi, G.; Lei, S.; Zhang, Y.; Zhang, S.; et al. Direct laser-patterned micro-supercapacitors from paintable MoS2 films. *Small* **2013**, *9*, 2905−2910.
(555) Shin, J.; Ko, J.; Jeong, S.; Won, P.; Lee, Y.; Kim, J.; Hong, S.; Jeon, N. L.; Ko, S. H. Monolithic digital patterning of polydimethylsiloxane with successive laser pyrolysis. *Nat. Mater.* **2021**, *20*, 100−107.
(556) Ko, S. H.; Pan, H.; Grigoropoulos, C. P.; Luscombe, C. K.; Fréchet, J. M. J.; Poulikakos, D. Air stable high resolution organic transistors by selective laser sintering of ink-jet printed metal nanoparticles. *Appl. Phys. Lett.* **2007**, *90*, 141103.
(557) Kwon, J.; Cho, H.; Eom, H.; Lee, H.; Suh, Y. D.; Moon, H.; Shin, J.; Hong, S.; Ko, S. H. Low-Temperature Oxidation-Free Selective Laser Sintering of Cu Nanoparticle Paste on a Polymer Substrate for the Flexible Touch Panel Applications. *ACS Appl. Mater. Interfaces* **2016**, *8*, 11575−11582.
(558) Nam, V. B.; Shin, J.; Yoon, Y.; Giang, T. T.; Kwon, J.; Suh, Y. D.; Yeo, J.; Hong, S.; Ko, S. H.; Lee, D. Highly Stable Ni-Based Flexible Transparent Conducting Panels Fabricated by Laser Digital Patterning. *Adv. Funct. Mater.* **2019**, *29*, 1806895.
(559) Gao, M.; Li, L.; Song, Y. Inkjet printing wearable electronic devices. *J. Mater. Chem. C* **2017**, *5*, 2971−2993.
(560) Majee, S.; Song, M.; Zhang, S.-L.; Zhang, Z.-B. Scalable inkjet printing of shear-exfoliated graphene transparent conductive films. *Carbon* **2016**, *102*, 51−57.
(561) Li, J.; Ye, F.; Vaziri, S.; Muhammed, M.; Lemme, M. C.; Ostling, M. Efficient inkjet printing of graphene. *Adv. Mater.* **2013**, *25*, 3985−3992.
(562) Han, S.-Y.; Lee, D.-H.; Herman, G. S.; Chang, C.-H. Inkjet-Printed High Mobility Transparent−Oxide Semiconductors. *J. Dispersion Technol.* **2009**, *5*, 520−524.
(563) Raut, H. K.; Ganesh, V. A.; Nair, A. S.; Ramakrishna, S. Anti-reflective coatings: A critical, in-depth review. *Energy Environ. Sci.* **2011**, *4*, 3779−3804.
(564) Song, Y. M.; Jang, S. J.; Yu, J. S.; Lee, Y. T. Bioinspired parabola subwavelength structures for improved broadband antire-flection. *Small* **2010**, *6*, 984−987.
(565) Ji, S.; Park, J.; Lim, H. Improved antireflection properties of moth eye mimicking nanopillars on transparent glass: flat antire-flection and color tuning. *Nanoscale* **2012**, *4*, 4603−4610.
(566) Leem, J. W.; Kim, S.; Lee, S. H.; Rogers, J. A.; Kim, E.; Yu, J. S. Efficiency Enhancement of Organic Solar Cells Using Hydrophobic Antireflective Inverted Moth-Eye Nanopatterned PDMS Films. *Adv. Energy Mater.* **2014**, *4*, 1301315.
(567) Kim, M. C.; Jang, S.; Choi, J.; Kang, S. M.; Choi, M. Moth-eye Structured Polydimethylsiloxane Films for High-Efficiency Perovskite Solar Cells. *Nano Micro Lett.* **2019**, *11*, 53.
(568) Ko, D.-H.; Tumbleston, J. R.; Henderson, K. J.; Euliss, L. E.; DeSimone, J. M.; Lopez, R.; Samulski, E. T. Biomimetic microlens array with antireflective "moth-eye" surface. *Soft Matter* **2011**, *7*, 6404−6407.
(569) Liu, Q.; Li, M.; Gu, Y.; Zhang, Y.; Wang, S.; Li, Q.; Zhang, Z. Highly aligned dense carbon nanotube sheets induced by multiple stretching and pressing. *Nanoscale* **2014**, *6*, 4338−4344.
(570) Ni, Z. H.; Yu, T.; Lu, Y. H.; Wang, Y. Y.; Feng, Y. P.; Shen, Z. X. Uniaxial strain on graphene: Raman spectroscopy study and band-gap opening. *ACS Nano* **2008**, *2*, 2301−2305.
(571) Wan, S.; Chen, Y.; Fang, S.; Wang, S.; Xu, Z.; Jiang, L.; Baughman, R. H.; Cheng, Q. High-strength scalable graphene sheets by freezing stretch-induced alignment. *Nat. Mater.* **2021**, *20*, 624−631.
(572) Hu, H.; Wang, S.; Wang, S.; Liu, G.; Cao, T.; Long, Y. Aligned Silver Nanowires Enabled Highly Stretchable and Transparent Electrodes with Unusual Conductive Property. *Adv. Funct. Mater.* **2019**, *29*, 1902922.
(573) Lee, Y. Y.; Choi, G. M.; Lim, S. M.; Cho, J. Y.; Choi, I. S.; Nam, K. T.; Joo, Y. C. Growth Mechanism of Strain-Dependent Morphological Change in PEDOT:PSS Films. *Sci. Rep.* **2016**, *6*, 25332.
(574) Sencadas, V.; Gregorio, R.; Lanceros-Méndez, S. α to β Phase Transformation and Microestructural Changes of PVDF Films Induced by Uniaxial Stretch. *J. Macromol. Sci. Part B Phys.* **2009**, *48*, 514−525.
(575) Xu, J.; Wu, H. C.; Zhu, C.; Ehrlich, A.; Shaw, L.; Nikolka, M.; Wang, S.; Molina-Lopez, F.; Gu, X.; Luo, S.; et al. Multi-scale ordering in highly stretchable polymer semiconducting films. *Nat. Mater.* **2019**, *18*, 594−601.
(576) Hartono, A.; Darwin, D.; Ramli, R.; Satira, S.; Djamal, M.; Herman, H., Electric field poling 2G V/m to improve piezoelectricity of PVDF thin film, *AIP Conf. Proc.*, 2016.
(577) Mahajan, M. S.; Marathe, D. M.; Ghosh, S. S.; Ganesan, V.; Sali, J. V. Changes in in-plane electrical conductivity of PEDOT:PSS thin films due to electric field induced dipolar reorientation. *RSC Adv.* **2015**, *5*, 86393−86401.
(578) Zheng, Q.; Zhang, B.; Lin, X.; Shen, X.; Yousefi, N.; Huang, Z.-D.; Li, Z.; Kim, J.-K. Highly transparent and conducting ultralarge graphene oxide/single-walled carbon nanotube hybrid films produced by Langmuir−Blodgett assembly. *J. Mater. Chem.* **2012**, *22*, 25072−25082.
(579) Yang, T.; Yang, J.; Shi, L.; Mäder, E.; Zheng, Q. Highly flexible transparent conductive graphene/single-walled carbon nanotube nanocomposite films produced by Langmuir−Blodgett assembly. *RSC Adv.* **2015**, *5*, 23650−23657.
(580) Liu, J. W.; Wang, J. L.; Huang, W. R.; Yu, L.; Ren, X. F.; Wen, W. C.; Yu, S. H. Ordering Ag nanowire arrays by a glass capillary: a portable, reusable and durable SERS substrate. *Sci. Rep.* **2012**, *2*, 987.
(581) Panjan, P.; Čekada, M.; Panjan, M.; Kek-Merl, D. Growth defects in PVD hard coatings. *Vacuum* **2009**, *84*, 209−214.
(582) Guo, C. F.; Ren, Z. Flexible transparent conductors based on metal nanowire networks. *Mater. Today* **2015**, *18*, 143−154.
(583) Cruz-Cruz, I.; Reyes-Reyes, M.; Aguilar-Frutis, M. A.; Rodriguez, A. G.; López-Sandoval, R. Study of the effect of DMSO concentration on the thickness of the PSS insulating barrier in PEDOT:PSS thin films. *Synth. Met.* **2010**, *160*, 1501−1506.
(584) Kim, D.; Bang, J.; Lee, W.; Ha, I.; Lee, J.; Eom, H.; Kim, M.; Park, J.; Choi, J.; Kwon, J.; et al. Highly stretchable and oxidation-resistive Cu nanowire heater for replication of the feeling of heat in a virtual world. *J. Mater. Chem. A* **2020**, *8*, 8281−8291.
(585) Kim, D.; Kwon, J.; Jung, J.; Kim, K.; Lee, H.; Yeo, J.; Hong, S.; Han, S.; Ko, S. H. A Transparent and Flexible Capacitive-Force Touch Pad from High-Aspect-Ratio Copper Nanowires with Enhanced Oxidation Resistance for Applications in Wearable Electronics. *Small Methods* **2018**, *2*, 1800077.
(586) Park, J. H.; Hwang, G. T.; Kim, S.; Seo, J.; Park, H. J.; Yu, K.; Kim, T. S.; Lee, K. J. Flash-Induced Self-Limited Plasmonic Welding of Silver Nanowire Network for Transparent Flexible Energy Harvester. *Adv. Mater.* **2017**, *29*, 1603473.

https://doi.org/10.1021/acs.chemrev.3c00139
Chem. Rev. 2023, 123, 9982−10078

(587) Zhang, K.; Li, J.; Fang, Y.; Luo, B.; Zhang, Y.; Li, Y.; Zhou, J.; Hu, B. Unraveling the solvent induced welding of silver nanowires for high performance flexible transparent electrodes. *Nanoscale* **2018**, *10*, 12981−12990.
(588) Tudor-Locke, C.; Bassett, D. R., Jr How many steps/day are enough? Preliminary pedometer indices for public health. *Sports Med.* **2004**, *34*, 1−8.
(589) Kim, H.-Y.; Kim, J.-Y.; Yoo, K.-T.; Yang, W.-J.; Byeon, J.-W. Failure mechanism of Ag nanowire-coated conductive transparent electrode for wearable devices under folding and torsional fatigue condition. *Microelectron. Reliab.* **2018**, *88*, 345−349.
(590) Dai, Z.; Ding, S.; Lei, M.; Li, S.; Xu, Y.; Zhou, Y.; Zhou, B. A superhydrophobic and anti-corrosion strain sensor for robust underwater applications. *J. Mater. Chem. A* **2021**, *9*, 15282−15293.
(591) Lim, S.; Son, D.; Kim, J.; Lee, Y. B.; Song, J.-K.; Choi, S.; Lee, D. J.; Kim, J. H.; Lee, M.; Hyeon, T.; et al. Transparent and Stretchable Interactive Human Machine Interface Based on Patterned Graphene Heterostructures. *Adv. Funct. Mater.* **2015**, *25*, 375−383.
(592) Liu, R.; Lai, Y.; Li, S.; Wu, F.; Shao, J.; Liu, D.; Dong, X.; Wang, J.; Wang, Z. L. Ultrathin, transparent, and robust self-healing electronic skins for tactile and non-contact sensing. *Nano Energy* **2022**, *95*, 107056.
(593) Jiang, Z.; Chen, N.; Yi, Z.; Zhong, J.; Zhang, F.; Ji, S.; Liao, R.; Wang, Y.; Li, H.; Liu, Z.; et al. A 1.3-micrometre-thick elastic conductor for seamless on-skin and implantable sensors. *Nat. Electron.* **2022**, *5*, 784−793.
(594) Ko, E. H.; Kim, H. J.; Lee, S. M.; Kim, T. W.; Kim, H. K. Stretchable Ag electrodes with mechanically tunable optical transmittance on wavy-patterned PDMS substrates. *Sci. Rep.* **2017**, *7*, 46739.
(595) Kim, B. S.; Kwon, H.; Kwon, H. J.; Pyo, J. B.; Oh, J.; Hong, S. Y.; Park, J. H.; Char, K.; Ha, J. S.; Son, J. G.; et al. Buckling Instability Control of 1D Nanowire Networks for a Large-Area Stretchable and Transparent Electrode. *Adv. Funct. Mater.* **2020**, *30*, 1910214.
(596) Mu, J.; Hou, C.; Wang, G.; Wang, X.; Zhang, Q.; Li, Y.; Wang, H.; Zhu, M. An Elastic Transparent Conductor Based on Hierarchically Wrinkled Reduced Graphene Oxide for Artificial Muscles and Sensors. *Adv. Mater.* **2016**, *28*, 9491−9497.
(597) Yang, S.; Ng, E.; Lu, N. Indium Tin Oxide (ITO) serpentine ribbons on soft substrates stretched beyond 100%. *Extreme Mech. Lett.* **2015**, *2*, 37−45.
(598) Lee, Y.; Kim, J.; Jang, B.; Kim, S.; Sharma, B. K.; Kim, J.-H.; Ahn, J.-H. Graphene-based stretchable/wearable self-powered touch sensor. *Nano Energy* **2019**, *62*, 259−267.
(599) Won, P.; Park, J. J.; Lee, T.; Ha, I.; Han, S.; Choi, M.; Lee, J.; Hong, S.; Cho, K. J.; Ko, S. H. Stretchable and Transparent Kirigami Conductor of Nanowire Percolation Network for Electronic Skin Applications. *Nano Lett.* **2019**, *19*, 6087−6096.
(600) An, B. W.; Gwak, E. J.; Kim, K.; Kim, Y. C.; Jang, J.; Kim, J. Y.; Park, J. U. Stretchable, Transparent Electrodes as Wearable Heaters Using Nanotrough Networks of Metallic Glasses with Superior Mechanical Properties and Thermal Stability. *Nano Lett.* **2016**, *16*, 471−478.
(601) Wang, Y.; Zhu, C.; Pfattner, R.; Yan, H.; Jin, L.; Chen, S.; Molina-Lopez, F.; Lissel, F.; Liu, J.; Rabiah, N. I.; et al. A highly stretchable, transparent, and conductive polymer. *Sci. Adv.* **2017**, *3*, No. e1602076.
(602) Lipomi, D. J.; Lee, J. A.; Vosgueritchian, M.; Tee, B. C. K.; Bolander, J. A.; Bao, Z. Electronic Properties of Transparent Conductive Films of PEDOT:PSS on Stretchable Substrates. *Chem. Mater.* **2012**, *24*, 373−382.
(603) Jiang, Y.; Zhang, Z.; Wang, Y. X.; Li, D.; Coen, C. T.; Hwaun, E.; Chen, G.; Wu, H. C.; Zhong, D.; Niu, S.; et al. Topological supramolecular network enabled high-conductivity, stretchable organic bioelectronics. *Science* **2022**, *375*, 1411−1417.
(604) Tan, P.; Wang, H.; Xiao, F.; Lu, X.; Shang, W.; Deng, X.; Song, H.; Xu, Z.; Cao, J.; Gan, T.; et al. Solution-processable, soft, self-adhesive, and conductive polymer composites for soft electronics. *Nat. Commun.* **2022**, *13*, 358.
(605) Yan, J.; Malakooti, M. H.; Lu, Z.; Wang, Z.; Kazem, N.; Pan, C.; Bockstaller, M. R.; Majidi, C.; Matyjaszewski, K. Solution processable liquid metal nanodroplets by surface-initiated atom transfer radical polymerization. *Nat. Nanotechnol.* **2019**, *14*, 684−690.
(606) Shi, L.; Zhu, T.; Gao, G.; Zhang, X.; Wei, W.; Liu, W.; Ding, S. Highly stretchable and transparent ionic conducting elastomers. *Nat. Commun.* **2018**, *9*, 2630.
(607) Li, R. a.; Fan, T.; Chen, G.; Zhang, K.; Su, B.; Tian, J.; He, M. Autonomous Self-Healing, Antifreezing, and Transparent Conductive Elastomers. *Chem. Mater.* **2020**, *32*, 874−881.
(608) Chen, X.; He, M.; Zhang, X.; Lu, T.; Hao, W.; Zhao, Y.; Liu, Y. Metal-Free and Stretchable Conductive Hydrogels for High Transparent Conductive Film and Flexible Strain Sensor with High Sensitivity. *Macromol. Chem. Phys.* **2020**, *221*, 2000054.
(609) Feig, V. R.; Tran, H.; Lee, M.; Bao, Z. Mechanically tunable conductive interpenetrating network hydrogels that mimic the elastic moduli of biological tissue. *Nat. Commun.* **2018**, *9*, 2740.
(610) Liu, Y.; Liu, J.; Chen, S.; Lei, T.; Kim, Y.; Niu, S.; Wang, H.; Wang, X.; Foudeh, A. M.; Tok, J. B.; et al. Soft and elastic hydrogel-based microelectronics for localized low-voltage neuromodulation. *Nat. Biomed. Eng.* **2019**, *3*, 58−68.
(611) Lu, B.; Yuk, H.; Lin, S.; Jian, N.; Qu, K.; Xu, J.; Zhao, X. Pure PEDOT:PSS hydrogels. *Nat. Commun.* **2019**, *10*, 1043.
(612) Won, D.; Kim, J.; Choi, J.; Kim, H.; Han, S.; Ha, I.; Bang, J.; Kim, K. K.; Lee, Y.; Kim, T. S.; et al. Digital selective transformation and patterning of highly conductive hydrogel bioelectronics by laser-induced phase separation. *Sci. Adv.* **2022**, *8*, No. eabo3209.
(613) Kim, C. C.; Lee, H. H.; Oh, K. H.; Sun, J. Y. Highly stretchable, transparent ionic touch panel. *Science* **2016**, *353*, 682−687.
(614) Keplinger, C.; Sun, J. Y.; Foo, C. C.; Rothemund, P.; Whitesides, G. M.; Suo, Z. Stretchable, transparent, ionic conductors. *Science* **2013**, *341*, 984−987.
(615) Chortos, A.; Bao, Z. Skin-inspired electronic devices. *Mater. Today* **2014**, *17*, 321−331.
(616) Carlsson, M.; Cain, P.; Holmqvist, C.; Stahlberg, F.; Lundback, S.; Arheden, H. Total heart volume variation throughout the cardiac cycle in humans. *Am. J. Physiol. Heart Circ. Physiol.* **2004**, *287*, H243−H250.
(617) Katiyar, A. K.; Davidson, A. A.; Jang, H.; Hwangbo, Y.; Han, B.; Lee, S.; Hagiwara, Y.; Shimada, T.; Hirakata, H.; Kitamura, T.; et al. Ultrasoft silicon nanomembranes: thickness-dependent effective elastic modulus. *Nanoscale* **2019**, *11*, 15184−15194.
(618) Kim, Y.; Suh, J. M.; Shin, J.; Liu, Y.; Yeon, H.; Qiao, K.; Kum, H. S.; Kim, C.; Lee, H. E.; Choi, C.; et al. Chip-less wireless electronic skins by remote epitaxial freestanding compound semiconductors. *Science* **2022**, *377*, 859−864.
(619) Choi, M. K.; Park, I.; Kim, D. C.; Joh, E.; Park, O. K.; Kim, J.; Kim, M.; Choi, C.; Yang, J.; Cho, K. W.; et al. Thermally Controlled, Patterned Graphene Transfer Printing for Transparent and Wearable Electronic/Optoelectronic System. *Adv. Funct. Mater.* **2015**, *25*, 7109−7118.
(620) Greco, F.; Zucca, A.; Taccola, S.; Menciassi, A.; Fujie, T.; Haniuda, H.; Takeoka, S.; Dario, P.; Mattoli, V. Ultra-thin conductive free-standing PEDOT/PSS nanofilms. *Soft Matter* **2011**, *7*, 10642−10650.
(621) Cheng, S.; Lou, Z.; Zhang, L.; Guo, H.; Wang, Z.; Guo, C.; Fukuda, K.; Ma, S.; Wang, G.; Someya, T.; et al. Ultrathin Hydrogel Films toward Breathable Skin-Integrated Electronics. *Adv. Mater.* **2023**, *35*, 2206793.
(622) Xu, F.; Wang, X.; Zhu, Y.; Zhu, Y. Wavy Ribbons of Carbon Nanotubes for Stretchable Conductors. *Adv. Funct. Mater.* **2012**, *22*, 1279−1283.
(623) Lee, S.; Sasaki, D.; Kim, D.; Mori, M.; Yokota, T.; Lee, H.; Park, S.; Fukuda, K.; Sekino, M.; Matsuura, K.; et al. Ultrasoft electronics to monitor dynamically pulsing cardiomyocytes. *Nat. Nanotechnol.* **2019**, *14*, 156−160.

https://doi.org/10.1021/acs.chemrev.3c00139
Chem. Rev. 2023, 123, 9982−10078

(624) Fan, J. A.; Yeo, W. H.; Su, Y.; Hattori, Y.; Lee, W.; Jung, S. Y.; Zhang, Y.; Liu, Z.; Cheng, H.; Falgout, L.; et al. Fractal design concepts for stretchable electronics. *Nat. Commun.* **2014**, *5*, 3266.
(625) Kim, H. W.; Kim, T. Y.; Park, H. K.; You, I.; Kwak, J.; Kim, J. C.; Hwang, H.; Kim, H. S.; Jeong, U. Hygroscopic Auxetic On-Skin Sensors for Easy-to-Handle Repeated Daily Use. *ACS Appl. Mater. Interfaces* **2018**, *10*, 40141−40148.
(626) Kapnisi, M.; Mansfield, C.; Marijon, C.; Guex, A. G.; Perbellini, F.; Bardi, I.; Humphrey, E. J.; Puetzer, J. L.; Mawad, D.; Koutsogeorgis, D. C.; et al. Auxetic Cardiac Patches with Tunable Mechanical and Conductive Properties toward Treating Myocardial Infarction. *Adv. Funct. Mater.* **2018**, *28*, 1800618.
(627) Wang, X.; Zhang, Y.; Zhang, X.; Huo, Z.; Li, X.; Que, M.; Peng, Z.; Wang, H.; Pan, C. A Highly Stretchable Transparent Self-Powered Triboelectric Tactile Sensor with Metallized Nanofibers for Wearable Electronics. *Adv. Mater.* **2018**, *30*, 1706738.
(628) Soltanian, S.; Rahmanian, R.; Gholamkhass, B.; Kiasari, N. M.; Ko, F.; Servati, P. Highly Stretchable, Sparse, Metallized Nanofiber Webs as Thin, Transferrable Transparent Conductors. *Adv. Energy Mater.* **2013**, *3*, 1332−1337.
(629) Fan, X.; Nie, W.; Tsai, H.; Wang, N.; Huang, H.; Cheng, Y.; Wen, R.; Ma, L.; Yan, F.; Xia, Y. PEDOT:PSS for Flexible and Stretchable Electronics: Modifications, Strategies, and Applications. *Adv. Sci.* **2019**, *6*, 1900813.
(630) Bian, Y.; Liu, K.; Ran, Y.; Li, Y.; Gao, Y.; Zhao, Z.; Shao, M.; Liu, Y.; Kuang, J.; Zhu, Z.; et al. Spatially nanoconfined N-type polymer semiconductors for stretchable ultrasensitive X-ray detection. *Nat. Commun.* **2022**, *13*, 7163.
(631) Yang, W.; Gong, Y.; Yao, C. Y.; Shrestha, M.; Jia, Y.; Qiu, Z.; Fan, Q. H.; Weber, A.; Li, W. A fully transparent, flexible PEDOT:PSS-ITO-Ag-ITO based microelectrode array for ECoG recording. *Lab Chip* **2021**, *21*, 1096−1108.
(632) Yuk, H.; Lu, B.; Zhao, X. Hydrogel bioelectronics. *Chem. Soc. Rev.* **2019**, *48*, 1642−1667.
(633) Liu, J.; Qu, S.; Suo, Z.; Yang, W. Functional hydrogel coatings. *Natl. Sci. Rev.* **2021**, *8*, nwaa254.
(634) Rao, L.; Zhou, H.; Li, T.; Li, C.; Duan, Y. Y. Polyethylene glycol-containing polyurethane hydrogel coatings for improving the biocompatibility of neural electrodes. *Acta Biomater.* **2012**, *8*, 2233−2242.
(635) Zhao, X.; Chen, X.; Yuk, H.; Lin, S.; Liu, X.; Parada, G. Soft Materials by Design: Unconventional Polymer Networks Give Extreme Properties. *Chem. Rev.* **2021**, *121*, 4309−4372.
(636) Lu, Y.; Wang, D.; Li, T.; Zhao, X.; Cao, Y.; Yang, H.; Duan, Y. Y. Poly(vinyl alcohol)/poly(acrylic acid) hydrogel coatings for improving electrode-neural tissue interface. *Biomaterials* **2009**, *30*, 4143−4151.
(637) Heo, D. N.; Song, S. J.; Kim, H. J.; Lee, Y. J.; Ko, W. K.; Lee, S. J.; Lee, D.; Park, S. J.; Zhang, L. G.; Kang, J. Y.; et al. Multifunctional hydrogel coatings on the surface of neural cuff electrode for improving electrode-nerve tissue interfaces. *Acta Biomater.* **2016**, *39*, 25−33.
(638) Hu, W.; Wang, R.; Lu, Y.; Pei, Q. An elastomeric transparent composite electrode based on copper nanowires and polyurethane. *J. Mater. Chem. C* **2014**, *2*, 1298−1305.
(639) Gao, Z.; Yiu, C.; Liu, Y.; Li, D.; Mei, L.; Zeng, Z.; Yu, X. Stretchable transparent conductive elastomers for skin-integrated electronics. *J. Mater. Chem. C* **2020**, *8*, 15105−15111.
(640) Hwang, B. U.; Lee, J. H.; Trung, T. Q.; Roh, E.; Kim, D. I.; Kim, S. W.; Lee, N. E. Transparent Stretchable Self-Powered Patchable Sensor Platform with Ultrasensitive Recognition of Human Activities. *ACS Nano* **2015**, *9*, 8801−8810.
(641) Tien, H.-W.; Huang, Y.-L.; Yang, S.-Y.; Wang, J.-Y.; Ma, C.-C. M. The production of graphene nanosheets decorated with silver nanoparticles for use in transparent, conductive films. *Carbon* **2011**, *49*, 1550−1560.
(642) Lipomi, D. J.; Vosgueritchian, M.; Tee, B. C.; Hellstrom, S. L.; Lee, J. A.; Fox, C. H.; Bao, Z. Skin-like pressure and strain sensors based on transparent elastic films of carbon nanotubes. *Nat. Nanotechnol.* **2011**, *6*, 788−792.
(643) Feng, C.; Liu, K.; Wu, J.-S.; Liu, L.; Cheng, J.-S.; Zhang, Y.; Sun, Y.; Li, Q.; Fan, S.; Jiang, K. Flexible, Stretchable, Transparent Conducting Films Made from Superaligned Carbon Nanotubes. *Adv. Funct. Mater.* **2010**, *20*, 885−891.
(644) Won, P.; Valentine, C. S.; Zadan, M.; Pan, C.; Vinciguerra, M.; Patel, D. K.; Ko, S. H.; Walker, L. M.; Majidi, C. 3D Printing of Liquid Metal Embedded Elastomers for Soft Thermal and Electrical Materials. *ACS Appl. Mater. Interfaces* **2022**, *14*, 55028−55038.
(645) Lee, W.; Kim, H.; Kang, I.; Park, H.; Jung, J.; Lee, H.; Park, H.; Park, J. S.; Yuk, J. M.; Ryu, S.; et al. Universal assembly of liquid metal particles in polymers enables elastic printed circuit board. *Science* **2022**, *378*, 637−641.
(646) Cho, C.; Shin, W.; Kim, M.; Bang, J.; Won, P.; Hong, S.; Ko, S. H. Monolithically Programmed Stretchable Conductor by Laser-Induced Entanglement of Liquid Metal and Metallic Nanowire Backbone. *Small* **2022**, *18*, 2202841.
(647) Kim, M.; Cho, C.; Shin, W.; Park, J. J.; Kim, J.; Won, P.; Majidi, C.; Ko, S. H. Nanowire-assisted freestanding liquid metal thin-film patterns for highly stretchable electrodes on 3D surfaces. *npj Flexible Electron.* **2022**, *6*, 99.
(648) Li, R. a.; Chen, G.; He, M.; Tian, J.; Su, B. Patternable transparent and conductive elastomers towards flexible tactile/strain sensors. *J. Mater. Chem. C* **2017**, *5*, 8475−8481.
(649) Li, R. a.; Chen, G.; Fan, T.; Zhang, K.; He, M. Transparent conductive elastomers with excellent autonomous self-healing capability in harsh organic solvent environments. *J. Mater. Chem. A* **2020**, *8*, 5056−5061.
(650) Zhang, L.; Shi, G. Preparation of Highly Conductive Graphene Hydrogels for Fabricating Supercapacitors with High Rate Capability. *J. Phys. Chem. C* **2011**, *115*, 17206−17212.
(651) Navaei, A.; Saini, H.; Christenson, W.; Sullivan, R. T.; Ros, R.; Nikkhah, M. Gold nanorod-incorporated gelatin-based conductive hydrogels for engineering cardiac tissue constructs. *Acta Biomater.* **2016**, *41*, 133−146.
(652) Solazzo, M.; Krukiewicz, K.; Zhussupbekova, A.; Fleischer, K.; Biggs, M. J.; Monaghan, M. G. PEDOT:PSS interfaces stabilised using a PEGylated crosslinker yield improved conductivity and biocompatibility. *J. Mater. Chem. B* **2019**, *7*, 4811−4820.
(653) Wei, H.; Lei, M.; Zhang, P.; Leng, J.; Zheng, Z.; Yu, Y. Orthogonal photochemistry-assisted printing of 3D tough and stretchable conductive hydrogels. *Nat. Commun.* **2021**, *12*, 2082.
(654) Yuk, H.; Lu, B.; Lin, S.; Qu, K.; Xu, J.; Luo, J.; Zhao, X. 3D printing of conducting polymers. *Nat. Commun.* **2020**, *11*, 1604.
(655) Teo, M. Y.; RaviChandran, N.; Kim, N.; Kee, S.; Stuart, L.; Aw, K. C.; Stringer, J. Direct Patterning of Highly Conductive PEDOT:PSS/Ionic Liquid Hydrogel via Microreactive Inkjet Printing. *ACS Appl. Mater. Interfaces* **2019**, *11*, 37069−37076.
(656) Zhou, Y.; Wan, C.; Yang, Y.; Yang, H.; Wang, S.; Dai, Z.; Ji, K.; Jiang, H.; Chen, X.; Long, Y. Highly Stretchable, Elastic, and Ionic Conductive Hydrogel for Artificial Soft Electronics. *Adv. Funct. Mater.* **2019**, *29*, 1806220.
(657) Sun, J. Y.; Keplinger, C.; Whitesides, G. M.; Suo, Z. Ionic skin. *Adv. Mater.* **2014**, *26*, 7608−7614.
(658) Deng, J.; Yuk, H.; Wu, J.; Varela, C. E.; Chen, X.; Roche, E. T.; Guo, C. F.; Zhao, X. Electrical bioadhesive interface for bioelectronics. *Nat. Mater.* **2021**, *20*, 229−236.
(659) Mehdizadeh, M.; Yang, J. Design strategies and applications of tissue bioadhesives. *Macromol. Biosci.* **2013**, *13*, 271−288.
(660) Yuk, H.; Varela, C. E.; Nabzdyk, C. S.; Mao, X.; Padera, R. F.; Roche, E. T.; Zhao, X. Dry double-sided tape for adhesion of wet tissues and devices. *Nature* **2019**, *575*, 169−174.
(661) Wei, B.; Liu, J.; Ouyang, L.; Kuo, C. C.; Martin, D. C. Significant enhancement of PEDOT thin film adhesion to inorganic solid substrates with EDOT-acid. *ACS Appl. Mater. Interfaces* **2015**, *7*, 15388−15394.

https://doi.org/10.1021/acs.chemrev.3c00139
Chem. Rev. 2023, 123, 9982−10078

(662) Ouyang, L.; Wei, B.; Kuo, C. C.; Pathak, S.; Farrell, B.; Martin, D. C. Enhanced PEDOT adhesion on solid substrates with electrografted P(EDOT-NH2). *Sci. Adv.* **2017**, *3*, 1600448.
(663) Yang, M.; Yang, T.; Deng, H.; Wang, J.; Ning, S.; Li, X.; Ren, X.; Su, Y.; Zang, J.; Li, X.; et al. Poly(5-nitroindole) Thin Film as Conductive and Adhesive Interfacial Layer for Robust Neural Interface. *Adv. Funct. Mater.* **2021**, *31*, 2105857.
(664) Inoue, A.; Yuk, H.; Lu, B.; Zhao, X. Strong adhesion of wet conducting polymers on diverse substrates. *Sci. Adv.* **2020**, *6*, No. eaay5394.
(665) Boehler, C.; Oberueber, F.; Schlabach, S.; Stieglitz, T.; Asplund, M. Long-Term Stable Adhesion for Conducting Polymers in Biomedical Applications: IrOx and Nanostructured Platinum Solve the Chronic Challenge. *ACS Appl. Mater. Interfaces* **2017**, *9*, 189−197.
(666) Ganji, M.; Hossain, L.; Tanaka, A.; Thunemann, M.; Halgren, E.; Gilja, V.; Devor, A.; Dayeh, S. A. Monolithic and Scalable Au Nanorod Substrates Improve PEDOT-Metal Adhesion and Stability in Neural Electrodes. *Adv. Healthcare Mater.* **2018**, *7*, 1800923.
(667) Fan, Y. J.; Li, X.; Kuang, S. Y.; Zhang, L.; Chen, Y. H.; Liu, L.; Zhang, K.; Ma, S. W.; Liang, F.; Wu, T.; et al. Highly Robust, Transparent, and Breathable Epidermal Electrode. *ACS Nano* **2018**, *12*, 9326−9332.
(668) Wei, S.; Yin, R.; Tang, T.; Wu, Y.; Liu, Y.; Wang, P.; Wang, K.; Mei, M.; Zou, R.; Duan, X. Gas-Permeable, Irritation-Free, Transparent Hydrogel Contact Lens Devices with Metal-Coated Nanofiber Mesh for Eye Interfacing. *ACS Nano* **2019**, *13*, 7920−7929.
(669) Peng, X.; Dong, K.; Zhang, Y.; Wang, L.; Wei, C.; Lv, T.; Wang, Z. L.; Wu, Z. Sweat-Permeable, Biodegradable, Transparent and Self-powered Chitosan-Based Electronic Skin with Ultrathin Elastic Gold Nanofibers. *Adv. Funct. Mater.* **2022**, *32*, 2112241.
(670) Zhou, W.; Yao, S.; Wang, H.; Du, Q.; Ma, Y.; Zhu, Y. Gas-Permeable, Ultrathin, Stretchable Epidermal Electronics with Porous Electrodes. *ACS Nano* **2020**, *14*, 5798−5805.
(671) Yeon, H.; Lee, H.; Kim, Y.; Lee, D.; Lee, Y.; Lee, J. S.; Shin, J.; Choi, C.; Kang, J. H.; Suh, J. M.; et al. Long-term reliable physical health monitoring by sweat pore-inspired perforated electronic skins. *Sci. Adv.* **2021**, *7*, No. eabg8459.
(672) Lim, C.; Hong, Y. J.; Jung, J.; Shin, Y.; Sunwoo, S. H.; Baik, S.; Park, O. K.; Choi, S. H.; Hyeon, T.; Kim, J. H.; et al. Tissue-like skin-device interface for wearable bioelectronics by using ultrasoft, mass-permeable, and low-impedance hydrogels. *Sci. Adv.* **2021**, *7*, No. eabd3716.
(673) Fang, Y.; Li, Y.; Li, Y.; Ding, M.; Xie, J.; Hu, B. Solution-Processed Submicron Free-Standing, Conformal, Transparent, Breathable Epidermal Electrodes. *ACS Appl. Mater. Interfaces* **2020**, *12*, 23689−23696.
(674) Yang, X.; Li, L.; Wang, S.; Lu, Q.; Bai, Y.; Sun, F.; Li, T.; Li, Y.; Wang, Z.; Zhao, Y.; et al. Ultrathin, Stretchable, and Breathable Epidermal Electronics Based on a Facile Bubble Blowing Method. *Adv. Electron. Mater.* **2020**, *6*, 2000306.
(675) Li, Y. L.; Liu, Y. H.; Chen, L. S.; Xu, J. L. A Conformable, Gas-Permeable, and Transparent Skin-Like Micromesh Architecture for Glucose Monitoring. *Adv. Healthcare Mater.* **2021**, *10*, 2100046.
(676) Zhu, D. Y.; Rong, M. Z.; Zhang, M. Q. Self-healing polymeric materials based on microencapsulated healing agents: From design to preparation. *Prog. Polym. Sci.* **2015**, *49*, 175−220.
(677) Kang, J.; Tok, J. B. H.; Bao, Z. A. Self-healing soft electronics. *Nat. Electron.* **2019**, *2*, 144−150.
(678) Cao, Y.; Tan, Y. J.; Li, S.; Lee, W. W.; Guo, H. C.; Cai, Y. Q.; Wang, C.; Tee, B. C. K. Self-healing electronic skins for aquatic environments. *Nat. Electron.* **2019**, *2*, 75−82.
(679) Son, D.; Kang, J.; Vardoulis, O.; Kim, Y.; Matsuhisa, N.; Oh, J. Y.; To, J. W.; Mun, J.; Katsumata, T.; Liu, Y.; et al. An integrated self-healable electronic skin system fabricated via dynamic reconstruction of a nanostructured conducting network. *Nat. Nanotechnol.* **2018**, *13*, 1057−1065.
(680) Luo, C. S.; Wan, P.; Yang, H.; Shah, S. A. A.; Chen, X. Healable Transparent Electronic Devices. *Adv. Funct. Mater.* **2017**, *27*, 1606339.
(681) Parida, K.; Kumar, V.; Jiangxin, W.; Bhavanasi, V.; Bendi, R.; Lee, P. S. Highly Transparent, Stretchable, and Self-Healing Ionic-Skin Triboelectric Nanogenerators for Energy Harvesting and Touch Applications. *Adv. Mater.* **2017**, *29*, 1702181.
(682) Kim, S. M.; Jeon, H.; Shin, S. H.; Park, S. A.; Jegal, J.; Hwang, S. Y.; Oh, D. X.; Park, J. Superior Toughness and Fast Self-Healing at Room Temperature Engineered by Transparent Elastomers. *Adv. Mater.* **2018**, *30*, 1705145.
(683) Rahman, M. F.; Wang, J.; Patterson, T. A.; Saini, U. T.; Robinson, B. L.; Newport, G. D.; Murdock, R. C.; Schlager, J. J.; Hussain, S. M.; Ali, S. F. Expression of genes related to oxidative stress in the mouse brain after exposure to silver-25 nanoparticles. *Toxicol. Lett.* **2009**, *187*, 15−21.
(684) Luo, J.; Hein, C.; Pierson, J.-F.; Mücklich, F. Localised corrosion attacks and oxide growth on copper in phosphate-buffered saline. *Mater. Charact.* **2019**, *158*, 109985.
(685) Wang, C.; Yokota, T.; Someya, T. Natural Biopolymer-Based Biocompatible Conductors for Stretchable Bioelectronics. *Chem. Rev.* **2021**, *121*, 2109−2146.
(686) Li, C.; Guo, C.; Fitzpatrick, V.; Ibrahim, A.; Zwierstra, M. J.; Hanna, P.; Lechtig, A.; Nazarian, A.; Lin, S. J.; Kaplan, D. L. Design of biodegradable, implantable devices towards clinical translation. *Nat. Rev. Mater.* **2020**, *5*, 61−81.
(687) Liu, Y.; Qi, N.; Song, T.; Jia, M.; Xia, Z.; Yuan, Z.; Yuan, W.; Zhang, K. Q.; Sun, B. Highly flexible and lightweight organic solar cells on biocompatible silk fibroin. *ACS Appl. Mater. Interfaces* **2014**, *6*, 20670−20675.
(688) Cui, Y.; Zhang, F.; Chen, G.; Yao, L.; Zhang, N.; Liu, Z.; Li, Q.; Zhang, F.; Cui, Z.; Zhang, K.; et al. A Stretchable and Transparent Electrode Based on PEGylated Silk Fibroin for In Vivo Dual-Modal Neural-Vascular Activity Probing. *Adv. Mater.* **2021**, *33*, 2100221.
(689) Gilshteyn, E. P.; Lin, S.; Kondrashov, V. A.; Kopylova, D. S.; Tsapenko, A. P.; Anisimov, A. S.; Hart, A. J.; Zhao, X.; Nasibulin, A. G. A One-Step Method of Hydrogel Modification by Single-Walled Carbon Nanotubes for Highly Stretchable and Transparent Electronics. *ACS Appl. Mater. Interfaces* **2018**, *10*, 28069−28075.
(690) Ji, D.; Park, J. M.; Oh, M. S.; Nguyen, T. L.; Shin, H.; Kim, J. S.; Kim, D.; Park, H. S.; Kim, J. Superstrong, superstiff, and conductive alginate hydrogels. *Nat. Commun.* **2022**, *13*, 3019.
(691) Dvir, T.; Timko, B. P.; Brigham, M. D.; Naik, S. R.; Karajanagi, S. S.; Levy, O.; Jin, H.; Parker, K. K.; Langer, R.; Kohane, D. S. Nanowired three-dimensional cardiac patches. *Nat. Nanotechnol.* **2011**, *6*, 720−725.
(692) Qin, Z.; Sun, X.; Zhang, H.; Yu, Q.; Wang, X.; He, S.; Yao, F.; Li, J. A transparent, ultrastretchable and fully recyclable gelatin organohydrogel based electronic sensor with broad operating temperature. *J. Mater. Chem. A* **2020**, *8*, 4447−4456.
(693) Choi, S.; Han, S. I.; Jung, D.; Hwang, H. J.; Lim, C.; Bae, S.; Park, O. K.; Tschabrunn, C. M.; Lee, M.; Bae, S. Y.; et al. Highly conductive, stretchable and biocompatible Ag-Au core-sheath nanowire composite for wearable and implantable bioelectronics. *Nat. Nanotechnol.* **2018**, *13*, 1048−1056.
(694) Kim, D.; Bang, J.; Won, P.; Kim, Y.; Jung, J.; Lee, J.; Kwon, J.; Lee, H.; Hong, S.; Jeon, N. L.; et al. Biocompatible Cost-Effective Electrophysiological Monitoring with Oxidation-Free Cu−Au Core−Shell Nanowire. *Adv. Mater. Technol.* **2020**, *5*, 2000661.
(695) Lee, H.; Hong, S.; Lee, J.; Suh, Y. D.; Kwon, J.; Moon, H.; Kim, H.; Yeo, J.; Ko, S. H. Highly Stretchable and Transparent Supercapacitor by Ag-Au Core-Shell Nanowire Network with High Electrochemical Stability. *ACS Appl. Mater. Interfaces* **2016**, *8*, 15449−15458.
(696) Kim, K. K.; Kim, M.; Pyun, K.; Kim, J.; Min, J.; Koh, S.; Root, S. E.; Kim, J.; Nguyen, B.-N. T.; Nishio, Y.; et al. A substrate-less nanomesh receptor with meta-learning for rapid hand task recognition. *Nat. Electron.* **2022**, *6*, 64−75.
(697) Moon, H.; Lee, H.; Kwon, J.; Suh, Y. D.; Kim, D. K.; Ha, I.; Yeo, J.; Hong, S.; Ko, S. H. Ag/Au/Polypyrrole Core-shell Nanowire Network for Transparent, Stretchable and Flexible Supercapacitor in Wearable Energy Devices. *Sci. Rep.* **2017**, *7*, 41981.

https://doi.org/10.1021/acs.chemrev.3c00139
Chem. Rev. 2023, 123, 9982−10078

(698) Lin, M.; Hu, H.; Zhou, S.; Xu, S. Soft wearable devices for deep-tissue sensing. *Nat. Rev. Mater.* **2022**, *7*, 850−869.
(699) Zhang, X.; Ye, T.; Meng, X.; Tian, Z.; Pang, L.; Han, Y.; Li, H.; Lu, G.; Xiu, F.; Yu, H. D.; et al. Sustainable and Transparent Fish Gelatin Films for Flexible Electroluminescent Devices. *ACS Nano* **2020**, *14*, 3876−3884.
(700) Fu, R. X.; Luo, W. H.; Nazempour, R.; Tan, D. X.; Ding, H.; Zhang, K. Y.; Yin, L.; Guan, J. S.; Sheng, X. Implantable and Biodegradable Poly(L-lactic acid) Fibers for Optical Neural Interfaces. *Adv. Opt. Mater.* **2018**, *6*, 1700941.
(701) Lu, D.; Liu, T. L.; Chang, J. K.; Peng, D.; Zhang, Y.; Shin, J.; Hang, T.; Bai, W.; Yang, Q.; Rogers, J. A. Transient Light-Emitting Diodes Constructed from Semiconductors and Transparent Conductors that Biodegrade Under Physiological Conditions. *Adv. Mater.* **2019**, *31*, 1902739.
(702) Gao, X.; Huang, L.; Wang, B.; Xu, D.; Zhong, J.; Hu, Z.; Zhang, L.; Zhou, J. Natural Materials Assembled, Biodegradable, and Transparent Paper-Based Electret Nanogenerator. *ACS Appl. Mater. Interfaces* **2016**, *8*, 35587−35592.
(703) Zhu, H.; Xiao, Z.; Liu, D.; Li, Y.; Weadock, N. J.; Fang, Z.; Huang, J.; Hu, L. Biodegradable transparent substrates for flexible organic-light-emitting diodes. *Energy Environ. Sci.* **2013**, *6*, 2105−2111.
(704) Feng, S.; Cao, S.; Tian, Z.; Zhu, H.; Kong, D. Maskless Patterning of Biodegradable Conductors by Selective Laser Sintering of Microparticle Inks and Its Application in Flexible Transient Electronics. *ACS Appl. Mater. Interfaces* **2019**, *11*, 45844−45852.
(705) Iqbal, N.; Khan, A. S.; Asif, A.; Yar, M.; Haycock, J. W.; Rehman, I. U. Recent concepts in biodegradable polymers for tissue engineering paradigms: a critical review. *Int. Mater. Rev.* **2019**, *64*, 91−126.
(706) Kim, M. S.; Ahn, H. H.; Shin, Y. N.; Cho, M. H.; Khang, G.; Lee, H. B. An in vivo study of the host tissue response to subcutaneous implantation of PLGA- and/or porcine small intestinal submucosa-based scaffolds. *Biomaterials* **2007**, *28*, 5137−5143.
(707) Zheng, Y. F.; Gu, X. N.; Witte, F. Biodegradable metals. *Mater. Sci. Eng.: R: Rep.* **2014**, *77*, 1−34−1.
(708) Wang, Y.; Rudym, D. D.; Walsh, A.; Abrahamsen, L.; Kim, H. J.; Kim, H. S.; Kirker-Head, C.; Kaplan, D. L. In vivo degradation of three-dimensional silk fibroin scaffolds. *Biomaterials* **2008**, *29*, 3415−3428.
(709) Odelius, K.; Hoglund, A.; Kumar, S.; Hakkarainen, M.; Ghosh, A. K.; Bhatnagar, N.; Albertsson, A. C. Porosity and pore size regulate the degradation product profile of polylactide. *Biomacromolecules* **2011**, *12*, 1250−1258.
(710) Lee, D. M.; Rubab, N.; Hyun, I.; Kang, W.; Kim, Y. J.; Kang, M.; Choi, B. O.; Kim, S. W. Ultrasound-mediated triboelectric nanogenerator for powering on-demand transient electronics. *Sci. Adv.* **2022**, *8*, No. eabl8423.
(711) Imani, I. M.; Kim, B.; Xiao, X.; Rubab, N.; Park, B. J.; Kim, Y. J.; Zhao, P.; Kang, M.; Kim, S. W. Ultrasound-Driven On-Demand Transient Triboelectric Nanogenerator for Subcutaneous Antibacterial Activity. *Adv. Sci.* **2023**, *10*, 2204801.
(712) Yun, J. Recent progress in thermal management for flexible/wearable devices. *Soft Science* **2023**, *3*, 12.
(713) Li, Q.; Yuan, Z.; Zhang, C.; Hu, S.; Chen, Z.; Wu, Y.; Chen, P.; Qi, H.; Ye, D. Tough, Highly Oriented, Super Thermal Insulating Regenerated All-Cellulose Sponge-Aerogel Fibers Integrating a Graded Aligned Nanostructure. *Nano Lett.* **2022**, *22*, 3516−3524.
(714) An, L.; Liang, B.; Guo, Z.; Wang, J.; Li, C.; Huang, Y.; Hu, Y.; Li, Z.; Armstrong, J. N.; Zhou, C.; et al. Wearable Aramid−Ceramic Aerogel Composite for Harsh Environment. *Adv. Eng. Mater.* **2021**, *23*, 2001169.
(715) Jung, Y.; Ha, I.; Kim, M.; Ahn, J.; Lee, J.; Ko, S. H. High heat storing and thermally diffusive artificial skin for wearable thermal management. *Nano Energy* **2023**, *105*, 107979.
(716) Nie, S.; Cai, M.; Yang, H.; Shen, L.; Wang, S.; Zhu, Y.; Song, J. Soft, stretchable thermal protective substrates for wearable electronics. *NPJ Flexible Electron.* **2022**, *6*, 36.
(717) Gao, T.; Yang, Z.; Chen, C.; Li, Y.; Fu, K.; Dai, J.; Hitz, E. M.; Xie, H.; Liu, B.; Song, J.; et al. Three-Dimensional Printed Thermal Regulation Textiles. *ACS Nano* **2017**, *11*, 11513−11520.
(718) Yang, G.; Zhang, X.; Pan, D.; Zhang, W.; Shang, Y.; Su, F.; Ji, Y.; Liu, C.; Shen, C. Highly Thermal Conductive Poly(vinyl alcohol) Composites with Oriented Hybrid Networks: Silver Nanowire Bridged Boron Nitride Nanoplatelets. *ACS Appl. Mater. Interfaces* **2021**, *13*, 32286−32294.
(719) Kim, M.; Lee, D.; Son, S.; Yang, Y.; Lee, H.; Rho, J. Visibly Transparent Radiative Cooler under Direct Sunlight. *Adv. Opt. Mater.* **2021**, *9*, 2002226.
(720) Wang, M.; Yan, Z.; Wang, T.; Cai, P.; Gao, S.; Zeng, Y.; Wan, C.; Wang, H.; Pan, L.; Yu, J.; et al. Gesture recognition using a bioinspired learning architecture that integrates visual data with somatosensory data from stretchable sensors. *Nat. Electron.* **2020**, *3*, 563−570−563.
(721) Roh, E.; Hwang, B. U.; Kim, D.; Kim, B. Y.; Lee, N. E. Stretchable, Transparent, Ultrasensitive, and Patchable Strain Sensor for Human-Machine Interfaces Comprising a Nanohybrid of Carbon Nanotubes and Conductive Elastomers. *ACS Nano* **2015**, *9*, 6252−6261.
(722) Ho, M. D.; Ling, Y.; Yap, L. W.; Wang, Y.; Dong, D.; Zhao, Y.; Cheng, W. Percolating Network of Ultrathin Gold Nanowires and Silver Nanowires toward "Invisible" Wearable Sensors for Detecting Emotional Expression and Apexcardiogram. *Adv. Funct. Mater.* **2017**, *27*, 1700845.
(723) Choi, D. Y.; Kim, M. H.; Oh, Y. S.; Jung, S. H.; Jung, J. H.; Sung, H. J.; Lee, H. W.; Lee, H. M. Highly Stretchable, Hysteresis-Free Ionic Liquid-Based Strain Sensor for Precise Human Motion Monitoring. *ACS Appl. Mater. Interfaces* **2017**, *9*, 1770−1780.
(724) Wang, L.; Gao, G.; Zhou, Y.; Xu, T.; Chen, J.; Wang, R.; Zhang, R.; Fu, J. Tough, Adhesive, Self-Healable, and Transparent Ionically Conductive Zwitterionic Nanocomposite Hydrogels as Skin Strain Sensors. *ACS Appl. Mater. Interfaces* **2019**, *11*, 3506−3515.
(725) Chang, Q.; He, Y.; Liu, Y.; Zhong, W.; Wang, Q.; Lu, F.; Xing, M. Protein Gel Phase Transition: Toward Superiorly Transparent and Hysteresis-Free Wearable Electronics. *Adv. Funct. Mater.* **2020**, *30*, 1910080.
(726) Nie, B.; Li, R.; Cao, J.; Brandt, J. D.; Pan, T. Flexible transparent iontronic film for interfacial capacitive pressure sensing. *Adv. Mater.* **2015**, *27*, 6055−6062.
(727) Sarwar, M. S.; Dobashi, Y.; Preston, C.; Wyss, J. K.; Mirabbasi, S.; Madden, J. D. Bend, stretch, and touch: Locating a finger on an actively deformed transparent sensor array. *Sci. Adv.* **2017**, *3*, No. e1602200.
(728) Pyo, S.; Choi, J.; Kim, J. Flexible, Transparent, Sensitive, and Crosstalk-Free Capacitive Tactile Sensor Array Based on Graphene Electrodes and Air Dielectric. *Adv. Electron. Mater.* **2018**, *4*, 1700427.
(729) Kim, K.-B.; Jang, W.; Cho, J. Y.; Woo, S. B.; Jeon, D. H.; Ahn, J. H.; Hong, S. D.; Koo, H. Y.; Sung, T. H. Transparent and flexible piezoelectric sensor for detecting human movement with a boron nitride nanosheet (BNNS). *Nano Energy* **2018**, *54*, 91−98.
(730) Xu, Z.; Wan, X.; Mo, X.; Lin, S.; Chen, S.; Chen, J.; Pan, Y.; Zhang, H.; Jin, H.; Duan, J.; et al. Electrostatic Assembly of Laminated Transparent Piezoelectrets for Epidermal and Implantable Electronics. *Nano Energy* **2021**, *89*, 106450.
(731) Fan, F. R.; Lin, L.; Zhu, G.; Wu, W.; Zhang, R.; Wang, Z. L. Transparent triboelectric nanogenerators and self-powered pressure sensors based on micropatterned plastic films. *Nano Lett.* **2012**, *12*, 3109−3014.
(732) Hwang, H. J.; Kim, J. S.; Kim, W.; Park, H.; Bhatia, D.; Jee, E.; Chung, Y. S.; Kim, D. H.; Choi, D. An Ultra-Mechanosensitive Visco-Poroelastic Polymer Ion Pump for Continuous Self-Powering Kinematic Triboelectric Nanogenerators. *Adv. Energy Mater.* **2019**, *9*, 1803786.
(733) Trung, T. Q.; Ramasundaram, S.; Hwang, B. U.; Lee, N. E. An All-Elastomeric Transparent and Stretchable Temperature Sensor for Body-Attachable Wearable Electronics. *Adv. Mater.* **2016**, *28*, 502−509.

https://doi.org/10.1021/acs.chemrev.3c00139
Chem. Rev. 2023, 123, 9982−10078

(734) An, B. W.; Heo, S.; Ji, S.; Bien, F.; Park, J. U. Transparent and flexible fingerprint sensor array with multiplexed detection of tactile pressure and skin temperature. *Nat. Commun.* **2018**, *9*, 2458.
(735) Park, T. H.; Park, S.; Yu, S.; Park, S.; Lee, J.; Kim, S.; Jung, Y.; Yi, H. Highly Sensitive On-Skin Temperature Sensors Based on Biocompatible Hydrogels with Thermoresponsive Transparency and Resistivity. *Adv. Healthcare Mater.* **2021**, *10*, 2100469.
(736) Kim, J. H.; Kim, S. R.; Kil, H. J.; Kim, Y. C.; Park, J. W. Highly Conformable, Transparent Electrodes for Epidermal Electronics. *Nano Lett.* **2018**, *18*, 4531−4540.
(737) Zhao, Y.; Zhang, S.; Yu, T.; Zhang, Y.; Ye, G.; Cui, H.; He, C.; Jiang, W.; Zhai, Y.; Lu, C.; et al. Ultra-conformal skin electrodes with synergistically enhanced conductivity for long-time and low-motion artifact epidermal electrophysiology. *Nat. Commun.* **2021**, *12*, 4880.
(738) Park, D. W.; Ness, J. P.; Brodnick, S. K.; Esquibel, C.; Novello, J.; Atry, F.; Baek, D. H.; Kim, H.; Bong, J.; Swanson, K. I.; et al. Electrical Neural Stimulation and Simultaneous in Vivo Monitoring with Transparent Graphene Electrode Arrays Implanted in GCaMP6f Mice. *ACS Nano* **2018**, *12*, 148−157.
(739) Cho, Y. U.; Lee, J. Y.; Jeong, U. J.; Park, S. H.; Lim, S. L.; Kim, K. Y.; Jang, J. W.; Park, J. H.; Kim, H. W.; Shin, H.; et al. Ultra-Low Cost, Facile Fabrication of Transparent Neural Electrode Array for Electrocorticography with Photoelectric Artifact-Free Optogenetics. *Adv. Funct. Mater.* **2022**, *32*, 2105568.
(740) Oh, J.-W.; Heo, J.; Kim, T. H. An electrochemically modulated single-walled carbon nanotube network for the development of a transparent flexible sensor for dopamine. *Sens. Actuators, B* **2018**, *267*, 438−447.
(741) Zhang, Q.; Wang, X.; Decker, V.; Meyerhoff, M. E. Plasticizer-Free Thin-Film Sodium-Selective Optodes Inkjet-Printed on Transparent Plastic for Sweat Analysis. *ACS Appl. Mater. Interfaces* **2020**, *12*, 25616−25624.
(742) Li, J.; Jiang, M.; Su, M.; Tian, L.; Shi, W.; Yu, C. Stretchable and Transparent Electrochemical Sensor Based on Nanostructured Au on Carbon Nanotube Networks for Real-Time Analysis of H2O2 Release from Cells. *Anal. Chem.* **2021**, *93*, 6723−6730.
(743) Huang, C.; Hao, Z.; Wang, Z.; Wang, H.; Zhao, X.; Pan, Y. An Ultraflexible and Transparent Graphene-Based Wearable Sensor for Biofluid Biomarkers Detection. *Adv. Mater. Technol.* **2022**, *7*, 2101131.
(744) Gong, S.; Lai, D. T. H.; Su, B.; Si, K. J.; Ma, Z.; Yap, L. W.; Guo, P.; Cheng, W. Highly Stretchy Black Gold E-Skin Nanopatches as Highly Sensitive Wearable Biomedical Sensors. *Adv. Electron. Mater.* **2015**, *1*, 1400063.
(745) Lu, N.; Lu, C.; Yang, S.; Rogers, J. Highly Sensitive Skin-Mountable Strain Gauges Based Entirely on Elastomers. *Adv. Funct. Mater.* **2012**, *22*, 4044−4050.
(746) Wang, Y.; Wang, L.; Yang, T. T.; Li, X.; Zang, X. B.; Zhu, M.; Wang, K. L.; Wu, D. H.; Zhu, H. W. Wearable and Highly Sensitive Graphene Strain Sensors for Human Motion Monitoring. *Adv. Funct. Mater.* **2014**, *24*, 4666−4670.
(747) Moin, A.; Zhou, A.; Rahimi, A.; Menon, A.; Benatti, S.; Alexandrov, G.; Tamakloe, S.; Ting, J.; Yamamoto, N.; Khan, Y.; et al. A wearable biosensing system with in-sensor adaptive machine learning for hand gesture recognition. *Nat. Electron.* **2021**, *4*, 54−63.
(748) Kim, K. K.; Ha, I.; Kim, M.; Choi, J.; Won, P.; Jo, S.; Ko, S. H. A deep-learned skin sensor decoding the epicentral human motions. *Nat. Commun.* **2020**, *11*, 2149.
(749) Amjadi, M.; Kyung, K.-U.; Park, I.; Sitti, M. Stretchable, Skin-Mountable, and Wearable Strain Sensors and Their Potential Applications: A Review. *Adv. Funct. Mater.* **2016**, *26*, 1678−1698.
(750) You, I.; Kim, B.; Park, J.; Koh, K.; Shin, S.; Jung, S.; Jeong, U. Stretchable E-Skin Apexcardiogram Sensor. *Adv. Mater.* **2016**, *28*, 6359−6364.
(751) Zhu, S. E.; Ghatkesar, M. K.; Zhang, C.; Janssen, G. C. A. M. Graphene based piezoresistive pressure sensor. *Appl. Phys. Lett.* **2013**, *102*, 161904.
(752) Lee, J.; Kwon, H.; Seo, J.; Shin, S.; Koo, J. H.; Pang, C.; Son, S.; Kim, J. H.; Jang, Y. H.; Kim, D. E.; et al. Conductive fiber-based ultrasensitive textile pressure sensor for wearable electronics. *Adv. Mater.* **2015**, *27*, 2433−2439.
(753) Lei, Z.; Wang, Q.; Sun, S.; Zhu, W.; Wu, P. A Bioinspired Mineral Hydrogel as a Self-Healable, Mechanically Adaptable Ionic Skin for Highly Sensitive Pressure Sensing. *Adv. Mater.* **2017**, *29*, 1700321.
(754) Zhou, J.; Gu, Y.; Fei, P.; Mai, W.; Gao, Y.; Yang, R.; Bao, G.; Wang, Z. L. Flexible piezotronic strain sensor. *Nano Lett.* **2008**, *8*, 3035−3040.
(755) Sun, Q.; Seung, W.; Kim, B. J.; Seo, S.; Kim, S. W.; Cho, J. H. Active Matrix Electronic Skin Strain Sensor Based on Piezopotential-Powered Graphene Transistors. *Adv. Mater.* **2015**, *27*, 3411−3417.
(756) Wang, X.; Zhang, H.; Dong, L.; Han, X.; Du, W.; Zhai, J.; Pan, C.; Wang, Z. L. Self-Powered High-Resolution and Pressure-Sensitive Triboelectric Sensor Matrix for Real-Time Tactile Mapping. *Adv. Mater.* **2016**, *28*, 2896−2903.
(757) Fang, Y.; Zou, Y.; Xu, J.; Chen, G.; Zhou, Y.; Deng, W.; Zhao, X.; Roustaei, M.; Hsiai, T. K.; Chen, J. Ambulatory Cardiovascular Monitoring Via a Machine-Learning-Assisted Textile Triboelectric Sensor. *Adv. Mater.* **2021**, *33*, 2104178.
(758) Yamada, T.; Hayamizu, Y.; Yamamoto, Y.; Yomogida, Y.; Izadi-Najafabadi, A.; Futaba, D. N.; Hata, K. A stretchable carbon nanotube strain sensor for human-motion detection. *Nat. Nanotechnol.* **2011**, *6*, 296−301.
(759) Kim, K. K.; Hong, S.; Cho, H. M.; Lee, J.; Suh, Y. D.; Ham, J.; Ko, S. H. Highly Sensitive and Stretchable Multidimensional Strain Sensor with Prestrained Anisotropic Metal Nanowire Percolation Networks. *Nano Lett.* **2015**, *15*, 5240−5247.
(760) Amjadi, M.; Pichitpajongkit, A.; Lee, S.; Ryu, S.; Park, I. Highly stretchable and sensitive strain sensor based on silver nanowire-elastomer nanocomposite. *ACS Nano* **2014**, *8*, 5154−5163.
(761) Mutiso, R. M.; Sherrott, M. C.; Rathmell, A. R.; Wiley, B. J.; Winey, K. I. Integrating simulations and experiments to predict sheet resistance and optical transmittance in nanowire films for transparent conductors. *ACS Nano* **2013**, *7*, 7654−7663.
(762) Hempel, M.; Nezich, D.; Kong, J.; Hofmann, M. A novel class of strain gauges based on layered percolative films of 2D materials. *Nano Lett.* **2012**, *12*, 5714−5718.
(763) Bang, J.; Coskun, S.; Pyun, K. R.; Doganay, D.; Tunca, S.; Koylan, S.; Kim, D.; Unalan, H. E.; Ko, S. H. Advances in protective layer-coating on metal nanowires with enhanced stability and their applications. *Appl. Mater. Today* **2021**, *22*, 100909.
(764) Zang, Y.; Zhang, F.; Di, C.-a.; Zhu, D. Advances of flexible pressure sensors toward artificial intelligence and health care applications. *Mater. Horiz.* **2015**, *2*, 140−156.
(765) Tian, K.; Bae, J.; Bakarich, S. E.; Yang, C.; Gately, R. D.; Spinks, G. M.; in het Panhuis, M.; Suo, Z.; Vlassak, J. J. 3D Printing of Transparent and Conductive Heterogeneous Hydrogel-Elastomer Systems. *Adv. Mater.* **2017**, *29*, 1604827.
(766) Zhang, W.; Wang, R.; Sun, Z.; Zhu, X.; Zhao, Q.; Zhang, T.; Cholewinski, A.; Yang, F. K.; Zhao, B.; Pinnaratip, R.; et al. Catechol-functionalized hydrogels: biomimetic design, adhesion mechanism, and biomedical applications. *Chem. Soc. Rev.* **2020**, *49*, 433−464.
(767) Sun, H.; Zhao, Y.; Wang, C.; Zhou, K.; Yan, C.; Zheng, G.; Huang, J.; Dai, K.; Liu, C.; Shen, C. Ultra-Stretchable, durable and conductive hydrogel with hybrid double network as high performance strain sensor and stretchable triboelectric nanogenerator. *Nano Energy* **2020**, *76*, 105035.
(768) Zhang, Q.; Wang, Y. L.; Xia, Y.; Zhang, P. F.; Kirk, T. V.; Chen, X. D. Textile-Only Capacitive Sensors for Facile Fabric Integration without Compromise of Wearability. *Adv. Mater. Technol.* **2019**, *4*, 1900485.
(769) Xin, Y.; Zhou, J.; Xu, X.; Lubineau, G. Laser-engraved carbon nanotube paper for instilling high sensitivity, high stretchability, and high linearity in strain sensors. *Nanoscale* **2017**, *9*, 10897−10905.
(770) You, B.; Han, C. J.; Kim, Y.; Ju, B.-K.; Kim, J.-W. A wearable piezocapacitive pressure sensor with a single layer of silver nanowire-based elastomeric composite electrodes. *J. Mater. Chem. A* **2016**, *4*, 10435−10443.

https://doi.org/10.1021/acs.chemrev.3c00139
Chem. Rev. 2023, 123, 9982−10078

(771) Wang, J.; Jiu, J.; Araki, T.; Nogi, M.; Sugahara, T.; Nagao, S.; Koga, H.; He, P.; Suganuma, K. Silver Nanowire Electrodes: Conductivity Improvement Without Post-treatment and Application in Capacitive Pressure Sensors. *Nano Micro Lett.* **2015**, *7*, 51−58.
(772) Hu, W.; Niu, X.; Zhao, R.; Pei, Q. Elastomeric transparent capacitive sensors based on an interpenetrating composite of silver nanowires and polyurethane. *Appl. Phys. Lett.* **2013**, *102*, 083303.
(773) Ha, M.; Lim, S.; Park, J.; Um, D.-S.; Lee, Y.; Ko, H. Bioinspired Interlocked and Hierarchical Design of ZnO Nanowire Arrays for Static and Dynamic Pressure-Sensitive Electronic Skins. *Adv. Funct. Mater.* **2015**, *25*, 2841−2849.
(774) Vuorinen, T.; Zakrzewski, M.; Rajala, S.; Lupo, D.; Vanhala, J.; Palovuori, K.; Tuukkanen, S. Printable, Transparent, and Flexible Touch Panels Working in Sunlight and Moist Environments. *Adv. Funct. Mater.* **2014**, *24*, 6340−6347.
(775) Jeong, C. K.; Hyeon, D. Y.; Hwang, G.-T.; Lee, G.-J.; Lee, M.-K.; Park, J.-J.; Park, K.-I. Nanowire-percolated piezoelectric copolymer-based highly transparent and flexible self-powered sensors. *J. Mater. Chem. A* **2019**, *7*, 25481−25489.
(776) Jaffe, H. Piezoelectric Ceramics. *J. Am. Ceram. Soc.* **1958**, *41*, 494−498.
(777) Gong, H.; Zhang, Y.; Quan, J.; Che, S. Preparation and properties of cement based piezoelectric composites modified by CNTs. *Curr. Appl. Phys.* **2011**, *11*, 653−656.
(778) Tao, K.; Chen, Z.; Yu, J.; Zeng, H.; Wu, J.; Wu, Z.; Jia, Q.; Li, P.; Fu, Y.; Chang, H.; et al. Ultra-Sensitive, Deformable, and Transparent Triboelectric Tactile Sensor Based on Micro-Pyramid Patterned Ionic Hydrogel for Interactive Human-Machine Interfaces. *Adv. Sci.* **2022**, *9*, 2104168.
(779) Wu, C.; Wang, A. C.; Ding, W.; Guo, H.; Wang, Z. L. Triboelectric Nanogenerator: A Foundation of the Energy for the New Era. *Adv. Energy Mater.* **2019**, *9*, 1802906.
(780) Froudarakis, M. E.; Klimathianaki, M.; Pougounias, M. Systemic inflammatory reaction after thoracoscopic talc poudrage. *Chest* **2006**, *129*, 356−361.
(781) Walia, S.; Mondal, I.; Kulkarni, G. U. Patterned Cu-Mesh-Based Transparent and Wearable Touch Panel for Tactile, Proximity, Pressure, and Temperature Sensing. *ACS Appl. Electron. Mater.* **2019**, *1*, 1597−1604.
(782) Zhang, C.; Zhou, Y.; Han, H.; Zheng, H.; Xu, W.; Wang, Z. Dopamine-Triggered Hydrogels with High Transparency, Self-Adhesion, and Thermoresponse as Skinlike Sensors. *ACS Nano* **2021**, *15*, 1785−1794.
(783) Wu, J.; Wu, Z.; Wei, Y.; Ding, H.; Huang, W.; Gui, X.; Shi, W.; Shen, Y.; Tao, K.; Xie, X. Ultrasensitive and Stretchable Temperature Sensors Based on Thermally Stable and Self-Healing Organo-hydrogels. *ACS Appl. Mater. Interfaces* **2020**, *12*, 19069−19079.
(784) Bian, Z.; Song, J.; Webb, R. C.; Bonifas, A. P.; Rogers, J. A.; Huang, Y. Thermal analysis of ultrathin, compliant sensors for characterization of the human skin. *RSC Adv.* **2014**, *4*, 5694−5697.
(785) Yeo, W. H.; Kim, Y. S.; Lee, J.; Ameen, A.; Shi, L.; Li, M.; Wang, S.; Ma, R.; Jin, S. H.; Kang, Z.; et al. Multifunctional epidermal electronics printed directly onto the skin. *Adv. Mater.* **2013**, *25*, 2773−2778.
(786) Won, S. M.; Song, E.; Zhao, J.; Li, J.; Rivnay, J.; Rogers, J. A. Recent Advances in Materials, Devices, and Systems for Neural Interfaces. *Adv. Mater.* **2018**, *30*, 1800534.
(787) Seo, J. W.; Kim, K.; Seo, K. W.; Kim, M. K.; Jeong, S.; Kim, H.; Ghim, J. W.; Lee, J. H.; Choi, N.; Lee, J. Y.; et al. Artifact-Free 2D Mapping of Neural Activity In Vivo through Transparent Gold Nanonetwork Array. *Adv. Funct. Mater.* **2020**, *30*, 2000896.
(788) Kuzum, D.; Takano, H.; Shim, E.; Reed, J. C.; Juul, H.; Richardson, A. G.; de Vries, J.; Bink, H.; Dichter, M. A.; Lucas, T. H.; et al. Transparent and flexible low noise graphene electrodes for simultaneous electrophysiology and neuroimaging. *Nat. Commun.* **2014**, *5*, 5259.
(789) Park, D. W.; Brodnick, S. K.; Ness, J. P.; Atry, F.; Krugner-Higby, L.; Sandberg, A.; Mikael, S.; Richner, T. J.; Novello, J.; Kim, H.; et al. Fabrication and utility of a transparent graphene neural electrode array for electrophysiology, in vivo imaging, and optogenetics. *Nat. Protoc.* **2016**, *11*, 2201−2222.
(790) Nishimura, A.; Suwabe, R.; Ogihara, Y.; Yoshida, S.; Abe, H.; Osawa, S. I.; Nakagawa, A.; Tominaga, T.; Nishizawa, M. Totally transparent hydrogel-based subdural electrode with patterned salt bridge. *Biomed. Microdevices* **2020**, *22*, 57.
(791) Wang, L.; Zhong, C.; Ke, D.; Ye, F.; Tu, J.; Wang, L.; Lu, Y. Ultrasoft and Highly Stretchable Hydrogel Optical Fibers for In Vivo Optogenetic Modulations. *Adv. Opt. Mater.* **2018**, *6*, 1800427.
(792) Kozai, T. D.; Vazquez, A. L. Photoelectric artefact from optogenetics and imaging on microelectrodes and bioelectronics: New Challenges and Opportunities. *J.Mater. Chem. B* **2015**, *3*, 4965−4978.
(793) Sempionatto, J. R.; Lasalde-Ramírez, J. A.; Mahato, K.; Wang, J.; Gao, W. Wearable chemical sensors for biomarker discovery in the omics era. *Nat. Rev. Chem.* **2022**, *6*, 899−915.
(794) Jia, W.; Bandodkar, A. J.; Valdes-Ramirez, G.; Windmiller, J. R.; Yang, Z.; Ramirez, J.; Chan, G.; Wang, J. Electrochemical tattoo biosensors for real-time noninvasive lactate monitoring in human perspiration. *Anal. Chem.* **2013**, *85*, 6553−6560.
(795) Tseng, P.; Napier, B.; Garbarini, L.; Kaplan, D. L.; Omenetto, F. G. Functional, RF-Trilayer Sensors for Tooth-Mounted, Wireless Monitoring of the Oral Cavity and Food Consumption. *Adv. Mater.* **2018**, *30*, 1703257.
(796) Park, S. I.; Xiong, Y.; Kim, R. H.; Elvikis, P.; Meitl, M.; Kim, D. H.; Wu, J.; Yoon, J.; Yu, C. J.; Liu, Z.; et al. Printed assemblies of inorganic light-emitting diodes for deformable and semitransparent displays. *Science* **2009**, *325*, 977−981.
(797) Choi, M. K.; Yang, J.; Kim, D. C.; Dai, Z.; Kim, J.; Seung, H.; Kale, V. S.; Sung, S. J.; Park, C. R.; Lu, N.; et al. Extremely Vivid, Highly Transparent, and Ultrathin Quantum Dot Light-Emitting Diodes. *Adv. Mater.* **2018**, *30*, 1703279.
(798) King, P. J.; Higgins, T. M.; De, S.; Nicoloso, N.; Coleman, J. N. Percolation effects in supercapacitors with thin, transparent carbon nanotube electrodes. *ACS Nano* **2012**, *6*, 1732−1741.
(799) Jo, K.; Lee, S.; Kim, S.-M.; In, J. B.; Lee, S.-M.; Kim, J.-H.; Lee, H.-J.; Kim, K.-S. Stacked Bilayer Graphene and Redox-Active Interlayer for Transparent and Flexible High-Performance Supercapacitors. *Chem. Mater.* **2015**, *27*, 3621−3627.
(800) Zhang, C. J.; Anasori, B.; Seral-Ascaso, A.; Park, S. H.; McEvoy, N.; Shmeliov, A.; Duesberg, G. S.; Coleman, J. N.; Gogotsi, Y.; Nicolosi, V. Transparent, Flexible, and Conductive 2D Titanium Carbide (MXene) Films with High Volumetric Capacitance. *Adv. Mater.* **2017**, *29*, 1702678.
(801) Liu, X.; Wang, J.; Yang, G. Amorphous nickel oxide and crystalline manganese oxide nanocomposite electrode for transparent and flexible supercapacitor. *Chem. Eng. J.* **2018**, *347*, 101−110.
(802) Zhong, Y.; Zhang, X.; He, Y.; Peng, H.; Wang, G.; Xin, G. Simultaneously Armored and Active Graphene for Transparent and Flexible Supercapacitors. *Adv. Funct. Mater.* **2018**, *28*, 1801998.
(803) Zhang, G.; Zhao, Y.; Hu, J.; Liu, H.; Chen, T.; Yu, H.; Duan, H. Freestanding ultralight metallic micromesh for high-energy density flexible transparent supercapacitors. *J. Mater. Chem. A* **2022**, *10*, 22182−22193.
(804) Yuan, Y.; Jiang, L.; Li, X.; Zuo, P.; Zhang, X.; Lian, Y.; Ma, Y.; Liang, M.; Zhao, Y.; Qu, L. Ultrafast Shaped Laser Induced Synthesis of MXene Quantum Dots/Graphene for Transparent Supercapacitors. *Adv. Mater.* **2022**, *34*, 2110013.
(805) Yang, Y.; Jeong, S.; Hu, L.; Wu, H.; Lee, S. W.; Cui, Y. Transparent lithium-ion batteries. *Proc. Natl. Acad. Sci. U.S.A.* **2011**, *108*, 13013−13018.
(806) Oukassi, S.; Baggetto, L.; Dubarry, C.; Le Van-Jodin, L.; Poncet, S.; Salot, R. Transparent Thin Film Solid-State Lithium Ion Batteries. *ACS Appl. Mater. Interfaces* **2019**, *11*, 683−690.
(807) Singh, S. B.; Tran, D. T.; Jeong, K. U.; Kim, N. H.; Lee, J. H. A Flexible and Transparent Zinc-Nanofiber Network Electrode for Wearable Electrochromic, Rechargeable Zn-Ion Battery. *Small* **2022**, *18*, 2104462.

https://doi.org/10.1021/acs.chemrev.3c00139
Chem. Rev. 2023, 123, 9982−10078

(808) Liu, T.; Chen, X.; Tervoort, E.; Kraus, T.; Niederberger, M. Design and Fabrication of Transparent and Stretchable Zinc Ion Batteries. *ACS Appl. Energy Mater.* **2021**, *4*, 6166−6179.
(809) Choi, M.-Y.; Choi, D.; Jin, M.-J.; Kim, I.; Kim, S.-H.; Choi, J.-Y.; Lee, S. Y.; Kim, J. M.; Kim, S.-W. Mechanically Powered Transparent Flexible Charge-Generating Nanodevices with Piezoelectric ZnO Nanorods. *Adv. Mater.* **2009**, *21*, 2185−2189.
(810) Badatya, S.; Kumar, A.; Sharma, C.; Srivastava, A. K.; Chaurasia, J. P.; Gupta, M. K. Transparent flexible graphene quantum dot-(PVDF-HFP) piezoelectric nanogenerator. *Mater. Lett.* **2021**, *290*, 129493.
(811) Bharti, D. K.; Gupta, M. K.; Kumar, R.; Sathish, N.; Srivastava, A. K. Non-centrosymmetric zinc silicate-graphene based transparent flexible piezoelectric nanogenerator. *Nano Energy* **2020**, *73*, 104821.
(812) Shepelin, N. A.; Sherrell, P. C.; Goudeli, E.; Skountzos, E. N.; Lussini, V. C.; Dicinoski, G. W.; Shapter, J. G.; Ellis, A. V. Printed recyclable and self-poled polymer piezoelectric generators through single-walled carbon nanotube templating. *Energy Environ. Sci.* **2020**, *13*, 868−883.
(813) Liu, G.; Tang, Y.; Soomro, A. M.; Shen, P.; Lu, S.; Cai, Y.; Wang, H.; Yang, Q.; Chen, H.; Shi, Y.; et al. Vertically aligned ZnO nanoarray directly orientated on Cu paper by h-BN monolayer for flexible and transparent piezoelectric nanogenerator. *Nano Energy* **2023**, *109*, 108265.
(814) Pu, X.; Liu, M.; Chen, X.; Sun, J.; Du, C.; Zhang, Y.; Zhai, J.; Hu, W.; Wang, Z. L. Ultrastretchable, transparent triboelectric nanogenerator as electronic skin for biomechanical energy harvesting and tactile sensing. *Sci. Adv.* **2017**, *3*, No. e1700015.
(815) Zhao, G.; Zhang, Y.; Shi, N.; Liu, Z.; Zhang, X.; Wu, M.; Pan, C.; Liu, H.; Li, L.; Wang, Z. L. Transparent and stretchable triboelectric nanogenerator for self-powered tactile sensing. *Nano Energy* **2019**, *59*, 302−310.
(816) Guo, X.; Yang, F.; Sun, X.; Bai, Y.; Liu, G.; Liu, W.; Wang, R.; He, X. Anti-Freezing Self-Adhesive Self-Healing Degradable Touch Panel with Ultra-Stretchable Performance Based on Transparent Triboelectric Nanogenerators. *Adv. Funct. Mater.* **2022**, *32*, 2201230.
(817) Park, H.; Oh, S. J.; Kim, D.; Kim, M.; Lee, C.; Joo, H.; Woo, I.; Bae, J. W.; Lee, J. H. Plasticized PVC-Gel Single Layer-Based Stretchable Triboelectric Nanogenerator for Harvesting Mechanical Energy and Tactile Sensing. *Adv. Sci.* **2022**, *9*, 2201070.
(818) Yang, C.; Souchay, D.; Kneiss, M.; Bogner, M.; Wei, H. M.; Lorenz, M.; Oeckler, O.; Benstetter, G.; Fu, Y. Q.; Grundmann, M. Transparent flexible thermoelectric material based on non-toxic earth-abundant p-type copper iodide thin film. *Nat. Commun.* **2017**, *8*, 16076.
(819) Paul, B.; Khranovskyy, V.; Yakimova, R.; Eklund, P. Donor-doped ZnO thin films on mica for fully-inorganic flexible thermoelectrics. *Mater. Res. Lett.* **2019**, *7*, 239−243.
(820) Coroa, J.; Morais Faustino, B. M.; Marques, A.; Bianchi, C.; Koskinen, T.; Juntunen, T.; Tittonen, I.; Ferreira, I. Highly transparent copper iodide thin film thermoelectric generator on a flexible substrate. *RSC Adv.* **2019**, *9*, 35384−35391.
(821) Zhao, W.; Jiang, M.; Wang, W.; Liu, S.; Huang, W.; Zhao, Q. Flexible Transparent Supercapacitors: Materials and Devices. *Adv. Funct. Mater.* **2021**, *31*, 2009136.
(822) Hall, P. J.; Bain, E. J. Energy-storage technologies and electricity generation. *Energy Policy* **2008**, *36*, 4352−4355.
(823) Wei, D.; Wakeham, S. J.; Ng, T. W.; Thwaites, M. J.; Brown, H.; Beecher, P. Transparent, flexible and solid-state supercapacitors based on room temperature ionic liquid gel. *Electrochem. Commun.* **2009**, *11*, 2285−2287.
(824) Qiu, T.; Luo, B.; Giersig, M.; Akinoglu, E. M.; Hao, L.; Wang, X.; Shi, L.; Jin, M.; Zhi, L. Au@MnO2 core-shell nanomesh electrodes for transparent flexible supercapacitors. *Small* **2014**, *10*, 4136−4141.
(825) Cai, G.; Darmawan, P.; Cui, M.; Wang, J.; Chen, J.; Magdassi, S.; Lee, P. S. Highly Stable Transparent Conductive Silver Grid/PEDOT:PSS Electrodes for Integrated Bifunctional Flexible Electrochromic Supercapacitors. *Adv. Energy Mater.* **2016**, *6*, 1501882.
(826) Kim, C.; Yang, K. S. Electrochemical properties of carbon nanofiber web as an electrode for supercapacitor prepared by electrospinning. *Appl. Phys. Lett.* **2003**, *83*, 1216−1218.
(827) Palchoudhury, S.; Ramasamy, K.; Gupta, R. K.; Gupta, A. Flexible Supercapacitors: A Materials Perspective. *Front. Mater.* **2019**, *5*, 83.
(828) Choudhary, N.; Li, C.; Moore, J.; Nagaiah, N.; Zhai, L.; Jung, Y.; Thomas, J. Asymmetric Supercapacitor Electrodes and Devices. *Adv. Mater.* **2017**, *29*, 1605336.
(829) Hu, M.; Zhang, H.; Hu, T.; Fan, B.; Wang, X.; Li, Z. Emerging 2D MXenes for supercapacitors: status, challenges and prospects. *Chem. Soc. Rev.* **2020**, *49*, 6666−6693.
(830) Sasaki, T.; Ukyo, Y.; Novak, P. Memory effect in a lithium-ion battery. *Nat. Mater.* **2013**, *12*, 569−575.
(831) Zhou, G.; Li, F.; Cheng, H.-M. Progress in flexible lithium batteries and future prospects. *Energy Environ. Sci.* **2014**, *7*, 1307−1338.
(832) Pender, J. P.; Jha, G.; Youn, D. H.; Ziegler, J. M.; Andoni, I.; Choi, E. J.; Heller, A.; Dunn, B. S.; Weiss, P. S.; Penner, R. M.; et al. Electrode Degradation in Lithium-Ion Batteries. *ACS Nano* **2020**, *14*, 1243−1295.
(833) Liu, Y.; He, G.; Jiang, H.; Parkin, I. P.; Shearing, P. R.; Brett, D. J. L. Cathode Design for Aqueous Rechargeable Multivalent Ion Batteries: Challenges and Opportunities. *Adv. Funct. Mater.* **2021**, *31*, 2010445.
(834) Cheng, Y.; Luo, L.; Zhong, L.; Chen, J.; Li, B.; Wang, W.; Mao, S. X.; Wang, C.; Sprenkle, V. L.; Li, G.; et al. Highly Reversible Zinc-Ion Intercalation into Chevrel Phase Mo6S8 Nanocubes and Applications for Advanced Zinc-Ion Batteries. *ACS Appl. Mater. Interfaces* **2016**, *8*, 13673−13677.
(835) Starner, T. Human-powered wearable computing. *IBM Syst. J.* **1996**, *35*, 618−629.
(836) Khalid, S.; Raouf, I.; Khan, A.; Kim, N.; Kim, H. S. A Review of Human-Powered Energy Harvesting for Smart Electronics: Recent Progress and Challenges. *Int. J. Precis. Eng. Manuf. Green Technol.* **2019**, *6*, 821−851.
(837) Zhao, Z.; Dai, Y.; Dou, S. X.; Liang, J. Flexible nanogenerators for wearable electronic applications based on piezoelectric materials. *Mater. Today Energy* **2021**, *20*, 100690.
(838) Lin, Z. H.; Yang, Y.; Wu, J. M.; Liu, Y.; Zhang, F.; Wang, Z. L. BaTiO3 Nanotubes-Based Flexible and Transparent Nanogenerators, J. Phys. *Chem. Lett.*, **2012**, *3*, 3599−3604.
(839) Kim, S. K.; Bhatia, R.; Kim, T.-H.; Seol, D.; Kim, J. H.; Kim, H.; Seung, W.; Kim, Y.; Lee, Y. H.; Kim, S.-W. Directional dependent piezoelectric effect in CVD grown monolayer MoS2 for flexible piezoelectric nanogenerators. *Nano Energy* **2016**, *22*, 483−489.
(840) Zhu, R.; Chung, C. H.; Cha, K. C.; Yang, W.; Zheng, Y. B.; Zhou, H.; Song, T. B.; Chen, C. C.; Weiss, P. S.; Li, G.; et al. Fused silver nanowires with metal oxide nanoparticles and organic polymers for highly transparent conductors. *ACS Nano* **2011**, *5*, 9877−9882.
(841) Jung, Y.; Choi, J.; Yoon, Y.; Park, H.; Lee, J.; Ko, S. H. Soft multi-modal thermoelectric skin for dual functionality of underwater energy harvesting and thermoregulation. *Nano Energy* **2022**, *95*, 107002.
(842) Fatima, N.; Karimov, K. S.; Nabi, J. U.; Meng, H.; Ahmad, Z.; Riaz, M.; Bashir, M. M.; Khan, M. I.; Ali, R.; Khan, A.; et al. Semi-transparent thermo-electric cells based on bismuth telluride and its composites with CNTs and graphene. *J. Optoelectron. Adv. Mater.* **2019**, *21*, 333−337.
(843) Zhang, Y.; Huo, Z.; Wang, X.; Han, X.; Wu, W.; Wan, B.; Wang, H.; Zhai, J.; Tao, J.; Pan, C.; et al. High precision epidermal radio frequency antenna via nanofiber network for wireless stretchable multifunction electronics. *Nat. Commun.* **2020**, *11*, 5629.
(844) Park, J.; Kim, J.; Kim, K.; Kim, S. Y.; Cheong, W. H.; Park, K.; Song, J. H.; Namgoong, G.; Kim, J. J.; Heo, J.; et al. Wearable, wireless gas sensors using highly stretchable and transparent structures of nanowires and graphene. *Nanoscale* **2016**, *8*, 10591−10597.

https://doi.org/10.1021/acs.chemrev.3c00139
Chem. Rev. 2023, 123, 9982−10078

(845) Hong, S.; Kang, S. H.; Kim, Y.; Jung, C. W. Transparent and Flexible Antenna for Wearable Glasses Applications. *IEEE Trans. Antennas Propag.* **2016**, *64*, 2797−2804.
(846) Birch, N.; Graham, J.; Priestley, T.; Heywood, C.; Sakel, M.; Gall, A.; Nunn, A.; Signal, N. Results of the first interim analysis of the RAPPER II trial in patients with spinal cord injury: ambulation and functional exercise programs in the REX powered walking aid. *J. NeuroEng. Rehabil.* **2017**, *14*, 60.
(847) Marconi, D.; Baldoni, A.; McKinney, Z.; Cempini, M.; Crea, S.; Vitiello, N. A novel hand exoskeleton with series elastic actuation for modulated torque transfer. *Mechatronics* **2019**, *61*, 69−82.
(848) Laschi, C.; Mazzolai, B.; Cianchetti, M. Soft robotics: Technologies and systems pushing the boundaries of robot abilities. *Sci. Rob.* **2016**, *1*, No. eaah3690.
(849) Li, M.; Pal, A.; Aghakhani, A.; Pena-Francesch, A.; Sitti, M. Soft actuators for real-world applications. *Nat. Rev. Mater.* **2022**, *7*, 235−249.
(850) Sonar, H. A.; Gerratt, A. P.; Lacour, S. P.; Paik, J. Closed-Loop Haptic Feedback Control Using a Self-Sensing Soft Pneumatic Actuator Skin. *Soft Robot* **2020**, *7*, 22−29.
(851) Breger, J. C.; Yoon, C.; Xiao, R.; Kwag, H. R.; Wang, M. O.; Fisher, J. P.; Nguyen, T. D.; Gracias, D. H. Self-folding thermo-magnetically responsive soft microgrippers. *ACS Appl. Mater. Interfaces* **2015**, *7*, 3398−3405.
(852) Fusco, S.; Sakar, M. S.; Kennedy, S.; Peters, C.; Bottani, R.; Starsich, F.; Mao, A.; Sotiriou, G. A.; Pane, S.; Pratsinis, S. E.; et al. An integrated microrobotic platform for on-demand, targeted therapeutic interventions. *Adv. Mater.* **2014**, *26*, 952−957.
(853) In, H.; Kang, B. B.; Sin, M.; Cho, K.-J. Exo-Glove: A Wearable Robot for the Hand with a Soft Tendon Routing System. *IEEE Rob. Autom. Mag.* **2015**, *22*, 97−105.
(854) Kim, D.; Kang, B. B.; Kim, K. B.; Choi, H.; Ha, J.; Cho, K. J.; Jo, S. Eyes are faster than hands: A soft wearable robot learns user intention from the egocentric view. *Sci. Robot.* **2019**, *4*, No. eaav2949.
(855) Yuk, H.; Lin, S.; Ma, C.; Takaffoli, M.; Fang, N. X.; Zhao, X. Hydraulic hydrogel actuators and robots optically and sonically camouflaged in water. *Nat. Commun.* **2017**, *8*, 14230.
(856) Wang, Z.; Cui, H.; Liu, M.; Grage, S. L.; Hoffmann, M.; Sedghamiz, E.; Wenzel, W.; Levkin, P. A. Tough, Transparent, 3D-Printable, and Self-Healing Poly(ethylene glycol)-Gel (PEGgel). *Adv. Mater.* **2022**, *34*, 2107791.
(857) Yuan, W.; Hu, L. B.; Yu, Z. B.; Lam, T.; Biggs, J.; Ha, S. M.; Xi, D. J.; Chen, B.; Senesky, M. K.; Grüner, G.; et al. Fault-Tolerant Dielectric Elastomer Actuators using Single-Walled Carbon Nanotube Electrodes. *Adv. Mater.* **2008**, *20*, 621−625.
(858) Wu, J.; Zang, J.; Rathmell, A. R.; Zhao, X.; Wiley, B. J. Reversible sliding in networks of nanowires. *Nano Lett.* **2013**, *13*, 2381−2386.
(859) Kellaris, N.; Gopaluni Venkata, V.; Smith, G. M.; Mitchell, S. K.; Keplinger, C. Peano-HASEL actuators: Muscle-mimetic, electro-hydraulic transducers that linearly contract on activation. *Sci. Rob.* **2018**, *3*, No. eaar3276.
(860) Christianson, C.; Goldberg, N. N.; Deheyn, D. D.; Cai, S.; Tolley, M. T. Translucent soft robots driven by frameless fluid electrode dielectric elastomer actuators. *Sci. Rob.* **2018**, *3*, No. eaat1893.
(861) Wang, Y.; Zhang, P.; Huang, H.; Zhu, J. Bio-Inspired Transparent Soft Jellyfish Robot. *Soft Robot* **2023**, *10*, 590−600.
(862) Wang, Y.; Li, P.; Gupta, U.; Ouyang, J.; Zhu, J. Tunable Soft Lens of Large Focal Length Change. *Soft Robot* **2022**, *9*, 705−712.
(863) Behl, M.; Kratz, K.; Zotzmann, J.; Nochel, U.; Lendlein, A. Reversible bidirectional shape-memory polymers. *Adv. Mater.* **2013**, *25*, 4466−4469.
(864) Zhang, F.; Xiong, L.; Ai, Y.; Liang, Z.; Liang, Q. Stretchable Multiresponsive Hydrogel with Actuatable, Shape Memory, and Self-Healing Properties. *Adv. Sci.* **2018**, *5*, 1800450.
(865) He, Q.; Wang, Z.; Wang, Y.; Minori, A.; Tolley, M. T.; Cai, S. Electrically controlled liquid crystal elastomer-based soft tubular actuator with multimodal actuation. *Sci. Adv.* **2019**, *5*, No. eaax5746.
(866) Huang, X.; Zhang, F.; Leng, J. Metal mesh embedded in colorless shape memory polyimide for flexible transparent electric-heater and actuators. *Appl. Mater. Today* **2020**, *21*, 100797.
(867) Koga, T.; Tomimori, K.; Higashi, N. Transparent, High-Strength, and Shape Memory Hydrogels from Thermo-Responsive Amino Acid-Derived Vinyl Polymer Networks. *Macromol. Rapid Commun.* **2020**, *41*, 1900650.
(868) Nguyen, P. H.; Zhang, W. Design and Computational Modeling of Fabric Soft Pneumatic Actuators for Wearable Assistive Devices. *Sci. Rep.* **2020**, *10*, 9638.
(869) Mosadegh, B.; Polygerinos, P.; Keplinger, C.; Wennstedt, S.; Shepherd, R. F.; Gupta, U.; Shim, J.; Bertoldi, K.; Walsh, C. J.; Whitesides, G. M. Pneumatic Networks for Soft Robotics that Actuate Rapidly. *Adv. Funct. Mater.* **2014**, *24*, 2163−2170.
(870) Ke, X.; Jang, J.; Chai, Z.; Yong, H.; Zhu, J.; Chen, H.; Guo, C. F.; Ding, H.; Wu, Z. Stiffness Preprogrammable Soft Bending Pneumatic Actuators for High-Efficient, Conformal Operation. *Soft Robot* **2022**, *9*, 613−624.
(871) Kim, T. K.; Kim, J. K.; Jeong, O. C. Measurement of nonlinear mechanical properties of PDMS elastomer. *Microelectron. Eng.* **2011**, *88*, 1982−1985.
(872) Li, S.; Vogt, D. M.; Rus, D.; Wood, R. J. Fluid-driven origami-inspired artificial muscles. *Proc. Natl. Acad. Sci. U.S.A.* **2017**, *114*, 13132−13137.
(873) Gorissen, B.; Melancon, D.; Vasios, N.; Torbati, M.; Bertoldi, K. Inflatable soft jumper inspired by shell snapping. *Sci. Rob.* **2020**, *5*, No. eabb1967.
(874) Siefert, E.; Reyssat, E.; Bico, J.; Roman, B. Bio-inspired pneumatic shape-morphing elastomers. *Nat. Mater.* **2019**, *18*, 24−28.
(875) Unger, M. A.; Chou, H. P.; Thorsen, T.; Scherer, A.; Quake, S. R. Monolithic microfabricated valves and pumps by multilayer soft lithography. *Science* **2000**, *288*, 113−116.
(876) Xie, Z.; Domel, A. G.; An, N.; Green, C.; Gong, Z.; Wang, T.; Knubben, E. M.; Weaver, J. C.; Bertoldi, K.; Wen, L. Octopus Arm-Inspired Tapered Soft Actuators with Suckers for Improved Grasping. *Soft Robot* **2020**, *7*, 639−648.
(877) Martinez, R. V.; Fish, C. R.; Chen, X.; Whitesides, G. M. Elastomeric Origami: Programmable Paper-Elastomer Composites as Pneumatic Actuators. *Adv. Funct. Mater.* **2012**, *22*, 1376−1384.
(878) Rehman, T.; Nafea, M.; Faudzi, A. A.; Saleh, T.; Ali, M. S. M. PDMS-based dual-channel pneumatic micro-actuator. *Smart Mater. Struct.* **2019**, *28*, 115044.
(879) Shepherd, R. F.; Ilievski, F.; Choi, W.; Morin, S. A.; Stokes, A. A.; Mazzeo, A. D.; Chen, X.; Wang, M.; Whitesides, G. M. Multigait soft robot. *Proc. Natl. Acad. Sci. U.S.A.* **2011**, *108*, 20400−20403.
(880) Pelrine, R.; Kornbluh, R.; Pei, Q.; Joseph, J. High-speed electrically actuated elastomers with strain greater than 100%. *Science* **2000**, *287*, 836−839.
(881) Zhang, Q. M.; Li, H.; Poh, M.; Xia, F.; Cheng, Z. Y.; Xu, H.; Huang, C. An all-organic composite actuator material with a high dielectric constant. *Nature* **2002**, *419*, 284−287.
(882) Acome, E.; Mitchell, S. K.; Morrissey, T. G.; Emmett, M. B.; Benjamin, C.; King, M.; Radakovitz, M.; Keplinger, C. Hydraulically amplified self-healing electrostatic actuators with muscle-like performance. *Science* **2018**, *359*, 61−65.
(883) Chen, Y.; Zhao, H.; Mao, J.; Chirarattananon, P.; Helbling, E. F.; Hyun, N. P.; Clarke, D. R.; Wood, R. J. Controlled flight of a microrobot powered by soft artificial muscles. *Nature* **2019**, *575*, 324−329.
(884) Brochu, P.; Pei, Q. Advances in dielectric elastomers for actuators and artificial muscles. *Macromol. Rapid Commun.* **2010**, *31*, 10−36.
(885) Yuan, C.; Roach, D. J.; Dunn, C. K.; Mu, Q.; Kuang, X.; Yakacki, C. M.; Wang, T. J.; Yu, K.; Qi, H. J. 3D printed reversible shape changing soft actuators assisted by liquid crystal elastomers. *Soft Matter* **2017**, *13*, 5558−5568.
(886) Lin, C.-Y.; Hu, N.-W.; Chang, H.-W.; Lu, C.-Y.; Chen, C.-Y.; Wu, C.-C. Efficient transparent small-molecule organic light-emitting

devices adopting laminated transparent top electrodes. *Org. Electron.* **2016**, *28*, 25−30.
(887) Ryu, S. Y.; Noh, J. H.; Hwang, B. H.; Kim, C. S.; Jo, S. J.; Kim, J. T.; Hwang, H. S.; Baik, H. K.; Jeong, H. S.; Lee, C. H.; et al. Transparent organic light-emitting diodes consisting of a metal oxide multilayer cathode. *Appl. Phys. Lett.* **2008**, *92*, 023306.
(888) Bulovic, V.; Gu, G.; Burrows, P.; Forrest, S.; Thompson, M. Transparent light-emitting devices. *Nature* **1996**, *380*, 29.
(889) Chen, L.; Lee, M.-H.; Wang, Y.; Lau, Y. S.; Syed, A. A.; Zhu, F. Interface dipole for remarkable efficiency enhancement in all-solution-processable transparent inverted quantum dot light-emitting diodes. *J. Mater. Chem. C* **2018**, *6*, 2596−2603.
(890) Park, S.; Lim, J. T.; Jin, W.-Y.; Lee, H.; Kwon, B.-H.; Cho, N. S.; Han, J.-H.; Kang, J.-W.; Yoo, S.; Lee, J.-I. Efficient Large-Area Transparent OLEDs Based on a Laminated Top Electrode with an Embedded Auxiliary Mesh. *ACS Photonics* **2017**, *4*, 1114−1122.
(891) Yao, L.; Fang, X.; Gu, W.; Zhai, W.; Wan, Y.; Xie, X.; Xu, W.; Pi, X.; Ran, G.; Qin, G. Fully Transparent Quantum Dot Light-Emitting Diode with a Laminated Top Graphene Anode. *ACS Appl. Mater. Interfaces* **2017**, *9*, 24005−24010.
(892) Lee, J.; Choi, S.; Lee, T. W.; Hwang, Y. H.; Park, Y.; Jeong, S. Y.; Choi, K. C. RGB-Color Textile-Based Flexible and Transparent OLEDs Considering Aesthetics. *Adv. Mater. Interfaces* **2023**, *10*, 2202114.
(893) Wang, D.; Hauptmann, J.; May, C.; Hofstetter, Y. J.; Vaynzof, Y.; Müller, T. Roll-to-roll fabrication of highly transparent Ca:Ag top-electrode towards flexible large-area OLED lighting application. *Flexible Printed Electron.* **2021**, *6*, 035001.
(894) Jiang, W.; Lee, S.; Zhao, K.; Lee, K.; Han, H.; Oh, J.; Lee, H.; Kim, H.; Koo, C. M.; Park, C. Flexible and Transparent Electrode of Hybrid Ti3C2TX MXene−Silver Nanowires for High-Performance Quantum Dot Light-Emitting Diodes. *ACS Nano* **2022**, *16*, 9203−9213.
(895) Xie, C.; Zhao, X.; Ong, E. W. Y.; Tan, Z. K. Transparent near-infrared perovskite light-emitting diodes. *Nat. Commun.* **2020**, *11*, 4213.
(896) Bae, S.; Kim, S. J.; Shin, D.; Ahn, J.-H.; Hong, B. H. Towards industrial applications of graphene electrodes. *Phys. Scr.* **2012**, *T146*, 014024.
(897) Lu, H.-Y.; Chou, C.-Y.; Wu, J.-H.; Lin, J.-J.; Liou, G.-S. Highly transparent and flexible polyimide−AgNW hybrid electrodes with excellent thermal stability for electrochromic applications and defogging devices. *J. Mater. Chem. C* **2015**, *3*, 3629−3635.
(898) Cheong, W. S.; Kim, Y. H.; Lee, J. M.; Hong, C. H.; Choi, H. Y.; Kwak, Y. J.; Kim, Y. J.; Kim, Y. S. High-Performance Transparent Electrodes for Automobile Windshield Heaters Prepared by Combining Metal Grids and Oxide/Metal/Oxide Transparent Electrodes. *Adv. Mater. Technol.* **2019**, *4*, 1800550.
(899) Choi, S.; Park, J.; Hyun, W.; Kim, J.; Kim, J.; Lee, Y. B.; Song, C.; Hwang, H. J.; Kim, J. H.; Hyeon, T.; et al. Stretchable Heater Using Ligand-Exchanged Silver Nanowire Nanocomposite for Wearable Articular Thermotherapy. *ACS Nano* **2015**, *9*, 6626−6633.
(900) Hazarika, A.; Deka, B. K.; Kim, D. Y.; Park, Y.-B.; Park, H. W. Smart gating of the flexible Ag@CoxMo1-xP and rGO-loaded composite based personal thermal management device inspired by the neuroanatomic circuitry of endotherms. *Chem. Eng. J.* **2021**, *421*, 127746.
(901) Jung, D.; Kim, D.; Lee, K. H.; Overzet, L. J.; Lee, G. S. Transparent film heaters using multi-walled carbon nanotube sheets. *Sens. Actuators, A* **2013**, *199*, 176−180.
(902) Kang, J.; Kim, H.; Kim, K. S.; Lee, S. K.; Bae, S.; Ahn, J. H.; Kim, Y. J.; Choi, J. B.; Hong, B. H. High-performance graphene-based transparent flexible heaters. *Nano Lett.* **2011**, *11*, 5154−5158.
(903) Kim, H.; Lee, H.; Ha, I.; Jung, J.; Won, P.; Cho, H.; Yeo, J.; Hong, S.; Han, S.; Kwon, J.; et al. Biomimetic Color Changing Anisotropic Soft Actuators with Integrated Metal Nanowire Percolation Network Transparent Heaters for Soft Robotics. *Adv. Funct. Mater.* **2018**, *28*, 1801847.
(904) Nair, N. M.; Pakkathillam, J. K.; Kumar, K.; Arunachalam, K.; Ray, D.; Swaminathan, P. Printable Silver Nanowire and PEDOT:PSS Nanocomposite Ink for Flexible Transparent Conducting Applications. *ACS Appl. Electron. Mater.* **2020**, *2*, 1000−1010.
(905) Langley, D. P.; Lagrange, M.; Giusti, G.; Jimenez, C.; Brechet, Y.; Nguyen, N. D.; Bellet, D. Metallic nanowire networks: effects of thermal annealing on electrical resistance. *Nanoscale* **2014**, *6*, 13535−13543.
(906) Huang, Q.; Lilley, C. M.; Divan, R. An in situ investigation of electromigration in Cu nanowires. *Nanotechnology* **2009**, *20*, 075706.
(907) Yang, Y.; Chen, S.; Li, W.; Li, P.; Ma, J.; Li, B.; Zhao, X.; Ju, Z.; Chang, H.; Xiao, L.; et al. Reduced Graphene Oxide Conformally Wrapped Silver Nanowire Networks for Flexible Transparent Heating and Electromagnetic Interference Shielding. *ACS Nano* **2020**, *14*, 8754−8765.
(908) Shiu, E. Y. C.; Leung, N. H. L.; Cowling, B. J. Controversy around airborne versus droplet transmission of respiratory viruses: implication for infection prevention. *Curr. Opin. Infect. Dis.* **2019**, *32*, 372−379.
(909) Chin, A. W. H.; Chu, J. T. S.; Perera, M. R. A.; Hui, K. P. Y.; Yen, H. L.; Chan, M. C. W.; Peiris, M.; Poon, L. L. M. Stability of SARS-CoV-2 in different environmental conditions. *Lancet Microbe* **2020**, *1*, No. e10.
(910) Jung, W.; Lee, J. S.; Han, S.; Ko, S. H.; Kim, T.; Kim, Y. H. An efficient reduced graphene-oxide filter for PM2.5 removal. *J. Mater. Chem. A* **2018**, *6*, 16975−16982.
(911) Jeong, S.; Cho, H.; Han, S.; Won, P.; Lee, H.; Hong, S.; Yeo, J.; Kwon, J.; Ko, S. H. High Efficiency, Transparent, Reusable, and Active PM2.5 Filters by Hierarchical Ag Nanowire Percolation Network. *Nano Lett.* **2017**, *17*, 4339−4346.
(912) Han, S.; Kim, J.; Lee, Y.; Bang, J.; Kim, C. G.; Choi, J.; Min, J.; Ha, I.; Yoon, Y.; Yun, C. H.; et al. Transparent Air Filters with Active Thermal Sterilization. *Nano Lett.* **2022**, *22*, 524−532.
(913) Gao, W.; Emaminejad, S.; Nyein, H. Y. Y.; Challa, S.; Chen, K.; Peck, A.; Fahad, H. M.; Ota, H.; Shiraki, H.; Kiriya, D.; et al. Fully integrated wearable sensor arrays for multiplexed in situ perspiration analysis. *Nature* **2016**, *529*, 509−514.
(914) Guo, Y.; Zhang, X.-S.; Wang, Y.; Gong, W.; Zhang, Q.; Wang, H.; Brugger, J. All-fiber hybrid piezoelectric-enhanced triboelectric nanogenerator for wearable gesture monitoring. *Nano Energy* **2018**, *48*, 152−160.
(915) Yu, Y.; Peng, S.; Blanloeuil, P.; Wu, S.; Wang, C. H. Wearable Temperature Sensors with Enhanced Sensitivity by Engineering Microcrack Morphology in PEDOT:PSS-PDMS Sensors. *ACS Appl. Mater. Interfaces* **2020**, *12*, 36578−36588.
(916) Shin, J.; Jeong, S.; Kim, J.; Choi, Y. Y.; Choi, J.; Lee, J. G.; Kim, S.; Kim, M.; Rho, Y.; Hong, S.; et al. Dynamic Pore Modulation of Stretchable Electrospun Nanofiber Filter for Adaptive Machine Learned Respiratory Protection. *ACS Nano* **2021**, *15*, 15730−15740.
(917) Song, Y.; Min, J.; Yu, Y.; Wang, H.; Yang, Y.; Zhang, H.; Gao, W. Wireless battery-free wearable sweat sensor powered by human motion. *Sci. Adv.* **2020**, *6*, No. eaay9842.
(918) Yin, L.; Cao, M.; Kim, K. N.; Lin, M.; Moon, J.-M.; Sempionatto, J. R.; Yu, J.; Liu, R.; Wicker, C.; Trifonov, A.; et al. A stretchable epidermal sweat sensing platform with an integrated printed battery and electrochromic display. *Nat. Electron.* **2022**, *5*, 694−705.
(919) Kim, J.; Park, J.; Park, Y. G.; Cha, E.; Ku, M.; An, H. S.; Lee, K. P.; Huh, M. I.; Kim, J.; Kim, T. S.; et al. A soft and transparent contact lens for the wireless quantitative monitoring of intraocular pressure. *Nat. Biomed. Eng.* **2021**, *5*, 772−782.
(920) Yetisen, A. K.; Jiang, N.; Castaneda Gonzalez, C. M.; Erenoglu, Z. I.; Dong, J.; Dong, X.; Stosser, S.; Brischwein, M.; Butt, H.; Cordeiro, M. F.; et al. Scleral Lens Sensor for Ocular Electrolyte Analysis. *Adv. Mater.* **2020**, *32*, 1906762.
(921) Lee, H.; Choi, T. K.; Lee, Y. B.; Cho, H. R.; Ghaffari, R.; Wang, L.; Choi, H. J.; Chung, T. D.; Lu, N.; Hyeon, T.; et al. A graphene-based electrochemical device with thermoresponsive micro-

https://doi.org/10.1021/acs.chemrev.3c00139
Chem. Rev. 2023, 123, 9982−10078

needles for diabetes monitoring and therapy. *Nat. Nanotechnol.* **2016**, *11*, 566−572.
(922) Lee, H.; Lee, Y.; Song, C.; Cho, H. R.; Ghaffari, R.; Choi, T. K.; Kim, K. H.; Lee, Y. B.; Ling, D.; Lee, H.; et al. An endoscope with integrated transparent bioelectronics and theranostic nanoparticles for colon cancer treatment. *Nat. Commun.* **2015**, *6*, 10059.
(923) Wang, J.; Chen, Y.; Hao, S.; Peng, X.; Hu, L. Deep learning for sensor-based activity recognition: A survey. *Pattern Recognit. Lett.* **2019**, *119*, 3−11−3.
(924) Cui, Z.; Wang, W.; Xia, H.; Wang, C.; Tu, J.; Ji, S.; Tan, J. M. R.; Liu, Z.; Zhang, F.; Li, W.; et al. Freestanding and Scalable Force-Softness Bimodal Sensor Arrays for Haptic Body-Feature Identification. *Adv. Mater.* **2022**, *34*, 2207016.
(925) Wang, M.; Tu, J.; Huang, Z.; Wang, T.; Liu, Z.; Zhang, F.; Li, W.; He, K.; Pan, L.; Zhang, X.; et al. Tactile Near-Sensor Analogue Computing for Ultrafast Responsive Artificial Skin. *Adv. Mater.* **2022**, *34*, 2201962.
(926) Ko, S. H.; Rogers, J. Functional Materials and Devices for XR (VR/AR/MR) Applications. *Adv. Funct. Mater.* **2021**, *31*, 2106546.
(927) Yu, X.; Xie, Z.; Yu, Y.; Lee, J.; Vazquez-Guardado, A.; Luan, H.; Ruban, J.; Ning, X.; Akhtar, A.; Li, D.; et al. Skin-integrated wireless haptic interfaces for virtual and augmented reality. *Nature* **2019**, *575*, 473−479.
(928) Lee, J.; Sul, H.; Lee, W.; Pyun, K. R.; Ha, I.; Kim, D.; Park, H.; Eom, H.; Yoon, Y.; Jung, J.; et al. Stretchable Skin-Like Cooling/Heating Device for Reconstruction of Artificial Thermal Sensation in Virtual Reality. *Adv. Funct. Mater.* **2020**, *30*, 1909171.
(929) Yun, S.; Park, S.; Park, B.; Ryu, S.; Jeong, S. M.; Kyung, K.-U. A Soft and Transparent Visuo-Haptic Interface Pursuing Wearable Devices. *IEEE Trans. Ind. Electron.* **2020**, *67*, 717−724.
(930) Rahman, M. H.; Rahman, M. J.; Cristobal, O. L.; Saad, M.; Kenné, J. P.; Archambault, P. S. Development of a whole arm wearable robotic exoskeleton for rehabilitation and to assist upper limb movements. *Robotica* **2015**, *33*, 19−39.
(931) Yu, S.; Huang, T.-H.; Wang, D.; Lynn, B.; Sayd, D.; Silivanov, V.; Park, Y. S.; Tian, Y.; Su, H. Design and Control of a High-Torque and Highly Backdrivable Hybrid Soft Exoskeleton for Knee Injury Prevention During Squatting. *IEEE Rob. Autom. Lett.* **2019**, *4*, 4579−4586.

https://doi.org/10.1021/acs.chemrev.3c00139
Chem. Rev. 2023, 123, 9982−10078